#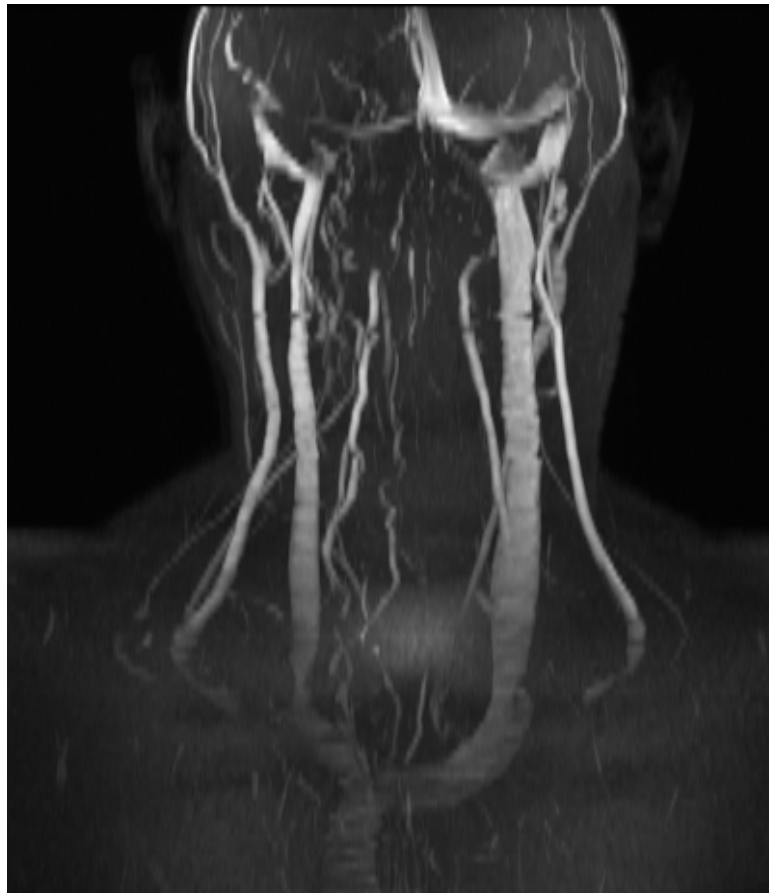 Mathematical modelling and simulation of the human circulation with emphasis on the venous system: application to the CCSVI condition

Lucas Omar Müller

UNIVERSITÀ DEGLI STUDI DI TRENTO

**Dipartimento di Ingegneria Civile,
Ambientale e Meccanica**

2014

Abstract

Recent advances in medical science regarding the role of the venous system in the development of neurological conditions has renewed the attention of researchers in this district of the cardiovascular system. The main goal of this thesis is to perform a theoretical study of Chronic CerebroSpinal Venous Insufficiency (CCSVI), a venous pathology that has been associated to Multiple Sclerosis. CCSVI is a condition in which main cerebral venous drainage pathways are obstructed. Its impact in cerebral hemodynamics and its connection to Multiple Sclerosis is subject of current debate in the medical community. In order to perform a credible study of the haemodynamical aspects of CCSVI, a sufficiently accurate mathematical model of the problem under investigation must be used. The venous system has not received the same attention as the arterial counterpart by the medical community. As a consequence, the mathematical modeling and numerical simulation of the venous system lies far behind that of the arterial system. The venous system is a low-pressure system, formed by very thin-walled vessels, if compared to arteries, that are likely to collapse under the action of gravitational or external forces. These properties set special requirements on the mathematical models and numerical schemes to be used. In this thesis we present a closed-loop multi-scale mathematical model of the cardiovascular system, where medium to large arteries and veins are represented as one-dimensional (1D) vessels, whereas the heart, the pulmonary circulation, capillary beds and intracranial pressure are modeled as lumped parameter models. A characteristic feature of our closed-loop model is the detailed description of head and neck veins. Due to the large inter-subject variability of the venous system, we perform a patient-specific characterization of major veins of the head and neck using MRI data collected in collaboration with the Magnetic Resonance Research Facility of the Wayne State University, Detroit (USA). Computational results are carefully validated using published data for the arterial system and most regions of the venous system. For head and neck veins validation is carried out through a detailed comparison of simulation results against patient-specific Phase-Contrast MRI flow quantification data. Regarding the development of novel numerical schemes, we construct high-order accurate, robust and efficient numerical schemes for 1D blood flow in elastic and viscoelastic vessels, as well as a solver for vessel networks. The solver is validated in the context of an *in vitro* network of vessels for which experimental and numerical results are available. After validation of both, the mathematical model and the numerical methodology, we use our theoretical tool to study the influence of different CCSVI patterns on cerebral hemodynamics. CCSVI patterns are defined by the medical literature as combinations of venous obstructions at different locations. Here we used two strategies. First, we take a venous configuration corresponding to a healthy control and explore the effect of different CCSVI patterns by modifying this network. Then, we characterize our venous network with the geometry of a real CCSVI patient and compare results with the ones obtained for the healthy control. The presented model provides a powerful tool to study still unresolved aspects of cerebral blood flow physiology, as well as several venous pathologies. Furthermore, it constitutes an ideal platform for improving currently used algorithms and for integrating fundamental physiological processes, such as detailed hemodynamics, regulatory mechanisms and transport of substances.

Acknowledgments

My first thought goes to my wife Wenddi. Her support and encouragement have been fundamental during this long-term project. I am proud and honored for having the opportunity to build our family together. I would also like to express my profound gratitude to my family. Without the many sacrifices made by my parents I could have never completed this long journey.

I was extremely fortunate to have met Prof. Eleuterio F. Toro during my undergraduate studies. I am grateful for his guidance during these years and for the many opportunities that he has offered me. I hope to have fully absorbed his dedication to science and will always be grateful for this opportunity.

I would like to thank Prof. Carlos Parés and his group at the University of Málaga. My stay at their institute and the work carried out together was an essential initiation to the numerical solution of non-conservative hyperbolic systems. A thought goes also to Prof. Michael Dumbser. He was always available when I had doubts regarding the numerical methodology adopted in this thesis.

I am pleased to acknowledge Gino I. Montecinos for the time spent together during this PhD project. He has become a precious friend and his support as applied mathematician has been fundamental at many stages of my work. A thought goes also to Alfonso Caiazzo, his help in making the code developed during the completion of this thesis more readable and modular was fundamental.

An essential aspect of my PhD research project was the opportunity offered to me by Prof. E. M. Haacke (MR Research Facility, Wayne State University, Detroit, USA) to visit his research facility during two months in order to gather the MRI data used in this work. During my stay in Detroit I learned a lot about the anatomy of the venous system and became familiar with MRI imaging techniques. In this context I would also like to mention the support received from David Utriainen.

I would like to thank Prof. Zamboni and his team, for the many instructive visits to Ferrara and Bologna and their visits to Trento. These meetings were fundamental for two reasons: understanding the physiology of the venous system and finding motivation for the development of our work.

A special thank goes to Prof. Carmelo Anile, from the Institute of Neurosurgery of the Catholic University in Rome, for useful discussions on cerebral venous hemodynamics and his contribution to the extension of our mathematical model.

A thought goes to the International Society of Neurovascular Disease. At the beginning of this research project we took part to an annual meeting as spectators and with the time we were given the opportunity to actively participate. This fact shows that this society is truly interested in the insights that mathematics can give to their research.

I would also like to warmly thank Dr. Jordy Alastruey (King's College and St Thomas' Hospital, London, UK) for very helpful discussions that contributed to the development of my solver for blood flow in networks of vessels and for sharing with me his numerical results and experimental measurements. This information was essential for the validation of my work.

I conclude this section expressing my gratitude to the PhD School in Environmental Engineering at the Department of Civil, Environmental and Mechanical Engineering of the University of Trento, for the financial support of this PhD research project in terms of scholarships and allowances for participating to relevant conferences and schools.

viii

Contents

Scientific production

Papers published or submitted during this PhD research project:

- L. O. Müller, G. I. Montecinos, and E. F. Toro. Some issues in modelling venous haemo-dynamics. In P. García-Navarro M. E. Vázquez-Cendón, A. Hidalgo and L. Cea, editors, *Numerical Methods for Hyperbolic Equations: Theory and Applications. An international conference to honour Professor E. F. Toro*, pages 347–354. Taylor & Francis Group, Boca Raton London New York Leiden, 2013.

- L. O. Müller, C. Parés, and E. F. Toro. Well-balanced high-order numerical schemes for one-dimensional blood flow in vessels with varying mechanical properties. *Journal of Computational Physics*, 242:53 – 85, 2013.

- L. O. Müller and E. F. Toro. Well-balanced high-order solver for blood flow in networks of vessels with variable properties. *International Journal for Numerical Methods in Biomedical Engineering*, 29:1388–1411, 2013.

- L. O. Müller and E. F. Toro. A global multiscale mathematical model for the human circulation with emphasis on the venous system. *International Journal for Numerical Methods in Biomedical Engineering*, pages n/a–n/a, 2014. In Press.

- G. Montecinos, L. Müller, and E. F. Toro. Hyperbolic reformulation of a 1D viscoelastic blood flow model and ADER finite volume schemes. *Journal of Computational Physics*, 2014. In Press.

- A. Caiazzo, G. Montecinos, L. O. Müller, E. M. Haacke, and E. F. Toro. Computational haemodynamics in stenotic internal jugular veins. *Journal of Mathematical Biology*. Submitted for publication to the Journal of Mathematical Biology in May 2013.

- L. O. Müller and E. F. Toro. An enhanced closed-loop model for the study of cerebral venous blood flow. Submitted for publication to the Journal of Biomechanics in March 2014.

- L. O. Müller, E. F. Toro, and E. M. Haacke. A theoretical study of the CCSVI condition. Submitted for publiction to the Journal of the Royal Society Interface in March 2014.

List of Figures

List of Tables

Chapter 1

Introduction

1.1 Motivation and goals: CCSVI

Recently, Zamboni and coworkers described a disease called Chronic Cerebro-Spinal Venous Insufficiency (CCSVI) [183, 181]. CCSVI regards malformations or obstructions in veins that are responsible for the cerebral venous return. Due to the many alternative pathways that blood has available for leaving the brain [175], CCSVI patients do not show the dramatic symptoms observed when flow in cerebral arteries is altered. Nevertheless, CCSVI seems to have a strong association to Multiple Sclerosis (MS), as shown in [183, 144, 79]. MS has been always regarded as an autoimmune disease and its association to CCSVI has created considerable debate in the medical community. Results of studies on the association of both pathologies are controversial [60, 134], even though a meta-analysis study that takes into account results of a large number of papers dealing with this topic speaks in favor of an association between both diseases [96]. Moreover, there is evidence of altered vasculature at the level of small-sized brain veins [188] and low brain perfusion [184] in CCSVI patients.

Perhaps the most relevant aspect of CCSVI is that, in most cases, it can be easily treated by performing a balloon angioplasty in order to eliminate obstructions and blockages. This kind of treatment was performed in MS patients with, in many cases, tremendous benefits [182]. Currently, many large scale studies are trying to confirm/reject these results.

Most of the controversy regarding CCSVI is related to the way it is diagnosed. In order to obtain a CCSVI diagnosis, a patient has to fulfill two out of five criteria [181]. These criteria are assessed with Eco-Color Doppler Ultrasound (US) and here lies the weakest point of the procedure. In fact, US measurement of venous blood flow and morphology requires experienced professionals. Normally, US machines are tuned to image arteries and not veins. Moreover, the inter-subject variability of venous morphology and the collapsability of veins add complexity to the performance of a correct diagnosis. Unfortunately, procedures based on subject-independent techniques, such as Magnetic Resonance Imaging, can not be considered since the diagnosis of CCSVI takes into account measurements for the subject in both, supine and upright positions.

Our goal is that of constructing a mathematical model of the cardiovascular system that will allow to perform a theoretical assessment of the hemodynamical aspects of CCSVI. Such a model aims at providing an objective understanding on the fluid dynamics of CCSVI. This motivating example sets two requirements on our model. First, the description of head and neck veins should be sufficiently detailed, including the numerous collateral pathways of cerebral venous return [138]. Second, the model should include the main systemic veins in order to take into account some specific characteristics of the disease under study. We have therefore chosen to construct a closed-loop model of the entire cardiovascular system with emphasis on the venous district. The reader must note that previous work on the modelling of the venous system is rare and this fact constituted an additional challenge. In fact, we first had to develop proper numerical schemes to model blood flow in veins. Only then an accurate enough model of the venous system could be put in place. In order to achieve this goal, collaboration with medical imaging experts was of fundamental importance, since they provided the correct background on venous anatomy, as well as a large dataset of medical imaging of head and neck veins.

In the next section we review the main fields of research that are relevant to this work.

1.2   Mathematical modelling and numerical methods

Cardiovascular modelling

Cardiovascular mathematics is a challenging and considerably active branch of applied and computational mathematics. The complexity of the computational domain, the deformable nature of vessels and the different scales involved force the adoption of a multi-scale approach. In the vast literature regarding this topic one finds three-dimensional models that combine the modelling of the fluid and the vessel walls, one-dimensional models in which quantities are averaged across the vessel cross-sectional area, and lumped parameter models in which a further averaging is operated so that one ends up with a zero-dimensional model of the spatial domain. For a comprehensive review on the state of the art see [73]. In this context, one-dimensional models play a major role. They are normally used to model the entire domain of interest, in combination with lumped parameter models for a portion of the domain [2]. In some cases, regions of particular interest are treated with three-dimensional models [32], which are then coupled to one-dimensional models that describe the majority of the domain. The relevance of one-dimensional models for describing general flow patterns, such as pressure wave propagation and average velocities, was pointed out in the work of Grinberg *et al.* [77]; they also pointed out the need for high-order numerical schemes, valued by their contribution to efficiency of models to be used in large scale simulations.

The number of publications on one-dimensional models for the arterial system is considerably large. Most probably the first one-dimensional model of the cardiovascular system is the one proposed by Schaaf & Abbrecht [137]. The model comprised main arteries and was solved using the method of characteristics. Successively, Avolio [18] presented a more complete one-dimensional model, comprising 128 arterial segments. This model has been widely used as a basis for more complex models [29, 31]. The most successful one-dimensional model is certainly the one proposed by Stergiopulos *et al.* [149], which has been the basis for many theoretical and practical studies [142, 133, 50, 103]. Another interesting example on the development of one-dimensional models is the work by Matthys *et al.* [109], see also [2], where an *in vitro* model of the arterial system is constructed in order to validate numerical outputs of one-dimensional models. This model constitutes a relevant benchmark for any code for blood flow in networks of vessels, since geometrical and mechanical properties of vessels are carefully characterized. Moreover, flow rate and pressure was measured at several points of the network, allowing for a comprehensive validation of numerical results.

The above mentioned publications regard seminal works and relevant examples. Nevertheless, the number of papers dealing with the development of one-dimensional models and their application to study physiological and pathological conditions is extremely high, see [168] for a review. As we will see in the next paragraph, the situation changes drastically if we consider the available literature on one-dimensional models of the venous system.

Venous system modelling

In 1969, the journal IEEE Transactions on Bio-medical Engineering published an entire issue on the venous system. Main points identified by contributors included a description of mechanical properties of veins, their functioning and, consequently, their modelling. At that time the modelling community was well aware of the difficulties to be faced in order to model the venous system. The most relevant problems, or differences, compared to the arterial counterpart, concerned the collapsibility of veins and the effect of external forces, such as gravity and external pressure, on venous flow [37]. In their introductory letter to that issue, Noordergraaf and Kresch [125] put in evidence the increasing interest in the role played by the venous system in heart dynamics and circulation in general. They concluded prospecting a renewed interest in the modelling community in this research field. Two remarkable contributions of the 1969 issue of IEEE Transactions on Bio-medical Engineering are the works by Snyder & Rideout [146] and by Moreno *et al.* [112]. Both contributions represented early attempts to model the complete cardiovascular system, giving special attention to the description of the venous district. Snyder and Rideout [146] proposed a closed-loop lumped parameter model including vessel collapse, external pressure by respiration, venous tone regulation and gravity.

Unfortunately, not much progress has been done since those early days in the field of venous haemodynamics modelling. Most of the available work concerns the description of flow in collapsible tubes [140, 91, 69] and related numerical applications to rather simple problems [132, 35, 36]. Recently, some interesting works that combine research on mechanical properties of veins and the numerical resolution of related one-dimensional models have been published [20, 75, 108]. Some work on modelling of venous networks with one-dimensional approaches is available in the literature. Zagzoule and MarcVergnes [180] presented a model for cerebral circulation with major arteries, intracranial veins and the jugular veins. Cirovic *et al.* [52] modelled cerebral blood flow using the network proposed in [180] and including high gravitational acceleration, observing jugular vein collapse. Sheng *et al.* [141] presented an open-loop model with a one-dimensional description of arteries, veins and capillaries. Following the work of Sheng *et al.*, Alirezaye-Davatgar [6] proposed a similar model; no emphasis on results for the venous system is given. Vassilevski *et al.* [170] proposed a closed-loop model of the cardiovascular system with a one-dimensional description of veins; no details on the construction of the venous network, such as network topology, vessel dimensions and mechanical parameters, are provided. Finally, Ho *et al.* [84] reported the construction of a patient-specific one-dimensional model of the cerebral venous system, imposing artificial boundary conditions at the level of the superior vena cava and terminal veins.

Closed-loop models of the CVS

Closed-loop models of the cardiovascular system with a one-dimensional description of major vessels are rare. Two prominent examples are the closed-loop models proposed by Liang *et al.* [102] and by Blanco *et al.* [30]. In both cases the arterial system is modelled using a one-dimensional approach, while the heart, the pulmonary circulation, capillaries and veins are treated as lumped parameter compartments.

Numerical methods for blood flow in vessels with varying properties

The subject of one-dimensional models for blood flow in the presence of discontinuous vessel properties has been addressed in the past. Examples include Čanič [40] and the more recent work of Toro and Siviglia [160]. In [160] the authors put forward a simple mathematical model for one-dimensional blood flow in vessels with variable, even discontinuous, mechanical properties. This model has very recently been extended [161] to include other relevant parameters, such as reference cross-sectional area and external pressure. In both [160] and [161] Toro and Siviglia propose a new mathematical formulation of the problem, carry out a thorough analysis of the equations and provide the solution of the resulting Riemann problem in the case of discontinuous variation of mechanical and geometrical properties. In both of these works the authors draw attention to the challenging problem of designing suitable numerical methods to solve the hyperbolic equations accurately.

The refined numerical treatment of source terms in hyperbolic balance laws was first addressed by Roe [135]. In analogy to the choice of numerical fluxes, Roe proposed the use of *upwinding* as a way of devising better numerical schemes for source terms. Effective schemes along these lines were later proposed by various authors, see [26], [97] and [171], for example. The numerical treatment of *geometric-type* source terms has by now been thoroughly studied in the community concerned with the numerical solution of the shallow water equations, where such source terms arise from variable bottom topography [27, 39, 44]. In some of these developments, the concept of *well-balanced* schemes has been adopted, reflecting the fact that in the absence of time derivatives the schemes must respect the correct balance between the advective term (the flux) and the source term. These schemes are able to correctly reproduce steady solutions in the presence of source terms. As a way of designing useful schemes for hyperbolic balance laws, the framework of path-conservative numerical schemes, as suggested in [129], is gaining increasing popularity.

The issue of well-balanced schemes for one-dimensional blood flow has already been addressed in the past. Sherwin *et al.* [142], for example, proposed to use a two-rarefaction Riemann solver at locations where material properties vary abruptly and succeeded in devising a well-balanced scheme, though in terms of non-conservative variables. Recently, Delestre and Lagree [58] have also proposed a well-balanced finite-volume scheme for blood flow in the framework of Hydrostatic Reconstruction [15]. They just considered the case of a single parameter, namely variable reference cross-sectional area.

1.3 Contributions of the thesis

The work presented in this thesis can be divided into three main parts: development of efficient and high-order accurate numerical schemes for one-dimensional blood flow in vessels with varying properties, construction of a closed-loop model of the CVS with emphasis in the venous system and assessment of hemodynamical aspects of CCSVI. We briefly discuss the work performed in each one of these fields.

Development of numerical schemes for one-dimensional blood flow in vessels with varying properties

In Müller *et al.* [114] we used the simplified mathematical model proposed in [160] as a starting point to construct a well-balanced, high-order path-conservative numerical scheme for computing one-dimensional blood flow in both, arteries and veins (collapsible vessels). The proposed numerical scheme preserves, exactly, steady solutions in any flow regime, that is sub-, super- and trans-critical. This work can be found in section 3.1 of this thesis.

In a successive contribution we designed an efficient one-dimensional solver for both arteries and veins, using a reformulation of the classical one-dimensional blood flow model proposed by Toro and Siviglia [161]. We adopted the framework of path-conservative finite volume-type schemes and extended the Dumbser-Osher-Toro Riemann solver [67] for constructing well-balanced fluctuations for a first-order non-oscillatory scheme. Then we extended the resulting first-order scheme to higher order of accuracy in both space and time by adopting the ADER methodology [159], with the approach proposed in [64] for solving the associated generalised Riemann problem. The full methodology was then extended to deal with realistic networks of vessels, adopting standard techniques for the treatment of boundary conditions and vessel junctions. We validated our numerical scheme through two classes of problems. The first class consists of problems for which exact solutions exist, smooth and discontinuous. Then we validated both the model and the numerical scheme against results from an *in vitro* model [109] involving a network of compliant vessels, for which both experimental measurements and state-of-the-art numerical solutions have been published. This contribution can be found in section 3.2 of this thesis.

During the course of this PhD research project, the thesis' author contributed to the development of a novel solver for one-dimensional blood flow in viscoelastic vessels. This work was published in [110] and is not included in this thesis.

Construction of a closed-loop model of the CVS with emphasis on the venous system

We developed a closed-loop model of the CVS which enriches currently available closed-loop models, adding a one-dimensional description of the venous district. This model will constitute the basis on which the above discussed challenges of the venous system will be approached and, hopefully, resolved. A distinctive aspect of this work, is the performance of a patient-specific characterization of major veins of the head and neck. This approach is motivated by the great inter-subject variability of the venous system [138, 175]. In order to achieve this goal, we represent major head and neck veins of our venous network using Magnetic Resonance Imaging derived geometrical information [167]. Moreover, we are able to compare our computational results with MRI-derived time-resolved flow quantification data [70], again, in a patient-specific manner. This is possible because MRI imaging of venous structures and flow quantification are made within the same MRI session. The results of this work are reported in section 4.1 of this thesis.

Departing from the early work by Ursino [165], we enriched our model with a lumped parameter model of the intracranial pressure. By doing so, we coupled volume changes in the cerebral vasculature to pulsations in intracranial pressure. This choice is motivated by the association of CCSVI to MS, and recent developments in medical research that associate MS to altered CSF dynamics [107, 185]. Moreover, we enriched our network of cerebral veins and included a Starling resistor mechanism in these vessels, which ensures that pressure in cerebral veins is always higher than intracranial pressure. We validated our computational results by comparing them versus MRI-derived flow data and assessed the main factors for the determination of cerebral venous flow waveforms. Details on the enhanced model for the cerebral venous circulation can be found in section 4.2 of this thesis. Moreover, in section 4.3 we perform a simple sensitivity analysis.

Assessment of hemodynamical aspects of CCSVI

Zamboni *et al.* [183] identified four CCSVI patterns, corresponding to combinations of venous anomalies in different locations of the venous network. These anomalies can be stenoses, malformed valves, twisting of vessels or missing vessels. We assessed the impact of extracranial venous anomalies in two different ways. First, we considered the model proposed in [115], which corresponds to a healthy control, and introduced stenoses in the venous network in order to reproduce two of the four CCSVI patterns described by Zamboni *et al.* [183]. Second, we consider a real Multiple Sclerosis patient, which was also diagnosed positive for CCSVI. We personalized our model with patient-specific morphology of head and neck veins and assessed the resulting flow patterns, validating our results by comparing them to flow quantification data and discussing the main differences between the cerebral venous hemodynamics of the healthy control and the Multiple Sclerosis patient. The content of chapter 5 illustrates these results.

Chapter 2

Mathematical model

2.1 Blood flow in arteries and veins: the one-dimensional model

One-dimensional blood flow models result from averaging the incompressible Navier-Stokes equations over the vessel cross-section under some assumptions, including axial symmetry. Also, the structural mechanics of the vessel wall is simplified; relevant assumptions are radial displacement and elastic material properties. For a full derivation of the model see, for example, [73]. Even under such strong simplifications of reality, these models preserve the essential physical features of wave propagation in compliant vessels. The resulting one-dimensional equations for blood flow in elastic vessels are given by the following first-order, non-linear hyperbolic system

$$
\begin{cases}
\partial_t A + \partial_x q = 0\,, \\
\partial_t q + \partial_x \left(\hat{\alpha} \dfrac{q^2}{A} \right) + \dfrac{A}{\rho} \partial_x p = -f\,,
\end{cases}
\tag{2.1}
$$

where x is the axial coordinate along the longitudinal axis of the vessel; t is time; $A(x,t)$ is the cross-sectional area of the vessel; $q(x,t)$ is the flow rate; $p(x,t)$ is the average internal pressure over a cross-section; $f(x,t)$ is the friction force per unit length of the tube; ρ is the fluid density and $\hat{\alpha}$ is a coefficient that depends on the assumed velocity profile. Throughout this work we will take $\hat{\alpha} = 1$, which corresponds to a blunt velocity profile.

To close the system we adopt a tube law, whereby the internal pressure $p(x,t)$ is related to the cross-sectional area $A(x,t)$ and other parameters, namely

$$
p(x,t) = p_e(x,t) + \psi(x,t)\,.
\tag{2.2}
$$

Here $p_e(x,t)$ is the external pressure, prescribed, and $\psi(x,t)$ is the transmural pressure, assumed of the form

$$
\psi(x,t) = \psi(A(x,t), K(x), A_0(x)) = K(x)\phi(A(x,t), A_0(x))\,.
\tag{2.3}
$$

$K(x) = K(E(x), h_0(x))$ is a positive function that contains the combined variation in x of $E(x)$, the Young modulus, and of $h_0(x)$, the wall thickness; see [35] for details. The function $\phi(A, x)$ is assumed of the form

$$
\phi(A(x,t), A_0(x)) = \left(\frac{A(x,t)}{A_0(x)} \right)^m - \left(\frac{A(x,t)}{A_0(x)} \right)^n\,,
\tag{2.4}
$$

where $A_0(x)$ is the vessel cross-sectional area for a reference configuration, for which the transmural pressure is zero. The parameters m and n are obtained from higher-order models or simply computed from experimental measurements. We remark that there are mathematical constraints for the choice of m and n to satisfy hyperbolicity of the equations and for the genuinely non-linear character of the characteristic fields associated with the pressure related eigenvalues; full details are given in [161]. Throughout this work we assume $m > 0$ and $n \in (-2, 0)$. Typical values for collapsible tubes, such as veins, are: $m = 10$, $n = -1.5$; for

arteries $m = 0.5$, $n = 0$. Relations (2.3)-(2.4) arise from a mechanical model of the vessel wall displacement under the simplifying assumption of static equilibrium [72].

The spatial variation of the vessel properties K, A_0 and of the external pressure p_e give

$$\partial_x p = \partial_x p_e + K\phi_A \partial_x A + K\phi_{A_0}\partial_x A_0 + \phi\partial_x K \,, \tag{2.5}$$

where

$$\phi_A = \frac{\partial\phi}{\partial A}\,, \quad \phi_{A_0} = \frac{\partial\phi}{\partial A_0}\,.$$

Substituting (2.5) into (2.1) gives

$$\begin{cases} \partial_t A + \partial_x q = 0\,, \\ \partial_t q + \partial_x\left(\hat{\alpha}\dfrac{q^2}{A}\right) + \dfrac{A}{\rho}K\phi_A\partial_x A = -\dfrac{A}{\rho}\left(\partial_x p_e + K\phi_{A_0}\partial_x A_0 + \phi\partial_x K\right) - f\,. \end{cases} \tag{2.6}$$

The right-hand-side of the momentum balance equation includes *geometric-type* source terms, which, as stated in chapter 1, must be treated carefully.

2.2 The Toro-Siviglia model for blood flow in elastic vessels with variable geometrical and mechanical properties

In this work we adopt the reformulation of (2.6), proposed in [161], namely

$$\partial_t\mathbf{Q} + \mathbf{A}(\mathbf{Q})\partial_x\mathbf{Q} = \boldsymbol{S}(\boldsymbol{Q})\,, \tag{2.7}$$

where $\mathbf{Q}$ is given by

$$\mathbf{Q} = \left[A, q, K, A_0, p_e\right]^T\,, \tag{2.8}$$

and the coefficient matrix $\mathbf{A}(\mathbf{Q})$ is

$$\mathbf{A}(\mathbf{Q}) = \begin{bmatrix} 0 & 1 & 0 & 0 & 0 \\ c^2 - u^2 & 2u & \frac{A}{\rho}\phi & K\frac{A}{\rho}\phi_{A_0} & \frac{A}{\rho} \\ 0 & 0 & 0 & 0 & 0 \\ 0 & 0 & 0 & 0 & 0 \\ 0 & 0 & 0 & 0 & 0 \end{bmatrix}\,. \tag{2.9}$$

Here $u = q/A$ is the cross-sectional averaged velocity of the fluid, $\boldsymbol{S}(\boldsymbol{Q})$ is a source term vector

$$\boldsymbol{S}(\boldsymbol{Q}) = [0, -f, 0, 0, 0]^T \tag{2.10}$$

and c is the wave speed

$$c = \sqrt{\frac{A}{\rho}K\phi_A}\,. \tag{2.11}$$

System (2.7) is constructed from (2.6) by regarding the variable parameters $K(x)$, $A_0(x)$ and $p_e(x,t)$ to be new unknowns, satisfying

$$\partial_t K = 0\,, \quad \partial_t A_0 = 0\,, \quad \partial_t p_e = F(x,t)\,, \tag{2.12}$$

where $F(x,t)$ is a prescribed function for the external pressure. For a thorough mathematical analysis of system (2.7) see [161]. Here we recall some of the main features of the system, needed for the construction of numerical schemes presented in chapter 3. The eigenvalues of (2.9) are

$$\lambda_1 = u - c\,, \quad \lambda_2 = \lambda_3 = \lambda_4 = 0\,, \quad \lambda_5 = u + c\,. \tag{2.13}$$

The right eigenvectors of $\boldsymbol{A}(\boldsymbol{Q})$ corresponding to eigenvalues (2.13) are

$$\boldsymbol{R}_1 = \gamma_1 \begin{bmatrix} 1 \\ u-c \\ 0 \\ 0 \\ 0 \end{bmatrix}, \quad \boldsymbol{R}_2 = \gamma_2 \begin{bmatrix} \frac{A}{\rho} \frac{\phi}{u^2-c^2} \\ 0 \\ 1 \\ 0 \\ 0 \end{bmatrix}, \quad \boldsymbol{R}_3 = \gamma_3 \begin{bmatrix} \frac{A}{\rho} \frac{K\phi_{A_0}}{u^2-c^2} \\ 0 \\ 0 \\ 1 \\ 0 \end{bmatrix},$$

$$\boldsymbol{R}_4 = \gamma_4 \begin{bmatrix} \frac{A}{\rho} \frac{1}{u^2-c^2} \\ 0 \\ 0 \\ 0 \\ 1 \end{bmatrix}, \quad \boldsymbol{R}_5 = \gamma_5 \begin{bmatrix} 1 \\ u+c \\ 0 \\ 0 \\ 0 \end{bmatrix},$$

(2.14)

where γ_i, for $i = 1, ..., 5$, are arbitrary scaling factors.

Under a suitable assumption for coefficients m and n, system (2.7) is hyperbolic, though not strictly hyperbolic. Hyperbolicity is lost when $|u| = c$, leading to resonance. As noted in [161] there is a possible loss of uniqueness.

The first and fifth characteristic fields are genuinely non-linear and are associated with shocks and rarefactions, whereas the remaining fields are linearly degenerate (LD) and are associated with stationary contact discontinuities. See [161] for conditions on parameters m and n for this to be true. The Riemann invariants associated with the genuinely non-linear fields are

$$\Gamma_1 = u - \int_{A^*}^{A} \frac{c(\tau)}{\tau} d\tau, \quad \Gamma_5 = u + \int_{A^*}^{A} \frac{c(\tau)}{\tau} d\tau,$$

(2.15)

where A^* is the cross-sectional area at a reference state. The Riemann invariants associated with the LD fields are given by

$$\Gamma_1^{LD} = p + \frac{1}{2}\rho u^2, \quad \Gamma_2^{LD} = q.$$

(2.16)

2.3 Correct choice of the mathematical formulation

The second equation of system (2.1) can be written in terms of the flow rate q or of the velocity u. The first choice regards a conserved quantity, the momentum, and is therefore called conservative formulation, whereas velocity is not a conserved quantity and therefore if the momentum equation is written in terms of u we speak about a non-conservative formulation. Here it is important to remark that we are referring to the choice of variables and not to the fact of writing the governing equations in conservative or non-conservative form. As the non-conservative formulation is often used to solve problems that include elastic jumps, we would like to assess the errors that may be introduced by this formulation. Accordingly, in this section we solve the Riemann problem exactly for both formulations and identify critical features that may arise when modelling collapsible vessels, such as veins.

2.3.1 Exact solution of the Riemann problem for the A, q (conservative) formulation

This problem was previously solved by Brook *et al.* [35] and later by Toro and Siviglia [160] for an augmented system to account for variable material (even discontinuous) properties. Here we collect their results very succinctly. The homogeneous version of system (2.1), without variations of mechanical and geometrical properties, can be written in conservation-law form as

$$\partial_t \mathbf{Q} + \partial_x \mathbf{F}(\mathbf{Q}) = 0,$$

(2.17)

where the conserved variables and flux are respectively

$$\mathbf{Q} = \begin{bmatrix} q_1 \\ q_2 \end{bmatrix} = \begin{bmatrix} A \\ Au \end{bmatrix}$$

(2.18)

and

$$\mathbf{F}(\mathbf{Q}) = \begin{bmatrix} Au \\ Au^2 + C \end{bmatrix} . \tag{2.19}$$

Here $C = \int_{A_0}^{A} c(\tau)^2 d\tau$, is a primitive of the *wave speed* c (2.11). We are taking as the reference state in the integral to be the equilibrium area A_0. The Jacobian of the system is

$$\mathbf{A}(\mathbf{Q}) = \begin{bmatrix} 0 & 1 \\ c^2 - u^2 & 2u \end{bmatrix} . \tag{2.20}$$

The eigenvalues of (2.20) are $\lambda_1 = u - c$ and $\lambda_2 = u + c$. The Riemann invariants, for later use, are

$$\begin{cases} \Gamma_1 = u - \displaystyle\int_{A_0}^{A} \frac{c(\tau)}{\tau} d\tau, \\[4mm] \Gamma_2 = u + \displaystyle\int_{A_0}^{A} \frac{c(\tau)}{\tau} d\tau. \end{cases} \tag{2.21}$$

We find the exact solution $\mathbf{Q}_{LR}(x/t)$ of the Riemann problem for system (2.7) with initial conditions

$$\mathbf{Q}(x, 0) = \begin{cases} \mathbf{Q}_L \text{ if } x < 0, \\ \mathbf{Q}_R \text{ if } x > 0. \end{cases} \tag{2.22}$$

We first find the constant state $\mathbf{Q}^*$ between the non-linear waves in the x-t plane. See [157] for details on the solution strategy. Appropriate functions connecting $\mathbf{Q}^*$ to the data states $\mathbf{Q}_L$ (left) and $\mathbf{Q}_R$ (right) give rise to the non-linear equation

$$f(A) = f_R(A, A_R) + f_L(A, A_L) + u_R - u_L = 0 , \tag{2.23}$$

where f_L and f_R are

$$f_K = \begin{cases} \displaystyle\int_{A_K}^{A} \frac{c(\tau)}{\tau} d\tau & \text{if } A \leq A_K, \\[4mm] \sqrt{B_K \dfrac{A - A_K}{A A_K}} & \text{if } A > A_K. \end{cases} \tag{2.24}$$

$$\begin{aligned} B_K &= \frac{K}{\rho} \left(\frac{m}{m+1} \frac{A^{m+1} - A_K^{m+1}}{A_0^m} \right) \\ &\quad - \frac{K}{\rho} \left(\frac{n}{n+1} \frac{A^{n+1} - A_K^{n+1}}{A_0^n} \right) . \end{aligned} \tag{2.25}$$

The root of the nonlinear equation (2.23) yields A_*. Finally, the speed u_* is computed as (see [157] for details)

$$\begin{aligned} u_* &= \frac{1}{2}(u_L + u_R) \\ &\quad + \frac{1}{2}\left[f_R(A_*, A_R) - f_L(A_*, A_L) \right]. \end{aligned} \tag{2.26}$$

The velocity of propagation of the elastic jump is

$$S_L = u_L - \frac{M_L}{A_L}, \quad S_R = u_R + \frac{M_R}{A_R}, \tag{2.27}$$

where the mass flux is given by

$$M_K = \sqrt{B_K \frac{A_* A_K}{A_* - A_K}} . \tag{2.28}$$

We omit the details for the solution inside rarefaction fans.

2.3.2 Exact solution of the Riemann problem for the A, u (non-conservative) formulation

For smooth solutions system (2.1) can be written in terms of A and u, still expressed in (mathematical) conservation-law form (2.17). Now the vector of unknowns is

$$\mathbf{Q} = \begin{bmatrix} q_1 \\ q_2 \end{bmatrix} = \begin{bmatrix} A \\ u \end{bmatrix} \tag{2.29}$$

and the flux vector is

$$\mathbf{F}(\mathbf{Q}) = \begin{bmatrix} Au \\ \frac{1}{2}u^2 + \frac{p}{\rho} \end{bmatrix}, \tag{2.30}$$

where p is the internal pressure (2.2). The Jacobian of the system is

$$\mathbf{A}(\mathbf{Q}) = \begin{bmatrix} u & A \\ c^2 - u^2 & u \end{bmatrix}. \tag{2.31}$$

The eigenvalues and wave speed for (2.31) are identical to those of Jacobian (2.20), but the eigenvectors of (2.31) are different. However the resulting Riemann invariants coincide.

Now the functions f_L and f_R in (2.23) are

$$f_K = \begin{cases} \displaystyle\int_{A_K}^{A} \frac{c(\tau)}{\tau} d\tau & \text{if } A \leq A_K, \\[2mm] \displaystyle\sqrt{\frac{2}{\rho} \frac{p - p_K}{A^2 - A_K^2}} (A - A_K) & \text{if } A > A_K. \end{cases} \tag{2.32}$$

The speed u_* is computed from (2.26), with f_L and f_R from (2.32). The expression defining the elastic jump speed has the form of (2.27), but in this case mass fluxes are

$$M_K = \sqrt{\frac{2}{\rho} \frac{p_* - p_L}{A_*^2 - A_K^2}} A_* A_K. \tag{2.33}$$

2.3.3 Shock speed prediction

The elastic jump speeds for both formulations differ, as can be seen by comparing (2.28) and (2.33). Moreover, functions defining the solution of the Riemann problem also differ, since relations (2.24) and (2.32) are not equivalent. Hence, in general solutions are not equivalent, at the analytical level.

In particular, there is a parameter that strongly influences how solutions differ, namely the wave speed (2.11). The wave speed varies considerably with the ratio $\alpha = \frac{A}{A_0}$, as shown in figure 2.1. For elastic jumps the shock speeds in both formulations are different and they are very different as the shock strength increases and this is particularly the case for nearly collapsed states (figure 2.2). This consideration is supported by the fact that for low α we may still have large $\frac{A_*}{A}$ ratios, as in the case of a nearly collapsed vessels. In other words, the magnitude of errors computed by using the non-conservative formulation is large for the case of nearly collapsed states, which can generate large elastic-jump strengths. This limitation of the non-conservative formulation will become evident when showing results on a numerical test for the collapse of a giraffe jugular vein, see section 2.3.4. We have pointed out possible errors that may be introduced in the numerical solution of the problem if an inappropriate formulation of the mathematical model is used. Moreover, errors may be larger for collapsible tubes. Another important conclusion is that in collapsed states, the wave speed (2.11) will decrease considerably, making the transition from subcritical to supercritical flow regimes feasible. These considerations indicate that the numerical scheme should be able to capture elastic jumps, or sharp gradients in general, in a correct manner and to deal with supercritical as well as subcritical regimes. This last property is not common in one-dimensional numerical models for blood flow in arteries, but seems to be mandatory for models applied to collapsible vessels, such as veins.
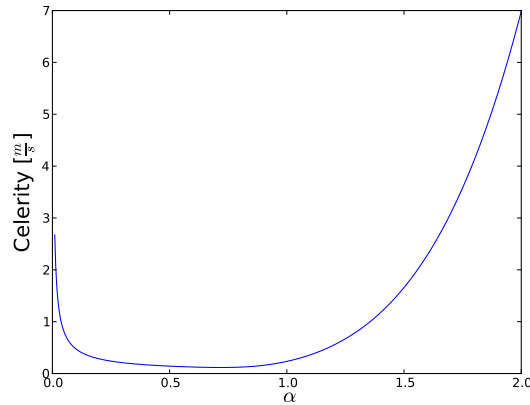
Figure 2.1: Wave speed (2.11). Parameters: $A_0 = 0.001m^2$, $m = 10$, $n = -1.5$, $\rho = 1050\frac{kg}{m^3}$, $K = 5Pa$.
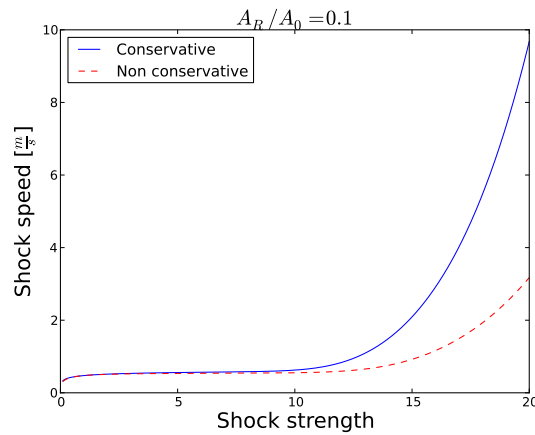
Figure 2.2: Elastic jump speeds obtained using the conservative and non-conservative formulations. Parameters: $A_0 = 0.001m^2$, $m = 10$, $n = -1.5$, $\rho = 1050\frac{kg}{m^3}$, $K = 5Pa$

2.3.4   Collapse of a giraffe jugular vein

Although numerical schemes have not been yet introduced to the reader, we have chosen to show at this stage numerical results that put in evidence the above made considerations on the correct choice of the model formulation. Details on the numerical methodology used to obtain these results are given in [113]. This test was proposed by Pedley *et al.* [132] for the stationary case and solved later for the unsteady case by Brook *et al.* [36].

The test is very useful because it addresses several issues that we have identified as crucial for the development of numerical schemes for flow in collapsible tubes. The tube collapses and the transient phase involves the transition through a critical point from supercritical to subcritical regime via an elastic jump. The scheme will thus have to deal with different regimes and elastic jumps. Moreover, the solution of elastic jumps accentuates errors produced by the non-conservative formulation, since we have a strongly collapsed vessel. This condition was identified as critical in section 2.3.3.

Test parameters are: domain lenght: $L = 2\,m$; area at rest $A_0 = 0.0005\,m^2$; wall stiffness $K = 5\,Pa$; tube law coefficients $m = 10$ and $n = -1.5$ initial conditions: $A(x,0) = (0.2 + 1.8\xi)\,A_0$, $(Au)(x,0) = (Au)_0 = 40\,\frac{ml}{s}$ and boundary conditions: $A(2,t) = 2A_0$, $(Au)(0,t) = (Au)_0$.

The development of the transient phase can be described as follows: two forces act in contrasting ways, gravity tends to empty the vessel, while downstream boundary conditions tend

to inflate it. The emptying due to gravity generates a supercritical flow in the upstream portion of the vessel, while downstream boundary conditions impose subcritical flow. Connection of both conditions is achieved via an elastic jump. The problem was solved using a second order ADER scheme with a CFL number $CFL = 0.9$ for both formulations, the conservative and the non-conservative ones. Figure 2.3 shows discrepancies between numerical solutions during the transient phase, deriving from observations made in section 2.3.3. The same discrepancies are found when the stationary solution is reached (figure 2.4).
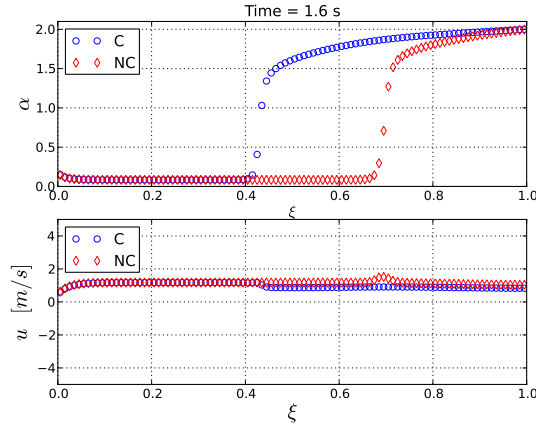
Figure 2.3: Giraffe jugular vein collapse test. Solution at output time $t = 1.6s$, during the transient phase. C: conservative formulation; NC: non-conservative formulation.
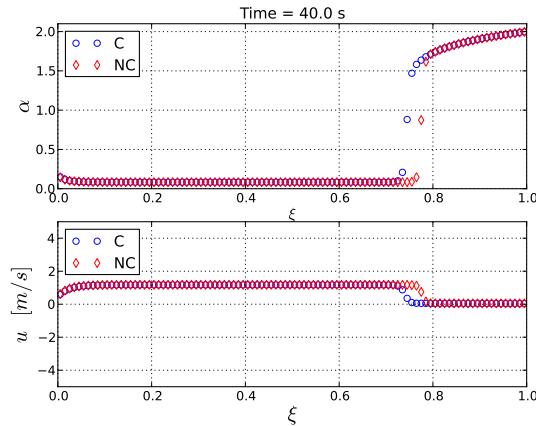
Figure 2.4: Giraffe jugular vein collapse test. Solution at output time $t = 40.0s$, corresponding to the steady solution. C: conservative formulation; NC: non-conservative formulation.

In the next section we analyse a further aspect of the mathematical model which may have profound consequences in the design of a robust and accurate numerical scheme for solving system (2.1), namely the source term.

2.4 Source term stiffness

If we consider source terms, such as gravitational forces and dissipation due to viscous forces, system (2.1) can be rewritten as

$$\partial_t \mathbf{Q} + \partial_x \mathbf{F}(\mathbf{Q}) = \mathbf{S}(\mathbf{Q}), \tag{2.34}$$

where $\mathbf{Q}$ is given in (2.18) and the flux vector $\mathbf{F}(\mathbf{Q})$ is (2.19). The source term is given by

$$\mathbf{S}(\mathbf{Q}) = \begin{bmatrix} 0 \\ Ag - Ru \end{bmatrix}. \tag{2.35}$$

The function R is obtained from an assumed velocity profile; here we adopt the one proposed in [132]

$$R = \frac{8\pi\nu A_{ref}^{\frac{1}{2}}}{A^{\frac{1}{2}}}, \tag{2.36}$$

where ν is the kinematic viscosity and A_{ref} is a reference cross-sectional area. If $A_{ref} = A$ one recovers the friction term for tubes which when collapsing maintain a circular shape. When setting $A_{ref} = A_0$, R represents the friction term for a tube that assumes an elliptical shape during collapse (as for highly compliant vessels, such as veins).

In this section we concentrate our attention on the study of the stiffness of the source term. A source term can be considered stiff if

$$\Delta t \, max_i \{|\beta_i|\} > 1, \quad i = 1, \dots, N, \tag{2.37}$$

where β_i is the i-th eigenvalue of the Jacobian of (2.35), $\frac{\partial \mathbf{S}(\mathbf{Q})}{\partial \mathbf{Q}}$, and N is the number of unknowns of the system.

Assuming a CFL-number $CFL = 1$ we can express relation (2.37) in terms of ratios between the eigenvalues of the dissipative/productive process and the characteristic speeds for the advective process, namely

$$\Delta x \frac{max_i \{|\beta_i|\}}{max_i \{|\lambda_i|\}} > 1 . \tag{2.38}$$

See [64]. Replacing (2.36) in source term (2.35) gives

$$\mathbf{S}(\mathbf{Q}) = \begin{bmatrix} 0 \\ gq_1 - 8\pi\nu A_0^{\frac{1}{2}} \frac{u}{A^{\frac{1}{2}}} \end{bmatrix}. \tag{2.39}$$

Its Jacobian is

$$\frac{\partial \mathbf{S}(\mathbf{Q})}{\partial \mathbf{Q}} = \begin{bmatrix} 0 & 0 \\ g + 12\pi\nu A_0^{\frac{1}{2}} \frac{u}{A^{\frac{3}{2}}} & -8\pi\nu A_0^{\frac{1}{2}} \frac{1}{A^{\frac{3}{2}}} \end{bmatrix}. \tag{2.40}$$

The eigenvalues of (2.40) are

$$\beta_1 = 0, \quad \beta_2 = -8\pi\nu A_0^{\frac{1}{2}} \frac{1}{A^{\frac{3}{2}}} = -8\pi\nu \frac{1}{\alpha^{\frac{1}{2}} A}. \tag{2.41}$$

We carry out an approximate analysis of the order of magnitude of ratio (2.38) for physiological values of the parameters involved with $A : O(10^{-4} \div 10^{-7})$, $u : O(10^0)$, $c : O(10^0)$, $\nu : O(10^{-6})$. We obtain

$$\Delta x \frac{8\pi\nu \frac{1}{\alpha^{\frac{1}{2}} A}}{u + c} \approx \Delta x \frac{\frac{O(10^1) O(10^{-6})}{\alpha^{\frac{1}{2}} O(10^{-4} \div 10^{-7})}}{O(10^0)}$$

$$\approx O(10^{-1} \div 10^2) \frac{\Delta x}{\alpha^{\frac{1}{2}}}. \tag{2.42}$$

The resulting ratio corresponds to a source term that may become stiff. The parameter α in (2.42) makes it evident that the collapse of a vessel may easily lead to an increase of (2.42) by one order of magnitude.

Considerations made in this section show us that the model applied to collapsible tubes may have stiff source terms, which means that one must choose appropriate numerical schemes for the modelling of collapsible tubes to treat stiff source terms correctly. This task is not trivial and only few schemes available in the literature are potential candidates.

2.5   Concluding remarks

We have described a one-dimensional mathematical model for blood flow in large to medium-sized arteries and veins. Assuming constant material properties we have studied two possible formulations of the equations, a conservative and a non-conservative one. Then we have solved exactly the Riemann problem for both formulations and have assessed their suitability for various scenarios. We have in addition discussed the source terms present in both formulations and their potential stiffness, with the associated numerical complications.

In the next chapter we describe the development of two numerical schemes for one-dimensional blood in elastic vessels with variable mechanical and geometrical properties.

Chapter 3

Numerical methods

There is an extensive literature on the numerical solution of one-dimensional blood flow models. All kinds of numerical methodologies were used to solve the underlying mathematical model: the finite-difference Lax-Wendroff scheme [41, 103]; the discontinuous Galerkin scheme [143, 2]; finite element schemes [164, 72] and finite volume schemes [58]. These references represent some examples, but the available literature is extremely vast. In this chapter we describe the development of two high-order finite volume-type numerical schemes for one-dimensional blood flow in vessels with varying mechanical and geometrical properties.

3.1 Well-balanced high-order numerical schemes for one-dimensional blood flow in vessels with varying mechanical properties

3.1.1 Introduction

Cardiovascular mathematics is a challenging and considerably active branch of applied and computational mathematics. The complexity of the computational domain, the deformable nature of vessels and the different scales involved force the adoption of a multi-scale approach. In the vast literature regarding this topic one finds three-dimensional models that combine the modelling of the fluid and the vessel walls, one-dimensional models in which quantities are averaged across the vessel cross-sectional area, and lumped parameter models in which a further averaging is operated so that one ends up with a zero-dimensional model of the spatial domain. For a comprehensive review on the state-of-the-art see [73]. In this context, one-dimensional models play a major role. They are normally used to model the entire domain of interest, in combination with lumped parameter models for a portion of the domain [2]. In some cases, regions of particular interest are treated with three-dimensional models [32], which are then coupled to one-dimensional models that describe the majority of the domain. The relevance of one-dimensional models for describing general flow patterns, such as pressure wave propagation and average velocities, was pointed out in the work of Grinberg *et al.* [77]; they also pointed out the need for high-order numerical schemes, valued by their contribution to efficiency of models to be used in large scale simulations.

Mechanical properties of vessels may vary in space due to the placement of a stent, to the presence of a stenosis or simply to physiological variations. In the case of one-dimensional models, the variation of mechanical properties generates a source term involving the spatial derivative of a parameter related to mechanical properties of the vessel, the wall stiffness K, and the cross-sectional area of the vessel A, which is a state variable of the model. This source term prevents us from writing the governing equations in conservation-law form. The presence of such source terms have theoretical and practical implications in both the mathematical properties of the model and the numerical schemes to be used to obtain approximate solutions. In the literature, the additional source term arising from the variation of mechanical properties is normally treated as an additional source term (see [35, 72], for example). This approach will have implications on the numerical solutions by creating non-physical spurious oscillations. In

other words, the resulting numerical scheme will be unable to correctly compute steady and unsteady solutions. It is well known that other properties that define the vessel geometry may vary along its longitudinal axis. The most prominent example is that of the cross-sectional area at reference state A_0. In fact, arteries are tapered and in many applications this special feature is included in the geometrical description of the arterial network. Another relevant parameter is the external pressure p_e, which represents the pressure exerted by tissues that surround the vessel. While in this section we consider the numerical treatment of source terms related only to variations of mechanical properties, this work aims to be a first step towards a numerical treatment of all relevant variables. In fact, the methodology developed in this section is applicable to other parameters such as A_0 and p_e.

Recently, Toro & Siviglia [160] presented a reformulation of the classic one-dimensional model for blood flow in vessels with varying mechanical properties, including the case in which variations are discontinuous; analysis of the system was carried out and the exact solution of the corresponding Riemann problem was also given. For an extension of this work see [161]. The main purpose of this section is to develop well-balanced, high-order numerical schemes for the Toro-Siviglia model [160] by adopting the ADER framework [159]. The three building blocks of the ADER finite volume schemes are: a first-order monotone numerical flux, a non-linear spatial reconstruction operator and the solution of the Generalised Riemann Problem (GRP) at each cell interface in order to compute the numerical flux [162]. Here we use the ADER-type scheme proposed in [64] and extended to non-conservative systems in [63] and [65]. In this version of the scheme the data is evolved locally within the cell space-time volume using an implicit local discontinuous Galerkin finite element scheme. We work in the context of the theory developed by Dal Maso *et al.* [56] that defines weak solutions for non-conservative hyperbolic systems. The schemes presented here are part of a family of numerical schemes developed to solve non-conservative hyperbolic systems, the path-conservative numerical schemes, introduced by Parés [129]. In order to construct a first-order well-balanced numerical flux we apply the Generalised Hydrostatic Reconstruction technique [47] to the system under study. We modify a conventional operator, based in the methodology presented in [45] for obtaining well-balanced spatial reconstruction operators, noting that the conventional ones do not have well-balanced properties. We then modify the implicit local discontinuous Galerkin data evolution procedure in the solution of the GRP in order to preserve well-balanced properties. Finally, we solve several steady and unsteady problems in order to demonstrate that well-balanced properties are mandatory for obtaining correct numerical solutions for both steady and time-dependent problems.

The rest of this section is structured as follows. In subsection 3.1.2 we present the mathematical model under study. Next, in subsection 3.1.3, we perform a detailed analysis of the integral curves of the linearly degenerate field of the mathematical model that is crucial for the design of well-balanced numerical schemes. In subsection 3.1.4 we introduce the Generalised Hydrostatic Reconstruction and describe its implementation for the model that is being studied, proving the well-balanced properties of the resulting numerical scheme. We proceed further in subsection 3.1.5 with the description of the extension of the well-balanced scheme to high-order of accuracy in space and time. In subsection 3.1.6 we present numerical results regarding the order of accuracy of the scheme, its ability to capture steady solutions and results for Riemann problems for which an exact solution is available. We conclude with subsection 3.1.7, where final considerations are made.

3.1.2   Mathematical model

We recall the one-dimensional blood flow model introduced in section 2.1, given by

$$
\begin{cases}
\partial_t A + \partial_x q = 0 \,, \\
\partial_t q + \partial_x \left(\hat{\alpha} \dfrac{q^2}{A} \right) + \dfrac{A}{\rho} \partial_x p = A\, g - f \,.
\end{cases}
\tag{3.1}
$$

$A(x,t)$ represents the cross-subsectional area of the vessel, $q(x,t)$ the mass-flux, $p(x,t)$ the average internal pressure over the cross-subsection, ρ the fluid density, g the acceleration due to gravity along the longitudinal axis of the vessel and $f(x,t)$ the friction force per unit length

of the tube. The value of $\hat{\alpha}$ is determined by the velocity profile. Throughout this work we will consider $\hat{\alpha} = 1$ in the momentum equation, which corresponds to a blunt velocity profile, and will neglect friction forces and gravity effects. For a full description of the derivation of the model see [73].

As there are more unknowns than equations one needs a closure condition via a tube law in which pressure is expressed in terms of cross-subsectional area. The internal pressure $p(x,t)$ can be expressed as

$$p(x,t) = p_e(x,t) + \psi(x,t) \,. \tag{3.2}$$

We consider constant external pressure p_e and for the transmural pressure $\psi(x,t)$ the following expression is adopted

$$\psi(x,t) = K(x)\phi(A, A_0) \,, \tag{3.3}$$

where $K(x)$ is a known positive function of the vessel wall Young modulus $E(x)$ and the wall thickness $h_0(x)$ (see [35] for details). Moreover, $\phi(A, A_0)$ is

$$\phi(A, A_0) = \left(\frac{A(x,t)}{A_0(x)}\right)^m - \left(\frac{A(x,t)}{A_0(x)}\right)^n \,. \tag{3.4}$$

$A_0(x)$ represents the vessel cross-subsectional area in an unloaded configuration. Normally, m and n are parameters derived from higher order models or simply computed from experimental measurements. Throughout this work we will assume $m > 0$ and $n \in (-2, 0)$. Typical values for collapsible tubes, such as veins, are: $m = 10$, $n = -1.5$. For arteries we have: $m = 0.5$, $n = 0$. Equations (3.3)-(3.4) come from a mechanical model of the vessel wall displacement under the simplifying assumption of static equilibrium [72].

In this section we consider the case for which only K varies with x, but A_0 is taken as a constant. Thus

$$\phi = \phi(A) \,.$$

As a consequence we have that

$$\partial_x p = K'(x)\phi(A) + K(x)\phi'(A)\partial_x A \,. \tag{3.5}$$

As a preliminary step we introduce the following functions to be used later on

$$\Phi(A) = \int_{A_0}^A \phi(a)\, da = A_0\left(\frac{1}{m+1}\left(\frac{A}{A_0}\right)^{m+1} - \frac{1}{n+1}\left(\frac{A}{A_0}\right)^{n+1}\right) + A_0\frac{m-n}{(m+1)(n+1)} \,, \tag{3.6}$$

$$\tilde{\Phi}(A) = \int_{A_0}^A a\phi'(a)\, da = A_0\left(\frac{m}{m+1}\left(\frac{A}{A_0}\right)^{m+1} - \frac{n}{n+1}\left(\frac{A}{A_0}\right)^{n+1}\right) - A_0\frac{m-n}{(m+1)(n+1)} \,. \tag{3.7}$$

An easy calculation shows that the following equality holds

$$\tilde{\Phi}(A) + \Phi(A) = A\phi(A) \,.$$

Taking into account this last equality, (3.1) can be written in compact form as a system of balance laws

$$\partial_t \boldsymbol{Q} + \partial_x \boldsymbol{F}(\boldsymbol{Q}, K) = -\boldsymbol{S}(\boldsymbol{Q})\partial_x K \,, \tag{3.8}$$

where the conserved variables and flux vectors are

$$\boldsymbol{Q} = \begin{bmatrix} q_1 \\ q_2 \end{bmatrix} = \begin{bmatrix} A \\ q \end{bmatrix} \tag{3.9}$$

and

$$\boldsymbol{F}(\boldsymbol{Q}, K) = \begin{bmatrix} q \\ \dfrac{q^2}{A} + K\dfrac{\tilde{\Phi}(A)}{\rho} \end{bmatrix} \,. \tag{3.10}$$

The factor $\boldsymbol{S}(\boldsymbol{Q})$ of the source term is given by

$$\boldsymbol{S}(\boldsymbol{Q}) = \begin{bmatrix} 0 \\ \dfrac{\Phi(A)}{\rho} \end{bmatrix} . \tag{3.11}$$

Thus, the variation of K along x generates a source term in the momentum equation. Notice that, for $K = constant$, the system is conservative.

In this section we deal with a reformulation of system (3.8) as proposed in [160], in which the governing equations are written as an *augmented* quasi-linear first-order system, namely

$$\partial_t \boldsymbol{W} + \boldsymbol{A}(\boldsymbol{W})\partial_x \boldsymbol{W} = 0 , \tag{3.12}$$

where $\boldsymbol{W}$ is given by

$$\boldsymbol{W} = \begin{bmatrix} w_1 \\ w_2 \\ w_3 \end{bmatrix} = \begin{bmatrix} A \\ q \\ K \end{bmatrix} , \tag{3.13}$$

and the matrix $\boldsymbol{A}(\boldsymbol{W})$ is

$$\boldsymbol{A}(\boldsymbol{W}) = \begin{bmatrix} 0 & 1 & 0 \\ \dfrac{A}{\rho}K\phi'(A) - u^2 & 2u & \dfrac{A}{\rho}\phi(A) \\ 0 & 0 & 0 \end{bmatrix} , \tag{3.14}$$

where $u = q/A$.

System (3.12) was studied in detail by Toro & Siviglia [160], where the Riemann problem was solved exactly. Here we perform a brief review of the model and refer the reader to the cited publication for a detailed analysis.

The eigenvalues of (3.14) are

$$\lambda_1 = u - c , \quad \lambda_2 = 0 , \quad \lambda_3 = u + c , \tag{3.15}$$

where c, the wave speed, is given by

$$c = \sqrt{\dfrac{A}{\rho}K\phi'(A)} . \tag{3.16}$$

With an appropriate scaling, the right eigenvectors of system (3.12) are

$$\boldsymbol{R}_1 = \begin{bmatrix} 1 \\ u - c \\ 0 \end{bmatrix} , \quad \boldsymbol{R}_2 = \begin{bmatrix} \dfrac{A\phi(A)}{\rho(u^2 - c^2)} \\ 0 \\ 1 \end{bmatrix} , \quad \boldsymbol{R}_3 = \begin{bmatrix} 1 \\ u + c \\ 0 \end{bmatrix} . \tag{3.17}$$

Let us define the Froude number (Fr) as

$$Fr = \dfrac{|u|}{c} .$$

A state $\boldsymbol{W}$ is said to be subcritical if $Fr < 1$, critical if $Fr = 1$, and supercritical if $Fr > 1$. The system is strictly hyperbolic in the region

$$\tilde{\Omega} = \{[A, q, K]^T \in \mathbb{R}^3 \mid K > 0, A > 0, \} ,$$

provided that $|u| \neq c$. In the larger space of states

$$\Omega = \{[A, q, K]^T \in \mathbb{R}^3 \mid K \geq 0, A > 0\} ,$$

it may happen that $\lambda_1 = \lambda_3 = u$ if $K = 0$, but still the system is hyperbolic if $|u| \neq c$, as the matrix $\boldsymbol{A}(\boldsymbol{W})$ is diagonalisable. When $|u| = c$ we have $\lambda_1 = \lambda_2$ or $\lambda_3 = \lambda_2$, in which case the system loses strict hyperbolicity and *resonance* may occur.

The second characteristic field is obviously linearly degenerate (LD), while the first and third ones are genuinely non-linear in Ω. For the first one, some straightforward calculations show that

$$
\begin{aligned}
\nabla\lambda_1 \cdot \boldsymbol{R}_1 &= -\frac{1}{2}\sqrt{\frac{KA}{\rho\phi'(A)}}\left(3\frac{\phi'(A)}{A} + \phi''(A)\right) \\
&= -\frac{1}{2A_0^2}\sqrt{\frac{KA}{\rho\phi'(A)}}\left(\frac{A}{A_0}\right)^{n-2}\left(m(m+2)\left(\frac{A}{A_0}\right)^{m-n} - n(n+2)\right) < 0\,,
\end{aligned}
$$

if $n \in (-2,0)$. For the third characteristic field we obtain

$$
\begin{aligned}
\nabla\lambda_3 \cdot \boldsymbol{R}_3 &= \frac{1}{2}\sqrt{\frac{KA}{\rho\phi'(A)}}\left(3\frac{\phi'(A)}{A} + \phi''(A)\right) \\
&= \frac{1}{2A_0^2}\sqrt{\frac{KA}{\rho\phi'(A)}}\left(\frac{A}{A_0}\right)^{n-2}\left(m(m+2)\left(\frac{A}{A_0}\right)^{m-n} - n(n+2)\right) > 0\,.
\end{aligned}
$$

The Riemann invariants of the first characteristic field are

$$
\Gamma_1^1 = u + \int_{A^*}^A \frac{c(a)}{a}\,da, \quad \Gamma_1^2 = K\,, \tag{3.18}
$$

those of the third one

$$
\Gamma_3^1 = u - \int_{A^*}^A \frac{c(a)}{\tau}\,da, \quad \Gamma_3^2 = K\,. \tag{3.19}
$$

Finally, the Riemann invariants of the LD field are

$$
\Gamma_2^1 = p + \frac{1}{2}\rho u^2, \quad \Gamma_2^2 = q\,. \tag{3.20}
$$

Proposition 1. *The pair of functions (η, G) given by*

$$
\eta(\boldsymbol{W}) = \frac{q^2}{2A} + \frac{K}{\rho}\Phi(A)\,, \tag{3.21}
$$

$$
G(\boldsymbol{W}) = \frac{q^3}{2A^2} + \frac{p}{\rho}q\,, \tag{3.22}
$$

constitutes an entropy pair for (3.12).

Proof. Let $\boldsymbol{W}(x,t) = [A(x,t), q(x,t), K(x)]^T$ be a smooth solution of system (3.12). Then

$$
\begin{aligned}
\partial_t\eta(\boldsymbol{W}) &= \left(-\frac{q^2}{2A^2} + \frac{K}{\rho}\phi(A)\right)\partial_t A + \frac{q}{A}\partial_t q \\
&= -\left(-\frac{q^2}{2A^2} + \frac{K}{\rho}\phi(A)\right)\partial_x q - \frac{q}{A}\left(\partial_x\left(\frac{q^2}{A}\right) + \frac{A}{\rho}\partial_x p\right) \\
&= -\frac{3}{2}\frac{q^2}{A^2}\partial_x q + \frac{q^3}{A^3}\partial_x A - \left(\frac{p}{\rho}\partial_x q + \partial_x\left(\frac{p}{\rho}\right)q\right) \\
&= -\partial_x\left(\frac{q^3}{2A^2} + \frac{p}{\rho}q\right) \\
&= -\partial_x G(\boldsymbol{W})\,.
\end{aligned}
$$

The function η is convex and it is related to the mechanical energy.

$\square$

3.1.3 Integral curves of the LD characteristic field

As the integral curves of the LD characteristic field play an important role in the design of well-balanced numerical methods, we will study them in detail in this subsection. These curves are those of the space (A, q, K) contained in Ω, and given by the equations

$$q = \bar{q}, \quad p + \frac{1}{2}\rho u^2 = \Gamma, \tag{3.23}$$

where $\bar{q}$ and Γ are two constants corresponding to the Riemann invariants. Notice that, for $A \neq A_0$, K can be recast as

$$K = f(A) := \frac{\Gamma - \dfrac{\rho}{2}\dfrac{\bar{q}^2}{A^2}}{\phi(A)}. \tag{3.24}$$

This expression is useful for drawing the integral curves (3.23) in the $(A, K, q = \bar{q})$ phase plane for a given Γ.

Let us consider first the case $\bar{q} \neq 0$. By differentiating, we obtain

$$\frac{df}{dA} = \frac{1}{\phi(A)^2}\left(\frac{\rho\bar{q}^2\phi(A)}{A^3} - \left(\Gamma - \frac{1}{2}\rho\left(\frac{\bar{q}^2}{A^2}\right)\right)\phi'(A)\right).$$

Let us introduce the function

$$g(A) = \frac{\rho\bar{q}^2}{A^2}\left(\frac{1}{2} + \frac{\phi(A)}{A\phi'(A)}\right). \tag{3.25}$$

Some straightforward calculations show that

$$\frac{df}{dA} < 0 \quad \Longleftrightarrow \quad g(A) < \Gamma,$$

$$\frac{df}{dA} = 0 \quad \Longleftrightarrow \quad g(A) = \Gamma,$$

$$\frac{df}{dA} > 0 \quad \Longleftrightarrow \quad g(A) > \Gamma.$$

Moreover, if $A > A_0$ and $g(A) > \Gamma$, from the definition of $g(A)$ we deduce

$$\frac{\rho\bar{q}^2}{A^3\phi'(A)} > \frac{\Gamma - \dfrac{\rho}{2}\dfrac{\bar{q}^2}{A^2}}{\phi(A)} = f(A),$$

and thus

$$c^2 = \frac{A}{\rho}f(A)\phi'(A) < \frac{A\rho\bar{q}^2}{\rho A^3\phi'(A)}\phi'(A) = \frac{\bar{q}^2}{A^2} = u^2.$$

Therefore, the state $(A, \bar{q}, f(A))$ is subcritical. Analogous results hold for critical and subcritical states. For $A < A_0$ the results are inverted because $\phi(A) < 0$. Summing up:

- If f has an extremum in A^*, then $(A^*, \bar{q}, f(A^*))$ is critical.

- If f is decreasing in an interval contained in $(0, A_0)$ then the corresponding state $(A, \bar{q}, f(A))$ is supercritical.

- If f is increasing in an interval contained in $(0, A_0)$ then the corresponding state $(A, \bar{q}, f(A))$ is subcritical.

- If f is decreasing in an interval contained in (A_0, ∞) then the corresponding state $(A, \bar{q}, f(A))$ is subcritical.

- If f is increasing in an interval contained in (A_0, ∞) then the corresponding state $(A, \bar{q}, f(A))$ is supercritical.
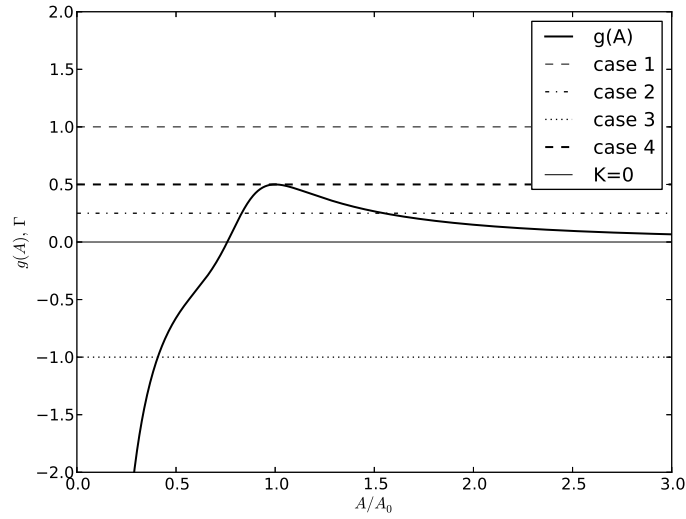
Figure 3.1: Graph of the function $g(A)$ (3.25) and four horizontal lines corresponding to four different values of Γ such that (1) $\Gamma > \frac{1}{2}\rho\left(\frac{\bar{q}}{A_0}\right)^2$, (2) $0 < \Gamma < \frac{1}{2}\rho\left(\frac{\bar{q}}{A_0}\right)^2$, (3) $\Gamma < 0$, (4) $\Gamma = \frac{1}{2}\rho\left(\frac{\bar{q}}{A_0}\right)^2$.

Therefore, the graph of the function g gives all the necessary information concerning the monotonicity of f and the regime of the states. It can be easily shown that $g(A)$ has an absolute maximum at $A = A_0$ whose value is

$$\frac{1}{2}\rho\left(\frac{\bar{q}}{A_0}\right)^2,$$

and

$$\lim_{A\to 0^+} g(A) = -\infty, \quad \lim_{A\to\infty} g(A) = 0.$$

Four cases are then possible (see figure 3.1) :

1. $\Gamma > \frac{1}{2}\rho\left(\frac{\bar{q}}{A_0}\right)^2$: in this case

$$g(A) < \Gamma, \quad \forall A.$$

   Therefore the graph of f is composed by two decreasing branches. Moreover, it can be easily shown that

$$\lim_{A\to 0^+} f(A) = \infty, \quad \lim_{A\to A_0^-} f(A) = -\infty, \quad \lim_{A\to A_0^+} f(A) = \infty, \lim_{A\to\infty} f(A) = 0.$$

   Figure 3.2(a) shows the graph of f. To obtain the integral curve, only the values for which $K \geq 0$ are retained. The integral curve is thus composed by two branches: the graph of f corresponding to the interval $(0, \bar{A}]$ with

$$\bar{A} = \sqrt{\frac{\rho}{2\Gamma}}\,\bar{q}, \tag{3.26}$$

   which is composed by supercritical states and the graph of f in (A_0, ∞), composed by subcritical states. Figure 3.2(b) shows the integral curve and the curve corresponding to $Fr = 1$.

2. $0 < \Gamma < \frac{1}{2}\rho\left(\frac{\bar{q}}{A_0}\right)^2$: in this case there are two values of A, $A_1 \in (0, A_0)$ and $A_2 \in (A_0, A)$ such that $g(A_i) = \Gamma$, $i = 1, 2$. The graph of f is strictly decreasing in $(0, A_1)$, strictly

(a)   (b)
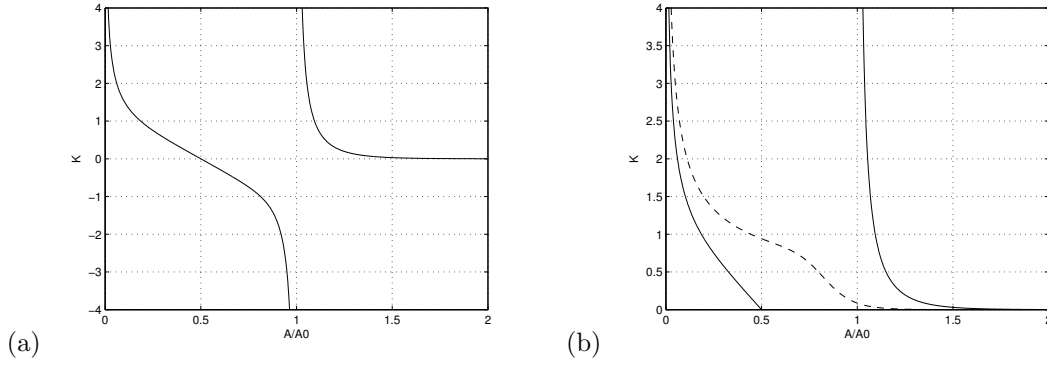
Figure 3.2: Case $\Gamma > \frac{1}{2}\rho\left(\frac{\bar{q}}{A_0}\right)^2$. (a) Graph of $K = f$. (b) Integral curve (continuous line) and critical states (dashed lines). This line separates the subcritical region (to the left) from the supercritical region (to the right).

(a)   (b)
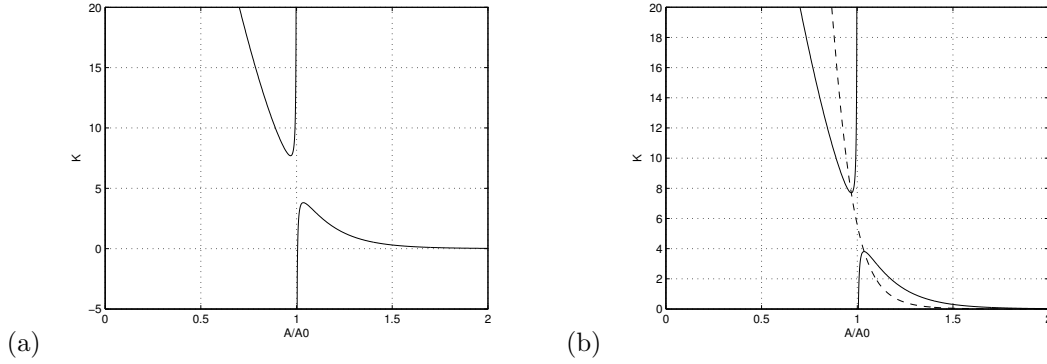
Figure 3.3: Case $0 < \Gamma < \frac{1}{2}\rho\left(\frac{\bar{q}}{A_0}\right)^2$. (a) Graph of $K = f$. (b) Integral curve (continuous line) and critical states (dashed lines).

increasing in (A_0, A_2), and strictly decreasing in (A_2, ∞). Moreover

$$\lim_{A \to 0^+} f(A) = \infty\,, \quad \lim_{A \to A_0^-} f(A) = \infty\,, \quad \lim_{A \to A_0^+} f(A) = -\infty\,, \lim_{A \to \infty} f(A) = 0\,.$$

Figure 3.3(a) shows the graph of f. The corresponding integral curve is obtained again by removing the part of the graph lying in the half-plane $K \leq 0$. It is composed by two branches: on the one hand, the graph of f in $(0, A_0)$ whose corresponding states are supercritical in (A, A_1), critical in A_1, and subcritical in (A_1, A_0). On the other hand, the graph of f in $[\bar{A}, \infty)$ where $\bar{A}$ is given again by (3.26), whose states are supercritical in $[\bar{A}, A_2)$, critical in A_2, and subcritical in (A_2, ∞). Figure 3.3(b) shows the integral curve and the curve corresponding to $Fr = 1$.

3. $\Gamma \leq 0$: in this case, there is only a value of A, $A_1 \in (0, A_0)$ such that $g(A_1) = \Gamma$. The graph of f is strictly decreasing in $(0, A_1)$ and strictly increasing in (A_1, A_0) and (A_0, ∞). Moreover,

$$\lim_{A \to 0^+} f(A) = \infty\,, \quad \lim_{A \to A_0^-} f(A) = \infty\,, \quad \lim_{A \to A_0^+} f(A) = -\infty\,, \lim_{A \to \infty} f(A) = 0\,.$$

Figure 3.4(a) shows the graph of f. The integral curve is only composed by the branch corresponding to $A < A_0$. Their states are supercritical in $(0, A_1)$, critical in A_1, and subcritical in (A_1, A_0): see figure 3.4(b).

(a)   (b)
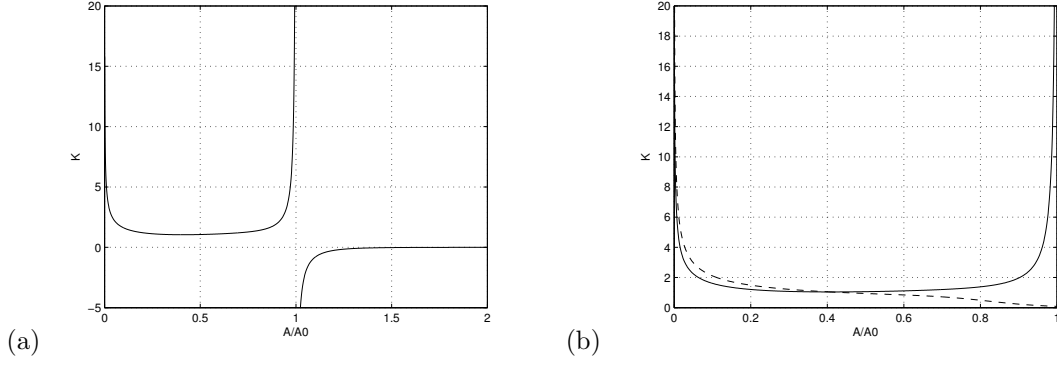
Figure 3.4: Case $\Gamma < 0$. (a) Graph of $K = f$. (b) Integral curve (continuous line) and critical states (dashed lines).

(a)   (b)
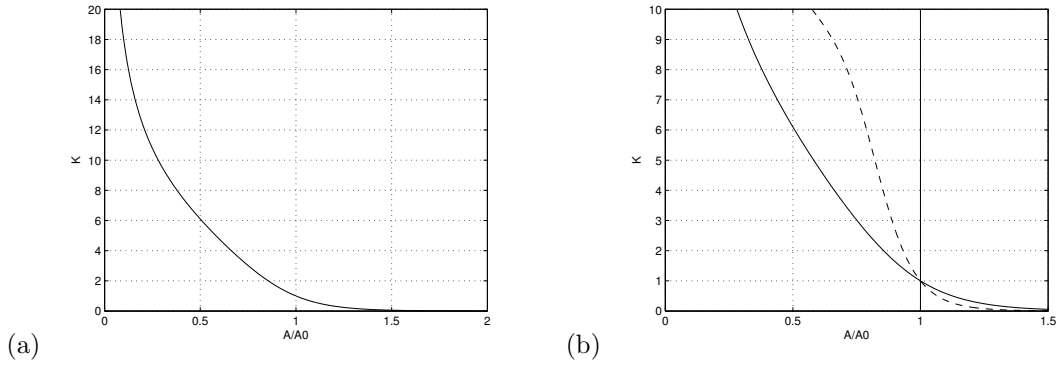
Figure 3.5: Case $\Gamma = \frac{1}{2}\rho\left(\frac{\bar{q}}{A_0}\right)^2$. (a) Graph of $K = f$. (b) Integral curve (continuous line) and critical states (dashed lines).

4. $\Gamma = \frac{1}{2}\rho\left(\frac{\bar{q}}{A_0}\right)^2$: in this case A_0 is the only value of A such that $g(A_0) = \Gamma$. Moreover, one has

$$\lim_{A\to 0^+} f(A) = \infty, \quad \lim_{A\to A_0^-} f(A) = \lim_{A\to A_0^+} f(A) = \frac{2\Gamma}{m-n}, \quad \lim_{A\to\infty} f(A) = 0\,.$$

The function f can be extended by continuity to $A = A_0$ and it is decreasing in $(0,\infty)$. In this case, the integral curve is composed again by two branches: the whole graph of f, whose states are supercritical in $(0, A_0)$, critical in A_0 and subcritical in (A_0, ∞), and the half-line

$$(A_0, \bar{q}, K)\,, \quad K \geq 0\,, \tag{3.27}$$

whose states are supercritical for $0 \leq K < 2\Gamma/(m-n)$ and subcritical for $K > \Gamma/(m-n)$, see figure 3.5(b).

Let us now consider the case $\bar{q} = 0$. In this case, all the states of the integral curve are subcritical and (3.24) reduces to

$$K = \frac{\Gamma}{\phi(A)}\,, \tag{3.28}$$

whose analysis is much simpler. There are three different situations:

1. If $\Gamma > 0$ the integral curve consists of only one branch defined in (A_0, ∞) which is decreasing, see figure 3.6(a).

2. If $\Gamma < 0$ the integral curve consists of only one branch defined in $(0, A_0)$ which is increasing, see figure 3.6(b).

(a)   (b)
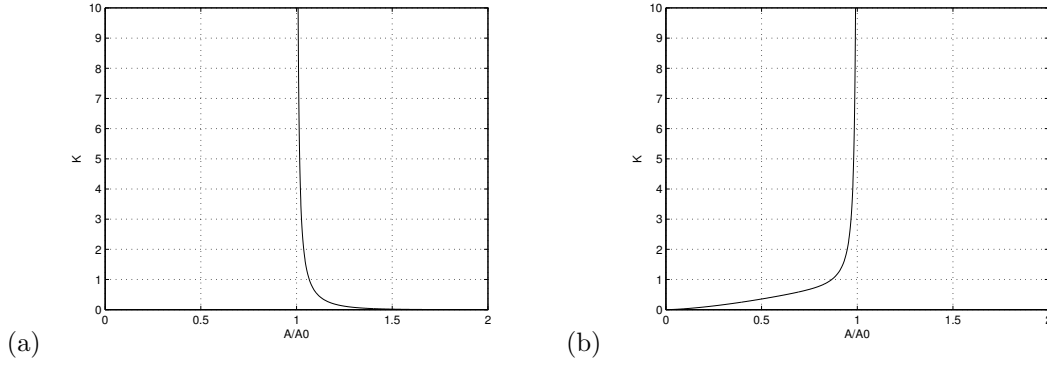
Figure 3.6: Case $\bar{q} = 0$. (a) $\Gamma > 0$.(b) $\Gamma > 0$.
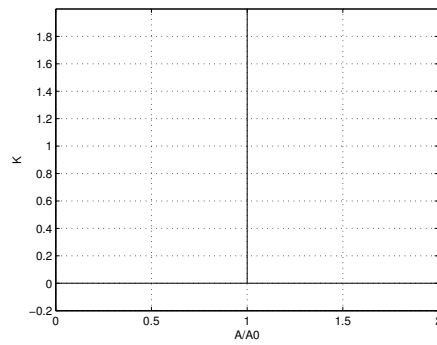
Figure 3.7: Case $\bar{q} = 0$, $\Gamma = 0$.

3. If $\Gamma = 0$, the integral curve is composed by the axis $K = 0$ and the half-line

$$(A_0, 0, K), \quad K \geq 0\,. \tag{3.29}$$

See figure 3.7.

Steady solutions of system (3.12) are strongly related to the integral curves of the LD field:

- Stationary contact discontinuities standing on a jump of the function K link two states that belong to the same integral curve of the LD field.

- Smooth steady solutions corresponding to a given smooth function $K(x)$ are computed by fixing the values of $\bar{q}$ and Γ, and then solving for every x the non-linear equation

$$\Gamma = \frac{\rho}{2} \left(\frac{q}{A} \right)^2 + K(x)\phi(A)\,, \tag{3.30}$$

to compute $A(x)$, noting that in some cases, as we have already seen, there is more than one positive root of this equation. Therefore, a steady solution has the form

$$x \mapsto (A(x, \bar{q}, \Gamma), \bar{q}, K(x))\,, \tag{3.31}$$

where $A(x, \bar{q}, \Gamma)$ is a smoothly selected solution of (3.30). It may be thus interpreted as a parametrisation of an arc of one of the above integral curves, being x the parameter.

Remark 1. *Notice that, according to figures 3.3(b) or 3.4(b), if $(A(x), \bar{q})$ is a transcritical steady solution such that*

$$A(x) < A_0\,, \quad \forall x\,,$$

then the critical state has to be reached at the point x_{min} where K is minimal. Analogously, figure 3.3(b) shows that, if $(A(x), \bar{q})$ is a transcritical solution such that

$$A(x) > A_0, \quad \forall x,$$

then the critical state has to be reached at the point of x_{max} where K is maximal. Moreover, for transcritical solutions where $A(x)$ takes values greater and lower than A_0 (see figure 3.5(b)), the critical point has to be located at a point x_{crit} such that

$$K(x_{crit}) = \frac{2\Gamma}{m - n}.$$

3.1.4 Generalised Hydrostatic Reconstruction

The Generalised Hydrostatic Reconstruction (GHR) was introduced by Castro *et al.* [47] as a generalisation of the numerical treatment of the geometrical source term of the shallow water system, proposed in [15] to obtain well-balanced numerical schemes for water-at-rest solutions. This generalisation was based on the interpretation of a particular choice of family of paths within the framework of path-conservative methods introduced in [129]. Other approaches to construct well-balanced numerical schemes are available, see [26, 97, 34].

In this subsection, we follow this technique to introduce a numerical scheme which is well-balanced for all the subcritical and the supercritical steady solutions of system (3.12). First, the general principle is stated. Next, the well-balanced numerical scheme is constructed in

$$\begin{aligned}
\Omega^- &= \{ \boldsymbol{W} \in \Omega \mid A < A_0 \}, \\
\Omega^+ &= \{ \boldsymbol{W} \in \Omega \mid A > A_0 \}.
\end{aligned}$$

Then, the numerical scheme is extended to Ω. The well-balanceness of the numerical scheme for transcritical steady solutions is discussed. Finally, the connection of the method with the path-conservative framework is described together with some remarks concerning the limitations of the numerical solutions.

GHR principle

Let us split the spatial domain into computational cells $I_i = [x_{i-\frac{1}{2}}, x_{i+\frac{1}{2}}]$ whose length, Δx, is supposed to be constant for simplicity, and let x_i be the centre of the cell I_i.

We want to design a path-conservative numerical scheme for system (3.12), in the sense introduced in [129], which has the following form

$$\boldsymbol{W}_i^{n+1} = \boldsymbol{W}_i^n - \frac{\Delta t}{\Delta x} \left(\boldsymbol{D}_{i+\frac{1}{2}}^- + \boldsymbol{D}_{i-\frac{1}{2}}^+ \right), \tag{3.32}$$

where Δt is the time step. $\boldsymbol{W}_i^n$ is

$$\boldsymbol{W}_i^n = \begin{bmatrix} \boldsymbol{Q}_i^n \\ K_i \end{bmatrix}, \quad \boldsymbol{Q}_i^n = \begin{bmatrix} A_i^n \\ q_i^n \end{bmatrix},$$

where A_i^n and q_i^n are the approximation of the average of the sought solution in the cell I_i at the instant t^n provided by the numerical method and K_i is, in the case of the first-order scheme, the average of the function K in the cell I_i

$$K_i = \frac{1}{\Delta x} \int_{x_{i-\frac{1}{2}}}^{x_{i+\frac{1}{2}}} K(x) \, dx.$$

$\boldsymbol{D}_{i+\frac{1}{2}}^\pm$ are numerical fluctuations

$$\boldsymbol{D}_{i+\frac{1}{2}}^\pm = \begin{pmatrix} D_{i+\frac{1}{2}}^\pm \\ 0 \end{pmatrix},$$

with

$$D_{i+\frac{1}{2}}^\pm = D^\pm(\boldsymbol{W}_L, \boldsymbol{W}_R). \tag{3.33}$$

$\boldsymbol{W}_L$ and $\boldsymbol{W}_R$ are states at the left and right side of the cell interface located at $x_{i+\frac{1}{2}}$. In the case of a first-order scheme we have that $\boldsymbol{W}_L = \boldsymbol{W}_i^n$ and $\boldsymbol{W}_R = \boldsymbol{W}_{i+1}^n$. The fluctuations $\boldsymbol{D}_{i+\frac{1}{2}}^{\pm}$ have to satisfy

$$\boldsymbol{D}_{i+\frac{1}{2}}^{\pm} = 0, \text{ if } \boldsymbol{W}_L = \boldsymbol{W}_R, \tag{3.34}$$

$$\boldsymbol{D}_{i+\frac{1}{2}}^{-} + \boldsymbol{D}_{i+\frac{1}{2}}^{+} = \int_0^1 \boldsymbol{A}\left(\Psi\left(\boldsymbol{W}_L, \boldsymbol{W}_R, s\right)\right) \frac{\partial \Psi}{\partial s}\left(\boldsymbol{W}_L, \boldsymbol{W}_R, s\right) \, ds, \tag{3.35}$$

for a certain family of paths $\Psi(\boldsymbol{W}_L, \boldsymbol{W}_R, s)$, i.e. for a Lipschitz-continuous function $\Psi : \Omega \times \Omega \times [0,1] \mapsto \Omega$ satisfying some regularity and consistency assumptions, such as:

$$\Psi(\boldsymbol{W}_L, \boldsymbol{W}_R, 0) = \boldsymbol{W}_L, \quad \Psi(\boldsymbol{W}_L, \boldsymbol{W}_R, 1) = \boldsymbol{W}_R;$$

$$\Psi(\boldsymbol{W}, \boldsymbol{W}, s) = \boldsymbol{W}, \quad \forall \boldsymbol{W}, s.$$

See [56] for details.

Although the first-order numerical scheme to be described will be derived using the general form, in practice the variable K is not advanced in time. In fact, dropping this artificial unknown, the scheme can be written as follows:

$$\boldsymbol{Q}_i^{n+1} = \boldsymbol{Q}_i^n - \frac{\Delta t}{\Delta x}\left(D_{i+\frac{1}{2}}^{-} + D_{i-\frac{1}{2}}^{+}\right). \tag{3.36}$$

Properties (3.34)-(3.35) imply that the numerical scheme is consistent for smooth solutions. Notice that, if K is discontinuous, the product $\boldsymbol{S}(\boldsymbol{Q})\partial_x K$ cannot be defined as a distribution when both $\boldsymbol{W}$ and K are discontinuous. The theory introduced in [56] allows to give a sense to this product as a measure, provided that a family of paths is prescribed. A path-conservative method is formally consistent with the definition associated to the chosen family Ψ.

Although for general non-conservative systems the limits of the numerical solutions provided by a path-conservative numerical method may be weak solutions in a different sense than the one associated to the chosen family of paths (see [46]), this is not the case for systems of balance laws with smooth enough source terms: see [119]. In particular, for the system considered here, if K is smooth enough, then if the numerical solution provided by a path-conservative method converges, its limit is a weak solution of the system independently of the chosen family of paths. Nevertheless, if K is discontinuous, in the presence of resonant situations, there may be more than one entropy weak solution and the limits of the numerical solutions do depend on the method.

Let us first introduce the fluctuations provided by the GHR and prove their well-balanced properties. Then, the path Ψ for which (3.35) holds will be described.

The idea on which the GHR is based is the following: let us consider the set Θ of all the supercritical and subcritical branches of integral curves θ of the LD field of (3.14) studied in the previous subsection, which are given by

$$\frac{1}{2}\rho u^2 + K\phi(A) = constant, \quad q = constant, \quad Fr > 1 \text{ or } Fr < 1. \tag{3.37}$$

Given a state $\boldsymbol{W} \in \Omega$ which is not critical, we will denote by $\theta_{\boldsymbol{W}}$ the unique curve of the set Θ passing by $\boldsymbol{W}$.

Let us choose a standard numerical flux $\boldsymbol{G}(\boldsymbol{Q}_L, \boldsymbol{Q}_R, K)$ consistent with the flux function $\boldsymbol{F}(\boldsymbol{Q}, K)$ in the following sense

$$\boldsymbol{G}(\boldsymbol{Q}, \boldsymbol{Q}, K) = \boldsymbol{F}(\boldsymbol{Q}, K), \quad \forall \boldsymbol{Q}, K.$$

Let us suppose that, given the states $\boldsymbol{W}_L = [\boldsymbol{Q}_L, K_L]^T$ and $\boldsymbol{W}_R = [\boldsymbol{Q}_R, K_R]^T$ at the left and at the right of the cell interface located at $x_{i+\frac{1}{2}}$, it is possible to choose a real number $K_{i+\frac{1}{2}} \in [K_L, K_R]$ and two reconstructed states

$$\boldsymbol{W}_{i+\frac{1}{2}}^{\pm} = \begin{bmatrix} \boldsymbol{Q}_{i+\frac{1}{2}}^{\pm} \\ K_{i+\frac{1}{2}} \end{bmatrix}, \tag{3.38}$$

that continuously depend on $\boldsymbol{W}_L$, $\boldsymbol{W}_R$ and satisfy:

(a) if $\boldsymbol{W}_L$ is not critical then $\boldsymbol{W}^-_{i+\frac{1}{2}} \in \theta_{\boldsymbol{W}_L}$;

(b) if $\boldsymbol{W}_R$ is not critical then $\boldsymbol{W}^+_{i+\frac{1}{2}} \in \theta_{\boldsymbol{W}_R}$;

(c) if $K_L = K_R = K$ then $K_{i+\frac{1}{2}} = K$;

(d) if $K_L = K_{i+\frac{1}{2}}$ then $\boldsymbol{Q}^-_{i+\frac{1}{2}} = \boldsymbol{Q}_L$;

(e) if $K_{i+\frac{1}{2}} = K_R$ then $\boldsymbol{Q}^+_{i+\frac{1}{2}} = \boldsymbol{Q}_R$;

(f) if $(Fr(\boldsymbol{W}_L)^2 - 1)(Fr(\boldsymbol{W}_R)^2 - 1) \geq 0$ and $\theta_{\boldsymbol{W}_L} = \theta_{\boldsymbol{W}_R}$ then $\boldsymbol{W}^-_{i+\frac{1}{2}} = \boldsymbol{W}^+_{i+\frac{1}{2}}$.

Then the fluctuations (3.33) are computed as follows:

$$D^+(\boldsymbol{W}_L, \boldsymbol{W}_R) = \boldsymbol{F}(\boldsymbol{Q}^+_{i+\frac{1}{2}}, K_{i+\frac{1}{2}}) - G(\boldsymbol{Q}^-_{i+\frac{1}{2}}, \boldsymbol{Q}^+_{i+\frac{1}{2}}, K_{i+\frac{1}{2}}), \qquad (3.39)$$

$$D^-(\boldsymbol{W}_L, \boldsymbol{W}_R) = G(\boldsymbol{Q}^-_{i+\frac{1}{2}}, \boldsymbol{Q}^+_{i+\frac{1}{2}}, K_{i+\frac{1}{2}}) - \boldsymbol{F}(\boldsymbol{Q}^-_{i+\frac{1}{2}}, K_{i+\frac{1}{2}}). \qquad (3.40)$$

If $K = constant$, some straightforward calculations allow one to show that, due to property (c), the numerical scheme (3.32) is equivalent to the conservative method:

$$\boldsymbol{Q}^{n+1}_i = \boldsymbol{Q}^n_i - \frac{\Delta t}{\Delta x}\left(\boldsymbol{G}_{i+\frac{1}{2}} - \boldsymbol{G}_{i-\frac{1}{2}},\right), \qquad (3.41)$$

where

$$\boldsymbol{G}_{i+\frac{1}{2}} = \boldsymbol{G}(\boldsymbol{Q}^n_i, \boldsymbol{Q}^n_{i+1}, K).$$

Proposition 2. *The numerical scheme* (3.32)*,* (3.39)*,* (3.40) *is well-balanced in the sense that it preserves the subcritical and supercritical steady solutions of the system. More precisely,*

- *Let $\boldsymbol{Q}(x) = [A(x), q(x)]^T$ be a subcritical or supercritical smooth steady solution of (3.1) for a given smooth function K. If the numerical method (3.32), (3.39), (3.40), is applied to*

$$\boldsymbol{Q}^0_i = \boldsymbol{Q}(x_i), \quad K_i = K(x_i),$$

then

$$\boldsymbol{Q}^n_i = \boldsymbol{Q}^0_i, \quad \forall n, \forall i.$$

- *Given a steady contact discontinuity of (3.12)*

$$\boldsymbol{W}(x, t) = \begin{cases} \boldsymbol{W}_L & if\ x < 0, \\ \boldsymbol{W}_R & if\ x > 0, \end{cases}$$

linking two subcritical or two supercritical states, if $x_{i+\frac{1}{2}} = 0$ and the numerical method (3.32), (3.39), (3.40) is applied to

$$\boldsymbol{Q}^0_i = \begin{cases} \boldsymbol{Q}_L & if\ i \leq 0, \\ \boldsymbol{Q}_R & if\ i > 0, \end{cases} \quad K_i = \begin{cases} K_L & if\ i \leq 0, \\ K_R & if\ i > 0, \end{cases}$$

then

$$\boldsymbol{Q}^n_i = \boldsymbol{Q}^0_i, \quad \forall n, \forall i.$$

Proof. If $\boldsymbol{Q}(x) = [A(x), q(x)]^T$ is a sub or supercritical smooth steady solution of (3.1) for a given smooth function K, then there exist two constants Γ and $\bar{q}$ such that

$$q(x) = \bar{q}, \quad \frac{\rho}{2}\frac{\bar{q}^2}{A(x)^2} + K(x)\phi(A(x)) = \Gamma.$$

Therefore, any two pair of neighbour states $\boldsymbol{W}^0_i = [Q(x_i), K(x_i)]^T$, $\boldsymbol{W}^0_{i+1} = [Q(x_{i+1}), K(x_{i+1})]^T$ belong to the same integral curve of the LD field and their regime (sub or supercritical) is the same. Therefore, property (f) implies

$$\boldsymbol{Q}^+_{i+\frac{1}{2}} = \boldsymbol{Q}^-_{i+\frac{1}{2}},$$

and then:

$$
\begin{aligned}
D^+(\boldsymbol{W}_L, \boldsymbol{W}_R) &= \boldsymbol{F}(\boldsymbol{Q}^+_{i+\frac{1}{2}}, K_{i+\frac{1}{2}}) - \boldsymbol{G}(\boldsymbol{Q}^+_{i+\frac{1}{2}}, \boldsymbol{Q}^+_{i+\frac{1}{2}}, K_{i+\frac{1}{2}}) = 0, \\
D^-(\boldsymbol{W}_L, \boldsymbol{W}_R) &= \boldsymbol{G}(\boldsymbol{Q}^-_{i+\frac{1}{2}}, \boldsymbol{Q}^-_{i+\frac{1}{2}}, K_{i+\frac{1}{2}}) - \boldsymbol{F}(\boldsymbol{Q}^-_{i+\frac{1}{2}}, K_{i+\frac{1}{2}}) = 0,
\end{aligned}
$$

due to the consistency of the numerical flux $\boldsymbol{G}$. As all fluctuations vanish, $Q^1_i = Q^0_i$ for all i and the result is proved. The proof for stationary contact discontinuities is similar.

$\square$

Remark 2. *A stationary contact discontinuity linking two states that belong to the same integral curve whose regime (sub or supercritical) are different is, a priori, an admissible weak solution, as the Riemann invariants of the LD field are preserved. Moreover, it is an entropy satisfying solution according to the pair (η, G) given by (3.21), (3.22): it can be easily checked that the preservation of the Riemann invariants implies that the jump of the entropy flux vanishes. Nevertheless, Lax's entropy criterion is not satisfied: in effect, if we denote by j^- the number of negative eigenvalues of $\boldsymbol{W}_L$ and by j^+ the number of positive eigenvalues of $\boldsymbol{W}_R$ then Lax entropy condition is satisfied if*

$$
j^- + j^+ = 2.
$$

But this is not the case if one of the states is subcritical and the other one is supercritical: for instance, if $\boldsymbol{W}_L$ is subcritical and $\boldsymbol{W}_R$ is supercritical, then $j^- + j^+ = 1$ or $j^- + j^+ = 3$ (depending on the sign of the eigenvalues of $\boldsymbol{W}_R$). Therefore, these weak solutions are not considered here to be admissible. The equality of the sign of the Froude numbers is required in property (f) in order to prevent the numerical scheme from preserving these non-admissible contact discontinuities. Notice that in these situations, one of the eigenvalues changes its sign across $x = 0$ at the initial condition. It is thus a resonant situation and, as pointed out in [160], uniqueness may be lost.

GHR in Ω^- Given two states $\boldsymbol{W}_L = [\boldsymbol{Q}_L, K_L]^T$ and $\boldsymbol{W}_R = [\boldsymbol{Q}_R, K_R]^T$ in Ω^-, we define the reconstructed states

$$
\boldsymbol{W}^\pm_{i+\frac{1}{2}} = \begin{bmatrix} A^\pm_{i+\frac{1}{2}} \\ q^\pm_{i+\frac{1}{2}} \\ K_{i+\frac{1}{2}} \end{bmatrix} \tag{3.42}
$$

as follows:

$$
q^-_{i+\frac{1}{2}} = q_L, \quad q^+_{i+\frac{1}{2}} = q_R, \quad K_{i+\frac{1}{2}} = \max(K_L, K_R). \tag{3.43}
$$

If $K_{i+\frac{1}{2}} = K_L$, then $A^-_{i+\frac{1}{2}} = A_L$. Otherwise, $A^-_{i+\frac{1}{2}}$ is computed as follows:

- If $\boldsymbol{W}_L$ is sub or supercritical, $A^-_{i+\frac{1}{2}}$ is the only the root of the equation

$$
\frac{\rho}{2} \left(\frac{q_L}{A} \right)^2 + K_{i+\frac{1}{2}} \, \phi(A) = \frac{\rho}{2} \left(\frac{q_L}{A_L} \right)^2 + K_L \, \phi(A_L), \tag{3.44}
$$

  such that $A^-_{i+\frac{1}{2}} < A_0$ and the regimes (sub or supercritical) of $\boldsymbol{W}_L$ and $\boldsymbol{W}^-_{i+\frac{1}{2}}$ are the same.

- If $\boldsymbol{W}_L$ is critical and $\boldsymbol{W}_R$ is sub or supercritical, $A^-_{i+\frac{1}{2}}$ is the only root of (3.44) such that $A^-_{i+\frac{1}{2}} < A_0$ and the regimes of $\boldsymbol{W}_R$ and $\boldsymbol{W}^-_{i+\frac{1}{2}}$ are the same.

Analogously, if $K_{i+\frac{1}{2}} = K_R$, then $A^+_{i+\frac{1}{2}} = A_R$. Otherwise, $A^+_{i+\frac{1}{2}}$ is computed as follows:

- If $\boldsymbol{W}_R$ is sub or supercritical, $A^+_{i+\frac{1}{2}}$ is the only root of

$$
\frac{\rho}{2} \left(\frac{q_R}{A} \right)^2 + K_{i+\frac{1}{2}} \, \phi(A) = \frac{\rho}{2} \left(\frac{q_R}{A_R} \right)^2 + K_R \, \phi(A_R). \tag{3.45}
$$

  such that $A^+_{i+\frac{1}{2}} < A_0$ and the regimes of $\boldsymbol{W}_R$ and $\boldsymbol{W}^+_{i+\frac{1}{2}}$ are the same.

- If $\boldsymbol{W}_R$ is critical and $\boldsymbol{W}_L$ is sub or supercritical, $A^+_{i+\frac{1}{2}}$ is the only root of (3.45) such that $A^+_{i+\frac{1}{2}} < A_0$ and the regimes of $\boldsymbol{W}_L$ and $\boldsymbol{W}^+_{i+\frac{1}{2}}$ are the same.

A close inspection of figures 3.2(b), 3.3(b), 3.4(b), 3.5(b), 3.6(b), and 3.7 shows that, given a subcritical or supercritical state $\boldsymbol{W}^* = [A^*, q^*, K^*]^T \in \Omega^-$ and given $\tilde{K} > K^*$, there is always one and only one value $\tilde{A}$ of A, such that the state $[\tilde{A}, q^*, \tilde{K}]^T$ belongs to Ω^-, lies on the same integral curve of the LD field, and whose regime is equal to that of $\boldsymbol{W}^*$. And if $\boldsymbol{W}^* \in \Omega^-$ is critical, there exist two values $\tilde{A}_{sub}$ and $\tilde{A}_{sup}$ such that the states $[\tilde{A}_{sub}, q^*, \tilde{K}]^T$ and $[\tilde{A}_{sup}, q^*, \tilde{K}]^T$ are subcritical and supercritical respectively, they belong to Ω^- and they lie on the integral curve of the LD field passing by $\boldsymbol{W}^*$. Therefore, the GH-reconstruction is well-defined. Notice that, once that $K_{i+\frac{1}{2}}$ is computed, only one of (3.44) and (3.45) has to be solved. Both are non-linear equations which are solved via a Newton method.

GHR in Ω^+

Given now two states $\boldsymbol{W}_L = [\boldsymbol{Q}_L, K_L]^T$ and $\boldsymbol{W}_R = [\boldsymbol{Q}_R, K_R]^T$ in Ω^+, the definition of the reconstructed states $\boldsymbol{W}^\pm_{i+\frac{1}{2}}$ is computed as in Ω^-, with the only difference that $K_{i+\frac{1}{2}}$ is defined now by

$$K_{i+\frac{1}{2}} = \min(K_L, K_R),$$

and that the requirement $A^\pm_{i+\frac{1}{2}} > A_0$ is imposed to the solutions of (3.44) and (3.45), instead of $A^\pm_{i+\frac{1}{2}} < A_0$.

Again, a close inspection of figures 3.2(b), 3.3(b), 3.5(b), 3.6(a), and 3.7 shows that, given a subcritical or supercritical state $\boldsymbol{W}^* = [A^*, q^*, K^*]^T \in \Omega^+$ and given $\tilde{K} < K^*$, there is always one and only one value $\tilde{A}$ of A, such that the state $[\tilde{A}, q^*, \tilde{K}]^T$ belongs to Ω^+, lies on the same integral curve of the LD field, and whose regime is equal to that of $\boldsymbol{W}^*$. Moreover, if $\boldsymbol{W}^* \in \Omega^-$ is critical, there exist two values $\tilde{A}_{sub}$ and $\tilde{A}_{sup}$ such that the states $[\tilde{A}_{sub}, q^*, \tilde{K}]^T$ and $[\tilde{A}_{sup}, q^*, \tilde{K}]^T$ are subcritical and supercritical respectively, they belong to Ω^+ and they lie on the integral curve of the LD field passing by $\boldsymbol{W}^*$. Therefore, the GH-reconstruction in Ω^+ is also well-defined.

It can be easily checked that reconstructed states satisfy the properties (a)-(f) both in Ω^- and Ω^+.

Extension to Ω

First, given two states $\boldsymbol{W}_L$, $\boldsymbol{W}_R$ such that $A_L = A_0$ and $A_R \neq A_0$ the reconstructions are computed as in 3.1.4 if $A_R < A_0$ and as in 3.1.4 if $A_R > A_0$.

Analogously, when $A_R = A_0$ and $A_L \neq A_0$ the reconstructions are computed as in 3.1.4 if $A_L < A_0$ and as in 3.1.4 if $A_L > A_0$.

Next, given two states $\boldsymbol{W}_L = [A_0, q_L, K_L]^T$, $\boldsymbol{W}_R = [A_0, q_R, K_R]^T$, we define

$$\boldsymbol{W}^\pm_{i+\frac{1}{2}} = \begin{bmatrix} A^\pm_{i+\frac{1}{2}} \\ q^\pm_{i+\frac{1}{2}} \\ K_{i+\frac{1}{2}} \end{bmatrix} \tag{3.46}$$

by

$$q^-_{i+\frac{1}{2}} = q_L, \quad q^+_{i+\frac{1}{2}} = q_R, \quad K_{i+\frac{1}{2}} = \frac{1}{2}(K_L + K_R), \quad A^\pm_{i+\frac{1}{2}} = A_0. \tag{3.47}$$

The properties (a)-(f) are still satisfied for the subcritical and the supercritical branches of the vertical half-line of figures 3.5(b) and 3.7.

Finally, let us consider two states $\boldsymbol{W}_L$, $\boldsymbol{W}_R$ such that

$$(A_L - A_0)(A_R - A_0) < 0.$$

From the analysis of the integral curve, we know that the only integral curves that may contain both states are those of the form depicted in figure 3.5(b). But, in this case, one of the states is subcritical and the other one is supercritical. In other words, property (f) is meaningless in this case. Therefore, the well-balanced property is not relevant and any choice of the fluctuations

allowing us to show that $D^{\pm}$ are continuous and that the numerical method is path-conservative is admissible. Our choice is the following: $\boldsymbol{W}^{\pm}_{i+\frac{1}{2}}$ are defined by (3.46) with

$$q^{-}_{i+\frac{1}{2}} = q_L, \quad q^{+}_{i+\frac{1}{2}} = q_R, \quad A^{-}_{i+\frac{1}{2}} = A_L, \quad A^{+}_{i+\frac{1}{2}} = A_R, \quad K_{i+\frac{1}{2}} = \frac{1}{2}(K_L + K_R). \tag{3.48}$$

and the fluctuations are computed as follows

$$D^{+}(\boldsymbol{W}_L, \boldsymbol{W}_R) = \boldsymbol{F}(\boldsymbol{Q}_R, K_R) - \boldsymbol{G}(\boldsymbol{Q}^{-}_{i+\frac{1}{2}}, \boldsymbol{Q}^{+}_{i+\frac{1}{2}}, K_{i+\frac{1}{2}}) + \boldsymbol{S}(\boldsymbol{Q}_R)\frac{K_R - K_L}{2}. \tag{3.49}$$

$$D^{-}(\boldsymbol{W}_L, \boldsymbol{W}_R) = \boldsymbol{G}(\boldsymbol{Q}^{-}_{i+\frac{1}{2}}, \boldsymbol{Q}^{+}_{i+\frac{1}{2}}, K_{i+\frac{1}{2}}) - \boldsymbol{F}(\boldsymbol{Q}_L, K_L) + \boldsymbol{S}(\boldsymbol{Q}_L)\frac{K_R - K_L}{2}. \tag{3.50}$$

If $(A^n_i - A_0)(A^n_{i+1} - A_0) < 0$, using these fluctuations in (3.36), it can be easily checked that the numerical method reduces to:

$$\boldsymbol{Q}^{n+1}_i = \boldsymbol{Q}^n_i - \frac{\Delta t}{\Delta x}\left(\boldsymbol{G}_{i+\frac{1}{2}} - \boldsymbol{G}_{i-\frac{1}{2}} + \boldsymbol{S}(\boldsymbol{Q}^n_i)\frac{K_{i+1} - K_{i-1}}{2}\right),$$

where

$$\boldsymbol{G}_{i+\frac{1}{2}} = \boldsymbol{G}(\boldsymbol{Q}^n_i, \boldsymbol{Q}^n_{i+1}, K_{i+\frac{1}{2}}).$$

The chosen fluctuations correspond thus to a centered discretization of the source term.

Well-balanceness for transcritical smooth solutions

- The above described numerical method is well-balanced for transcritical steady solutions such that $A(x) < A_0$ provided that the point x_{min}, for which $K(x_{min})$ reaches its minimum value, is placed at the center of a cell, i.e. $x_k = x_{min}$ for some index k. In effect, due to Proposition 2 we know that

$$D^{\pm}_{i+\frac{1}{2}} = 0, \quad \forall j \neq k-1, k.$$

As $K(x_k) < K(x_{k+1})$, according to subsubsection 3.1.4, the reconstructed states corresponding to the pair of states $\boldsymbol{W}^0_{k-1} = [A(x_{k-1}), \bar{q}, K(x_{k-1})]^T$ and $\boldsymbol{W}^0_k = [A(x_k), \bar{q}, K(x_k)]^T$ are given by

$$\boldsymbol{W}^{-}_{k-\frac{1}{2}} = \boldsymbol{W}^0_{k-1}, \quad \boldsymbol{W}^{+}_{k-\frac{1}{2}} = \begin{pmatrix} A^{+}_{k-\frac{1}{2}} \\ \bar{q} \\ K(x_{k-1}) \end{pmatrix},$$

where $A^{+}_{k-\frac{1}{2}}$ is the only root of the equation

$$\frac{\rho}{2}\left(\frac{\bar{q}}{A}\right)^2 + K(x_{k-1})\,\phi(A) = \frac{\rho}{2}\left(\frac{\bar{q}}{A(x_k)}\right)^2 + K(x_k)\,\phi(A(x_k)), \tag{3.51}$$

such that $\boldsymbol{W}^{-}_{k-\frac{1}{2}}$ has the same regime than $\boldsymbol{W}^0_{k-1}$. Obviously, this root is given by $A(x_{k-1})$, as $\boldsymbol{W}^0_{k-1}$ and $\boldsymbol{W}^0_k$ belong to the same integral curve of the LD field. Therefore,

$$\boldsymbol{W}^{+}_{k-\frac{1}{2}} = \boldsymbol{W}^{-}_{k-\frac{1}{2}} = \boldsymbol{W}^0_{k-1},$$

and thus $D^{\pm}_{k-\frac{1}{2}} = 0$. A similar argument shows that also $D^{\pm}_{k+\frac{1}{2}} = 0$.

- The numerical method is well-balanced for transcritical steady solutions such that $A(x) > A_0$ provided that the maximum point x_{max} of K is placed at the centre of a cell, i.e. $x_k = x_{max}$ for some index k. The proof is similar to the one of the previous case.

- The numerical method is well-balanced for transcritical steady solutions such that the sign of $A(x) - A_0$ changes at $x = x_{crit}$ provided that the x_{crit} is placed at the centre of a cell, i.e. $x_k = x_{crit}$ for some index k. The proof is again similar.

Continuity of the GHR operator The reconstruction operator described in the above subsections is not continuous in $A = A_0$. In effect, it can be easily shown that, given two states

$$\boldsymbol{W}_L^{\varepsilon,-} = \begin{pmatrix} A_0 - \varepsilon \\ q_L \\ K_L \end{pmatrix}, \quad \boldsymbol{W}_R^{\varepsilon,-} = \begin{pmatrix} A_0 - \varepsilon \\ q_R \\ K_R \end{pmatrix}.$$

the corresponding GH reconstructed states converge as $\varepsilon \to 0$ to

$$\boldsymbol{W}_{i+\frac{1}{2}}^- = \begin{pmatrix} A_0 \\ q_L \\ \max(K_L, K_R) \end{pmatrix}, \quad \boldsymbol{W}_{i+\frac{1}{2}}^+ = \begin{pmatrix} A_0 \\ q_R \\ \max(K_L, K_R) \end{pmatrix}.$$

If we now apply the same procedure to the states

$$\boldsymbol{W}_L^{\varepsilon,+} = \begin{pmatrix} A_0 + \varepsilon \\ q_L \\ K_L \end{pmatrix}, \quad \boldsymbol{W}_R^{\varepsilon,+} = \begin{pmatrix} A_0 + \varepsilon \\ q_R \\ K_R \end{pmatrix},$$

the limits of the reconstructed states are

$$\boldsymbol{W}_{i+\frac{1}{2}}^- = \begin{pmatrix} A_0 \\ q_L \\ \min(K_L, K_R) \end{pmatrix}, \quad \boldsymbol{W}_{i+\frac{1}{2}}^+ = \begin{pmatrix} A_0 \\ q_R \\ \min(K_L, K_R) \end{pmatrix}.$$

Finally, if this procedure is applied to the pairs $(\boldsymbol{W}_L^{\varepsilon,-}, \boldsymbol{W}_R^{\varepsilon,+})$ or $(\boldsymbol{W}_L^{\varepsilon,+}, \boldsymbol{W}_R^{\varepsilon,-})$ the limits are

$$\boldsymbol{W}_{i+\frac{1}{2}}^- = \begin{pmatrix} A_0 \\ q_L \\ \frac{K_L + K_R}{2} \end{pmatrix}, \quad \boldsymbol{W}_{i+\frac{1}{2}}^+ = \begin{pmatrix} A_0 \\ q_R \\ \frac{K_L + K_R}{2} \end{pmatrix}.$$

Only in this last case, the limit of the reconstructions coincide with the reconstructions of the limit states

$$\boldsymbol{W}_L = \begin{pmatrix} A_0 \\ q_L \\ K_L \end{pmatrix}, \quad \boldsymbol{W}_R = \begin{pmatrix} A_0 \\ q_R \\ K_R \end{pmatrix}.$$

Nevertheless, the fluctuation functions $D^\pm$ are continuous, provided that the chosen numerical flux $\boldsymbol{G}(\boldsymbol{Q}_L, \boldsymbol{Q}_R, K)$ satisfies the following property

$$\partial_K \boldsymbol{G}\left(\begin{pmatrix} A_0 \\ q_L \end{pmatrix}, \begin{pmatrix} A_0 \\ q_R \end{pmatrix}, K\right) = 0, \quad \forall q_L, q_R, \tag{3.52}$$

i.e. the numerical flux applied to two states satisfying $A = A_0$ is independent of K. This is a natural requirement, as the flux function satisfies

$$\partial_K \boldsymbol{F}\left(\begin{pmatrix} A_0 \\ q \end{pmatrix}, K\right) = \partial_K \left(\frac{q^2}{A}\right) = 0, \quad \forall q.$$

Indeed, if (3.52) is satisfied, it can be easily checked that, in all the above discussed cases, one has

$$\lim_{\varepsilon \to 0} D^\pm\left(\boldsymbol{W}_L^{\varepsilon,\pm}, \boldsymbol{W}_R^{\varepsilon,\pm}\right) = D^\pm\left(\boldsymbol{W}_L, \boldsymbol{W}_R\right).$$

Therefore, the lack of continuity at $A = A_0$ of the GH-reconstructions is not seen by the numerical method.

Path-conservativity of the first-order numerical scheme

The first-order well balanced numerical scheme (3.32) with fluctuations given by (3.39)-(3.40) for states such that $(A_L - A_0)(A_R - A_0) \geq 0$ and by (3.49)-(3.50) otherwise is path-conservative for the family of paths Ψ defined as follows: given two states $\boldsymbol{W}_L, \boldsymbol{W}_R$ the path linking them is a parametrisation in $[0, 1]$ of the composition of the following curves:

1. If $(A_L - A_0)(A_R - A_0) \geq 0$ and $K_{i+\frac{1}{2}} = K_L$ the path is composed by:

- The straight segment linking $\boldsymbol{W}_L$ and $\boldsymbol{W}^+_{i+\frac{1}{2}}$.

- The arc of integral curve of the LD field linking $\boldsymbol{W}^+_{i+\frac{1}{2}}$ and $\boldsymbol{W}_R$.

2. If $(A_L - A_0)(A_R - A_0) \geq 0$ and $K_{i+\frac{1}{2}} = K_R$ the path is composed by:

- The arc of integral curve of the LD field linking and $\boldsymbol{W}_L$ and $\boldsymbol{W}^-_{i+\frac{1}{2}}$.

- The straight segment linking $\boldsymbol{W}^-_{i+\frac{1}{2}}$ and $\boldsymbol{W}_R$.

3. If $(A_L - A_0)(A_R - A_0) < 0$ the path is composed by the straight segments linking the following pair of states:

- $(\boldsymbol{W}_L\,,\,\boldsymbol{W}^-_{i+\frac{1}{2}})$,

- $(\,\boldsymbol{W}^-_{i+\frac{1}{2}},\,\boldsymbol{W}^+_{i+\frac{1}{2}})$,

- $(\boldsymbol{W}^+_{i+\frac{1}{2}},\,\boldsymbol{W}_R)$.

In effect, from this definition of paths and taking into account that the arcs of integral curves of the characteristic field related to the null eigenvalue do not contribute to the integral, some easy computations show that,

$$\int_0^1 \boldsymbol{A}\left(\Psi\left(\boldsymbol{W}_L, \boldsymbol{W}_R, s\right)\right) \frac{\partial \Psi}{\partial s}\left(\boldsymbol{W}_L, \boldsymbol{W}_R, s\right)\, ds = \begin{bmatrix} \boldsymbol{F}(\boldsymbol{Q}^+_{i+\frac{1}{2}}, K_{i+\frac{1}{2}}) - \boldsymbol{F}(\boldsymbol{Q}^-_{i+\frac{1}{2}}, K_{i+\frac{1}{2}}) \\ 0 \end{bmatrix}$$

if $(A_L - A_0)(A_R - A_0) \geq 0$ and

$$\int_0^1 \boldsymbol{A}\left(\Psi\left(\boldsymbol{W}_L, \boldsymbol{W}_R, s\right)\right) \frac{\partial \Psi}{\partial s}\left(\boldsymbol{W}_L, \boldsymbol{W}_R, s\right)\, ds = \begin{bmatrix} \boldsymbol{F}(\boldsymbol{Q}_R, K_R) - \boldsymbol{F}(\boldsymbol{Q}_L, K_L) + \frac{1}{2}(\boldsymbol{S}(\boldsymbol{Q}_R) + \boldsymbol{S}(\boldsymbol{Q}_L))(K_R - K_L) \\ 0 \end{bmatrix}$$

otherwise. From these equalities and the definitions of the fluctuations, (3.35) can be easily checked.

Observe that, in practice, the numerical method is implemented in the form (3.36) using the expressions of the fluctuations given by (3.39)-(3.40) for states such that $(A_L - A_0)(A_R - A_0) \geq 0$ and by (3.49)-(3.50) otherwise. Therefore, it is not necessary to explicitly know a parameterization of the paths to apply the method.

3.1.5   High-order extension

In this subsection we extend the GHR scheme to high-order in space and time. First, we briefly introduce the high-order numerical scheme. Then, we modify the original high-order scheme in order to preserve exactly well-balanced properties.

High-order ADER schemes

We construct a non-linear numerical scheme of high-order of accuracy in space and time by adopting the ADER framework, see [159]. The ADER finite volume methods are fully discrete, perform a non-linear spatial reconstruction and then solve a generalised (or high-order) Riemann problem (GRP) at each cell interface. There are so far four methods for finding the approximate solution of the GRP. In the original method proposed in [162], the solution at the interface is expressed in terms of a time series expansion. The complete solution first involves the determination of the leading term via the solution of a classical Riemann problem for the states. Then, the high-order terms are determined via solutions to derivative Riemann problems, in which the application of the Cauchy-Kowalewski procedure is involved. The numerical flux is obtained from numerical integration of the physical flux function evaluated at the solution of the GRP at the interface, see [162]. For a comparative review of all four GRP solvers available see [111].

In this work we use the GRP solver proposed in [64] and extended to non-conservative systems in [63] and [65]. The necessary steps to obtain the high-order finite volume scheme are the following:

- non-linear spatial reconstruction based on cell averages at time t^n,

- solution of the GRP by the Dumbser-Enaux-Toro (DET) solver [64],

- numerical integration of fluctuations along cell interfaces and of non-conservative terms and source terms in space and time.

If we define a control volume $T_i = [x_{i-\frac{1}{2}}; x_{i+\frac{1}{2}}] \times [t^n; t^{n+1}]$ and integrate (3.12) using integration by parts we obtain

$$\boldsymbol{W}_i^{n+1} = \boldsymbol{W}_i^n - \frac{\Delta t}{\Delta x} \left(\boldsymbol{\mathcal{D}}_{i+\frac{1}{2}}^- + \boldsymbol{\mathcal{D}}_{i-\frac{1}{2}}^+ \right) - \frac{1}{\Delta x} \left[\boldsymbol{A}(\boldsymbol{W}_h) \partial_x \boldsymbol{W}_h \right]_i + \Delta t \boldsymbol{B}_i \,, \qquad (3.53)$$

where

$$\boldsymbol{\mathcal{D}}_{i+\frac{1}{2}}^\pm = \frac{1}{\Delta t} \int_{t^n}^{t^{n+1}} \boldsymbol{D}^\pm \left(\boldsymbol{W}_h(x_{i+\frac{1}{2}}^-, t), \boldsymbol{W}_h(x_{i+\frac{1}{2}}^+, t) \right) dt \,. \qquad (3.54)$$

For completeness, in we included the source term due to friction and gravity in (3.53), which is represented by

$$\boldsymbol{B}_i = \frac{1}{\Delta t \, \Delta x} \int_{t^n}^{t^{n+1}} \int_{x_{i-\frac{1}{2}}}^{x_{i+\frac{1}{2}}} \boldsymbol{B}(\boldsymbol{W}_h(x,t)) \, dx \, dt \,, \qquad (3.55)$$

with

$$\boldsymbol{B}(\boldsymbol{W}) = [0, A\,g - f, 0]^T \,.$$

Here, $\boldsymbol{D}_{i+\frac{1}{2}}^\pm$ are fluctuations defined in subsection 3.1.4 and $\boldsymbol{W}_h(x,t) = [\boldsymbol{Q}_h(x,t), K_h(x)]^T$ is an element-local space-time predictor from the space of piecewise space-time polynomials of degree M, whose computation will be introduced later. Contrary to the first-order scheme (3.32), in the case of a high-order scheme, there is an additional term in (3.53), given by

$$\left[\boldsymbol{A}(\boldsymbol{W}_h) \partial_x \boldsymbol{W}_h \right]_i = \int_{t^n}^{t^{n+1}} \int_{x_{i-\frac{1}{2}}}^{x_{i+\frac{1}{2}}} \boldsymbol{A}(\boldsymbol{W}_h(x,t)) \partial_x \boldsymbol{W}_h(x,t) \, dx \, dt \,. \qquad (3.56)$$

As it was mentioned for the first-order method, in practice the variable K is not advanced in time. If this variable is dropped, the numerical method can be written in the equivalent form:

$$\boldsymbol{Q}_i^{n+1} = \boldsymbol{Q}_i^n - \frac{\Delta t}{\Delta x} \left(\boldsymbol{\mathcal{D}}_{i+\frac{1}{2}}^- + \boldsymbol{\mathcal{D}}_{i-\frac{1}{2}}^+ \right) - \frac{\Delta t}{\Delta x} \left(\boldsymbol{\mathcal{F}}_{i+\frac{1}{2}}^- - \boldsymbol{\mathcal{F}}_{i-\frac{1}{2}}^+ \right) - \frac{1}{\Delta x} \boldsymbol{S}_i + \Delta t \hat{\boldsymbol{B}}_i \qquad (3.57)$$

where

$$\boldsymbol{\mathcal{F}}_{i+\frac{1}{2}}^\pm = \frac{1}{\Delta t} \int_{t^n}^{t^{n+1}} \boldsymbol{F} \left(\boldsymbol{Q}_h(x_{i+\frac{1}{2}}^\pm), K_h(x_{i+\frac{1}{2}}) \right) \qquad (3.58)$$

and

$$\boldsymbol{S}_i = \int_{t^n}^{t^{n+1}} \int_{x_{i-\frac{1}{2}}}^{x_{i+\frac{1}{2}}} \boldsymbol{S}(\boldsymbol{Q}_h(x,t)) \partial_x K_h(x) \, dx \, dt \,. \qquad (3.59)$$

The source term vector is now

$$\hat{\boldsymbol{B}}(\boldsymbol{Q}) = [0, A\,g - f]^T \,.$$

Moreover, if K_h is continuous, some easy computations show that the numerical method reduces to:

$$\boldsymbol{Q}_i^{n+1} = \boldsymbol{Q}_i^n - \frac{\Delta t}{\Delta x} \left(\boldsymbol{\mathcal{G}}_{i+\frac{1}{2}} - \boldsymbol{\mathcal{G}}_{i-\frac{1}{2}} \right) - \frac{1}{\Delta x} \boldsymbol{S}_i + \Delta t \hat{\boldsymbol{B}}_i \,, \qquad (3.60)$$

where

$$\boldsymbol{\mathcal{G}}_{i+\frac{1}{2}} = \frac{1}{\Delta t} \int_{t^n}^{t^{n+1}} \boldsymbol{G} \left(\boldsymbol{Q}_h(x_{i+\frac{1}{2}}^-, t), \boldsymbol{Q}_h(x_{i+\frac{1}{2}}^+, t), K_h(x_{i+\frac{1}{2}}) \right) dt. \qquad (3.61)$$

Non-linear spatial reconstruction

In our finite volume-type scheme we evolve cell averages $\boldsymbol{W}_i^n$ to $\boldsymbol{W}_i^{n+1}$. Therefore, at each time step we perform a non-linear spatial reconstruction based on cell averages $\boldsymbol{W}_j^n$, belonging to the stencil $\mathcal{S}_i$, for details see [62]. We use the WENO reconstruction operator [88] in order to obtain a spatial piecewise polynomial of degree M

$$\boldsymbol{\omega}_h^n = \boldsymbol{\omega}_h(x, t^n) = \sum_{l=1}^{M+1} \gamma_l(x) \hat{\boldsymbol{\omega}}_l^n \,, \tag{3.62}$$

where $\gamma_l(x)$ are the reconstruction basis functions and $\hat{\boldsymbol{\omega}}_l$ are the expansion coefficients of the seek piecewise polynomials. These coefficients are the output of the WENO reconstruction operator. We use a nodal base composed by Lagrange polynomials whose nodes coincide with a quadrature rule of appropriate order. As we will see later, we must choose a quadrature rule which extreme quadrature points coincide with the cell border in order to preserve steady solutions. In our case we use a Gauss-Lobatto quadrature rule.

The DET solver

The DET solver for the GRP solves an element-local weak form of system (3.12) with an implicit space-time Discontinuous Galerkin (DG) finite element method in order to obtain $\boldsymbol{W}_h$. Once that $\boldsymbol{W}_h$ is available for each cell of the spatial discretization, the solution to the GRP is found by solving a series of classical Riemann problems at the cell interface for a set of given time levels in order to numerically compute (3.54). In this work we use a particular formulation of the scheme that uses nodal space-time basis functions [83]. We give here a brief description of the method and refer to the above cited references for more details on the numerical scheme.

First we transform system (3.12) into a space-time reference element $T_E = [0;1] \times [0;1]$ with coordinates ξ and τ, given by $x = x_{i-\frac{1}{2}} + \xi \Delta x$ and $t = t^n + \tau \Delta t^n$:

$$\partial_\tau \boldsymbol{W}_h + \boldsymbol{A}^* \partial_\xi \boldsymbol{W}_h = \boldsymbol{B}^* \,, \tag{3.63}$$

with modified Jacobian and source term

$$\boldsymbol{A}^* := \frac{\Delta t}{\Delta x} \boldsymbol{A}(\boldsymbol{W}_h) \,, \quad \boldsymbol{B}^* := \Delta t \boldsymbol{B}(\boldsymbol{W}_h) \,.$$

We introduce the following operators that will be useful later on

$$[a, b]^\tau = \int_0^1 a(\xi, \tau) b(\xi, \tau) \, d\xi \quad \text{and} \quad < a, b >_{T_E} = \int_0^1 \int_0^1 a(\xi, \tau) b(\xi, \tau) \, d\xi \, d\tau \,. \tag{3.64}$$

Multiplying (3.63) by the space-time test function $\theta_k = \theta_k(\xi, \tau)$, integrating over the space-time reference element T_E and integrating by parts the time derivative term we obtain that

$$[\theta_k, \boldsymbol{W}_h]^1 - < \partial_\tau \theta_k, \boldsymbol{W}_h >_{T_E} + < \theta_k, \boldsymbol{A}^* \partial_\xi \boldsymbol{W}_h >_{T_E} = [\theta_k, \boldsymbol{\omega}_h]^0 + < \theta_k, \boldsymbol{B}^* >_{T_E} \,. \tag{3.65}$$

For $\boldsymbol{W}_h$ and $\boldsymbol{A}^* \partial_\xi \boldsymbol{W}_h$ we use the same space-time basis function θ_k, so that

$$\boldsymbol{W}_h(\xi, \tau) = \sum_{l=1}^{(M+1)^2} \theta_l(\xi, \tau) \hat{\boldsymbol{W}}_l := \theta_l \hat{\boldsymbol{W}}_l \,, \quad \boldsymbol{A}^* \partial_\xi \boldsymbol{W}_h(\xi, \tau) = \sum_{l=1}^{(M+1)^2} \theta_l(\xi, \tau) \widehat{\boldsymbol{A}^* \partial_\xi \boldsymbol{W}}_l := \theta_l \widehat{\boldsymbol{A}^* \partial_\xi \boldsymbol{W}}_l \,. \tag{3.66}$$

We obtain expansion coefficients $\hat{\boldsymbol{W}}_l$ by a fixed point iteration procedure, see [64] for details, in which at each iteration step we solve the following system

$$\left([\theta_k, \theta_l]^1 - < \partial_t \theta_k, \theta_l >_{T_E} \right) \hat{\boldsymbol{W}}_l^{m+1} - < \theta_k, \theta_l >_{T_E} \boldsymbol{B}^*(\hat{\boldsymbol{W}}_l^{m+1}) = [\theta, \boldsymbol{\omega}_h]^0 - < \theta_k, \theta_l >_{T_E} \widehat{\boldsymbol{A}^* \partial_\xi \boldsymbol{W}}_l^m \,. \tag{3.67}$$

In order to obtain an interpolation of the solution derivative $\partial_\xi \boldsymbol{W}_h$ we make the ansatz

$$\partial_\xi \boldsymbol{W}_h = \partial_\xi \left(\theta_l \hat{\boldsymbol{W}}_l \right) := \theta_l \widehat{\partial_\xi \boldsymbol{W}}_l$$

and use the weak identity

$$< \theta_k, \theta_l > \widehat{\partial_\xi \boldsymbol{W}}_l = < \theta_k, \partial_\xi \theta_l > \hat{\boldsymbol{W}}_l \,, \tag{3.68}$$

so that the approximation of the derivative is of the same order as the polynomial of the local space-time solution $\boldsymbol{W}_h$, see [63] for details.

High-order well-balanced reconstruction

The output of the WENO reconstruction operator is a piecewise polynomial of degree M for each cell of the spatial discretization

$$\boldsymbol{\omega}_i^n(x) = \begin{pmatrix} \tilde{A}_i(x) \\ \tilde{q}_i(x) \end{pmatrix} = \begin{pmatrix} \hat{A}_l^i \gamma_l(x) \\ \hat{q}_l^i \gamma_l(x) \end{pmatrix}. \tag{3.69}$$

Note that we did not include K in (3.69). In fact $K = K(x)$ is a prescribed function and its value, as well as its spatial derivative, are exactly evaluated by the high-order scheme at each node of the nodal space-time basis function.

A modification of the WENO reconstruction operator is necessary in order to preserve well-balanced properties of the high-order scheme since steady solutions of system (3.12) are not necessarily a polynomial. Therefore, no matter the accuracy of the spatial reconstruction, steady solutions will not be reconstructed exactly. We want to design a spatial reconstruction algorithm whose output, in the presence of a steady solution, is a projection of that solution into the space of piecewise polynomials $\boldsymbol{\omega}_i$. The output of this procedure are going to be values of A and q at the nodes of the spatial basis, which in the case of a steady solution will coincide with the exact ones. In order to achieve this, the cell averages for A and q of the initial condition, have to be computed using a numerical integration with the same quadrature rule used by the numerical scheme. We base our work in the methodology reported in [45], full details are given in this reference.

Noting that numerical integrations in (3.53) are performed using a Gaussian quadrature rule with N weights w_k and quadrature point positions x_k, the steps to be performed at each time step n for the i-th cell are the following ones:

1. Apply the WENO reconstruction operator on stencil $\mathcal{S}_i$ for A_i^n and q_i^n to obtain (3.69).

2. Taking into account the information given by the reconstructions of the first step, find, if possible, a Riemann invariant Γ_i^* such that

$$A_i^n = \frac{1}{\Delta x} \sum_{k=1}^{N} w_k^i A(x_k^i, q_i^n, \Gamma_i^*), \tag{3.70}$$

where w_k^i, x_k^i are the weights and points of the chosen quadrature rule, and $A(x, q_i^n, \Gamma_i^*)$ is a solution of (3.30) with $\bar{q} = q_i^n$ and $\Gamma = \Gamma_i^*$ whose computation will be described in 3.1.5.

3. If it is not possible to find a solution Γ_i^* of (3.70), the reconstructions found at the first step are kept.

4. Otherwise:

   (a) For every cell j belonging to the stencil $\mathcal{S}_i$, define $\boldsymbol{V}_j^n$ by

   $$\boldsymbol{V}_j^n = \begin{pmatrix} A_j^n - \dfrac{1}{\Delta x} \sum_{k=1}^{N} w_k^j A(x_k^j, q_j^n, \Gamma_i^*) \\ q_j^n - q_i^n \end{pmatrix}, \tag{3.71}$$

   that measure the deviation of the cell averages from the stationary solution found at the previous step.

   (b) Apply the WENO reconstruction operator to deviations $\boldsymbol{V}_j^n$ computed for the stencil in order to obtain a reconstruction

   $$\tilde{\boldsymbol{V}}_i(x) = \gamma_l(x) \hat{\boldsymbol{V}}_l$$

   .

(c) The piecewise polynomial $\boldsymbol{\omega}_i^n(x)$ with the following expansion coefficients is kept

$$\hat{\boldsymbol{\omega}}_l^n = \begin{pmatrix} A(x_l, q_i^n, \Gamma_i^*) \\ q_i^n \end{pmatrix} + \hat{\boldsymbol{V}}_l, \quad l = 1, ..., M + 1. \tag{3.72}$$

Algorithm for the second step

Let us assume that the mesh and the quadrature rules have been chosen so that the minimal value K_{min} and maximal values K_{max} of $K(x)$ are reached at some quadrature nodes. The main difficulty in solving (3.70) is the following one: given $\bar{q}$, Γ and a point x, the possible value of $A(x)$ corresponding to a steady solution has to be computed by solving the equation (3.30), and this equation can have zero, one, or two solutions (corresponding to positive/negative pressures and/or subcritical/supercritical states), as it has been seen in subsection 3.1.3.

In order to overcome this difficulty we proceed as follows:

1. From the reconstructions obtained at the first step, compute

$$Fr_i^2(x) = \frac{\rho \tilde{q}_i(x)^2}{\tilde{A}_i^3(x) K(x) \phi'(\tilde{A}_i(x))} \, .$$

2. If the functions $\tilde{A}_i(x) - A_0$ and $Fr_i^2(x) - 1$ do not change their signs in I_i, solve (3.70) by applying Newton's method with the initial guess

$$\Gamma_i = \frac{\rho}{2} \frac{(q_i^n)^2}{(A_i^n)^2} + K_i \phi(A_i^n) \, .$$

During the algorithm, given Γ, the value of $A(x_k^i, q_i^n, \Gamma)$ is given by the solution A of the corresponding equation (3.30) such that $A(x_k^i, q_i^n, \Gamma) - A_0$ has the same sign as $\tilde{A}_i(x_k) - A_0$ and whose corresponding state has the regime given by the sign of $Fr_i^2(x_k) - 1$.

3. If $\tilde{A}_i(x)$ is lower that A_0 and $Fr_i^2(x) - 1$ changes its sign, say from negative to positive, the only possible transcritical steady solutions such that $A < A_0$ reaches the critical point at the point where K is minimal (see figures 3.3(b) and 3.4(b)). Then, if $K(x)$ does not reach the value K_{min} at the cell I_i, the algorithm is stopped and we pass to step 3 of subsection 3.1.5. Otherwise, the sought steady solution has to be critical at the minimum point and thus the value of A at this point has to be such that $Fr = 1$ or, equivalently

$$\frac{\rho(q_i^n)^2}{K_{min}} = A^3 \phi'(A) \, .$$

The solution of this equation gives the value $\underline{A}$ at the minimum point of K and, according to the discussion in subsection 3.1.3, the corresponding Riemann invariant is

$$\underline{\Gamma} = g(\underline{A}) \, .$$

If Γ satisfies (3.70), then $\Gamma_i^* = \underline{\Gamma}$. Otherwise, the algorithm is stopped and we pass to step 3 of subsection 3.1.5.

4. If $\tilde{A}_i(x)$ is greater that A_0 and $Fr_i^2(x) - 1$ changes its sign, we proceed as in the previous case just replacing K_{min} by K_{max}, which is the maximum value of $K(x)$.

5. If both $\tilde{A}_i(x) - A_0$ and $Fr_i^2(x) - 1$ change their signs, but there are regions in which $\tilde{A}_i(x) < A_0$ and the regime is subcritical or regions in which $\tilde{A}_i(x) > A_0$ and the regime is supercritical, the algorithm is stopped, and we pass to step 3 of subsection 3.1.5. Otherwise, by the discussion in subsection 3.1.3 we know that, the only possible steady solution satisfying this property corresponds to

$$\Gamma^* = \frac{\rho}{2} \left(\frac{q_i^n}{2} \right)^2 \, .$$

Moreover, the value of K at the critical point has to satisfy

$$K(x) = \frac{2\Gamma^*}{m - n}. \tag{3.73}$$

If this last equation has no solution in I_i the algorithm is stopped. Otherwise, we check if the transcritical steady solution characterized by q_i^n, Γ^* having the critical point at the solution x^* of (3.73) satisfies (3.70). If the answer is positive, then $\Gamma_i^* = \Gamma^*$. Otherwise, the algorithm is stopped and we pass to step 3 of subsection 3.1.5.

Modification to the local discontinuous Galerkin time evolution

As initial condition for the iterative predictor (3.67), we assign $\boldsymbol{\omega}_h(x_k)$ to all nodes of the space-time basis function aligned to x_k. If we compute $\boldsymbol{A}^*\partial_\xi \boldsymbol{W}_h$ using $\widehat{\partial_\xi \boldsymbol{W}_l}$, we will spoil the well-balanced properties of the numerical scheme. As for the spatial reconstruction, we face again the problem of steady solutions which are not polynomials. The reconstructed spatial function $\boldsymbol{\omega}_h$ is a polynomial that intersects the steady solution at quadrature points. Therefore, its derivatives will not correspond to the exact derivatives of the steady solution. We are forced then to treat the term $< \theta_k, \boldsymbol{A}^*\partial_\xi \boldsymbol{W}_h >$ of the element-local space-time predictor (3.67) in a special manner.

It can be easily seen that the first component of vector $\boldsymbol{A}^*\partial_\xi \boldsymbol{W}_h$ is $\partial_\xi q_h$. In the case of steady solutions $q = constant$ in the entire domain and the approximation of its derivative given by the WENO reconstruction is the exact one for any order of accuracy of the numerical scheme. The second component of vector $\boldsymbol{A}^*\partial_\xi \boldsymbol{W}_h$ is

$$\left(\frac{A_h}{\rho} K_h \phi'(A_h) - \left(\frac{q_h}{A_h} \right)^2 \right) \partial_\xi A_h + 2\frac{q_h}{A_h}\partial_\xi q_h + \frac{A_h}{\rho}\phi(A_h)\partial_\xi K_h \,. \tag{3.74}$$

The term $\partial_\xi A_h$ will not necessarily be exact and the local space-time predictor (3.67) will not preserve steady solutions exactly. Therefore we rewrite the second component of $\boldsymbol{A}^*\partial_\xi \boldsymbol{W}_h$ as

$$\frac{q_h}{A_h}\partial_\xi q_h + A_h\partial_\xi \left(\frac{1}{2}\left(\frac{q_h}{A_h} \right)^2 + \frac{p(A_h, K_h)}{\rho} \right) \,. \tag{3.75}$$

If the current solution is laying on a steady solution, then $\partial_\xi q = 0$ and $\partial_\xi \left(\frac{1}{2}\left(\frac{q_h}{A_h} \right)^2 + \frac{p(A_h,K_h)}{\rho} \right) = 0$, so that the non-conservative product will be computed correctly for all nodes of the nodal basis function θ_k.

3.1.6 Numerical results

In this subsection we present numerical results obtained with the methods described in previous subsections. In addition to the details given above, we must specify the numerical flux used for the tests. We use the FORCE numerical flux [156, 158], which is a centred flux that satisfies property (3.52).

Empirical convergence rates

Here we carry out a convergence rate study of the proposed numerical schemes. The study is empirical, for which a reference, ideally exact, solution is needed. We *manufacture* an exact reference solution for system (3.8) using the following procedure. We prescribe functions

$$\hat{A}(x,t) = A_0 + a_0 \sin\left(2\frac{\pi}{L}x \right) \cos\left(2\frac{\pi}{T_0}t \right) \,, \tag{3.76}$$

and

$$\hat{q}(x,t) = q_0 - \frac{a_0 L}{T_0}\cos\left(2\frac{\pi}{L}x \right) \sin\left(2\frac{\pi}{T_0}t \right) \,, \tag{3.77}$$

for the cross-subsectional area $A(x,t)$ and for the mass flux $q(x,t)$ respectively. K is described by

$$\hat{K}(x,t) = K_0 \left(1 + k_0 \sin\left(2\frac{\pi}{L}x \right) \right) \,. \tag{3.78}$$

Obviously these are not solutions of the original equations. Substitution of these functions into the original equations yields the modified system

$$\partial_t \boldsymbol{W} + \boldsymbol{A}(\boldsymbol{W})\partial_x \boldsymbol{W} = \tilde{\boldsymbol{B}}(x,t). \tag{3.79}$$

The resulting system is not the original system, but a modified system with an extra source term. The functions (3.76) and (3.77) are exact solutions of the modified system (3.79). This is the system used to carry out the convergence rate study.

Problem parameters for all tests are: $A_0 = 10^{-4}\,m^2$, $m = 10.0$, $n = -1.5$ and $\rho = 1050.0\,kg\,m^{-3}$. A Courant-Friedrichs-Lewy number (CFL) of 0.9 was used for all computations that are reported here.

Table 3.1 shows empirical convergence rates for implementations ranging from second to fifth order, together with parameters of the problem. The error is measured in three norms, namely L_1, L_2 and L_∞. The expected order of accuracy is reached in all cases.

Scheme	N	L^1	L^2	L^∞	$\mathcal{O}(L^1)$	$\mathcal{O}(L^2)$	$\mathcal{O}(L^\infty)$
ADER 2	4	7.1993e-04	8.2673e-04	1.2786e-03	-	-	-
	8	1.5812e-04	1.8321e-04	3.2578e-04	2.19	2.17	1.97
	16	3.3614e-05	4.2977e-05	1.1742e-04	2.23	2.09	1.47
	32	7.3137e-06	9.5124e-06	2.9728e-05	2.20	2.17	1.98
ADER 3	4	3.3752e-04	3.9055e-04	6.2194e-04	-	-	-
	8	4.0518e-05	4.7225e-05	9.3107e-05	3.06	3.05	2.74
	16	4.4075e-06	5.1889e-06	1.0864e-05	3.20	3.18	3.10
	32	5.0233e-07	6.0484e-07	1.3057e-06	3.13	3.10	3.06
ADER 4	4	2.1603e-04	2.3277e-04	2.9694e-04	-	-	-
	8	1.1818e-05	1.5061e-05	3.2236e-05	4.19	3.95	3.20
	16	7.2174e-07	1.0098e-06	2.7646e-06	4.03	3.90	3.54
	32	4.7501e-08	6.3034e-08	1.7367e-07	3.93	4.00	3.99
ADER 5	4	1.4779e-04	1.7128e-04	2.7642e-04	-	-	
	8	4.9184e-06	5.7621e-06	1.1231e-05	4.91	4.89	4.62
	16	1.3864e-07	1.6309e-07	3.3373e-07	5.15	5.14	5.07
	32	4.1146e-09	4.9061e-09	1.0653e-08	5.07	5.05	4.97

Table 3.1: Empirical convergence rates for the ADER scheme applied to blood flow in veins with variable mechanical properties. Test parameters: $CFL = 0.9$, $A_0 = 10^{-4}\,m^2$, $a_0 = 2 \cdot 10^{-6}\,m^2$, $L = 1m$, $T_0 = 3s$, $q_0 = 0\,\frac{m^3}{s}$, $K_0 = 100\,Pa$, $k_0 = 0.01$.

Steady solutions with smooth K

In this subsection we prescribe a smooth variation of K, from K_0 to K_1 and a steady state initial condition. The numerical scheme should preserve the initial condition exactly for both, its first and high-order versions.

$K(x)$ varies according to the following expression

$$K(x) = \begin{cases} K_0 & \text{if } x < x_1 \text{ or } x > x_2, \\ a\,\xi^5 + b\,\xi^4 + c\,\xi^3 + K_0 & \text{if } x \geq x_1 \text{ and } x \leq x_1 + 2\delta, \\ K_1 & \text{if } x > x_1 + 2\delta \text{ and } x < x_2 - 2\delta, \\ \hat{a}\,\eta^5 + \hat{b}\,\eta^4 + \hat{c}\,\eta^3 + K_1 & \text{if } x \leq x_2 \text{ and } x \geq x_2 - 2\delta. \end{cases} \tag{3.80}$$

We have $\xi = \frac{x-x_1}{2\delta}$ and $\eta = \frac{x-x_2+2\delta}{2\delta}$ and $\Delta = K_1 - K_0$. We test the GHR scheme concerning the exact preservation of steady subcritical, supercritical and transcritical solutions in Ω^-, Ω^+ and Ω. Coefficients for polynomials appearing in (3.80) are reported for each case.

Initial conditions are given by specifying a discharge $q(x,0) = q_0$, whereas the cross-subsectional area is computed by solving (3.30) for a given $\Gamma_0 = \Gamma(A^*, q_0, K^*)$. Γ_0 is chosen by fixing a value for the cross-subsectional area A^* at a given point x^* where $K(x^*) = K^*$.

Common parameters to all tests are: $A_0 = 10^{-4}\,m^2$, $m = 10.0$, $n = -1.5$ and $\rho = 1050.0\,kg\,m^{-3}$. The numerical solutions are computed on a domain of length $L = 1\,m$, divided in 100 cells and using a $CFL = 0.9$.

Subcritical and supercritical steady solutions

Four tests are performed with the first-order and third-order numerical schemes. Parameters for (3.80) are: $x_1 = 0.2$, $x_2 = 0.8$, $\delta = 0.1$, $a = 6\Delta$, $\hat{a} = -a$, $b = -15\Delta$, $\hat{b} = -b$, $c = 10\Delta$, $\hat{c} = -c$. Figures 3.8(a) to (b) show the variation of K in space for tests SUB-1, SUB-2, SUB-3 and SUB-4, respectively.

Initial conditions are computed as explained in the previous subsection, using parameters specified in table 3.2.

Test	$x^*\,[m]$	$A^*\,[m^2]$	$K_0\,[Pa]$	$K_1\,[Pa]$	$q_0[m^3s^{-1}]$	Fr	$t_{end}\,[s]$
SUB-1	0	2.5 A_0	100	10	8.00e-04	0.128	0.1
SUB-2	0	0.4 A_0	100	1000	2.00e-05	0.665	0.3
SUP-1	0	1.5 A_0	100	10	1.52e-03	1.93	0.1
SUP-2	0	0.9 A_0	500	5000	2.25e-04	1.582	0.3

Table 3.2: Parameters for subcritical and supercritical steady solution tests.

Numerical results for the non-dimensional cross-subsectional area, together with the error with respect to the steady solution are reported in figure 3.9. The proposed numerical scheme preserves steady subcritical and supercritical solutions exactly in its first and third-order versions. Small errors for the third-order solutions are due to the tolerance by which (3.30) is solved during the well-balanced WENO reconstruction but are in any case negligible.

Transcritical steady solutions

Three transcritical tests are performed: one in Ω^- (TRA-1), another one in Ω^+ (TRA-2) and finally one in Ω (TRA-3). In tests TRA-1 and TRA-2, parameters for (3.80) are identical to the ones used in the previous subsection, with the only difference given by $\delta = 0.15$, so that the minimum (or maximum) value of K is reached at a single point $x_c = 0.5\,m$. This is necessary for obtaining smooth transcritical solutions, since they will occur at a point where $K_c = min(K)$ in Ω^- and vice versa, where $K_c = max(K)$ in Ω^+ (see figures 3.8(e) and 3.8(f)).

For TRA-3, the transcritical solution in Ω, K_c is given by (3.73), and $K(x)$ varies according to the following expression

$$K(x) = \begin{cases} K_0 & \text{if } x < x_1, \\ a\,\xi^5 + b\,\xi^4 + c\,\xi^3 + K_0 & \text{if } x \geq x_1 \text{ and } x \leq x_1 + 2\delta, \\ K_1 & \text{if } x > x_1 + 2\delta \text{ and} \end{cases} \qquad (3.81)$$

with $\Delta = K_1 - K_0$. Polynomial coefficients are the same as the ones given in the previous subsection. In this way, K is a decreasing function of x in $(0, 1)$, as shown in figure 3.8(g).

Test parameters for TRA-1 to TRA-3 are given in table 3.3, whereas numerical results for the non-dimensional cross-subsectional area and error with respect to the exact solution are shown in figure 3.10. In the case of TRA-1 and TRA-2 the regime is subcritical for $x < 0.5\,m$, critical for $x = 0.5\,m$ and supercritical for $x > 0.5\,m$. On the other hand, for TRA-3 the regime is supercritical for $x < 0.5\,m$, critical for $x = 0.5\,m$ and subcritical for $x > 0.5\,m$. We report first and third-order steady solutions. The choice of third order is related to the fact that using this order, the quadrature points of the spatial discretisation can be easily chosen so that an internal quadrature point coincides with $x_c = 0.5\,m$. Both, the first-order and third-order schemes preserve the steady solutions exactly.

Test	$x^*\,[m]$	$K_0\,[Pa]$	$K_c\,[Pa]$	$q_0[m^3s^{-1}]$	$t_{end}\,s$
TRA-1	0.5	100	50	1.98e-05	0.1
TRA-2	0.5	100	200	6.69e-04	0.1
TRA-3	0.5	100	80	9.93e-05	0.1

Table 3.3: Parameters for transcritical steady solution tests.

Wave propagation test

Here we study the propagation of a perturbation along a vessel with varying mechanical properties. For $K(x)$ we use relation (3.80) with $x_1 = 0.9$, $x_2 = 1.3$, $\delta = 0.01$, $K_0 = 100\,Pa$,

$K_1 = 2000\,Pa$. Initial conditions are $q(x,0) = 0\,m^3\,s^{-1}$ and the cross-subsectional area is set to satisfy an initially steady solution for

$$p(x,0) = K(x)\left(\left(\frac{A}{A_0}\right)^m - \left(\frac{A}{A_0}\right)^n\right) = K_0\left(2^m - 2^n\right),$$

with $A_0 = 10^{-4}\,m^2$. This steady solution is perturbed with

$$A = 2.1\,A_0 \text{ for } 0.2 < x < 0.4\,m.$$

Solutions are obtained using 100 equidistant cells and a $CFL = 0.9$ on a domain of length $L = 2\,m$. Numerical solutions are compared to a reference solution obtained using 1000 cells. Results are reported in figures 3.11 and 3.13, for output times $t_{end} = 0.01\,s$ and $t_{end} = 0.043\,s$, respectively. It can be clearly observed that the numerical solutions obtained with the proposed methodology correctly reproduce the reference solution.

Since the well-balanced spatial reconstruction algorithm presented in subsections 3.1.5 and 3.1.5 is computationally expensive, we solved the wave propagation problem using well-balanced fluctuations introduced in subsection 3.1.4 and a standard WENO reconstruction operator, as described in point 1 of subsection 3.1.5. Our goal is to assess both, the influence of the well-balanced reconstruction in the numerical solution and its implications in the computational cost of the numerical scheme. A comparison of CPU times is shown in table 3.4, together with the total number of time steps and the maximum number of iterations needed to obtain convergence in the fixed point iterative solver (3.67). Moreover, numerical solutions obtained using this particular combination are shown in figures 3.11-c and 3.13-c. It is clear that, while there is a speed-up of factor 2 by not using the well-balanced WENO reconstruction, the obtained numerical approximation fails to capture the correct solution.

Test	$T_{CPU}[\text{s}]$	$N_{\Delta t}$	N_{DET}^{MAX}
ADER-WB-WBR-3	1.38	91	13
ADER-WB-NWBR-3	0.64	91	25
ADER-NWB-3	3.02	94	31

Table 3.4: Performance of different numerical schemes for the wave propagation test. Output time $t_{end} = 0.043\,s$. Parameters shown: CPU time T_{CPU}, number of time steps $N_{\Delta t}$ and maximum number of iterations N_{DET}^{MAX} for the DET solver (3.67). Schemes: ADER-WB-WBR-3: third-order well-balanced ADER scheme with well-balanced WENO reconstruction; ADER-WB-NWBR-3: third-order well-balanced ADER scheme with conventional WENO reconstruction; ADER-NWB-3: non well-balanced third-order ADER scheme.

A final aspect to be considered is the effect of treating geometrical source terms as they appear in system (3.8). In order to do so we solve this system using a conservative finite volume scheme of first-order and a third-order ADER scheme. Numerical results are reported in figures 3.12 and 3.14. Both, the first and high-order schemes fail to capture the correct solution, converging always to a wrong one. Moreover, it is interesting to note that the CPU time of the high-order scheme is higher than the one reported for the proposed well-balanced high-order scheme, see table 3.4. This can be explained by observing the number of time steps and the number of iteration steps of the DET solver (3.67), both reported in table 3.4. The spurious oscillations generated by the incorrect treatment of the source term increases the number of time steps needed to reach the output time. Moreover, the fact of having $\partial_x K$ in the source term increases the number of iterations needed by the DET solver (3.67) to converge.

Riemann problems

In this subsection we numerically solve a set of Riemann problems for system (3.12). We solve Cauchy problems of the type

$$\left.\begin{array}{l} \partial_t \boldsymbol{W} + \boldsymbol{A}(\boldsymbol{W})\partial_x \boldsymbol{W} = \boldsymbol{0}, \quad x \in \mathcal{R}, \quad t > 0, \\ \boldsymbol{W}(x,0) = \begin{cases} \boldsymbol{W}_L & \text{if } x < x_G, \\ \boldsymbol{W}_R & \text{if } x > x_G. \end{cases} \end{array}\right\}. \qquad (3.82)$$

Table 3.5 shows the Riemann problem data. Common parameters for all tests are: $A_0 = 10^{-4} \, m^2$, $m = 10.0$, $n = -1.5$ and $\rho = 1050.0 \, kg \, m^{-3}$. The exact solution was computed using the methodology presented in [160].

Problem	α_L	$u_L \, [m/s]$	K_L	α_R	$u_R \, [m/s]$	K_R	$t_{end} \, [s]$	$x_G \, [m]$
RP-1	1.1	0.0	100.	1.5	0.0	500.0	0.03	0.3
RP-2	1.5	0.6	50.	1.1	1.5	500.0	0.06	0.5
RP-3	0.8	0.2	50.	0.7	-0.3	200.0	0.5	0.5

Table 3.5: Parameters for Riemann problems.

Figures 3.15 to 3.17 present exact and numerical results for the non-dimensional cross-subsectional area and the non-dimensional velocity $\bar{u} = u/c_0$. c_0 is a characteristic velocity computed as

$$c_0 = \sqrt{\frac{K^*}{\rho}} \, ,$$

with $K^* = min(K_L, K_R)$.

A domain of length $L = 1 \, m$, discretised by a mesh with 100 cells, and a $CFL = 0.9$, were used for all tests. RP-1 consists of a left travelling shock and a right travelling rarefaction and a stationary contact discontinuity, as for all Riemann problems regarding system (3.12). On the other hand, RP-2 is given by two rarefactions, one going to the left and one to the right. Finally RP-3 is given by two shocks, or elastic jumps, travelling away from the stationary contact discontinuity. Numerical solutions agree with the exact ones in a satisfactory manner for all tests. In particular, states immediately to the left and right of the stationary contact discontinuity are captured correctly by both, first and high-order results. Moreover, the improved sharpness of the solution at discontinuities and the better description of rarefaction fans is evident if first and high-order solutions are compared.

Table 3.6 shows the computational cost of each numerical scheme for all Riemann problems. As expected, the algorithm for the well-balanced WENO reconstruction presented in subsection 3.1.5, greatly increases the computational cost of the high-order scheme. We have then proceeded, as in the previous subsection, to solve the Riemann problems using a conventional WENO reconstruction given by point 1 of subsection 3.1.5. While the computational cost greatly decreases using such a combination, the numerical results obtained with this scheme do not correspond to the exact solution, as it can be seen in figures 3.15-c and 3.16-c. Moreover, if we refine the mesh we see that the numerical solution obtained using the non well-balanced reconstruction converges to a wrong solution (see figure 3.18).

Test	Scheme	$T_{CPU}[s]$
RP-1	WB-O1	0.01
RP-1	ADER-WB-WBR-3	1.59
RP-1	ADER-WB-NWBR-3	0.21
RP-2	WB-O1	0.01
RP-2	ADER-WB-WBR-3	1.35
RP-2	ADER-WB-NWBR-3	0.14
RP-3	WB-O1	0.02
RP-3	ADER-WB-WBR-3	8.84
RP-3	ADER-WB-NWBR-3	0.31

Table 3.6: CPU times for Riemann problems 1 to 3. WB-O1: well-balanced first-order scheme; ADER-WB-WBR-3: third-order well-balanced ADER scheme with well-balanced WENO reconstruction; ADER-WB-NWBR-3: third-order well-balanced ADER scheme with conventional WENO reconstruction.

3.1.7   Conclusions

A well-balanced high-order numerical scheme for one-dimensional blood flow in vessels with varying mechanical properties has been presented. After a description of the adopted mathematical model, the behaviour of integral curves of the linearly degenerate field of system (3.12), that are crucial for the design of well-balanced numerical schemes, was studied. Working in the framework of ADER finite volume schemes, the three building blocks of such schemes were modified in order to obtain well-balanced properties. A first-order well-balanced numerical flux was constructed using the Generalised Hydrostatic Reconstruction technique. Then, a non-linear spatial operator and a local data time evolution algorithm that preserve well-balanced properties were developed. Schemes up to fifth-order of accuracy in space and time were implemented. The order of accuracy of the proposed schemes was empirically checked by performing numerical convergence tests. Tests regarding the well-balanced property were presented for subcritical, supercritical and transcritical steady solutions, obtaining the expected, correct solutions. We note that the well-balanced property is not only a desirable feature of numerical methods for steady problems, as sometimes is stated; this is also an important property to correctly compute solutions to time-dependent problems with source terms, specially of the geometric type. Then, a set of Riemann problems was solved in order to test the robustness and accuracy of the scheme, showing that the numerical results correctly capture the exact solutions.

In the next section we develop a well-balanced numerical scheme for the full Toro & Siviglia [161] model, *i. e.* a model that includes the variation of other parameters, along x, found in the internal pressure $p(x, t)$, such as cross-subsectional area at a reference state A_0 and the external pressure p_e.
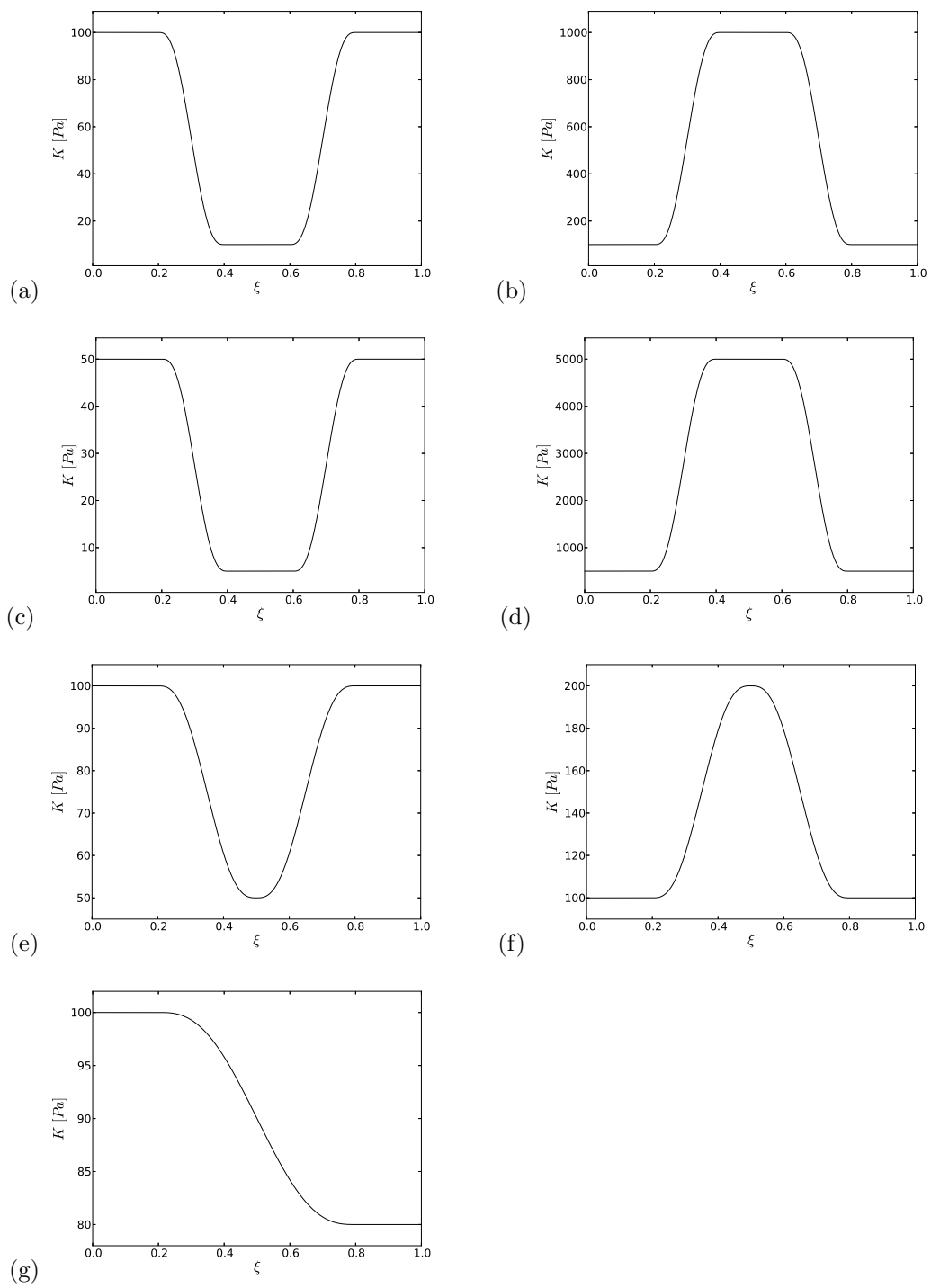
Figure 3.8: $K(x)$ for the presented steady state tests. (a) steady subcritical solution in Ω^+; (b) steady subcritical solution in Ω^-; (c) steady supercritical solution in Ω^+; (d) steady supercritical solution in Ω^-; (e) steady transcritical solution in Ω^+; (f) steady transcritical solution in Ω^-; (g) steady transcritical solution in Ω
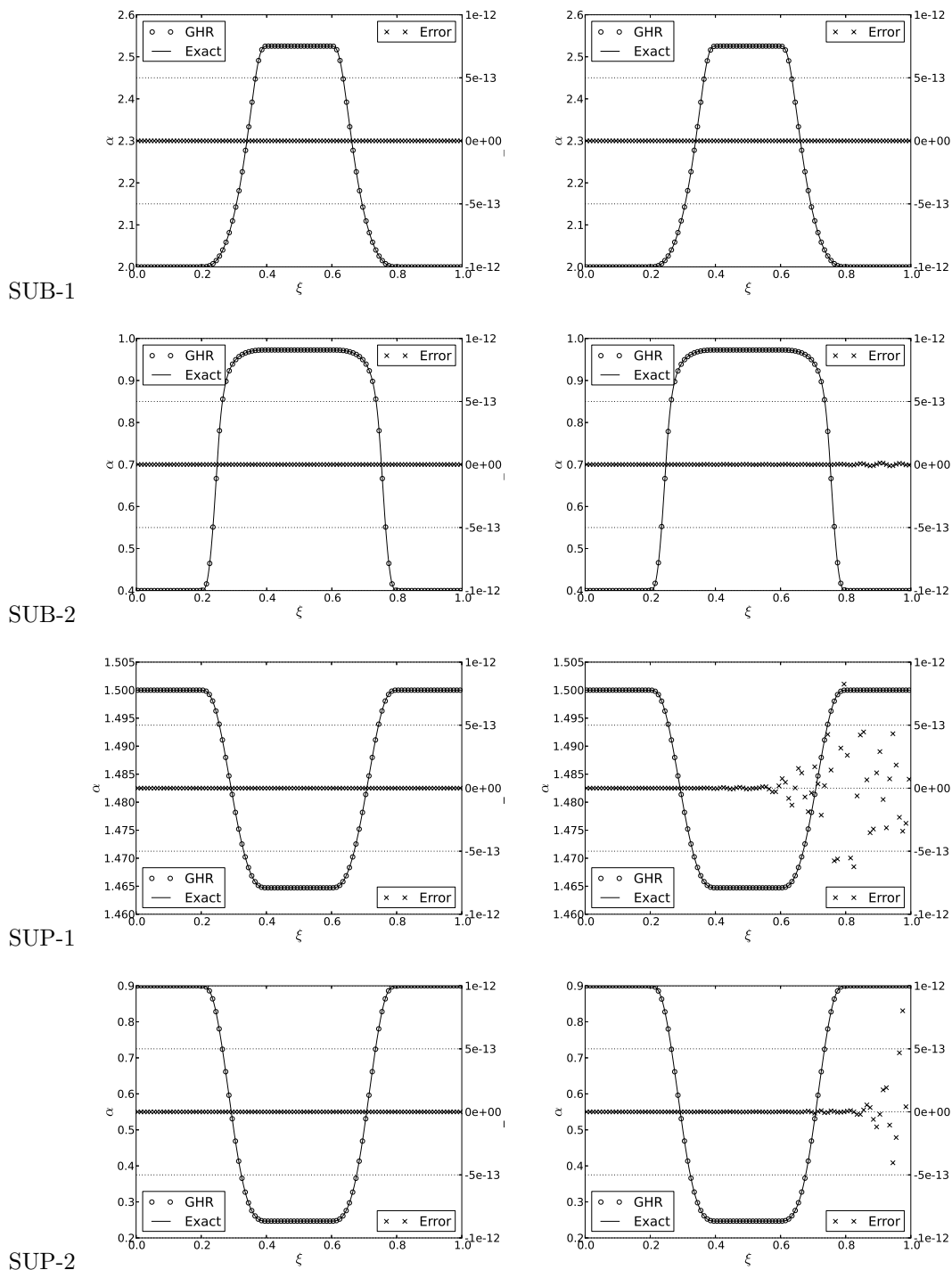
Figure 3.9: Steady tests for subcritical solutions (SUB-1 and SUB-2) and supercritical solutions (SUP-1 and SUP-2) with smooth variation of K. First and third-order results are shown in the left and right columns respectively. Quantities shown are non-dimensional cross-subsectional area (left vertical axis) and error with respect to the exact solution (right vertical axis).
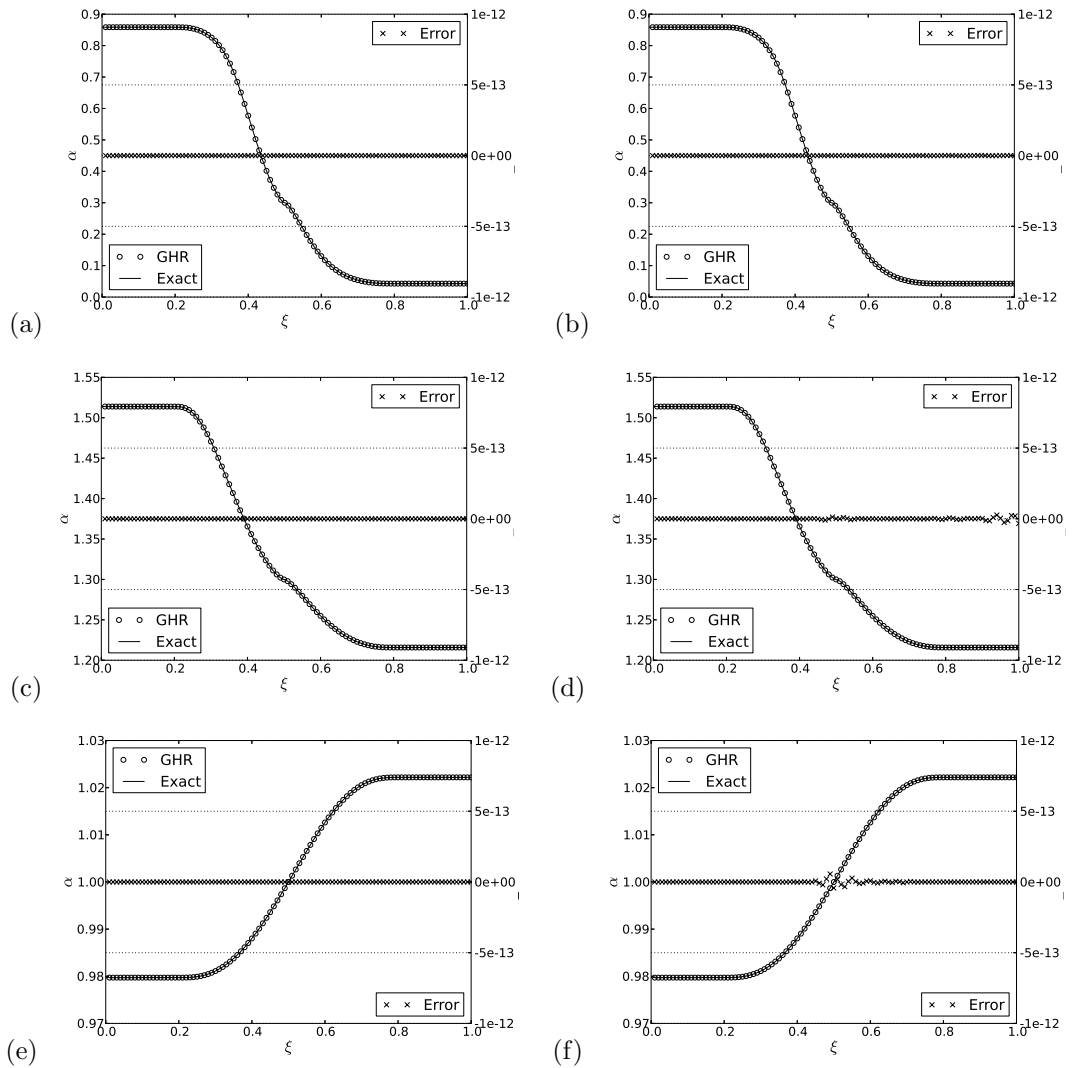
Figure 3.10: Steady tests for transcritical solution in Ω^- (TRA-1), in Ω^+ (TRA-2) and in Ω (TRA-3) with smooth variation of K. First and third-order results are shown in the left and right columns respectively. Quantities shown are non-dimensional cross-subsectional area (left vertical axis) and error with respect to the exact solution (right vertical axis).
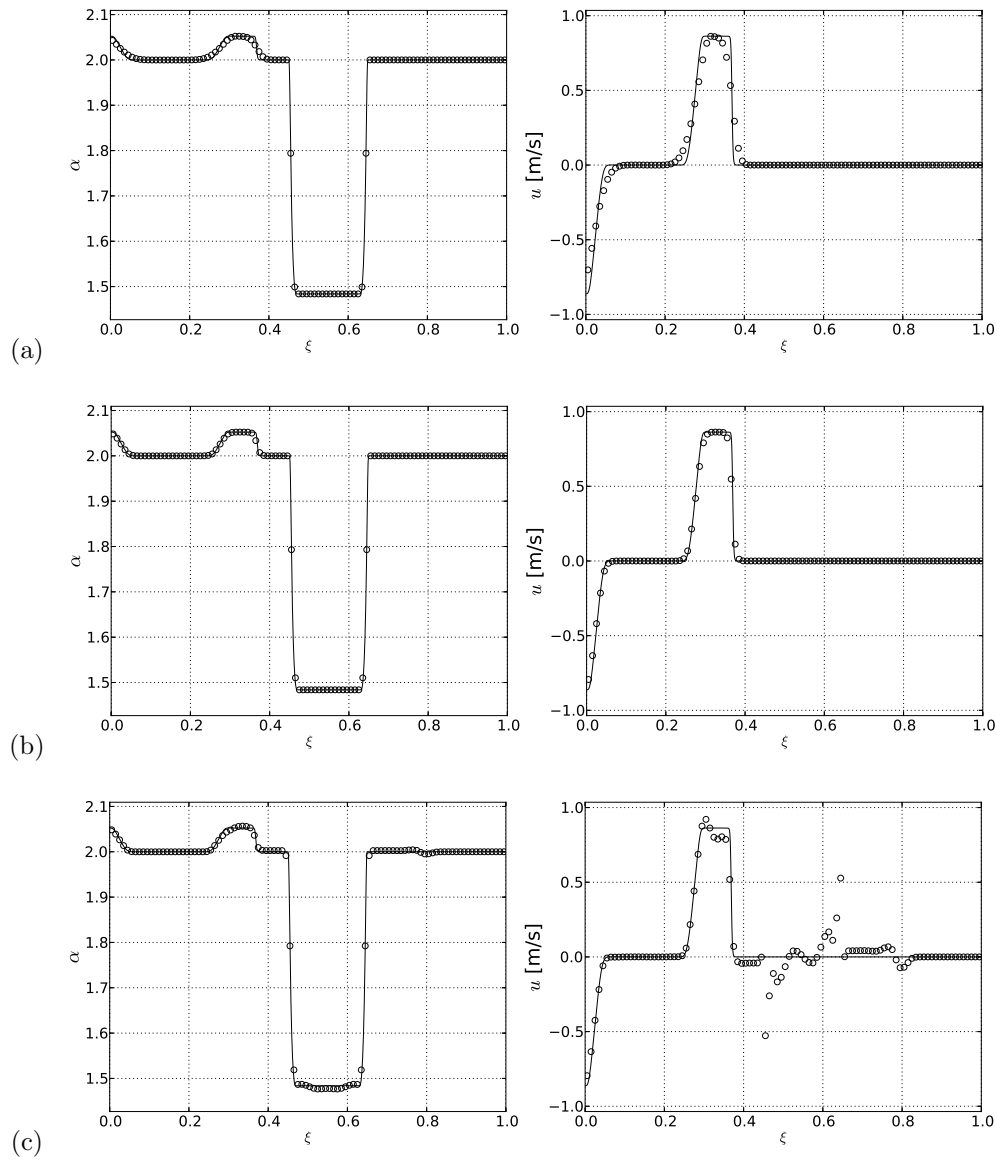
Figure 3.11: Wave propagation test at $t = 0.01\,s$. Non-dimensional cross-subsectional area α and velocity u for the first-order well-balanced scheme (a), the third-order well-balanced ADER scheme (b) and the third-order ADER scheme with non well-balanced WENO reconstruction (c).
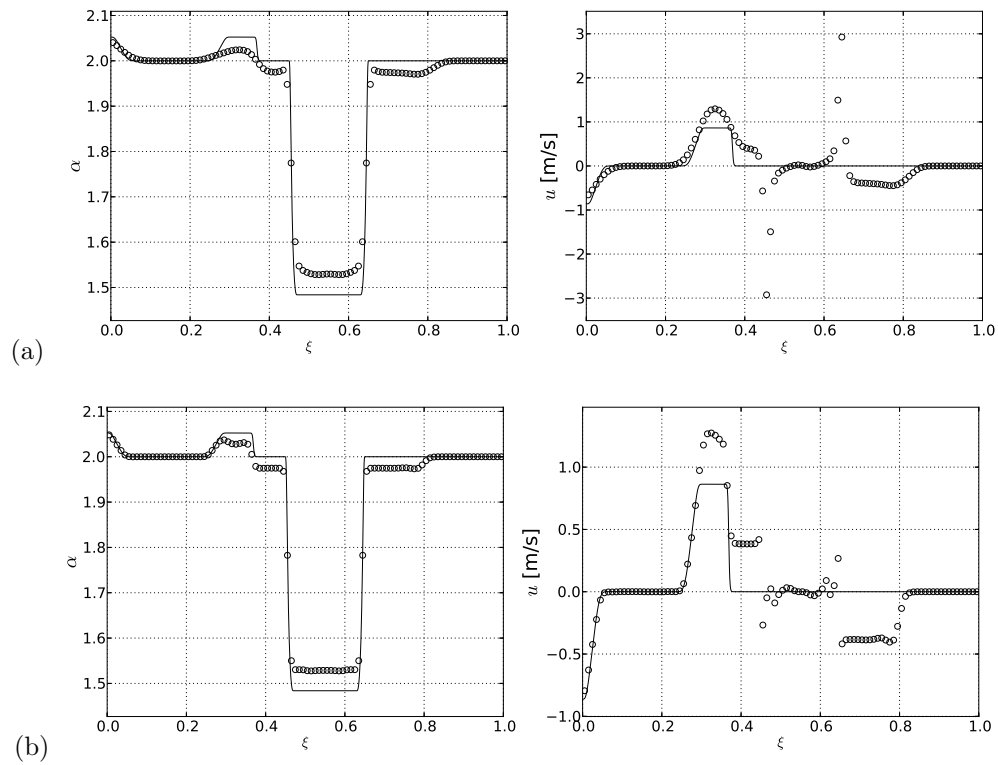
Figure 3.12: Wave propagation test at $t = 0.01\,s$. Non-dimensional cross-subsectional area α and velocity u for the first-order non well-balanced scheme (a) and the non well-balanced third-order ADER scheme (b).
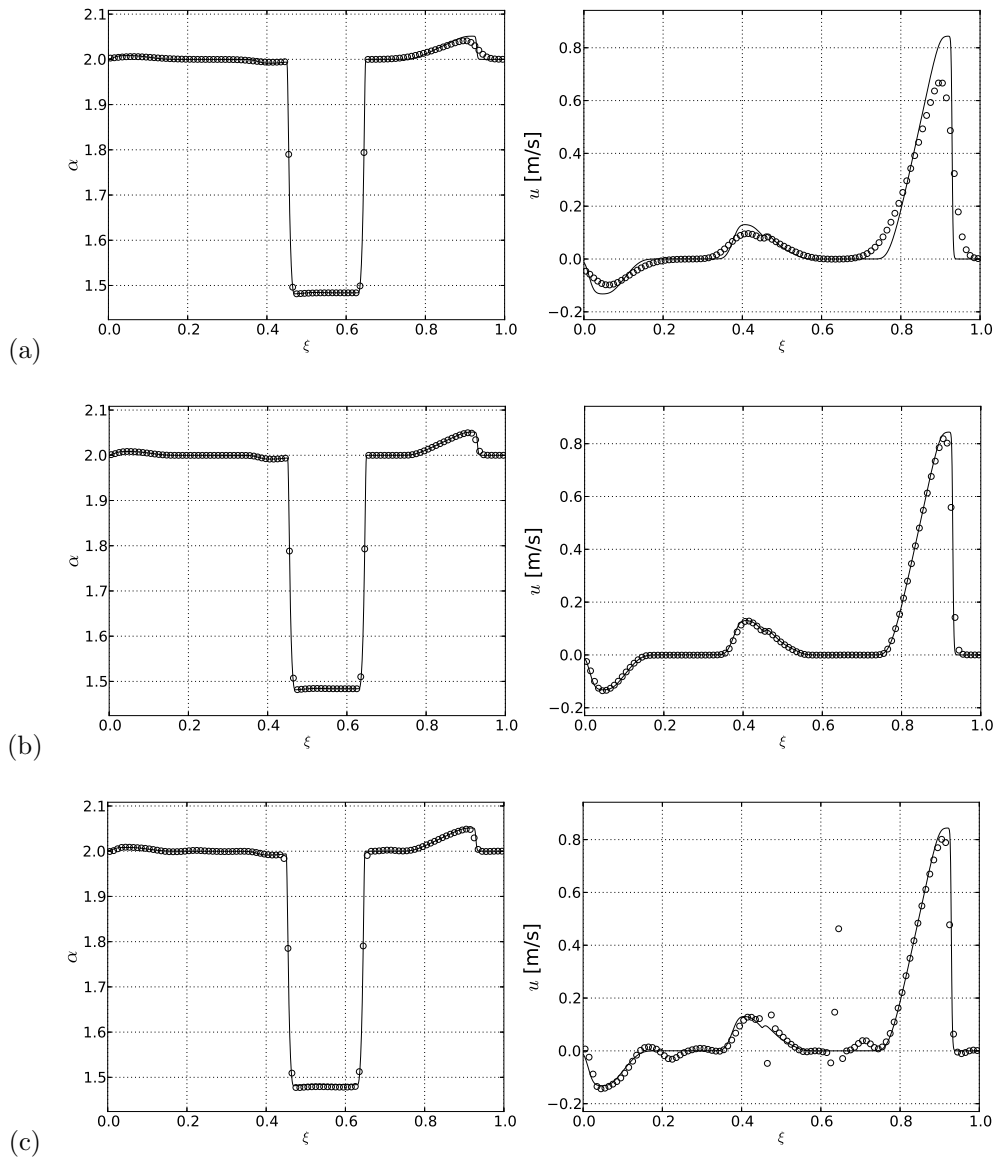
Figure 3.13: Wave propagation test at $t = 0.043\,s$. Non-dimensional cross-subsectional area α and velocity u for the first-order well-balanced scheme (a), the third-order well-balanced ADER scheme (b) and the third-order ADER scheme with non well-balanced WENO reconstruction (c).
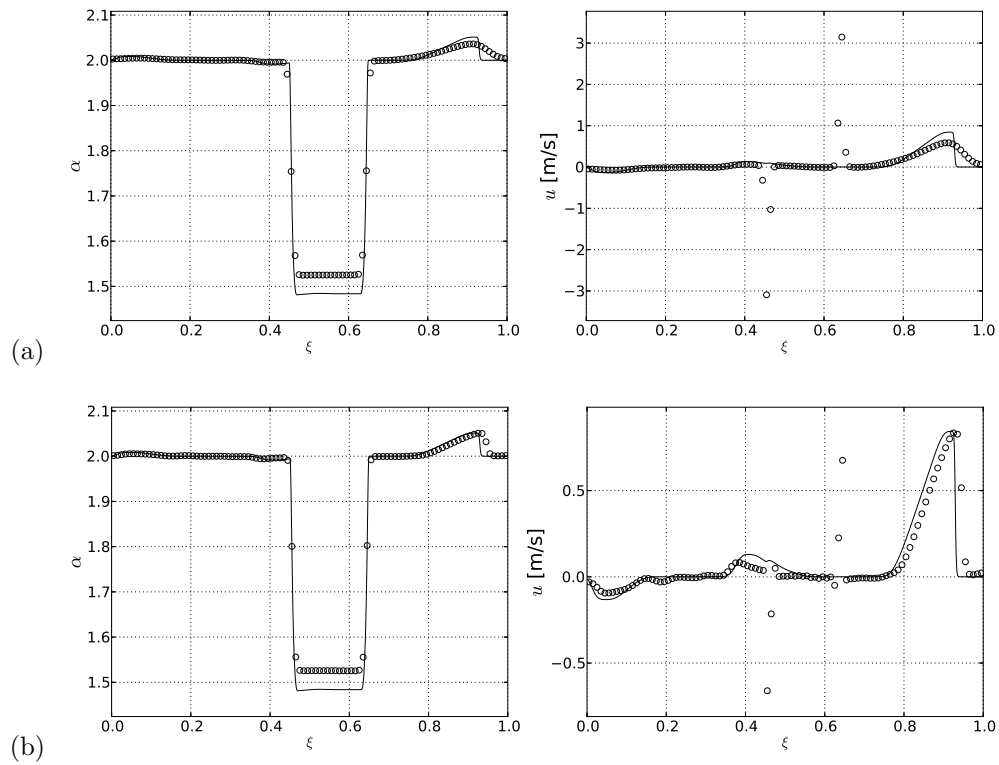
Figure 3.14: Wave propagation test at $t = 0.043\,s$. Non-dimensional cross-subsectional area α and velocity u for the first-order non well-balanced scheme (a) and the non well-balanced third-order ADER scheme (b).

(a)

(b)

(c)
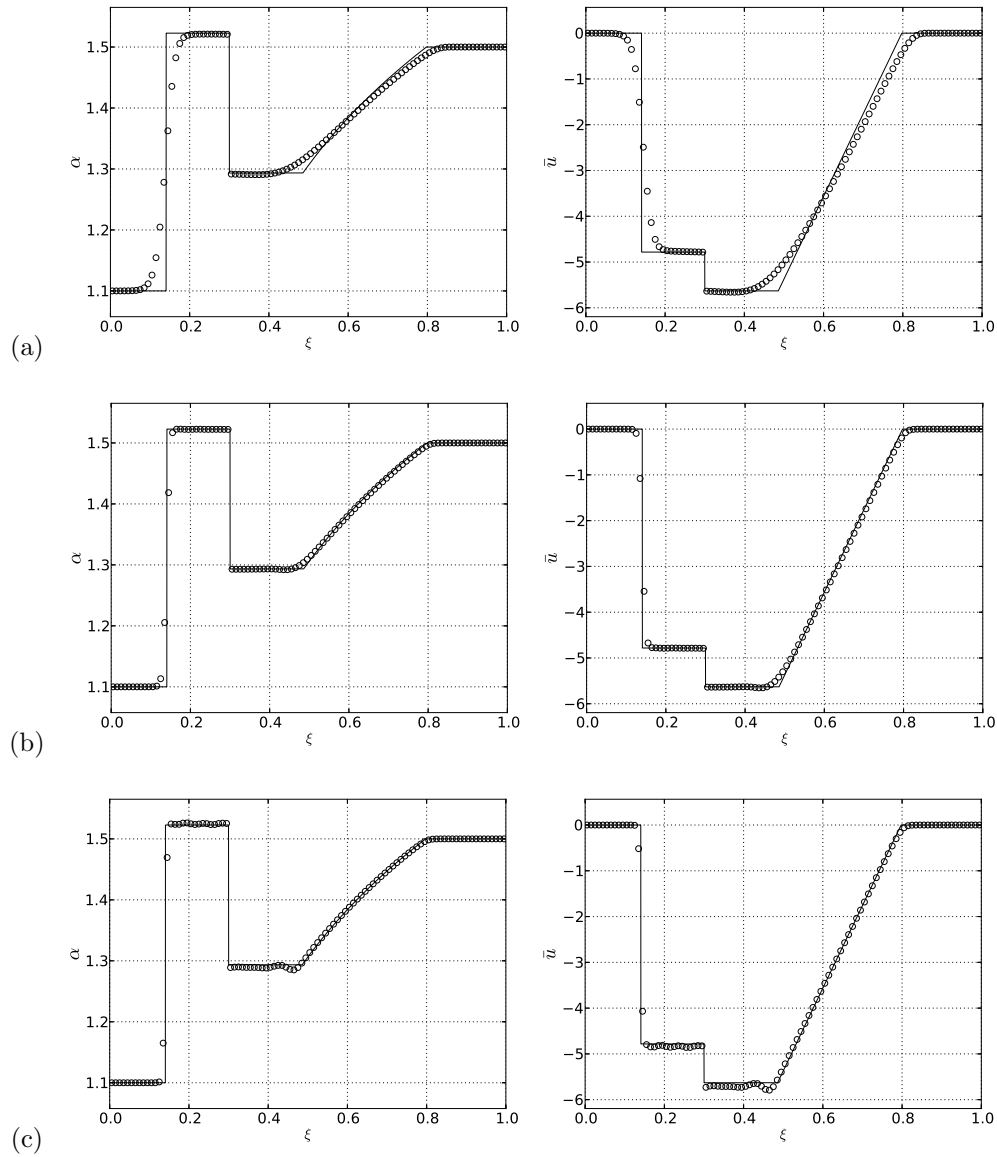
Figure 3.15: Riemann problem 1. Exact and numerical solutions for non-dimensional cross-subsectional area and non-dimensional velocity. Results for the first-order well-balanced scheme (a), third-order well-balanced ADER scheme (b) and third-order ADER scheme with conventional WENO reconstruction (c).
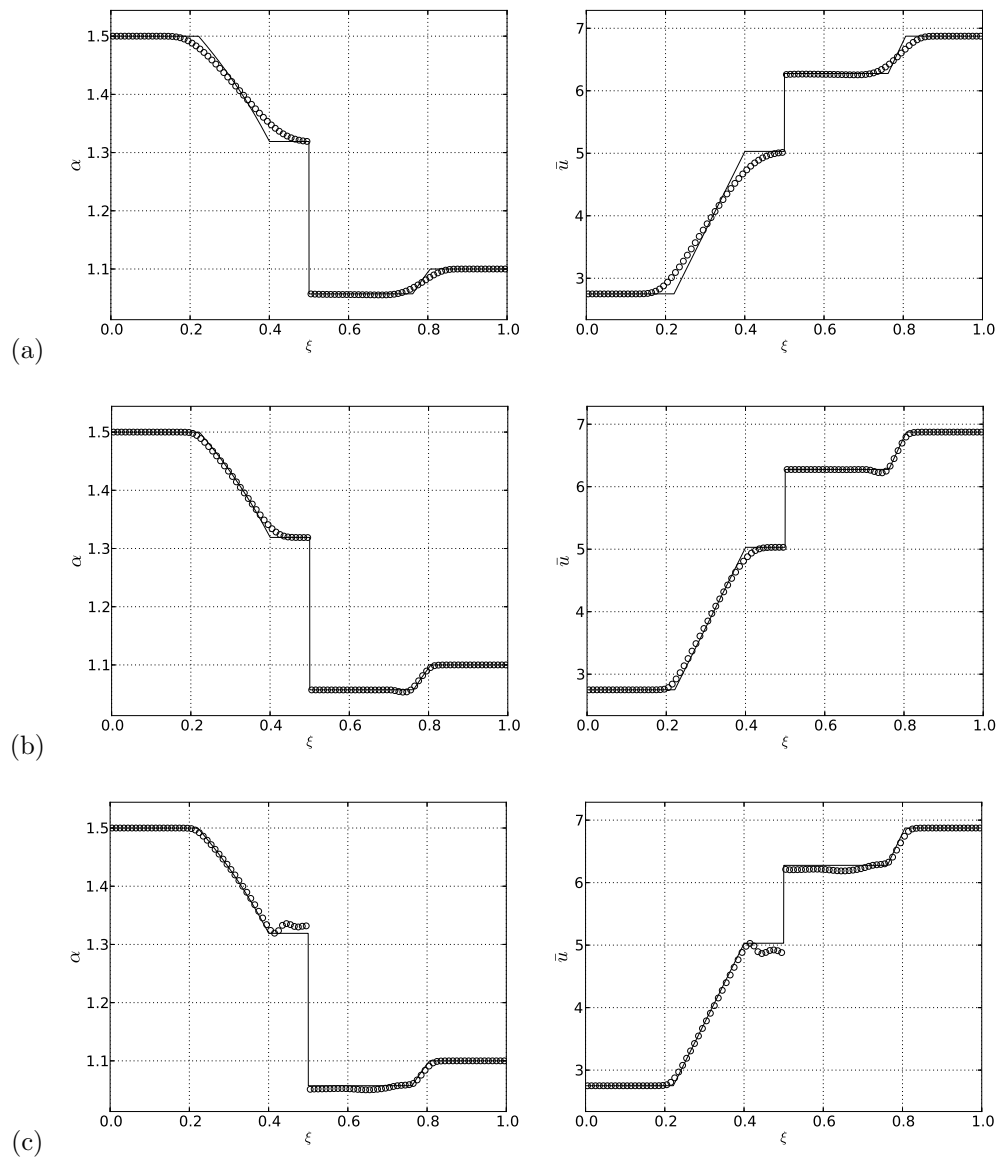
Figure 3.16: Riemann problem 2. Exact and numerical solutions for non-dimensional cross-subsectional area and non-dimensional velocity. Results for the first-order well-balanced scheme (a), third-order well-balanced ADER scheme (b) and third-order ADER scheme with conventional WENO reconstruction (c).
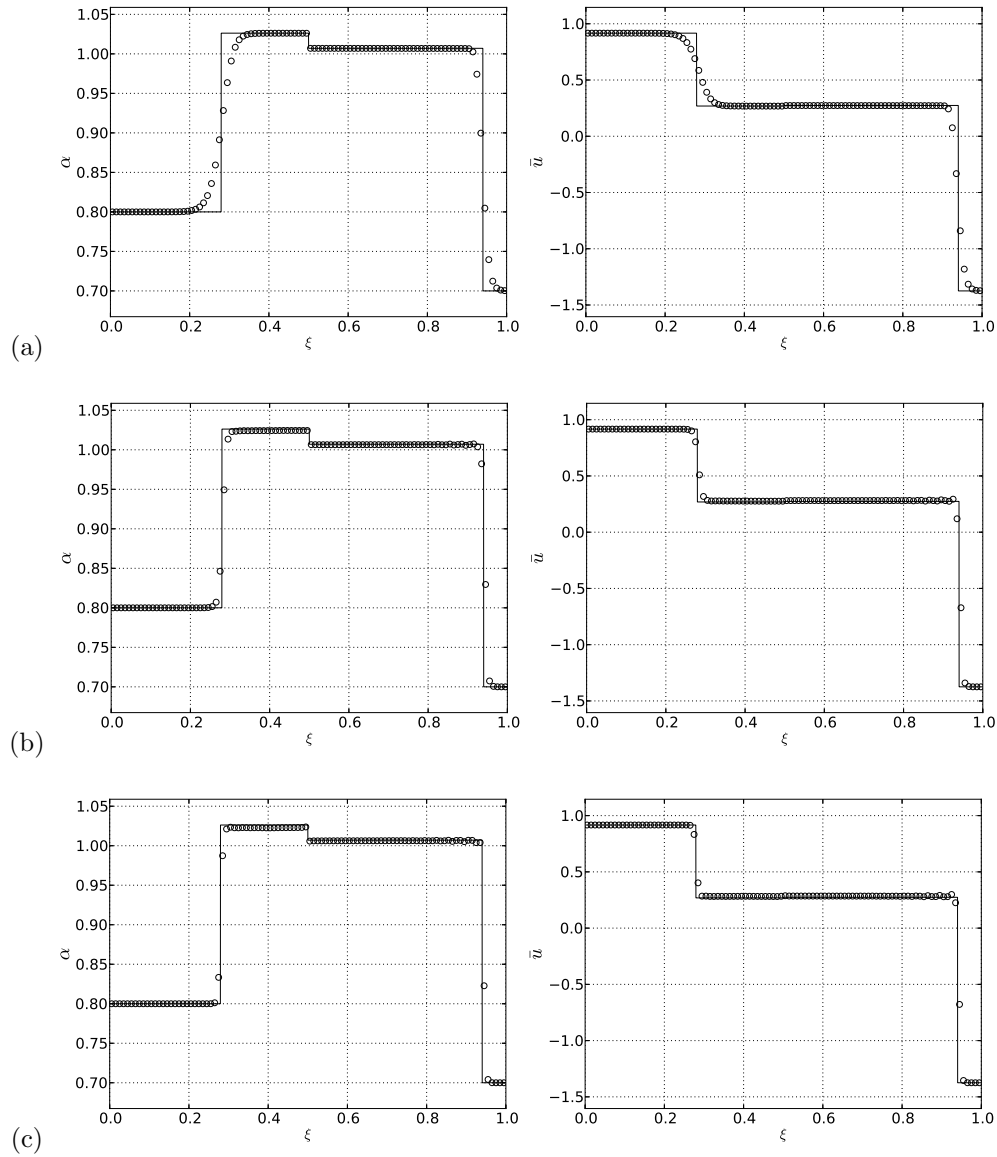
Figure 3.17: Riemann problem 3. Exact and numerical solutions for non-dimensional cross-subsectional area and non-dimensional velocity. Results for the first-order well-balanced scheme (a), third-order well-balanced ADER scheme (b) and third-order ADER scheme with conventional WENO reconstruction (c).
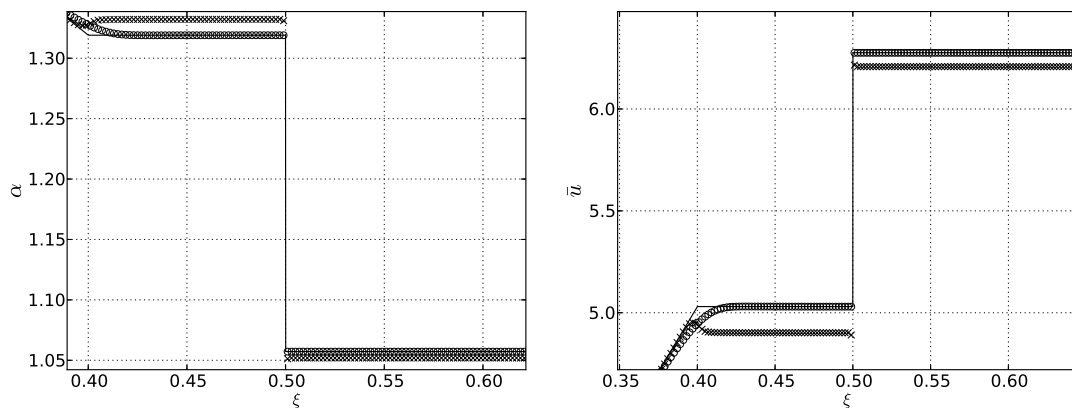
Figure 3.18: Detail of region around the contact discontinuity for Riemann problem 2. Red circles represent the solutions obtained with the proposed third-order well-balanced ADER scheme, whereas black crosses show the solution obtained with a thrid-order numerical scheme that performs a conventional WENO reconstruction and uses a straight segment as integration path for computing fluctuations, instead of using the path specified in subsection 3.1.4.

3.2   Well-balanced solver for blood flow in networks of vessels with variable properties

3.2.1   Introduction

In the modelling of many physiological situations it may be relevant to consider the variation of mechanical and geometrical properties of blood vessels along their length, such as tapering of arteries and situations arising from endovascular repair [40], for example. The presence of such variations gives rise to *geometric-type* source terms and prevents expressing the governing equations in conservation-law form, in terms of conserved variables. The mathematical analysis and the numerical approximation of such systems requires special care. If *geometric-type* source terms are treated in a conventional manner, spurious oscillations may be generated in the numerical solution; in the presence of large gradients or discontinuities, codes may simply crash. Moreover, the resulting schemes will be unable to correctly compute special but important cases, such as steady or stationary solutions [56, 129].

The subject of one-dimensional models for blood flow in the presence of discontinuous material properties has been addressed in the past. Examples include Čanič [40] and the more recent work of Toro and Siviglia [160]. In [160] the authors put forward a simple mathematical model for one-dimensional blood flow in vessels with variable, even discontinuous, mechanical properties. This model has very recently been extended [161] to include other relevant parameters, such as reference cross-sectional area and external pressure. In both [160] and [161] Toro and Siviglia propose a new mathematical formulation of the problem, carry out a thorough analysis of the equations and provide the exact solution of the resulting Riemann problem in the case of discontinuous variation of mechanical and geometrical properties. In both of these works the authors draw attention to the challenging problem of designing suitable numerical methods to solve the hyperbolic equations accurately.

The refined numerical treatment of source terms in hyperbolic balance laws was first addressed by Roe [135]. In analogy to the choice of numerical fluxes, Roe proposed the use of *upwinding* as a way of devising better numerical schemes for source terms. Effective schemes along these lines were later proposed by various authors, see [26], [97] and [171], for example. The numerical treatment of *geometric-type* source terms has by now been thoroughly studied in the community concerned with the numerical solution of the shallow water equations, where such source terms arise from variable bottom topography [27, 39, 44]. In some of these developments, the concept of *well-balanced* schemes has been adopted, reflecting the fact that in the absence of time derivatives the schemes must respect the correct balance between the advective term (the flux) and the source term. These schemes are able to correctly reproduce steady solutions in the presence of source terms. As a way of designing useful schemes for hyperbolic balance laws, the framework of path-conservative numerical schemes, as suggested in [129], is gaining increasing popularity. This is the approach adopted in this section.

A popular approach to the numerical solution of one-dimensional blood flow in the presence of *geometric* source terms is to write the governing equations in terms of non-conservative variables, such as cross-sectional area A and velocity u, for example. By so doing one can actually express the governing equations in *conservation-law form* and apply standard conservative numerical schemes. However, it is pertinent to point out that such formulations are not *physically conservative* and discontinuous solutions will have the wrong propagation speed. This point is proved theoretically in [157] for the shallow water equations. The same exercise can be carried out for the blood flow equations. Consequently, numerical solutions from this kind of formulations will be incorrect in the presence of elastic jumps. The importance of formulating the mathematical model in terms of conserved variables, that is cross-sectional area A and volumetric flow rate q, is clearly identified in [160, 161]. This issue is further discussed in Müller *et al.* [113], where the importance of a conservative formulation is addressed for the computation of solutions involving elastic jumps or sharp gradients.

The issue of well-balanced schemes for one-dimensional blood flow has already been addressed in the past. Sherwin *et al.* [142], for example, proposed to use a two-rarefaction Riemann solver at locations where material properties vary abruptly and succeeded in devising a well-balanced scheme, though in terms of non-conservative variables. Müller *et al.* [114] use the simplified mathematical model proposed in [160] as a starting point to construct a well-

balanced, high-order path-conservative numerical scheme for computing one-dimensional blood flow in both, arteries and veins (collapsible vessels). The proposed numerical scheme in [114] preserves, exactly, steady solutions in any flow regime, that is sub-, super- and trans-critical. Recently, Delestre and Lagree [58] have also proposed a well-balanced finite-volume scheme for blood flow in the framework of Hydrostatic Reconstruction [15]. They just considered the case of a single parameter, namely variable reference cross-sectional area.

In this section we are concerned with the design of an efficient one-dimensional solver for both arteries and veins, using the formulation based on the conservative variables proposed by Toro and Siviglia [161]. We adopt the framework of path-conservative finite volume-type schemes and extend the Dumbser-Osher-Toro Riemann solver [67] for constructing well-balanced fluctuations for a first-order non-oscillatory scheme. Then we extend the resulting first-order scheme to higher order of accuracy in both space and time by adopting the ADER methodology [159], with the approach proposed in [64] for solving the associated generalised Riemann problem. The full methodology is then extended to deal with realistic networks of vessels, adopting standard techniques for the treatment of boundary conditions and vessel junctions. We validate our numerical scheme through two classes of problems. The first class consists of problems for which exact solutions exist, smooth and discontinuous. Then we validated both the model and the numerical scheme against results from an *in vitro* model [109] involving a network of compliant vessels, for which both experimental measurements and state-of-the-art numerical solutions have been published.

The rest of this chapter proceeds as follows. In section 3.2.2 we present the governing equations. In section 3.2.3 we briefly review the Dumbser-Osher-Toro Riemann solver and propose a modified version that yields a well-balanced fluctuation. Section 3.2.4 is devoted to the extension of the first-order scheme to higher order of accuracy in space and time; reported implementations go from first to fifth order of accuracy in space and time; empirically computed convergence rates confirm the expected order of accuracy of the numerical scheme. In section 3.2.5 we solve a problem that includes a stationary wave and two Riemann problems chosen to resemble realistic situations, considering both, arteries and veins; we also validate our numerical scheme for a network of elastic vessels for which experimental measurements and numerical solutions are available. Conclusions are drawn in section 3.2.6.

3.2.2   Mathematical model

We recall once again the well established formulation for one-dimensional blood flow introduced in section 2, given by the system

$$\begin{cases} \partial_t A + \partial_x q = 0\,, \\ \partial_t q + \partial_x \left(\hat{\alpha} \dfrac{q^2}{A} \right) + \dfrac{A}{\rho} \partial_x p = -f\,. \end{cases} \tag{3.83}$$

$A(x,t)$ is the cross-sectional area of the vessel; $q(x,t)$ is the flow rate; $p(x,t)$ is the average internal pressure over a cross-section; $f(x,t)$ is the friction force per unit length of the tube; ρ is the fluid density and $\hat{\alpha}$ is a coefficient that depends on the assumed velocity profile. Throughout this work we will take $\hat{\alpha} = 1$, which corresponds to a blunt velocity profile. For a full description of the model see [73].

To close the system we adopt a tube law, whereby the internal pressure $p(x,t)$ is related to the cross-sectional area $A(x,t)$ and other parameters, namely

$$p(x,t) = p_e(x,t) + \psi(x,t)\,. \tag{3.84}$$

Here $p_e(x,t)$ is the external pressure, prescribed, and $\psi(x,t)$ is the transmural pressure, assumed of the form

$$\psi(x,t) = \psi(A(x,t), K(x), A_0(x)) = K(x)\phi(A(x,t), A_0(x))\,. \tag{3.85}$$

$K(x) = K(E(x), h_0(x))$ is a positive function that contains the combined variation in x of $E(x)$, the Young modulus, and of $h_0(x)$, the wall thickness; see [35] for details. The function $\phi(A,x)$ is assumed of the form

$$\phi(A(x,t), A_0(x)) = \left(\frac{A(x,t)}{A_0(x)} \right)^m - \left(\frac{A(x,t)}{A_0(x)} \right)^n\,, \tag{3.86}$$

where $A_0(x)$ is the vessel cross-sectional area for a reference configuration, for which the transmural pressure is zero. The parameters m and n are obtained from higher-order models or simply computed from experimental measurements. We remark that there are mathematical constraints for the choice of m and n to satisfy hyperbolicity of the equations and for the genuinely non-linear character of the characteristic fields associated with the pressure related eigenvalues; full details are given in [161]. Throughout this work we assume $m > 0$ and $n \in (-2, 0)$. Typical values for collapsible tubes, such as veins, are: $m = 10$, $n = -1.5$; for arteries $m = 0.5$, $n = 0$. Relations (3.85)-(3.86) arise from a mechanical model of the vessel wall displacement under the simplifying assumption of static equilibrium [72].

The spatial variation of the vessel properties K, A_0 and of the external pressure p_e give

$$\partial_x p = \partial_x p_e + K\phi_A \partial_x A + K\phi_{A_0}\partial_x A_0 + \phi\partial_x K \,, \tag{3.87}$$

where

$$\phi_A = \frac{\partial \phi}{\partial A} \,, \quad \phi_{A_0} = \frac{\partial \phi}{\partial A_0} \,.$$

Substituting (3.87) into (3.83) gives

$$\begin{cases} \partial_t A + \partial_x q = 0 \,, \\ \partial_t q + \partial_x \left(\hat{\alpha} \dfrac{q^2}{A} \right) + \dfrac{A}{\rho} K\phi_A \partial_x A = -\dfrac{A}{\rho} \left(\partial_x p_e + K\phi_{A_0}\partial_x A_0 + \phi\partial_x K \right) - f \,. \end{cases} \tag{3.88}$$

The right-hand-side of the momentum balance equation includes *geometric-type* source terms, which, as stated in section 1, must be treated carefully.

In this section we adopt the reformulation of (3.88), proposed in [161]. This model was already introduced in section 2.1 and is proposed once again here for completeness. The model reads

$$\partial_t \mathbf{Q} + \mathbf{A}(\mathbf{Q})\partial_x \mathbf{Q} = \boldsymbol{S}(\boldsymbol{Q}) \,, \tag{3.89}$$

where $\mathbf{Q}$ is given by

$$\mathbf{Q} = \left[A, q, K, A_0, p_e \right]^T \,, \tag{3.90}$$

and the coefficient matrix $\mathbf{A}(\mathbf{Q})$ is

$$\mathbf{A}(\mathbf{Q}) = \begin{bmatrix} 0 & 1 & 0 & 0 & 0 \\ c^2 - u^2 & 2u & \frac{A}{\rho}\phi & K\frac{A}{\rho}\phi_{A_0} & \frac{A}{\rho} \\ 0 & 0 & 0 & 0 & 0 \\ 0 & 0 & 0 & 0 & 0 \\ 0 & 0 & 0 & 0 & 0 \end{bmatrix} \,. \tag{3.91}$$

Here $u = q/A$ is the cross-sectional averaged velocity of the fluid, $\boldsymbol{S}(\boldsymbol{Q})$ is a source term vector

$$\boldsymbol{S}(\boldsymbol{Q}) = [0, -f, 0, 0, 0]^T \tag{3.92}$$

and c is the wave speed

$$c = \sqrt{\frac{A}{\rho} K\phi_A} \,. \tag{3.93}$$

System (3.89) is constructed from (3.83) by regarding the variable parameters $K(x)$, $A_0(x)$ and $p_e(x, t)$ to be new unknowns, satisfying

$$\partial_t K = 0 \,, \quad \partial_t A_0 = 0 \,, \quad \partial_t p_e = F(x, t) \,, \tag{3.94}$$

where $F(x, t)$ is a prescribed function for the external pressure. For a thorough mathematical analysis of system (3.89) see [161]. Here we recall some of the main features of the system needed for the construction of our numerical scheme. The eigenvalues of (3.91) are

$$\lambda_1 = u - c \,, \quad \lambda_2 = \lambda_3 = \lambda_4 = 0 \,, \quad \lambda_5 = u + c \,. \tag{3.95}$$

The right eigenvectors of $\boldsymbol{A}(\boldsymbol{Q})$ corresponding to eigenvalues (3.95) are

$$\boldsymbol{R}_1 = \gamma_1 \begin{bmatrix} 1 \\ u - c \\ 0 \\ 0 \\ 0 \end{bmatrix}, \quad \boldsymbol{R}_2 = \gamma_2 \begin{bmatrix} \frac{A}{\rho}\frac{\phi}{u^2-c^2} \\ 0 \\ 1 \\ 0 \\ 0 \end{bmatrix}, \quad \boldsymbol{R}_3 = \gamma_3 \begin{bmatrix} \frac{A}{\rho}\frac{K\phi_{A_0}}{u^2-c^2} \\ 0 \\ 0 \\ 1 \\ 0 \end{bmatrix},$$

$$\boldsymbol{R}_4 = \gamma_4 \begin{bmatrix} \frac{A}{\rho}\frac{1}{u^2-c^2} \\ 0 \\ 0 \\ 0 \\ 1 \end{bmatrix}, \quad \boldsymbol{R}_5 = \gamma_5 \begin{bmatrix} 1 \\ u + c \\ 0 \\ 0 \\ 0 \end{bmatrix}, \tag{3.96}$$

where γ_i, for $i = 1, ..., 5$, are arbitrary scaling factors.

Under a suitable assumption for coefficients m and n, system (3.89) is hyperbolic, though not strictly hyperbolic. Hyperbolicity is lost when $|u| = c$, leading to resonance. As noted in [161] there is a possible loss of uniqueness.

The first and fifth characteristic fields are genuinely non-linear and are associated with shocks and rarefactions, whereas the remaining fields are linearly degenerate (LD) and are associated with stationary contact discontinuities. See [161] for conditions on parameters m and n for this to be true. The Riemann invariants associated with the genuinely non-linear fields are

$$\Gamma_1 = u - \int_{A^*}^A \frac{c(\tau)}{\tau}d\tau, \quad \Gamma_5 = u + \int_{A^*}^A \frac{c(\tau)}{\tau}d\tau, \tag{3.97}$$

where A^* is the cross-sectional area at a reference state. The Riemann invariants associated with the LD fields are given by

$$\Gamma_1^{LD} = p + \frac{1}{2}\rho u^2, \quad \Gamma_2^{LD} = q. \tag{3.98}$$

In the next section we describe a scheme to solve (3.89) numerically.

3.2.3 Well-balanced scheme for one-dimensional blood flow

In this section we propose a first-order well-balanced numerical scheme. First we introduce the Dumbser-Osher-Toro Riemann solver in its original formulation. Thereafter, the solver is modified to account for specific features of the equations under study.

Brief review of the DOT solver

The Dumbser-Osher-Toro (DOT) Riemann solver was put forward in [66] as a modified version of the Osher-Solomon Riemann solver [128] for a conservative hyperbolic system . The DOT scheme has also been extended in [67] to deal with non-conservative hyperbolic systems. The DOT solver is inspired by the mathematical theory developed by Dal Maso, LeFloch and Murat [56] and may be seen as a path-conservative scheme, as defined in [129].

A finite volume-type scheme may be constructed by integrating (3.89) in space and time in the control volume $[x_{i-\frac{1}{2}}, x_{i+\frac{1}{2}}] \times [t^n, t^{n+1}]$, leading to

$$\boldsymbol{Q}_i^{n+1} = \boldsymbol{Q}_i^n - \frac{\Delta t}{\Delta x}\left(\boldsymbol{D}_{i+\frac{1}{2}}^- + \boldsymbol{D}_{i-\frac{1}{2}}^+\right) - \Delta t \boldsymbol{G}_i + \Delta t \boldsymbol{S}_i, \tag{3.99}$$

where

$$\boldsymbol{Q}_i^n = \frac{1}{\Delta x}\int_{x_{i-\frac{1}{2}}}^{x_{i+\frac{1}{2}}} \boldsymbol{Q}(x, t^n)\, dx, \tag{3.100}$$

$$\boldsymbol{G}_i = \frac{1}{\Delta t \Delta x}\int_{t^n}^{t^{n+1}}\int_{x_{i-\frac{1}{2}}}^{x_{i+\frac{1}{2}}} \boldsymbol{A}(\boldsymbol{Q})\partial_x \boldsymbol{Q}\, dx\, dt \tag{3.101}$$

$$S_i = \frac{1}{\Delta t \Delta x} \int_{t^n}^{t^{n+1}} \int_{x_{i-\frac{1}{2}}}^{x_{i+\frac{1}{2}}} S(Q(x,t)) dx dt \qquad (3.102)$$

and

$$D_{i+\frac{1}{2}}^{\pm} = \frac{1}{\Delta t} \int_{t^n}^{t^{n+1}} \mathcal{D}_{i+\frac{1}{2}}^{\pm} \left(Q_{i+\frac{1}{2}}^{-}(t), Q_{i+\frac{1}{2}}^{+}(t), \Psi(s) \right) dt \,. \qquad (3.103)$$

Here $\Delta x = x_{i+\frac{1}{2}} - x_{i-\frac{1}{2}}$; $\Delta t = t^{n+1} - t^n$; $Q_{i+\frac{1}{2}}^{\pm}(t)$ are limiting data states from left and right arising in the Generalized Riemann Problem (GRP) for system (3.89) at cell interface $x_{i+\frac{1}{2}}$. Details on the GRP will be given in section 3.2.4. Our numerical scheme departs from (3.99), with suitable approximations for the various integrals.

Given left and right data Q^- and Q^+ for the Riemann problem at the cell interface $x_{i+\frac{1}{2}}$, $\mathcal{D}^{\pm}(Q^-, Q^+, \Psi(s))$ are defined as fluctuations that depend on a path $\Psi(s)$ and have to satisfy

$$\mathcal{D}^{-}\left(Q^-, Q^+, \Psi(s)\right) + \mathcal{D}^{+}\left(Q^-, Q^+, \Psi(s)\right) = \int_0^1 A\left(\Psi\left(Q^-, Q^+, s\right)\right) \frac{\partial \Psi}{\partial s} ds \,,$$
$$\mathcal{D}^{\pm}(Q, Q, \Psi(s)) = 0 \,. \qquad (3.104)$$

The path $\Psi = \Psi(Q^-, Q^+, s)$, with $0 \le s \le 1$, is a Lipschitz continuous function that connects the left state Q^- to the right state Q^+ in phase-space, satisfying

$$\Psi\left(Q^-, Q^+, 0\right) = Q^-, \quad \Psi\left(Q^-, Q^+, 1\right) = Q^+ \,. \qquad (3.105)$$

The finite-volume type scheme (3.99) is completely determined once the numerical fluctuations $\mathcal{D}_{i+\frac{1}{2}}^{\pm}$ (analogous to the numerical flux), the numerical source S_i and the space-time integral in (3.99) are determined. Note that the integral in the first line of (3.99) vanishes for a first-order method and the scheme then reads

$$Q_i^{n+1} = Q_i^n - \frac{\Delta t}{\Delta x} \left(\mathcal{D}_{i+\frac{1}{2}}^{-} + \mathcal{D}_{i-\frac{1}{2}}^{+} \right) + \Delta t S_i \,. \qquad (3.106)$$

In an analogous manner to the determination of the numerical flux in a finite volume scheme, the fluctuations $\mathcal{D}_{i+\frac{1}{2}}^{\pm}$ are found by solving a classical Riemann problem (piece-wise constant data) for (3.89) with initial condition

$$Q(x,0) = \begin{cases} Q_{i+\frac{1}{2}}^{-} & \text{if } x < x_{i+\frac{1}{2}} \,, \\ Q_{i+\frac{1}{2}}^{+} & \text{if } x > x_{i+\frac{1}{2}} \,. \end{cases} \qquad (3.107)$$

In particular, for a first order scheme $Q_{i+\frac{1}{2}}^{-} = Q_i^n$ and $Q_{i+\frac{1}{2}}^{+} = Q_{i+1}^n$. Fluctuations in the DOT scheme, as proposed in [67], are computed as

$$\mathcal{D}_{i+\frac{1}{2}}^{\pm} = \frac{1}{2} \int_0^1 \left[A(\Psi(Q_{i+\frac{1}{2}}^{-}, Q_{i+\frac{1}{2}}^{+}, s)) \pm |A(\Psi(Q_{i+\frac{1}{2}}^{-}, Q_{i+\frac{1}{2}}^{+}, s))| \right] \frac{\partial \Psi}{\partial s} ds \,, \qquad (3.108)$$

with the absolute value operator of a matrix defined as

$$|A| = R|\Lambda|R^{-1}, \quad |\Lambda| = diag(|\lambda_1|, |\lambda_2|, ..., |\lambda_N|) \,, \qquad (3.109)$$

where R is the matrix of right eigenvectors of A and R^{-1} its inverse. The simplest choice of path Ψ is the *segment*, or *canonical*, path

$$\Psi(Q_{i+\frac{1}{2}}^{-}, Q_{i+\frac{1}{2}}^{+}, s) = Q_{i+\frac{1}{2}}^{-} + s(Q_{i+\frac{1}{2}}^{+} - Q_{i+\frac{1}{2}}^{-}) \,. \qquad (3.110)$$

In this case the final expression for fluctuations (3.108) reads

$$\mathcal{D}_{i+\frac{1}{2}}^{\pm} = \frac{1}{2} \left\{ \sum_{j=1}^{G} \omega_j \left[A(\Psi(s_j)) \pm |A(\Psi(s_j))| \right] \right\} \left(Q_{i+\frac{1}{2}}^{+} - Q_{i+\frac{1}{2}}^{-} \right) \,, \qquad (3.111)$$

after performing numerical integration in (3.108) using a Gaussian quadrature rule, in which case ω_j and s_j are the j-th weight and Gaussian point coordinate of a quadrature rule with G points. Usually, a Gaussian quadrature rule with 3 points yields satisfactory results, see [39] or [67] for a details.

Computational experience in various types of applications have shown that the simple segment path is suitable for obtaining satisfactory numerical solutions. However, for the problems of interest in this work, early numerical results indicated that a more sophisticated choice of path was necessary.

Modification of the integration path

Let $\gamma_p(s)$ be a curve in phase-space parametrized by a scalar parameter s. We define this curve to be an integral curve of the vector field $\boldsymbol{R}_p$ of system (3.89), if at each point $\gamma_p(s)$, the tangent vector $\gamma_p'(s)$ to the curve is an eigenvector of $\mathbf{A}(\gamma_p(s))$ in (3.91) corresponding to the eigenvalue $\lambda_p(\gamma_p(s))$. Furthermore, the expression for the integral curve gives rise to Generalised Riemann Invariants, which are functions of $\mathbf{Q}$ whose values are invariant along the integral curve $\gamma_p(s)$; see [98] for background. In the case of the linearly degenerate fields of (3.91) we have

$$p + \frac{1}{2}\rho u^2 = \bar{\Gamma}_1^{LD} \quad \text{and} \quad q = \bar{\Gamma}_2^{LD}, \tag{3.112}$$

where $\bar{\Gamma}_{1,2}^{LD}$ are constant values of both, total pressure and volumetric flow rate. Let us also introduce the set Γ_{LD} of all integral curves γ_{LD}, associated to the linearly degenerate field of (3.91).

Well-balanced schemes were originally motivated by the need to design numerical approximations to hyperbolic equations with source terms, in such a way as to achieve equilibrium between flux spatial gradient and algebraic source terms, near the steady state. See, for example, [97, 171] and references therein. The precise definition of a well-balanced scheme has evolved, becoming dependent on the particular approach adopted in the design process. The present section is concerned with a numerical scheme in a class of methods in which the source term is absorbed into an enlarged hyperbolic system with a modified eigenstructure. Then the definition of a well-balanced scheme becomes quite technical. For the work of this section the appropriate definition is that given in [130], which we reproduce below.

Well-balanced numerical scheme: A numerical scheme of the form (3.106) for system (3.89) is said to be exactly well-balanced for $\gamma_{LD} \in \Gamma_{LD}$ if, given any steady solution $\mathbf{Q}^{(s)}(x) \in \gamma_{LD}$, $\forall x \in (x_l, x_r) \subset \mathbb{R}$ and initial conditions such that $\boldsymbol{Q}_i^n \in \gamma_{LD} \ \forall i \in [1, ..., N]$, where N is the number of cells used to discretise the spatial domain (x_l, x_r), then

$$\boldsymbol{\mathcal{D}}_{i+\frac{1}{2}}^- + \boldsymbol{\mathcal{D}}_{i-\frac{1}{2}}^+ = 0, \quad \forall i \in [0, 1, ..., N]. \tag{3.113}$$

Taking into account that the eigenvalues associated with the stationary contact discontinuity are $\lambda_2 = \lambda_3 = \lambda_4 = 0$ and that the p-th right eigenvector is defined as

$$\boldsymbol{A}\boldsymbol{R}_p = \lambda_p \boldsymbol{R}_p, \tag{3.114}$$

it follows that a path-conservative numerical scheme (3.106) with fluctuations (3.108), will be well-balanced if we can guarantee that the path $\boldsymbol{\Psi}(\boldsymbol{Q}_{i+\frac{1}{2}}^-, \boldsymbol{Q}_{i+\frac{1}{2}}^+, s)$ linking two states $\boldsymbol{Q}_{i+\frac{1}{2}}^-$ and $\boldsymbol{Q}_{i+\frac{1}{2}}^+$ belonging to an integral curve γ_{LD}, is a parametrization of the arc defined by γ_{LD} [119]. The well-balanced property is also necessary for the correct numerical solution of unsteady problems, as extensively discussed in [129, 130, 46]. We also show numerical results supporting this fact in this section and in section 3.2.5.

The *segment* path (3.110), proposed in [67], has been widely used in the numerical solution of several physical problems involving both, conservative and non-conservative hyperbolic systems. For the shallow water equations, it guarantees that the resulting numerical scheme is exactly well-balanced for water-at-rest solutions, see [130]. This is due to the fact that for the shallow water equations, in fluid at rest conditions, the Riemann invariants associated with the LD field are

$$\Gamma_1^{LD,SWE} = h + b, \qquad \Gamma_2^{LD,SWE} = 0, \tag{3.115}$$

where h is the water depth and b is the bottom elevation. From the relation between h and b in (3.115), it is evident that the integral curve γ_{LD}^{SWE} in phase-plane (h, b) will be a straight line.

Early numerical experiments on the application of the DOT scheme to system (3.89) using the *segment* path (3.110) showed the inability of the scheme to preserve stationary solutions, that is solutions for which $u(x, t) = 0$. The reason can be deduced from the analysis of the Riemann invariants associated with the LD characteristic fields. Let us consider a stationary solution defined by states for which the Riemann invariants (3.98) are

$$p = K \left[\left(\frac{A}{A_0} \right)^m - \left(\frac{A}{A_0} \right)^n \right] + p_e = \bar{\Gamma}_1^{LD}, \quad 0 = \bar{\Gamma}_2^{LD} . \tag{3.116}$$

There is a non-linear dependence between K and A. In order to accommodate changes in K, A_0 or p_e, while preserving constancy of the right-hand side in (3.116), the cross-sectional area A will have to change non-linearly. In other words, the use of the *segment* path (3.110) will not preserve steady solutions, not even stationary ones.

Here we take advantage of the flexible formulation of the DOT Riemann solver, which enables us to numerically integrate along any path. This special characteristic of the DOT solver allows us to define a path that guarantees exact well-balanced properties (up to machine precision) for any steady solution. In this work we limit ourselves to develope a scheme that only preserves *stationary solutions* exactly, since the main goal of this section is that of proposing a fast and easy to implement numerical scheme that correctly solves problems where *geometric* source terms are present. This choice is justified by the following considerations:

- Exact well-balanced schemes for stationary solutions solve unsteady problems in a satisfactory manner as we will see later in this section and in section 3.2.5, where numerical results are compared to exact solutions and experimental measurements

- Given the first consideration, we note that ensuring exact well-balancing of any steady solution greatly complicates the implementation of the numerical scheme.

We propose a path which uses the *segment* path for all variables, except for the cross-sectional area A. The proposed path $\boldsymbol{\Psi}(s)$ reads

$$\boldsymbol{\Psi}(s) = \begin{bmatrix} \bar{A}(s) \\ \bar{q}(s) \\ \bar{K}(s) \\ \bar{A}_0(s) \\ \bar{p}_e(s) \end{bmatrix} = \begin{bmatrix} \bar{\phi}(s)^{-1} \\ q_{i+\frac{1}{2}}^- + s \left(q_{i+\frac{1}{2}}^+ - q_{i+\frac{1}{2}}^- \right) \\ K_{i+\frac{1}{2}}^- + s \left(K_{i+\frac{1}{2}}^+ - K_{i+\frac{1}{2}}^- \right) \\ A_{0,i+\frac{1}{2}}^- + s \left(A_{0,i+\frac{1}{2}}^+ - A_{0,i+\frac{1}{2}}^- \right) \\ p_{e,i+\frac{1}{2}}^- + s \left(p_{e,i+\frac{1}{2}}^+ - p_{e,i+\frac{1}{2}}^- \right) \end{bmatrix} . \tag{3.117}$$

$\bar{\phi}(s)$ is a path for relation (3.86), defined as

$$\bar{\phi}(s) = \frac{\bar{\Gamma}(s) - \bar{p}_e(s)}{\bar{K}(s)} , \tag{3.118}$$

where $\bar{\Gamma}(s)$ is

$$\bar{\Gamma}(s) = \bar{\Gamma}_{LD,i+\frac{1}{2}}^{1,-} + s \left(\bar{\Gamma}_{LD,i+\frac{1}{2}}^{1,+} - \bar{\Gamma}_{LD,i+\frac{1}{2}}^{1,-} \right) . \tag{3.119}$$

Once that $\bar{\phi}(s)$ is known, we compute $\bar{A}(s)$ from (3.86) using a globally convergent Newton method for $n \neq 0$. It is possible to verify that a solution always exits for $A > 0$ and is unique. When $n = 0$ the solution is explicit.

Parametrizations (3.118) and (3.119) are designed to guarantee that the numerical scheme will preserve stationary solutions exactly. In fact, in the case of fluid at rest, $\bar{\Gamma}(s)$ will be a constant since

$$\bar{\Gamma}_{LD,i+\frac{1}{2}}^{1,+} = \bar{\Gamma}_{LD,i+\frac{1}{2}}^{1,-} ,$$

and the resulting path will be a parametrization of the integral curve γ_{LD}.

Figure 3.19 shows the proposed path $\boldsymbol{\Psi}(s)$, on the (A, K) phase-plane, together with the integral curve γ_{LD} corresponding to the Riemann invariant associated to the LD field for a

fluid at rest solution. Use of the *segment* path would correspond to compute integral (3.108) in phase-space along a straight line and this would clearly result in a non well-balanced solution, as we shall see later in this section and in section 3.2.5.

The fluctuation for the DOT solver using the proposed path is

$$\mathcal{D}^{\pm}_{i+\frac{1}{2}} = \frac{1}{2} \left(\sum_{j=1}^{G} \omega_j \left\{ (\boldsymbol{A}(\boldsymbol{\Psi}(s_j)) \pm |\boldsymbol{A}(\boldsymbol{\Psi}(s_j))|) \left. \frac{\partial \boldsymbol{\Psi}}{\partial s} \right|_{s_j} \right\} \right). \tag{3.120}$$

Note that, because of our choice of path, vector $\frac{\partial \boldsymbol{\Psi}}{\partial s}$ can not be taken out of the integral (3.108), as done when using the *segment* path. Derivatives for most variables are easily computed, besides that for $\bar{A}(s)$, which might be an implicit function of ϕ, so that its derivative at each quadrature point $s = s_j$ is computed as

$$\frac{\partial \bar{A}}{\partial s}(s_j) = \left(\frac{\partial \bar{\phi}}{\partial s}(s_j) - \left. \frac{\partial \phi}{\partial \bar{A}_0} \right|_{s=s_j} \frac{\partial \bar{A}_0}{\partial s}(s_j) \right) \left(\left. \frac{\partial \phi}{\partial \bar{A}} \right|_{s=s_j} \right)^{-1}. \tag{3.121}$$
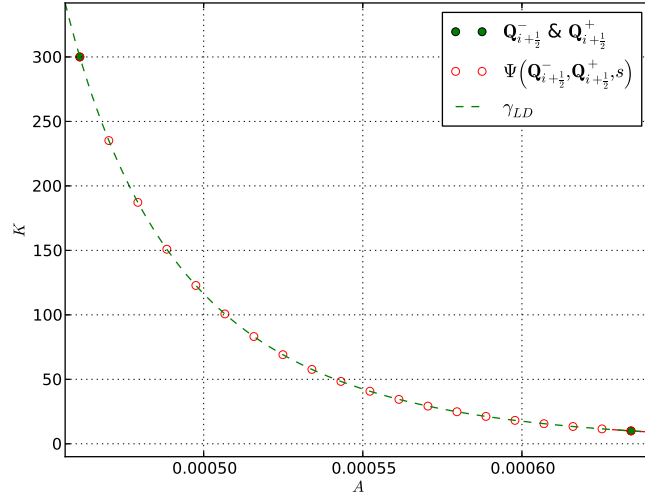
Figure 3.19: Integration path $\boldsymbol{\Psi}(s)$ (3.117), on the (A, K) phase-plane, and integral curve γ_{LD} associated with the LD field for the case of fluid at rest.

The numerical scheme (3.106) with fluctuations (3.120) and path (3.117) is a first-order well-balanced numerical scheme for system (3.89). In the next section we illustrate the performance of the proposed scheme for some test problems.

Numerical results for the DOT solver

We solve Riemann problems

$$\left. \begin{array}{l} \partial_t \boldsymbol{Q} + \boldsymbol{A}(\boldsymbol{Q})\partial_x \boldsymbol{Q} = \boldsymbol{0}, \quad x \in \mathcal{R}, \quad t > 0, \\ \boldsymbol{Q}(x, 0) = \begin{cases} \boldsymbol{Q}_L & \text{if } x < x_g, \\ \boldsymbol{Q}_R & \text{if } x > x_g \end{cases} \end{array} \right\} \tag{3.122}$$

for the homogeneous version of (3.89). As already said, Riemann problems (RPs) are the building block of our numerical scheme and, in general, of a broad class of finite volume-type schemes. If an exact solution to such a problem is available, it constitutes a useful tool to validate numerical schemes, since solutions to this kind of problems tend to challenge the numerical scheme to solve the variety of wave patterns given by the underlying PDEs. In this

section Riemann problems are solved exactly using an implementation of the exact solution to problem (3.122) put forward in [161].

The following RPs were designed using parameters reported in applications regarding cardiovascular mathematics. Besides the first RP, whose solution is stationary, the remaining RPs are idealised time-dependent tests for real world related situations and should be considered as a tool for checking the accuracy and robustness of the proposed numerical scheme for ranges of parameters found in the human body. Mechanical properties and geometrical characteristics for each RP are given in table 3.7, while initial conditions are specified in table 3.8. Chosen values resemble mechanical properties and geometric characteristics in the thoracic aorta (RP1 and RP2 with parameters taken from [4]) and in the internal jugular vein (RP3 with parameters based on [14] and [132]). For all tests the spatial domain was discretized with 100 cells and a Courant number of $CFL = 0.9$ was used.

Test	$L\,[m]$	$K_{ref}\,[Pa]$	m	n	$A_{0,ref}\,[m^2]$	x_g/L	$t_{end}\,[s]$
1	0.2	58725.0	1/2	0	3.1353×10^{-4}	0.5	0.1
2	0.2	58725.0	1/2	0	3.1353×10^{-4}	0.3	0.007
3	0.2	5.0	10	-3/2	1.0000×10^{-4}	0.3	0.025

Table 3.7: Parameters used for RPs 1 to 3: domain length L; reference stiffness K_{ref}; tube law exponential coefficients m and n; reference cross-sectional area $A_{0,ref}$; relative location of the initial discontinuity x_g/L; output time t_{end}.

Test	α_L	$\alpha_{0,L}$	u_L	K_L	$p_{e,L}$	α_R	$\alpha_{0,R}$	u_R	K_R	$p_{e,R}$
1	α_L^*	2.0	0.0	K_{ref}	75.0	α_R^*	1.0	0.0	$10.0\,K_{ref}$	85.0
2	1.6	0.5	1.	K_{ref}	30.0	1.05	1.0	0.0	$10.0\,K_{ref}$	0.0
3	0.9	1.1	0.0	K_{ref}	10.0	1.6	1.3	0.0	$10.0\,K_{ref}$	5.0

Table 3.8: State variables for RPs 1 to 3. α represents the non-dimensional cross-sectional area with respect to the reference area $A_{0,T} = \alpha_{0,T}\,A_{0,ref}$, with $T = L, R$. External pressure values are given in mmHg. α^* is a value obtained from solving (3.84) for A^*, imposing $p^* = 80.0\,mmHg$.

RP1 is designed to test the well-balanced properties of the DOT scheme. We set $p^*(x,0) = 80.0\,mmHg$ as initial condition and assign the corresponding cross-sectional area using (3.84). The problem presents variations in vessel wall stiffness K, cross-sectional area at reference state A_0 and external pressure p_e. Moreover, we have that $\alpha_L^* < 1.0$ and $\alpha_R^* > 1.0$. The exact solution of this problem is identically the initial condition and the numerical scheme will have to preserve this initial condition. Figure 3.20, top frame, shows numerical results from the DOT solver using the proposed path (3.117). The bottom frame shows corresponding results obtained using the *segment* path (3.110). Our scheme preserves the initial condition, while the results obtained with the non well-balanced scheme are erroneous, very far from the exact stationary solution.

In the case of RP2, we have set up the (idealized) problem of a systolic pressure and flow peak arriving to a certain region of the thoracic aorta. In order to challenge our numerical scheme we have also chosen to compress the left side of the aorta, that is the part which was already reached by the systolic peak. Moreover, we have set the portion of the aorta to the right of the initial discontinuity to be 10 times stiffer than the portion to the left. The wave pattern of such an idealized situation will result in a partial reflection of the incoming wave front. Numerical results are shown in figure 3.21. While results for the well-balanced DOT solver, top frame, compare well with the exact solution, the DOT solver using the *segment* path, bottom frame, is unable to correctly capture the states to the left and right of the stationary contact discontinuity. This example shows that the inability of the non well-balanced scheme to solve stationary problems will also influence its suitability to solve unsteady problems.

In RP3 we represent the case of an internal jugular vein (IJV) during a Valsalva maneuver, in which the subject exhales while closing all airways. This maneuver produces a high Central-Venous-Pressure (CVP), reaching values of around 40 mmHg, see [76]. In this idealised problem set up we consider the case for which the valve present at the proximal end, relative to the heart, of the IJV suddenly fails to fulfill its function of preventing venous reflux towards the head. We have chosen to set a negative pressure as initial condition in the distal portion of the IJV, which would correspond to the situation verified in a standing subject. Finally, the proximal end of the IJV was set to be 10 times stiffer than the distal one. The exact solution, as well as numerical results for this problem, are shown in figure 3.22. We observe that a strong elastic jump develops and travels towards the head, while a rarefaction travels in the direction of the heart. Also in this case we achieve good agreement between the exact solution and numerical results for the well-balanced DOT solver. To conclude, it is worth noting that for this case the non well-balanced scheme performs better than for the previous tests. This behaviour can be easily understood by having a look at figure 3.23. In this figure we show states across the stationary contact discontinuity, the integral curve γ_{LD} (continuous line) and the *segment* path (dashed line) in the non-dimensional $(\alpha, \hat{K})$ phase-plane for RP2 and RP3. We define non-dimensional quantities as

$$\alpha = \frac{A}{A^*} \quad \hat{K} = \frac{K}{K^*},$$

with $A^* = min(A_{0,L}, A_{0,R})$ and $K^* = min(K_L, K_R)$. The jump in α is smaller for RP3 in comparison to that for RP2. Therefore, using the *segment* path for RP3, implies small deviations from the integral curve γ_{LD}. Take for example, $\hat{K} = 4$. Using the *segment* path for RP2 implies an error in the evaluation of α of approximately $\Delta\alpha_{RP2} = \alpha_{LD} - \alpha_{seg} = 0.17$, whereas in the case of RP3 we have that $\Delta\alpha_{RP3} = \alpha_{LD} - \alpha_{seg} = 0.002$. The bigger deviation from the integral curve γ_{LD} by the *segment* path in RP2 is further penalizing the performance of the non well-balanced scheme by the fact that for this RP the wall stiffness K is 4 order of magnitude bigger than for RP3. In the hypothetical case of two RPs where the jump in α across the stationary contact discontinuity is equal for both tests, the value of K will be the key factor for the amplification/reduction of errors underwent by using an incorrect path.

The results shown so far are for a first-order scheme. In the next section we extend the proposed methodology to higher order of accuracy in both space and time.

3.2.4 High-order extension

In order to extend our first-order well-balanced scheme to high-order of accuracy in space and time we adopt the fully-discrete ADER framework [159]. ADER-type schemes require three main steps:

- Non-linear spatial reconstruction.

- Solution of the Generalized Riemann Problem (GRP) at cell interfaces to compute fluctuations (or numerical fluxes).

- In the presence of source terms, accurate space-time integration of source terms is also needed to compute the numerical source.

For path-conservative ADER schemes one also needs to accurately compute the double integral on the first line in (3.99).

For each of these steps there are several possibilities. In the case of the spatial reconstruction one could use any standard ENO or WENO reconstruction [81, 88]. Regarding the solution of the GRP, we refer the reader to [111] for a thorough review on four methods so far available. In this work we adopt the GRP solver proposed by Dumbser, Enaux and Toro [64], the DET solver. This has the advantage of avoiding the Cauchy-Kowalewski procedure and can deal with stiff source terms. This scheme has been applied successfully to severe tests problems that include vessel collapse, which result in stifness [113].
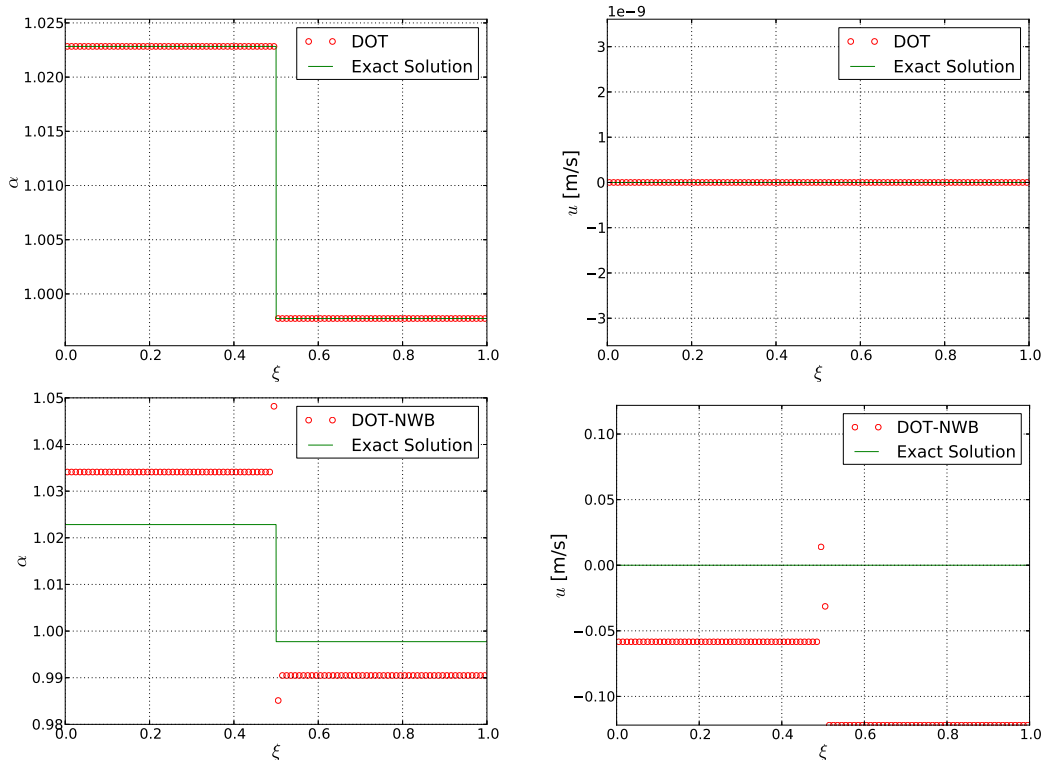
Figure 3.20: Results for RP1 obtained using the first-order DOT solver with well-balanced fluctuation (3.120) (top) and the first-order DOT solver with non well-balanced fluctuation (3.111) (bottom). Shown results are for non-dimensional cross-sectional area (left) and velocity (right) versus non-dimensional length. Note different ranges for velocity plots.

The ADER scheme

We proceed with a brief explanation of the steps followed for the implementation of the ADER scheme with the DET GRP solver. For a more detailed description see [64, 83, 67] and the above cited references.

Spatial reconstruction

For the spatial reconstruction we use the WENO methology [88], by which, for time level t^n, we reconstruct element-wise polynomials of the type

$$\boldsymbol{w}_h = \boldsymbol{w}_h(x, t^n) = \sum_{l=1}^{M+1} \psi_l(x)\hat{\boldsymbol{w}}_l \,, \tag{3.123}$$

where M is the polynomial degree of the spatial reconstruction, $\psi_l(x)$ are the corresponding basis functions and $\hat{\boldsymbol{w}}_l$ are the expansion coefficients. The expansion coefficients are computed by applying a reconstruction operator on cell averages $\boldsymbol{Q}_j^n$, over a defined stencil $\mathcal{S}_i$ (for details see [62]).

The DET solver

Once the spatial reconstruction is available, we proceed with the solution of the GRP at cell interface $x = x_{i+\frac{1}{2}}$ (locally at $x = 0$)

$$\left. \begin{aligned} \partial_t \boldsymbol{Q} + \boldsymbol{A}(\boldsymbol{Q})\partial_x \boldsymbol{Q} = \boldsymbol{0} \,, \quad x \in \mathcal{R} \,, \quad t > 0, \\ \boldsymbol{Q}(x,0) = \begin{cases} \boldsymbol{P}_i(x) & \text{if } x < 0 \,, \\ \boldsymbol{P}_{i+1}(x) & \text{if } x > 0 \,. \end{cases} \end{aligned} \right\} , \tag{3.124}$$
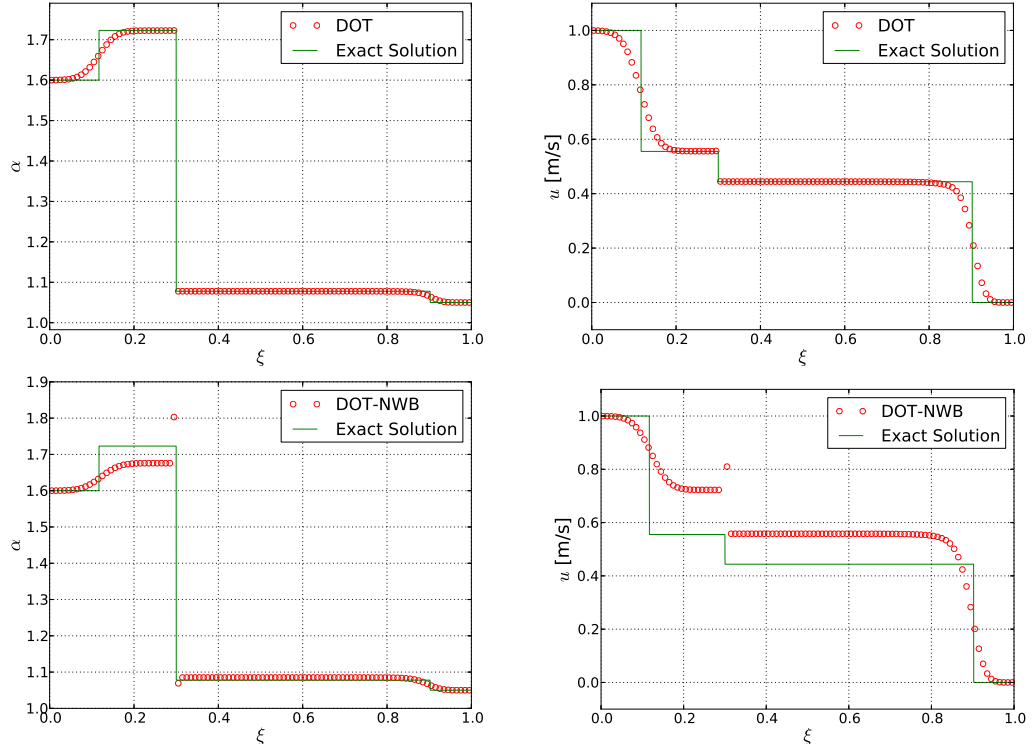
Figure 3.21: Exact solution and numerical results for RP2 regarding an (idealized) systolic pressure and peak flow arriving to a portion of the thoracic aorta with discontinuous mechanical properties and external compression. Results obtained using the first-order DOT solver with well-balanced fluctuation (3.120) (top) and the first-order DOT solver with non well-balanced fluctuation (3.111) (bottom). Shown results are for non-dimensional cross-sectional area (left) and velocity (right) versus non-dimensional length.

where $\boldsymbol{P}_i(x)$ and $\boldsymbol{P}_{i+1}(x)$ are non-linear reconstructions of the data to the left and right of the cell interface. The solution of the GRP will yield a time-dependent solution at the interface, locally along $x/t = 0$, and will be used to evaluate integrals in (3.103) to compute the fluctuations. We remark that the notation $x/t = 0$ to describe the interface means $x = 0$ and $t > 0$; when $t = 0$ one refers to the initial conditions of the problem and the solution of the PDE is strictly given for $t > 0$.

A feature of the DET solver is the time evolution of the initial data left and right of the interface. To this end, a space-time local Discontinuous-Galerking (DG) scheme is used, which will provide a local space-time polynomial $\boldsymbol{Q}_h = \boldsymbol{Q}_h(x, t)$ to be later used in (3.103), as well as in (3.102). We start by transforming system (3.89) to a reference space-time element $T_E = [0;1] \times [0;1]$ with normal coordinates ξ and τ, related to the physical domain by $x = x_{i-\frac{1}{2}} + \Delta x\, \xi$ and $t = t^n + \Delta t\, \tau$. The resulting system reads

$$\partial_\tau \boldsymbol{Q}_h + \boldsymbol{A}^* \partial_\xi \boldsymbol{Q}_h = \boldsymbol{S}^*, \tag{3.125}$$

with modified Jacobian and source term vector

$$\boldsymbol{A}^* := \frac{\Delta t}{\Delta x} \boldsymbol{A}(\boldsymbol{Q}_h), \quad \boldsymbol{S}^* := \Delta t \boldsymbol{S}(\boldsymbol{Q}_h).$$

In order to simplify the notation, we introduce the following operators:

$$[a, b]^\tau = \int_0^1 a(\xi, \tau)\, b(\xi, \tau)\, d\xi, \quad < a, b >_{T_E} = \int_0^1 \int_0^1 a(\xi, \tau)\, b(\xi, \tau)\, d\xi d\tau. \tag{3.126}$$

Next, we multiply (3.125) by a space-time basis function $\theta = \theta(\xi, \tau)$ and integrate over the reference element T_E. Using integration by parts for the time derivative term we obtain

$$[\theta, \boldsymbol{Q}_h]^1 - < \partial_t \theta, \boldsymbol{Q}_h >_{T_E} + < \theta, \boldsymbol{A}^* \partial_\xi \boldsymbol{Q}_h >_{T_E} = [\theta, \boldsymbol{w}_h]^0 + < \theta, \boldsymbol{S}^* >_{T_E}. \tag{3.127}$$
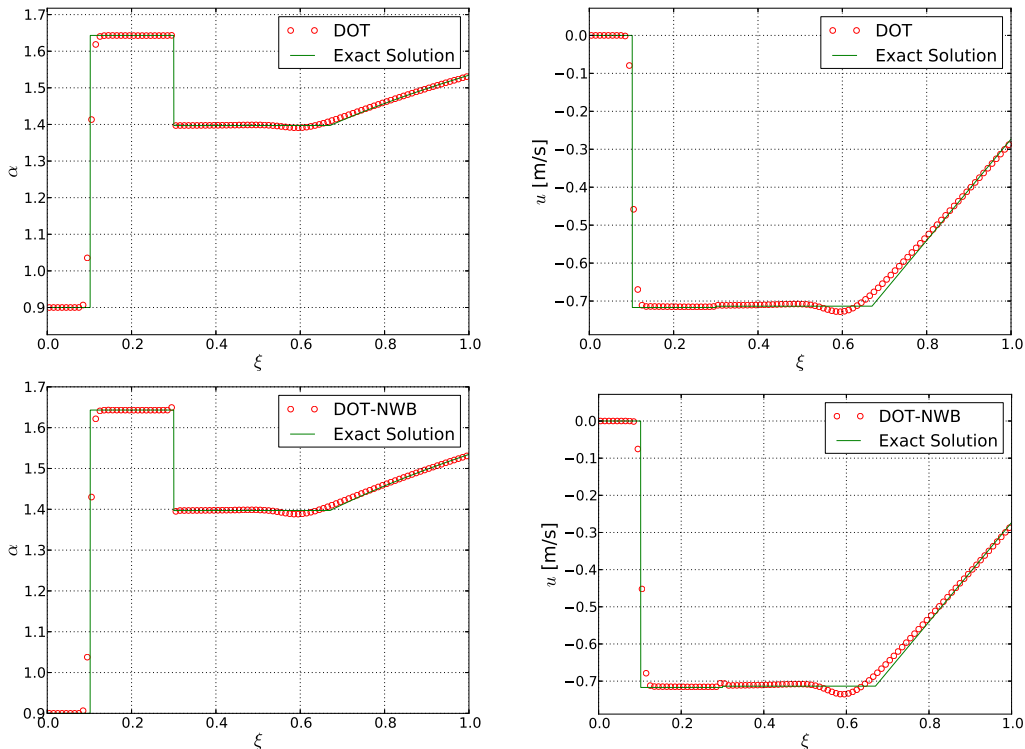
Figure 3.22: Exact solution and numerical results for RP3, regarding an (idealized) Valsava maneuver effect on an internal jugular vein with incompetent valve and discontinuous mechanical properties. Results obtained using the first-order DOT solver with well-balanced fluctuation (3.120) (top) and the first-order DOT solver with non well-balanced fluctuation (3.111) (bottom). We show results for non-dimensional cross-sectional area (left) and velocity (right) versus non-dimensional length.

We use the same space-time basis functions θ, for $\boldsymbol{Q}_h$ and $\boldsymbol{A}^*\partial_\xi\boldsymbol{Q}_h$, so that

$$\boldsymbol{Q}_h(\xi,\tau) = \sum_{l=1}^{(M+1)^2} \theta_l \hat{\boldsymbol{Q}}_l, \quad \boldsymbol{A}^*\partial_\xi\boldsymbol{Q}_h(\xi,\tau) = \sum_{l=1}^{(M+1)^2} \theta_l \widehat{\boldsymbol{A}^*\partial_\xi\boldsymbol{Q}}_l. \tag{3.128}$$

We obtain expansion coefficients $\hat{\boldsymbol{Q}}_l$ by a fixed point iteration procedure, see [64] for details, in which at each iteration step we solve the following system

$$\left([\theta_k,\theta_l]^1 - <\partial_t\theta_k,\theta_l>_{T_E}\right)\hat{\boldsymbol{Q}}_l^{m+1} - <\theta_k,\theta_l>_{T_E} \boldsymbol{S}^*(\hat{\boldsymbol{Q}}_l^{m+1}) = [\theta,\boldsymbol{w}_h]^0 - <\theta_k,\theta_l>_{T_E} \widehat{\boldsymbol{A}^*\partial_\xi\boldsymbol{Q}}_l^m. \tag{3.129}$$

The solution to the GRP at time τ is found by solving a classical Riemann problem using the space-time reconstructed states extrapolated to both sides of the cell interface, see [111]. The source term space-time average (3.102) and the non-conservative product space-time average present in (3.99) are computed by numerical integration using $\boldsymbol{Q}_h$ and a quadrature rule of appropriate accuracy. We adopt a nodal basis function given by Gauss-Lobatto quadrature points and the corresponding Lagrange polynomials intersecting these points for both polynomials, $\boldsymbol{w}_h$ and $\boldsymbol{Q}_h$ [83]. This choice reduces the computational cost for the solution of the GRP and for the evaluation of integrals present in (3.99), since states to be used at each quadrature point are already known.

Remarks. A couple of remarks on some practical aspects of the scheme are in order.

- **Well-balanced WENO reconstruction.** In order to preserve well-balanced properties of the numerical scheme, care is required in applying the WENO reconstruction operator. In fact, if we have a stationary solution $\boldsymbol{Q}^s$ with all states belonging to the integral curve

[RP2] [RP3]
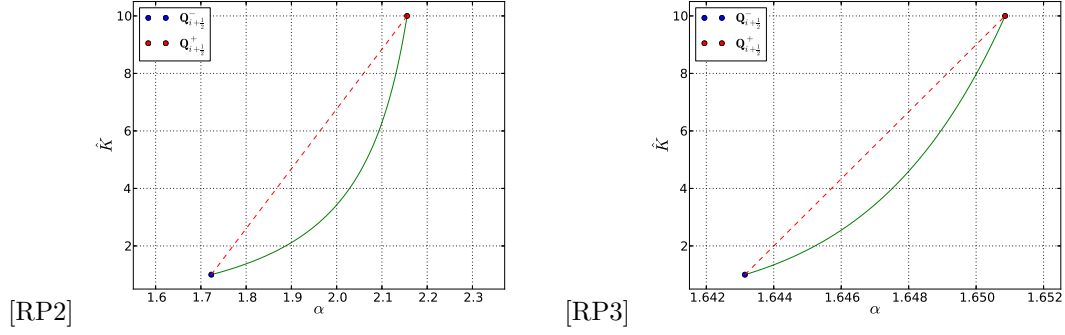
Figure 3.23: States across the stationary contact discontinuity, integral curve γ_{LD} (continuous line) and *segment* path (dashed line) in non-dimensional $(\alpha, \hat{K})$ phase-plane for RP2 and RP3.

γ_{LD} associated with the Riemann invariant of the LD field, then the output states $\boldsymbol{w}_h(x)$ of the WENO reconstruction operator must lie in the same integral curve γ_{LD}. We recall that in the case of a stationary solution, the associated Riemann invariant, besides the trivial condition $q^s(x,t) = 0$, is given by relation (3.116). Therefore, the reconstruction operator has to be applied to the internal pressure p instead of A, in order to preserve exact well-balanced solutions for the stationary case. This procedure is based on the same principle as that proposed in [63] for the shallow water equations.

- **Non-conservative products in the local DG data evolution procedure.** The term $\boldsymbol{A}^*\partial_\xi \boldsymbol{Q}_h$ present in (3.127) must be computed exactly in the case of a stationary solution. Normally, this term is obtained by first computing the expansion coefficients of spatial derivatives of $\boldsymbol{Q}_h$ using the following weak identity

$$< \theta_k, \theta_l > \widehat{\partial_\xi \boldsymbol{Q}}_l \,=< \theta_k, \partial_\xi \theta_l > \hat{\boldsymbol{Q}}_l \,, \qquad (3.130)$$

and then proceeding to a matrix vector product to obtain

$$\widehat{\boldsymbol{A}^*\partial_\xi \boldsymbol{Q}}_l = \boldsymbol{A}^*\widehat{\partial_\xi \boldsymbol{Q}}_l \,. \qquad (3.131)$$

(3.131) involves the use of $\widehat{\partial_\xi A}_l$, which again will not be exactly computed since $A^s(x)$ for a stationary solution will not necessarily be a polynomial. To overcome this problem we explicitly compute the second component of $\boldsymbol{A}^*\widehat{\partial_\xi \boldsymbol{Q}}_l$ so that

$$\boldsymbol{A}^*\widehat{\partial_\xi \boldsymbol{Q}}_l = \begin{bmatrix} \widehat{\partial_\xi q}_l \\ \frac{\hat{q}_l}{\hat{A}_l}\widehat{\partial_\xi q}_l + \hat{A}_l\widehat{\partial_\xi \beta}_l \\ 0 \\ 0 \\ 0 \end{bmatrix}. \qquad (3.132)$$

In this case, as for the spatial reconstruction, we keep tract of an auxiliary variable $\beta_h(\xi, \tau) = \theta_l \hat{\beta}_l$ during the local data evolution procedure. β is given by

$$\beta = \frac{1}{2}\left(\frac{q}{A}\right)^2 + \frac{p}{\rho} \,. \qquad (3.133)$$

Since for a stationary solution β is constant, it is computed exactly for any order of accuracy of our numerical scheme.

Empirical convergence rate study

Here we carry out a convergence rate study in order to verify that the expected theoretical order of accuracy of the proposed numerical scheme is actually attained. To this end we construct a test problem for a modified non-linear system of equations that is a perturbation of

the original system via a source term vector. In this manner we obtain a smooth, exact solution of a non-homogeneous non-linear system. Note that for this procedure to work, the numerical scheme must be able to compute solutions to non-homogeneous systems to the high-order of accuracy. We proceed to prescribe a smooth function $\hat{\boldsymbol{Q}}(x,t)$ that will be the exact solution of the perturbed system. Here we choose

$$\hat{\boldsymbol{Q}}(x,t) = \begin{bmatrix} \hat{A}(x,t) \\ \hat{q}(x,t) \\ \hat{K}(x) \\ \hat{A}_0 \\ \hat{p}_e(x) \end{bmatrix} = \begin{bmatrix} \tilde{A} + \tilde{a}\,sin\left(\frac{2\pi}{L}x\right)cos\left(\frac{2\pi}{T_0}t\right) \\ \tilde{q} - \tilde{a}\,\frac{L}{T_0}\,cos\left(\frac{2\pi}{L}x\right)sin\left(\frac{2\pi}{T_0}t\right) \\ \tilde{K} + \tilde{k}\,sin\left(\frac{2\pi}{L}x\right) \\ \tilde{A}_0 + \tilde{a}_0\,sin\left(\frac{2\pi}{L}x\right) \\ \tilde{P}_e + \tilde{p}_e\,sin\left(\frac{2\pi}{L}x\right) \end{bmatrix}. \tag{3.134}$$

Inserting (3.134) into (3.89) we obtain the following inhomogeneous system

$$\partial_t\mathbf{Q} + \mathbf{A}(\mathbf{Q})\partial_x\mathbf{Q} = \hat{\mathbf{S}}(x,t). \tag{3.135}$$

The resulting source term $\hat{\mathbf{S}}(x,t)$ reflects the fact that (3.134) is not a solution of the original system (3.89). $\hat{\mathbf{S}}(x,t)$ can be computed exactly using algebraic manipulators; its expression is not reproduced here. For the convergence rate study the following parameters were used: $L = 1.0\,m$, $T_0 = 1.0\,s$, $\tilde{A} = 4.0 \times 10^{-4}\,m^2$, $\tilde{a} = 4.0 \times 10^{-5}\,m^2$, $\tilde{q} = 0.0\,m^3\,s^{-1}$, $\tilde{K} = 50.0\,KPa$, $\tilde{k} = 500.0\,Pa$, $\tilde{P}_e = 0.0\,Pa$, $\tilde{p}_e = 50.0\,Pa$, $m = 1/2$ and $n = 0$.

Table 3.9 displays the empirical convergence rates for the proposed numerical scheme up to fifth-order of accuracy in space and time. Errors were measured in the norms L_1, L_2 and L_∞. The expected convergence rates are reached for all norms.

Remark on high accuracy. High accuracy means computational efficiency. Obviously, for a fixed mesh a low order scheme will generally be faster than its higher order extension. But this is not the way to evaluate the efficiency of numerical schemes. Instead, given an error dimmed to be acceptable, the question is which method will attain that error at the lowest computational cost. Figure 3.24 shows error versus CPU time for the second and fifth-order implementations of the ADER schemes presented in this section. The CPU time is that resulting from a sequence of successively refined meshes. It is seen that, for example, given an acceptable error of $E = 10^{-9}$, the fifth-order ADER method will be almost two orders of magnitude more efficient than the second-order ADER method. The first-order method, not shown, will appear as an almost horizontal line, suggesting that achieving the prescribed error of $E = 10^{-9}$ will be almost an impossible task in practice. The implication of the efficiency point just made is that for constructing a global, close model for the human circulation system, the high accuracy of the numerical method to be employed is of paramount importance. See also considerations made in section 3.2.5.

After the description of the high-order extension of the proposed numerical scheme and the empirical convergence rate study we proceed to validate its robustness and efficiency through a series of tests.

Tests with exact solutions containing discontinuities

Here we show numerical solutions to Riemann problems 1 to 3, described in section 3.2.3. Figure 3.25 displays results obtained from the third order ADER scheme of this section. The high-order scheme preserves all the good features of the first-order DOT scheme, such as well-balanced properties and correct solutions for the two unsteady Riemann problems 2 and 3. In addition, note that for RPs containing discontinuous solutions, there is an improvement of the resolution of both, elastic jumps and rarefactions, as compared to the first-order results shown in figures 3.21 and 3.22.

3.2.5 Validation for flow in networks of elastic blood vessels

In this section we implement a computational model to simulate flow in an *in vitro* model of the human arterial system. The *in vitro* model was presented in [109] and was further studied

Scheme	N	L^1	L^2	L^∞	$\mathcal{O}(L^1)$	$\mathcal{O}(L^2)$	$\mathcal{O}(L^\infty)$	$t_{CPU}\,[s]$
ADER-O2	4	1.07e-05	1.23e-05	2.55e-05	-	-	-	0.02
	8	2.49e-06	2.94e-06	7.64e-06	2.1	2.1	1.7	0.04
	16	5.69e-07	6.99e-07	2.02e-06	2.1	2.1	1.9	0.13
	32	1.34e-07	1.69e-07	5.13e-07	2.1	2.0	2.0	0.39
ADER-O3	4	4.20e-06	4.74e-06	8.50e-06	-	-	-	0.05
	8	5.64e-07	6.90e-07	1.46e-06	2.9	2.8	2.5	0.12
	16	7.17e-08	8.96e-08	1.97e-07	3.0	2.9	2.9	0.33
	32	8.99e-09	1.13e-08	2.51e-08	3.0	3.0	3.0	0.99
ADER-O4	4	1.02e-06	1.15e-06	1.69e-06	-	-	-	0.14
	8	1.40e-07	2.05e-07	5.73e-07	2.9	2.5	1.6	0.25
	16	1.17e-08	1.58e-08	4.44e-08	3.6	3.7	3.7	0.74
	32	8.22e-10	1.06e-09	2.97e-09	3.8	3.9	3.9	2.30
ADER-O5	4	1.78e-06	2.00e-06	3.40e-06	-	-	-	0.22
	8	6.92e-08	8.42e-08	1.71e-07	4.7	4.6	4.3	0.54
	16	2.28e-09	2.84e-09	6.17e-09	4.9	4.9	4.8	1.60
	32	7.57e-11	9.59e-11	2.41e-10	4.9	4.9	4.7	5.00

Table 3.9: Convergence results for the ADER scheme. N is the number of cells. Errors are computed for variable A. CPU times are reported for all tests.

in [2]. The model consists of 37 rubber tubes resembling major arteries, a pump to simulate the heart and terminal resistances fulfilling the role of the peripheral circulation. For details on the topography of the network, description of mechanical properties, geometry of the vessels, terminal resistances and flow rate measured at the root of the ascending aorta, see [109] and [2]. The experimental set up in [109] and the carefully reported details of all necessary parameters, allow the reader to implement the computational representation of the *in vitro* model. This makes possible a thorough validation of any given solver intended for one-dimensional blood flow simulation.

Application of the numerical scheme just proposed to the modelling of networks requires the treatment of specific boundary conditions and algorithms for treating vessel junctions. We must prescribe flow rate at the proximal end of the ascending aorta and terminal resistances at distal ends of the network. Flow rate and terminal resistances were treated as in [5]. For junctions, the methodology proposed in [143] was chosen.

The *in vitro* model has variations of reference cross-sectional area A_0 in most vessels, so that this test problem is perfectly suited to validate three aspects of the proposed methodology, namely (i) well-balanced properties of the numerical scheme and their relevance in the context of one-dimensional blood flow; (ii) ability to reproduce experimental measurements; and (iii) accuracy and efficiency of the resulting solver.

We adopted the same spatial discretisation used in [2]: vessels longer than 1.5 cm were divided in non-overlapping cells of a maximum length of 2 cm; for vessels shorter than 1.5 cm a single cell was used. Computations were performed using a $CFL = 0.9$, which results in an average time step of approximately $\Delta t = 7.7 \times 10^{-4}\,s$. We note that the time step Δt is computed at each time step, in order to advance as much as possible in time during each step, within the linear stability limit of unity of our explicit scheme. Experimental measurements for pressure and flow rate and numerical results reported in [2] were made available to us by Dr. Jordi Alastruey.

Assessing the influence of a correct WENO spatial reconstruction

For this section we devised a *trivial* test, called here the *dead man test*, which at first glance, might seem irrelevant, as blood flow in arteries is never stationary. We prescribe zero pressure and no flow as initial conditions and assign transparent boundary conditions at all distal ends of the network. The exact solution to this problem is identically the initial condition. Solving
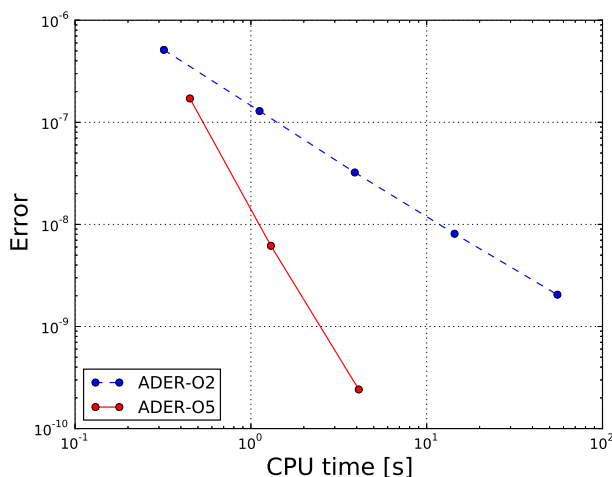
Figure 3.24: Error versus CPU time for second and fifth-order implementations of the ADER scheme.

this problem with a numerical scheme that naively treats the source terms will cause the code to crash. One reason for this is that supercritical flow will develop and the methodology used for dealing with junctions will not support this kind of flow regime. In figure 3.26 we show velocities at midpoint location versus time for all vessels of the network. The results on the left frame were obtained with a third-order implementation of the ADER scheme with a WENO reconstruction in terms of pressure p and volumetric flow rate q. The right frame of figure 3.26 shows the numerical solution obtained with a WENO reconstruction for cross-sectional area A and q. This example motivates a point already mentioned earlier. Even though the fluctuations and the local DG data evolution procedure are well-balanced, performing the WENO reconstruction of the wrong set of variables will produce spurious oscillations in the numerical solution.

Next we apply the non-well-balanced version of the ADER scheme that produces the wrong results of figure 3.26 to the unsteady problem reported in [109]. Figure 3.27 shows that this scheme will compute erroneous results, as in the case of the trivial *dead man test*. The consequences of such an approach observed in the case of a stationary test also affect the unsteady solution. In fact, flow rates at some locations are biased by the non well-balanced nature of the numerical scheme. In cases for which no reference solution is available, this kind of error can lead to totally erroneous results.

Numerical versus experimental results

In figure 3.28 we compare experimental measurements, numerical results reported in [2] and our numerical results for a third-order implementation of the ADER scheme. Results are for pressure and flow rate at different locations of the network. Our numerical results compare very well to both experiments and published state-of-the-art numerical results.

We observe larger amplitudes of high-frequency oscillations in the reference numerical results, compared to our approximation, especially for flow rates in the left renal and right carotid arteries. This behaviour can be explained by the following observations. The spatial discretization used in [2] implies using only one or two computational cells for some vessels. Contrary to the reference results, that where obtained using a discontinuous Galerkin (DG) numerical scheme that evolves spatial polynomials in time, we use a finite volume-type scheme. The higher the order of our finite volume-type scheme, the larger will be the stencil to be used in the non-linear WENO reconstruction. In many cases, the WENO stencil will involve cells that are outside of the computational domain. In such cases we use ghost cells, whose state values are given by prescribed boundary condition data. This procedure is not strictly equivalent to
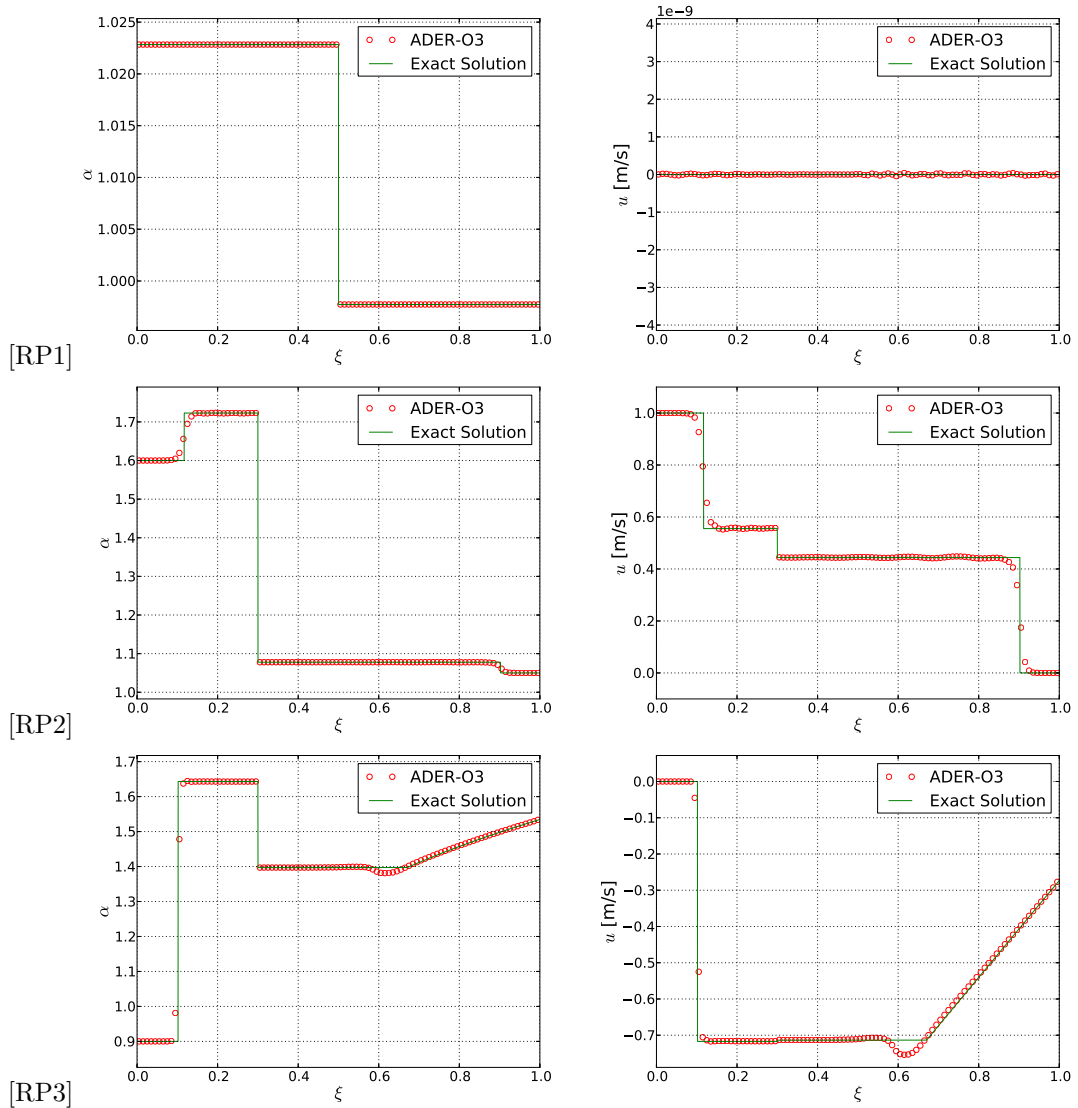
Figure 3.25: Results for Riemann problems 1 to 3 using the third-order ADER scheme with well-balanced fluctuation (3.120). Shown results are for non-dimensional cross-sectional area (left) and velocity (right) versus non-dimensional length.

the treatment of boundary conditions operated for the DG scheme in [2]. Moreover, we note that the non-linear spatial reconstruction will eventually damp some oscillations. This might seem an apparent drawback of our finite volume-type scheme. In reality, it is the WENO spatial reconstruction operator that allows us to solve problems with discontinuous or very sharp gradients, as shown in section 3.2.4.

Finally, it is worth noting that the amplitude of the high-frequency oscillations is overestimated by the purely elastic model used for the vessel walls and does not reflect the actual amplitudes registered in the experimental measurements. Alastruey *et al.* [2] have shown that using a visco-elastic vessel wall model provides a better numerical approximation of experimental measurements. Future work will regard the incorporation of such tube law models in our solver.

Computational cost and efficiency

The computational cost for one cardiac cycle of the test presented in the previous section is reported in table 3.10. CPU times include the treatment of junctions and the prescription of boundary conditions. The time step was defined at each time level by imposing a $CFL = 0.9$,
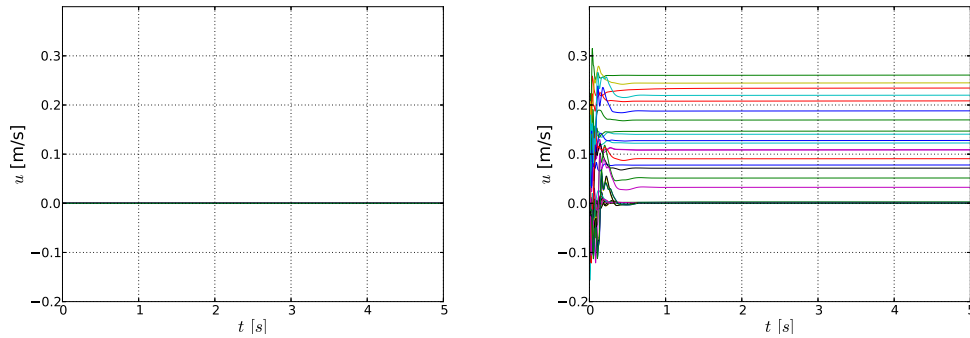
Figure 3.26: Computed velocities at midpoint location versus time for all 37 vessels of the *in vitro* model for *dead man test.* Left frame shows results obtained using a WENO reconstruction in terms of pressure p and volumetric flow rate q; right frame shows results obtained using a WENO reconstruction for cross-sectional area A and q.

with an average value of $\Delta t = 7.71 \times 10^{-4}\,s$, for the spatial discretization proposed in [2]; the code was run on a workstation with an Intel Core i7-2600 processor with 4 cores (3.40GHz clock speed) and 8 GB of RAM. Considering that the code for the network solver was not optimised, these results allow us to claim that our numerical scheme is computationally cheap. The main features of the numerical method are its low computational cost, the fact of being well-balanced and its robustness, even for its higher order implementations, that allows us to solve problems with large vessel deformations, as in the case of veins.

In figure 3.29 we show a comparison of numerical results for the first-order scheme presented in section 3.2.3 and for the high-order implementations up to fourth-order. The first-order results were obtained on a series of refined meshes (see table 3.10), whereas high-order solutions refer to the mesh used in [2]. As expected, doubling the number of cells at each refinement step yields a numerical solution similar to the corresponding high-order approximation. Nevertheless, the high-order solutions are always slightly more accurate and computationally cheaper than the first-order solutions, see table 3.10. These observations confirm our considerations made in section 3.2.4 with respect to the efficiency of high-order schemes.

Tests	nDOF	$\Delta x\,[cm]$	$t_{cpu}\,[s]$
DOT-O1	-	2	3.11
DOT-O1-REF1	-	1	17.78
DOT-O1-REF2	-	0.5	53.82
DOT-O1-REF3	-	0.25	151.31
ADER-O2	1124	2	4.60
ADER-O3	2529	2	8.99
ADER-O4	4496	2	21.37

Table 3.10: Computational cost for runs presented in this section. nDOF is number of degrees of freedom of the space-time polynomial $\boldsymbol{Q}_h = \boldsymbol{Q}_h(\xi,\tau) = \hat{\boldsymbol{Q}}_l\theta_l$, computed during the local predictor step and later used to solve the GRP.

3.2.6   Concluding remarks

We have constructed a well-balanced high-order numerical scheme for one-dimensional flow in blood vessels with variable mechanical and geometrical properties. Having adopted a suitable, recently proposed mathematical model we have devised a modified version of the DOT Riemann solver for non-conservative systems, so that the associated first-order monotone scheme preserves stationary solutions exactly. We have then extended the first-order DOT-based scheme to higher order of accuracy in space and time following the ADER approach. An empirical convergence rate study confirms that the expected theoretical order of accuracy is effectively
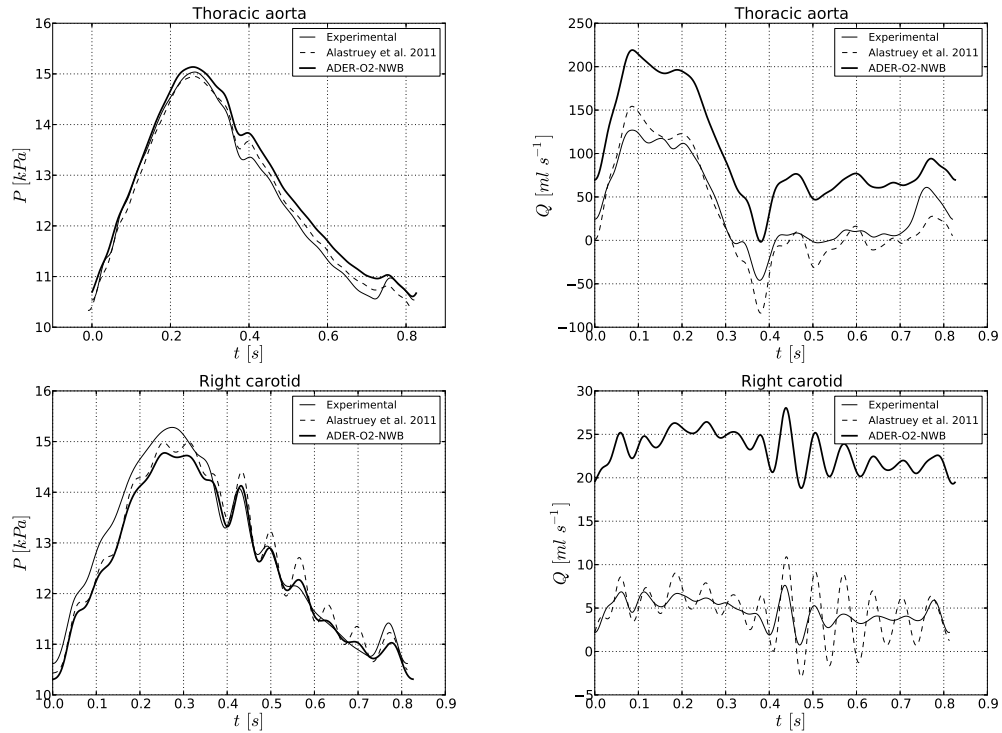
Figure 3.27: Performance of non well-balanced scheme for an unsteady problem.

achieved by the numerical scheme. Theoretically, the ADER approach allows arbitrary order of accuracy in space and time. Through a series of carefully chosen test problems we have verified the well-balanced property of the numerical scheme, as well as its ability to solve problems including elastic jumps and large gradients, for which exact solutions are available. The proposed numerical scheme is then applied to a network of elastic vessels for which experimental measurements and state-of-the art numerical solutions are available. The performance of our scheme turns out to be very satisfactory.
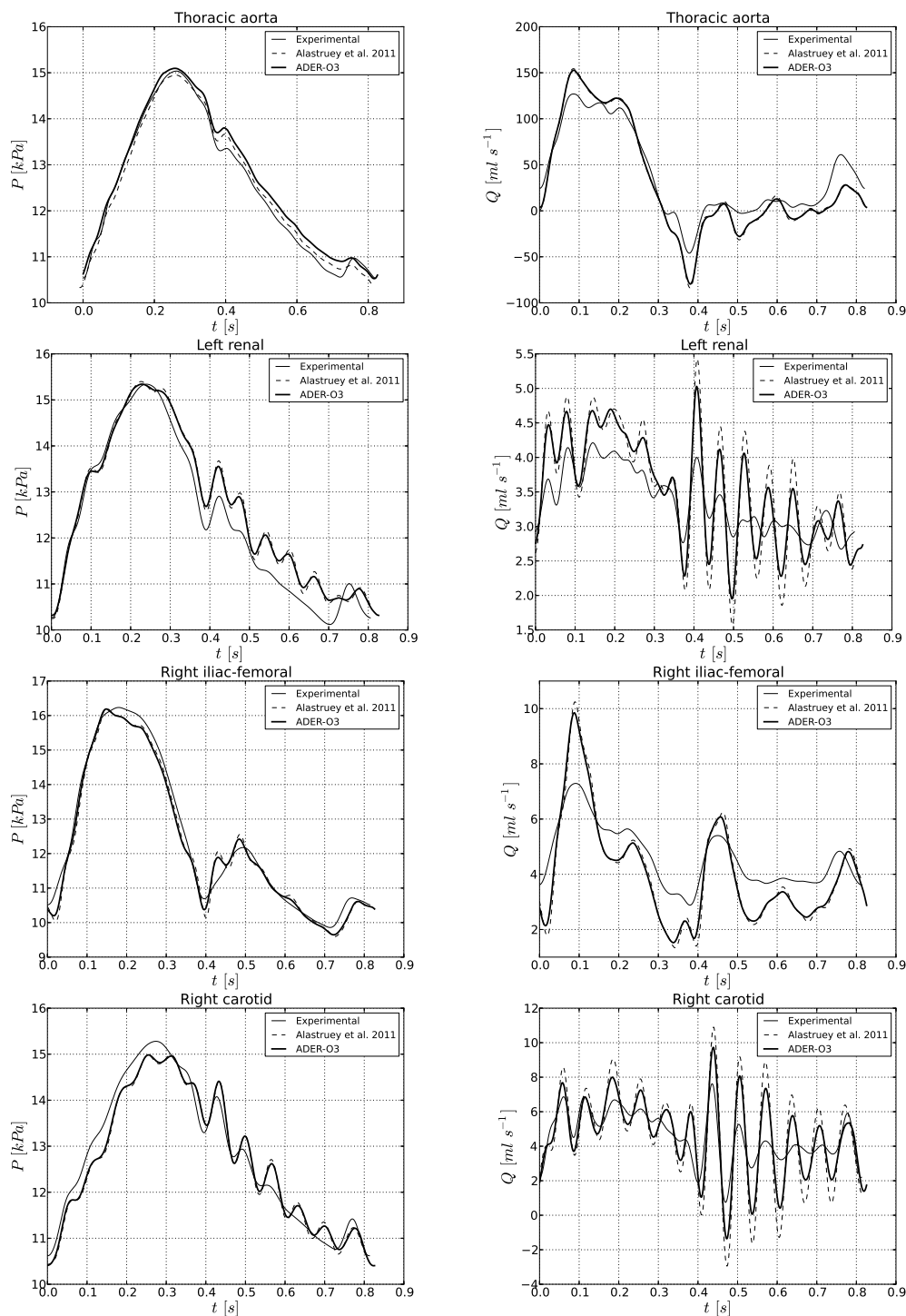
Figure 3.28: Comparison of our numerical results in third-order mode against experimental measurements and numerical results of [2].
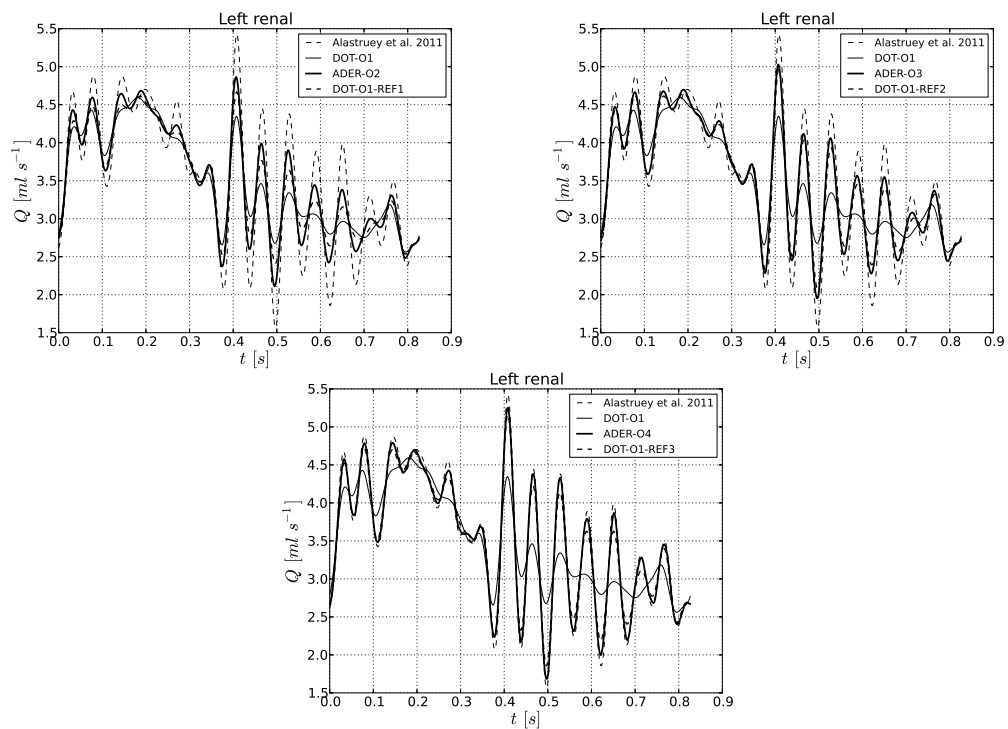
Figure 3.29: Comparison of numerical results obtained with the first-order scheme on refined grids and with the higher order implementations on the original grid. Higher order schemes deliver a more accurate solution with less computational time, see table 3.10.

Chapter 4

Global solver for blood flow in the human cardiovascular system with emphasis on veins

After having described the development of suitable numerical schemes for blood flow in elastic vessels in the previous chapter, here we illustrate how a closed-loop model of the cardiovascular system with emphasis on veins was constructed and validated. We also present an extension of the basic model that takes into account the interaction of the cerebral vasculature and intracranial pressure and a delicate mechanism regulating cerebral venous flow, *i. e.* the Starling resistor.

4.1 A global multi-scale mathematical model for the human circulation with emphasis on the venous system

4.1.1 Introduction

The present work is in part motivated by recent interest shown by the medical community on the venous system and its potential role in the development and clinical course of neurodegenerative diseases [79]. In particular, applications in mind include a theoretical study of two empirically discovered conditions, namely Chronic Cerebrospinal Venous Insufficiency [183] and Idiopathic Parkinson's Disease [80]. These motivating examples set two requirements on our model. First, the description of head and neck veins should be sufficiently detailed, including the numerous collateral pathways of cerebral venous return [138]. Second, the model should include the main systemic veins in order to take into account some specific characteristics of the pathologies under study. We have therefore chosen to construct a closed-loop model of the entire cardiovascular system with emphasis on the venous district.

In 1969, the journal IEEE Transactions on Bio-medical Engineering published an entire issue on the venous system. Main points identified by contributors included a description of mechanical properties of veins, their functioning and, consequently, their modelling. At that time the modelling community was well aware of the difficulties to be faced in order to model the venous system. The most relevant problems, or differences, compared to the arterial counterpart, concerned the collapsibility of veins and the effect of external forces, such as gravity and external pressure, on venous flow [37]. In their introductory letter to that issue, Noordergraaf and Kresch [125] put in evidence the increasing interest in the role played by the venous system in heart dynamics and circulation in general. They concluded prospecting a renewed interest in the modelling community in this research field. Two remarkable contributions of the 1969 issue of IEEE Transactions on Bio-medical Engineering are the works by Snyder & Rideout [146] and by Moreno *et al.* [112]. Both contributions represented early attempts to model the complete cardiovascular system, giving special attention to the description of the venous district. Snyder and Rideout [146] proposed a closed-loop lumped parameter model including vessel collapse,

external pressure by respiration, venous tone regulation and gravity.

Unfortunately, not much progress has been made since those early days in the field of venous haemodynamics modelling. Most of the available work concerns the description of flow in collapsible tubes [140, 91, 69] and related numerical applications to rather simple problems [132, 35, 36]. Recently, some interesting work has been published regarding the construction of tube laws for veins [20] and its application to one-dimensional modelling of blood flow in veins of the lower limb [75, 108]. Some work on modelling of venous networks with one-dimensional approaches is available in the literature. Zagzoule and MarcVergnes [180] presented a model for cerebral circulation with major arteries, intracranial veins and the jugular veins. Cirovic *et al.* [52] modelled cerebral blood flow using the network proposed in [180] and including high gravitational acceleration, observing jugular vein collapse. Sheng *et al.* [141] presented an open-loop model with a one-dimensional description of arteries, veins and capillaries. Following the work of Sheng *et al.*, Alirezaye-Davatgar [6] proposed a similar model; no emphasis on results for the venous system were given. Vassilevski *et al.* [170] proposed a closed-loop model of the cardiovascular system with a one-dimensional description of veins; no details on the construction of the venous network were provided. Finally, Ho *et al.* [84] reported the construction of a patient-specific one-dimensional model of the cerebral venous system, imposing artificial boundary conditions at the level of the superior vena cava and terminal veins.

Closed-loop models of the cardiovascular system with a one-dimensional description of major vessels are rare. Two prominent examples are the closed-loop models proposed by Liang *et al.* [102] and by Blanco *et al.* [30]. In both cases the arterial system is modelled using a one-dimensional approach, while the heart, pulmonary circulation, capillaries and veins are treated as lumped parameter compartments. We note that at the last stage of this PhD project we were made aware of an excellent and relevant piece of work concerning a closed-loop model and one-dimensional representation of the venous system; see Mynard [121]. Our model is a step forward in the context of closed-loop models since it includes a detailed one-dimensional description of the venous district. This model will constitute the basis on which the above discussed challenges of the venous system will be approached and, hopefully, resolved.

Variation of mechanical and geometrical properties of vessels along their longitudinal axis gives rise to *geometrical-type* source terms. These source terms cause severe problems if a naive discretisation is used. We chose to adopt a reformulation of the classical equations governing one-dimensional blood flow proposed in [161], where the system is written in quasi-linear form. Concerning the numerical method for solving the one-dimensional blood flow equations in veins and arteries, we adopt the ADER framework [159]. This framework allows the construction of non-linear schemes, to circumvent Godunov's theorem, of high order of accuracy in both space and time, while maintaining the necessary robustness required by the highly non-linear behaviour of veins. High order of accuracy in space and time is mandatory; it is in fact an efficiency requirement, most relevant for the simulation of complex systems, such as the human circulation. See [113] and [116] for the case of one-dimensional blood flow models, where an analysis of convergence rates, errors and CPU time is carried out. ADER finite volume schemes consist of two building blocks: (i) a non-linear spatial reconstruction operator and (ii) the solution of the Generalized Riemann Problem (GRP) at each cell interface to compute numerical fluxes [162]. For the solution of the GRP we adopt the Dumbser-Enaux-Toro (DET) solver [64, 63, 65]. All GRP solvers available, see [111], require a classical Riemann solver. Here we use the Dumbser-Osher-Toro (DOT) Riemann solver [66], as proposed in [116]. This numerical scheme is able to treat venous collapse, as well as transcritical flows [113], which might verify in veins [145]. For background on the ADER approach and recent developments see chapters 19 and 20 of [163] and references therein.

A distinctive aspect of this work, is the performance of a patient-specific characterization of major veins of the head and neck. This approach is motivated by the great inter-subject variability of the venous system [138, 175]. In order to achieve this goal, we represent major head and neck veins of our venous network using Magnetic Resonance Imaging derived geometrical information [167]. Moreover, we are able to compare our computational results with MRI-derived time-resolved flow quantification data [70], again, in a patient-specific manner. This is possible because MRI imaging of venous structures and flow quantification are made within the same MRI session.

The rest of this section is structured as follows. In section 4.1.2 we present the mathematical

models used to treat each compartment, whereas in section 4.1.3 we describe numerical schemes to compute the solution of the appropriate differential equations. In section 4.1.4 we report all parameters necessary to define the model. Next, in section 4.1.5 we show computational results for the heart, arterial and venous system, comparing them to literature data and to MRI-derived flow quantification data, where available. In section 4.1.6 we discuss results presented and future work. We conclude with section 4.1.7, where final considerations are made.

4.1.2 Mathematical models

Our closed-loop mathematical model is composed of a one-dimensional network of major arteries, see figure 4.1, a one-dimensional network of major veins, see figure 4.2, and lumped parameter models for heart and pulmonary circulation, see figure 4.3, and for arterioles, capillaries and venules, see figure 4.4. The numbering in the figures is a guide to the reader to find the geometrical and mechanical properties of vessels in the referred tables.

In the following sections we describe the mathematical models used for each one of these compartments.
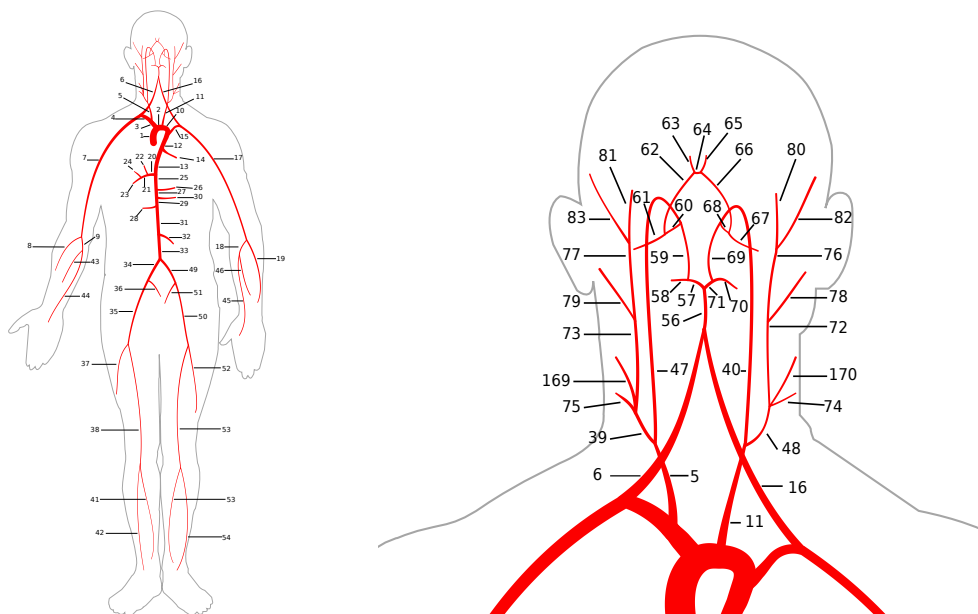
Figure 4.1: Arterial network composed of 85 arteries, taken from [101] (left). Detail of head and neck arteries (right). Numbers refer to table 4.3, where geometrical and mechanical parameters for each vessel are reported.

Blood flow in arteries and veins: one-dimensional model

One-dimensional blood flow models result from averaging the incompressible Navier-Stokes equations over the vessel cross-section under some assumptions, including axial symmetry. Also, the structural mechanics of the vessel wall is simplified; relevant assumptions are radial displacement and elastic material properties. For a full derivation of the model see, for example, [73]. Even under such strong simplifications of reality, these models preserve the essential physical features of wave propagation in compliant vessels. The resulting one-dimensional equations for blood flow in elastic vessels are given by the following first-order, non-linear hyperbolic system

$$
\begin{cases}
\partial_t A + \partial_x q = 0\,, \\
\partial_t q + \partial_x \left(\hat{\alpha} \dfrac{q^2}{A} \right) + \dfrac{A}{\rho} \partial_x p = -f\,,
\end{cases}
\tag{4.1}
$$

where x is the axial coordinate along the longitudinal axis of the vessel; t is the time; $A(x,t)$ is the cross-sectional area of the vessel; $q(x,t)$ is the flow rate; $p(x,t)$ is the average internal
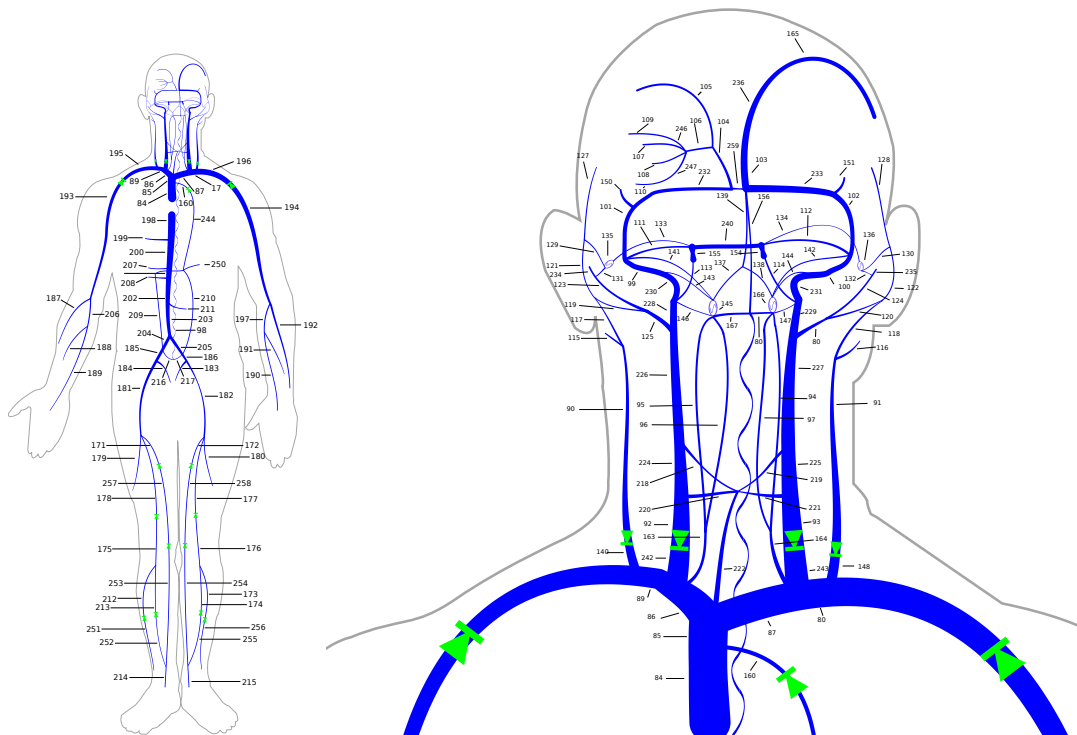
Figure 4.2: Schematic representation of venous network (left). Detail of head and neck veins (right). Numbers refer to table 4.8, where geometrical and mechanical parameters for each vessel are reported.

pressure over a cross-section; $f(x,t)$ is the friction force per unit length of the tube; ρ is the fluid density and $\hat{\alpha}$ is a coefficient that depends on the assumed velocity profile. Throughout this work we will take $\hat{\alpha} = 1$, which corresponds to a blunt velocity profile.

To close the system we adopt a tube law, whereby the internal pressure $p(x,t)$ is related to the cross-sectional area $A(x,t)$ and other parameters, namely

$$p(x,t) = p_e(x,t) + \psi(A; A_0, K, P_0). \tag{4.2}$$

Here $p_e(x,t)$ is the external pressure, prescribed, and $\psi(x,t)$ is the transmural pressure, assumed of the form

$$\psi(A(x,t); K(x), A_0(x), P_0) = K(x)\phi(A(x,t); A_0(x)) + P_0. \tag{4.3}$$

$K(x) = K(E(x), h_0(x))$ is a positive function that contains the combined variation in x of $E(x)$, the Young modulus, and of $h_0(x)$, the wall thickness; see [35] for details. P_0 is the reference pressure for which $A = A_0$, consequently, A_0 is a reference cross-sectional area. The function $\phi(A, x)$ is assumed of the form

$$\phi(A(x,t); A_0(x)) = \left(\frac{A(x,t)}{A_0(x)}\right)^m - \left(\frac{A(x,t)}{A_0(x)}\right)^n. \tag{4.4}$$

The parameters m and n are obtained from higher-order models or simply computed from experimental measurements. We remark that there are mathematical constraints for the choice of m and n to satisfy hyperbolicity of the equations and for the genuinely non-linear character of the characteristic fields associated with the pressure related eigenvalues; full details are given in [161]. Throughout this work we assume $m > 0$ and $n \in (-2, 0)$. In the next section we discuss the values that K, m and n may assume for different vascular districts.

If one takes into account the spatial variability of A_0, K and p_e and substitutes (4.2) into (4.1), the resulting momentum equation reads

$$\partial_t q + \partial_x \left(\hat{\alpha}\frac{q^2}{A}\right) + \frac{A}{\rho}K\phi_A\partial_x A = -\frac{A}{\rho}\left(\partial_x p_e + K\phi_{A_0}\partial_x A_0 + \phi\partial_x K\right) - f, \tag{4.5}$$
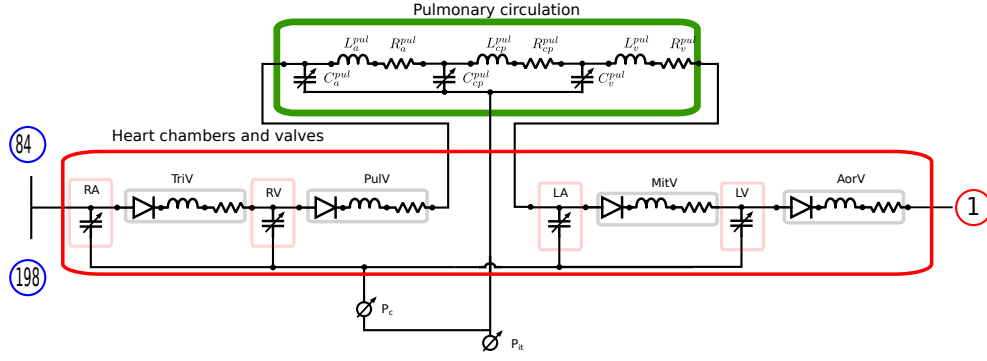
Figure 4.3: Lumped parameter model for heart and pulmonary circulation. RA, LA: right and left atrium; RV, LV: right and left ventricles. $TriV, PulV, MitV, AorV$: tricuspid, pulmonary, mitral and aortic valves. P_c and P_{it} are pericardium and intra-thoracic pressures, respectively. In the present work both pressures are put equal to zero.
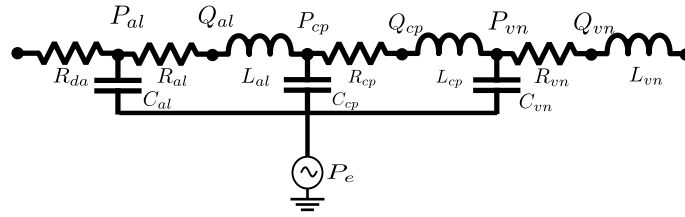
Figure 4.4: Lumped parameter network for a simple artery-vein connection. Arteries are connected to veins via arterioles, capillaries and venules. For each compartment we specify compliance C, inductance L and resistance R.

where

$$\phi_A = \frac{\partial \phi}{\partial A}, \quad \phi_{A_0} = \frac{\partial \phi}{\partial A_0}. \tag{4.6}$$

The right-hand-side of the momentum balance equation includes *geometric-type* source terms. It is a well-documented fact that a naive discretization of such terms may lead to serious numerical difficulties and hence a careful treatment of these is required [130, 119, 116]. To this end we adopt a reformulation of system (4.1) proposed in [161], namely

$$\partial_t \mathbf{Q} + \mathbf{A}(\mathbf{Q}) \partial_x \mathbf{Q} = \boldsymbol{S}(\boldsymbol{Q}), \tag{4.7}$$

where the state vector $\mathbf{Q}$ is given by

$$\mathbf{Q} = \left[A, q, K, A_0, p_e \right]^T \tag{4.8}$$

and the coefficient matrix $\mathbf{A}(\mathbf{Q})$ is

$$\mathbf{A}(\mathbf{Q}) = \begin{bmatrix} 0 & 1 & 0 & 0 & 0 \\ c^2 - u^2 & 2u & \frac{A}{\rho}\phi & K\frac{A}{\rho}\phi_{A_0} & \frac{A}{\rho} \\ 0 & 0 & 0 & 0 & 0 \\ 0 & 0 & 0 & 0 & 0 \\ 0 & 0 & 0 & 0 & 0 \end{bmatrix}. \tag{4.9}$$

Here $u = q/A$ is the cross-sectional averaged velocity of the fluid, $\boldsymbol{S}(\boldsymbol{Q})$ is a source term vector

$$\boldsymbol{S}(\boldsymbol{Q}) = [0, -f, 0, 0, 0]^T \tag{4.10}$$

and c is the wave speed

$$c = \sqrt{\frac{A}{\rho}\frac{\partial \psi}{\partial A}}. \tag{4.11}$$

Note that all geometric source terms have disappeared from the right hand side and are now in the principal part of the equations.

The eigenvalues of (4.9) are

$$\lambda_1 = u - c, \quad \lambda_2 = \lambda_3 = \lambda_4 = 0, \quad \lambda_5 = u + c \tag{4.12}$$

and the corresponding right eigenvectors of $\boldsymbol{A}(\boldsymbol{Q})$ are

$$\boldsymbol{R}_1 = \gamma_1 \begin{bmatrix} 1 \\ u - c \\ 0 \\ 0 \\ 0 \end{bmatrix}, \quad \boldsymbol{R}_2 = \gamma_2 \begin{bmatrix} \frac{A}{\rho}\frac{\phi}{u^2-c^2} \\ 0 \\ 1 \\ 0 \\ 0 \end{bmatrix}, \quad \boldsymbol{R}_3 = \gamma_3 \begin{bmatrix} \frac{A}{\rho}\frac{K\phi_{A_0}}{u^2-c^2} \\ 0 \\ 0 \\ 1 \\ 0 \end{bmatrix},$$

$$\boldsymbol{R}_4 = \gamma_4 \begin{bmatrix} \frac{A}{\rho}\frac{1}{u^2-c^2} \\ 0 \\ 0 \\ 0 \\ 1 \end{bmatrix}, \quad \boldsymbol{R}_5 = \gamma_5 \begin{bmatrix} 1 \\ u + c \\ 0 \\ 0 \\ 0 \end{bmatrix}, \tag{4.13}$$

where γ_i, for $i = 1, ..., 5$, are arbitrary scaling factors.

Under a suitable assumption for coefficients m and n, system (4.7) is hyperbolic, though not strictly hyperbolic. Hyperbolicity is lost when $|u| = c$, leading to resonance. As noted in [161] there is a possible loss of uniqueness. These aspects of the mathematical model are currently subject of study.

The first and fifth characteristic fields are genuinely non-linear and are associated with shocks and rarefactions, whereas the remaining fields are linearly degenerate and are associated with stationary contact discontinuities. See [161] for conditions on parameters m and n for this to be true. At this point we introduce the Riemann invariants associated with the genuinely non-linear fields

$$\Gamma_1 = u - \int_{A^*}^{A} \frac{c(\tau)}{\tau} d\tau, \quad \Gamma_5 = u + \int_{A^*}^{A} \frac{c(\tau)}{\tau} d\tau, \tag{4.14}$$

and the linearly degenerate fields (LD)

$$\Gamma_1^{LD} = p + \frac{1}{2}\rho u^2, \quad \Gamma_2^{LD} = q, \tag{4.15}$$

where A^* is the cross-sectional area at a reference state. These will be needed in discussing boundary conditions.

Mechanical properties of vessels and tube laws

Transmural pressure for arteries is commonly defined as

$$\psi_a(x,t) = K_a(x)\,\phi_a(A(x,t); A_0(x)) + P_0 = K_a(x)\left(\left(\frac{A(x,t)}{A_0(x)}\right)^{\frac{1}{2}} - 1\right) + P_0, \tag{4.16}$$

where $A_0(x)$ is the vessel cross-sectional area for which the transmural pressure $\psi_a = P_0$. K_a is given by

$$K_a(x) = \frac{E(x)\,h_0(x))}{(1 - \nu^2)\,R_0(x)}, \tag{4.17}$$

where ν is the Poisson ratio, equal to $1/2$ for incompressible solids and R_0 is the vessel radius at reference configuration. Relation (4.16), in combination with (4.17) are derived by considering static equilibrium of the vessel wall and small vessel deformations. See [73] for details.

Relation (4.16) correctly describes wave propagation patterns in arterial networks as extensively confirmed by existing literature, see [18, 2]. Therefore, we use (4.16) for describing the behaviour of arteries.

On the other hand, transmural pressure for veins is commonly described by

$$\psi_v(x,t) = K_v(x)\,\phi_v(A(x,t); A_0(x)) + P_0 = K_v(x)\left(\left(\frac{A(x,t)}{A_0(x)}\right)^m - \left(\frac{A(x,t)}{A_0(x)}\right)^n\right) + P_0\,. \quad (4.18)$$

Typical values for collapsible tubes, such as veins, are: $m = 10$, $n = -1.5$, see [140]. The vessel stiffness of veins K_v is

$$K_v(x) = \frac{E(x)}{12\,(1 - \nu^2)}\left(\frac{h_0(x)}{R_0(x)}\right)^3\,. \quad (4.19)$$

.

Relation (4.19) derives from considerations made for the collapse of thin-walled elastic tubes. When a thin-walled tube collapses, there is a contact region of the internal vessel walls which divides the cross-section into two tubes running in parallel. Flaherty *et al.* [71] derived an exact solution for this buckling behaviour which relates pressure and area as

$$-\frac{p - p_e}{K_v} = \left(\frac{A(x,t)}{A_0(x)}\right)^{-\frac{3}{2}}\,. \quad (4.20)$$

The validity of relation (4.20) for thin-walled latex tubes was confirmed in [140], for $A \leq A_0$. In practice, one commonly assigns a high value to m, so that for $A \leq A_0$ relation (4.18) behaves as (4.20).

In order to better understand the implications of using (4.18) in our mathematical model let us consider an example. Anliker *et al.* [11] measured the speed of pressure waves in the abdominal vena cava of a dog, obtaining values for wave speed c in the range of 2 to 3 m/s. Nippa *et al.* [124] measured wave speeds in different regions of a human in supine position, obtaining values ranging from 0.6 to 3 m/s. This experimental evidence suggests that wave speed values in the venous system range, roughly, from 1 to 3 m/s, as reported in [42]. Let us take numerical values reported in the literature necessary for computing c for a vein: $E = 1 \times 10^5\,Pa$ (table I of [42]) and $h/R_0 = 0.01$. With these values we obtain that $K_a = 1333.33\,Pa$ and $K_v = 0.0111\,Pa$. Taking these parameters, wave speeds for physiological pressure values lay within the above mentioned ranges for both tube laws. For example, for a pressure $p = 5\,mmHg$ we have $c_a = 0.875\,m\,s^{-1}$ and $c_v = 2.0\,m\,s^{-1}$. However, the behaviour of tube law (4.18) is drastically different from the one obtained using (4.16). Figure 4.5 shows pressure vs non-dimensional area $\alpha = A/A_0$ for the tube laws for arteries and veins, as well as their respective operative pressure ranges. The highly non-linear behaviour of the curve for veins contrasts sharply with that for arteries; veins are tremendously deformable, as compared to arteries; veins collapse while arteries do not. The highly non-linear behaviour of veins implies a judicious choice of numerical methods, on which the robustness of the full model depends.

For a subject in supine position, pressure changes along the venous system are small and deviations from a reference state will be small as well. Therefore, for this posture we expect that the global model will not be excessively sensitive to mechanical properties of veins. On the other hand, changes in posture will induce significant changes in pressure and consequently in the geometry of veins. Above the right atrium, neck veins will collapse and there will be a displacement of around $500 - 600\,ml$ of blood from the upper part of the body to the lower limbs [99]. These changes will crucially depend on the mechanical properties of veins.

It is important to remark that experimental evidence shows that the behaviour of veins in the collapse region is not as extreme as described by relation (4.18) with stiffness coefficient (4.19). Bassez *et al.* [20] measured pressure-area relations for lower limb veins, showing a slower collapse process. Even though they did not measured pressure directly, they extrapolated it from height differences between the point where the cross-section of the vein was measured and the right atrium, the validity of the description of the shape of the pressure-area relationship remains. Drzewiecki *et al.* [61] provide the same kind of evidence for a canine jugular vein, though here the non-linear character of the vein collapse is stronger than for lower limb veins. Moreover, Bassez *et al.* [20] performed an *in-vitro* study in which they assessed the influence of a surrounding gel on the collapse dynamics of thin-walled tubes. They showed that collapse tends to be less abrupt as the Young modulus of the surrounding gel increases. This fact confirms *in-vivo* measurements mentioned above, indicating that the fact that veins are attached to external tissue, or at least surrounded by it, will attenuate the collapse dynamics.

Considering the lack of data on mechanical properties of veins we have chosen to use, as a first approach, tube law (4.18) with coefficients $m = 10$ and $n = -3/2$. Taking into account the considerations made in the previous paragraph, vessel stiffness K_v will not be computed using (4.19), but will be estimated from pulse wave velocities, following a similar approached as the one used in [121]. We define a function for reference wave speeds in veins as

$$c_0 = c_{0,max} - (c_{0,max} - c_{0,min}) \left(\frac{r - r_{min}}{r_{max} - r_{min}} \right)^{\frac{1}{4}}, \qquad (4.21)$$

where r_{min} and r_{max} are the minimum and maximum vein radii in the network; $c_{0,max} = 3\,m\,s^{-1}$ and $c_{0,min} = 1\,m\,s^{-1}$. Note that reference wave speed c_0 is

$$c_0 = \sqrt{\frac{K_v}{\rho}(m - n)}. \qquad (4.22)$$

We set the reference pressure to be used in tube law (4.18) to $P_0 = 5\,mmHg$. Therefore, we estimate K_v from radii reported in table 4.8, corresponding to reference pressure P_0, and wave speeds c_0 computed using relation (4.21). Using this kind of approach, the values for K_v range between 100 and 400 Pa. The shape of tube law (4.18) using K_v with values of this order of magnitude can be seen in figure 4.5. The collapse behaviour of the resulting tube law is still highly non-linear, but not as extreme as the one obtained with K_v computed using relation (4.19).

The definition of mechanical properties of veins and closure relations remains the major weak point of our model and must be improved in the future. Therefore, we foresee to perform a study as the one presented in [20], especially for neck veins.
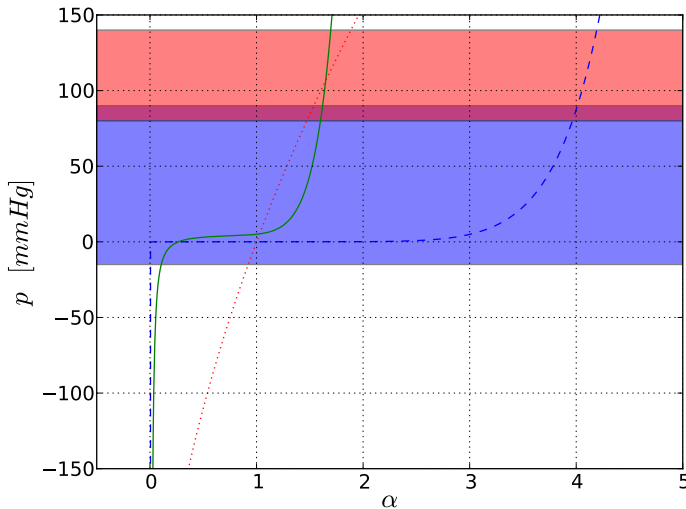
Figure 4.5: Pressure vs non-dimensional cross-sectional area for tube law (4.16) with $K_A = 50000\,Pa$ and $P_0 = 0\,mmHg$ (dotted line), for tube law (4.18) with $K_V = 0.011\,Pa$ and $P_0 = 0\,mmHg$ (dashed line) and for tube law (4.18) with $K_V = 91.3\,Pa$ and $P_0 = 5\,mmHg$ (continuous line). The top and middle rectangles represent physiological pressure ranges for arteries and veins, respectively.

Lumped parameter models

Blood flow in arterioles, capillaries and venules is modelled using lumped parameter models, also called 0-D models. These models can be derived from averaging the one-dimensional model (4.1) over the length of a vessel and making several assumptions, such as neglecting the convective term of the momentum equation (see [73] for background). Figure 4.6 shows a single

compartment, composed by a capacitor, a resistor and an inductor. In such a compartment the following equations hold

$$\frac{dP}{dt} = \frac{1}{C}(Q_{in} - Q) + \frac{dP_e}{dt},$$
$$\frac{dQ}{dt} = \frac{1}{L}(P - QR - P_{out}),$$

(4.23)

where $Q(t)$ and $P(t)$ are the state variables of the lumped compartment, that is flow rate and pressure, whereas R, L and C are its resistance, inductance and capacitance, respectively. Moreover, P_e represents the external pressure, which will be assumed to be zero if not specified. Q_{in} and P_{out} are variables belonging to other lumped compartments or deriving from boundary conditions, as we shall see later on. Single compartments are then combined to form peripheral beds that connect arteries to veins.
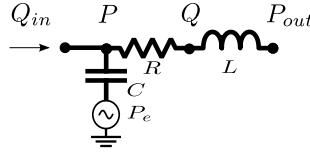
Figure 4.6: Single compartment used for lumped parameter models. The electric circuit analog comprises a capacitor with capacitance C, a resistor with resistance R and an inductor with inductance L.

Heart and pulmonary circulation

For the heart and pulmonary circulation we use a slightly modified version of the lumped parameter model proposed in [154] and extended in [102]. Figure 4.3 shows the various components of the model, including the four heart chambers and corresponding cardiac valves, as well as a simplified compartmental description of the pulmonary circulation, divided in arteries, capillaries and veins.

The model proposed in [102] is based on a prescribed variation in time of heart chambers elastances. Pressure in a cardiac chamber $P_{ch}(t)$ is given by

$$P_{ch}(t) = P_e + (E_A e(t) + E_B)(V_{ch} - V_{ch,0}) + S\frac{dV_{ch}}{dt},$$

(4.24)

where E_A and E_B are the amplitude and baseline values of the elastance, V_{ch} and $V_{ch,0}$ are the current chamber volume and dead chamber volume and S is the viscoelasticity coefficient of the cardiac wall and $e(t)$ is a normalized time-varying function that represents the forcing source for the closed-loop model. The function $e(t)$ differs for ventricles and atria. For atria we use

$$e_a(t) = \begin{cases} \frac{1}{2}\left\{1 + \cos\left[\pi(t + T - t_{ar})/T_{arp}\right]\right\} & 0 \leq t \leq t_{ar} + T_{arp} - T, \\ 0 & t_{ar} + T_{arp} - T < t \leq t_{ac}, \\ \frac{1}{2}\left\{1 - \cos\left[\pi(t - t_{ac})/T_{acp}\right]\right\} & t_{ac} < t \leq t_{ac} + T_{acp}, \\ \frac{1}{2}\left\{1 + \cos\left[\pi(t - t_{ar})/T_{arp}\right]\right\} & t_{ac} + T_{acp} < t \leq T \end{cases}$$

(4.25)

and for the ventricles

$$e_v(t) = \begin{cases} \frac{1}{2}\left[1 - \cos(\pi t/T_{vcp})\right] & 0 \leq t \leq T_{vcp}, \\ \frac{1}{2}\left\{1 + \cos\left[\pi(t - T_{vcp})/T_{vrp}\right]\right\} & T_{vcp} < t \leq T_{vcp} + T_{vrp}, \\ 0 & T_{vcp} + T_{vrp} < t \leq T_0. \end{cases}$$

(4.26)

T_0 is the duration of a cardiac cycle; T_{acp}, T_{vcp}, T_{arp}, and T_{vrp} represent the duration of atrial/ventricular contraction/relaxation, respectively; t_{ac} and t_{ar} are the times within the cardiac cycle at which atrial contraction and relaxation begin.

The flow rate through cardiac valves is modelled using the relation proposed in [102], which describes its time variation as

$$\frac{dQ_{cv}}{dt} = \frac{1}{L_{cv}} \left(\Delta P_{cv} - R_{cv}Q_{cv} - B_{cv}Q_{cv}|Q_{cv}| \right) , \tag{4.27}$$

where L_{cv}, R_{cv} and B_{cv} are coefficients for inertial terms, viscous losses and flow separation, respectively.

Pulmonary circulation is divided into arteries, capillaries and veins. Pressure in each pulmonary compartment is modelled using relation

$$P = E\Phi + S\frac{dV}{dt} , \tag{4.28}$$

where Φ is a volume constant, S is a coefficient of viscoelasticity, V is the volume of the pulmonary compartment and the elastance E is given by

$$E = E_0 e^{V/\Phi} , \tag{4.29}$$

with E_0 being a baseline elastance. Fluid is exchanged between pulmonary compartments using the second equation in (4.23). Mass fluxes are then used to update the compartment volume by imposing mass conservation.

In the next section we will describe how each of the mathematical models presented in this section are solved numerically.

4.1.3 Numerical methods

As we have seen in section 4.1.2, our closed-loop model is composed of a dimensionally heterogeneous spatial domain, comprising one-dimensional and lumped parameter models. The equations for the one-dimensional model are solved using state-of-the-art, high-order numerical schemes. Moreover, we have to deal with junctions that may connect several one-dimensional vessels and also with the coupling between one-dimensional and lumped parameter models.

Numerical scheme for one-dimensional blood flow

System (4.7) is solved using a high order finite volume-type numerical scheme. High order in space and time is mandatory because of efficiency requirements in order to achieve accurate results at a low cost, as shown in [113] and [116] for the case of one-dimensional blood flow models.

High order accuracy in space and time is achieved by adopting the ADER framework [159]. ADER finite volume schemes consist of two building blocks: a non-linear spatial reconstruction operator and solution of the Generalized Riemann Problem (GRP) at each cell interface to compute numerical fluxes [162]. See also [111] for a discussion on different GRP solvers available. For the solution of the GRP we adopt the Dumbser-Enaux-Toro (DET) solver. This solver was proposed in [64] and extended to non-conservative systems in [63] and [65]. All GRP solvers available, see [111], require a classical Riemann solver (piece-wise constant data). Here we use the Dumbser-Osher-Toro (DOT) Riemann solver [66], as proposed in [116]. The resulting high-order ADER scheme is able to treat venous collapse, as well as transcritical flows [113, 114]. For background on the ADER approach and recent developments see chapters 19 and 20 of [163] and references therein. For alternative approaches see the recent work reported in [48].

As we anticipated in section 4.1.2, in order to correctly account for the presence of *geometric-type* source terms we have chosen to adopt a reformulation of the classical equations for one-dimensional blood flow models, which implies the use of a well-balanced numerical scheme for this non-conservative system. Therefore, for the computation of a first order monotone numerical flux we use the Dumbser-Osher-Toro (DOT) Riemann solver, put forward in [66] as a modified version of the Osher-Solomon Riemann solver [128] for a conservative hyperbolic system. The DOT scheme has also been extended in [67] to deal with non-conservative hyperbolic systems.

The scheme used in this work was proposed in [116] and is a modification of the original DOT solver, that correctly solves (4.7). This solver is inspired by the mathematical theory developed

by Dal Maso, LeFloch and Murat [56] and may be seen as a path-conservative scheme, as defined in [129].

A finite volume-type path-conservative scheme may be constructed by integrating (4.7) in space and time in the control volume $[x_{i-\frac{1}{2}}, x_{i+\frac{1}{2}}] \times [t^n, t^{n+1}]$, leading to

$$\boldsymbol{Q}_i^{n+1} = \boldsymbol{Q}_i^n - \frac{\Delta t}{\Delta x}\left(\boldsymbol{D}_{i+\frac{1}{2}}^- + \boldsymbol{D}_{i-\frac{1}{2}}^+\right) + \Delta t \boldsymbol{S}_i - \Delta t \boldsymbol{G}_i^n, \tag{4.30}$$

where

$$\boldsymbol{Q}_i^n = \frac{1}{\Delta x} \int_{x_{i-\frac{1}{2}}}^{x_{i+\frac{1}{2}}} \boldsymbol{Q}(x, t^n)\, dx, \tag{4.31}$$

$$\boldsymbol{G}_i^n = \frac{1}{\Delta t \Delta x} \int_{t^n}^{t^{n+1}} \int_{x_{i-\frac{1}{2}}}^{x_{i+\frac{1}{2}}} \boldsymbol{A}(\boldsymbol{Q}) \partial_x \boldsymbol{Q}\, dx\, dt, \tag{4.32}$$

$$\boldsymbol{S}_i = \frac{1}{\Delta t \Delta x} \int_{t^n}^{t^{n+1}} \int_{x_{i-\frac{1}{2}}}^{x_{i+\frac{1}{2}}} \boldsymbol{S}(\boldsymbol{Q}(x, t))\, dx\, dt \tag{4.33}$$

and

$$\boldsymbol{D}_{i+\frac{1}{2}}^\pm = \frac{1}{\Delta t} \int_{t^n}^{t^{n+1}} \boldsymbol{\mathcal{D}}_{i+\frac{1}{2}}^\pm\left(\boldsymbol{Q}_{i+\frac{1}{2}}^-(t), \boldsymbol{Q}_{i+\frac{1}{2}}^+(t), \boldsymbol{\Psi}(s)\right) dt. \tag{4.34}$$

Here $\Delta x = x_{i+\frac{1}{2}} - x_{i-\frac{1}{2}}$; $\Delta t = t^{n+1} - t^n$; $\boldsymbol{Q}_{i+\frac{1}{2}}^\pm(t)$ are limiting data states from left and right arising in the GRP for system (4.7) at cell interface $x_{i+\frac{1}{2}}$. Given left and right data $\boldsymbol{Q}^-$ and $\boldsymbol{Q}^+$ for the Riemann problem at the cell interface $x_{i+\frac{1}{2}}$, $\boldsymbol{\mathcal{D}}^\pm(\boldsymbol{Q}^-, \boldsymbol{Q}^+, \boldsymbol{\Psi}(s))$ are defined as fluctuations that depend on a path $\boldsymbol{\Psi}(s)$. We refer the reader to [116] for a detailed description of the numerical scheme. This reference provides a detailed explanation of all the steps necessary to implement the DET solver, as well as to perform the numerical computation of fluctuations via the DOT solver.

Empirical convergence rate

In order to verify that the expected order of accuracy is reached, we perform a numerical convergence rate study. We prescribe a smooth function $\hat{\boldsymbol{Q}}(x, t)$ to be the exact solution. $\hat{\boldsymbol{Q}}(x, t)$ is

$$\hat{\boldsymbol{Q}}(x, t) = \begin{bmatrix} \hat{A}(x, t) \\ \hat{q}(x, t) \\ \hat{K}(x) \\ \hat{A}_0 \\ \hat{p}_e(x) \end{bmatrix} = \begin{bmatrix} \tilde{A} + \tilde{a}\, sin\left(\frac{2\pi}{L}x\right) cos\left(\frac{2\pi}{T_0}t\right) \\ \tilde{q} - \tilde{a}\,\frac{L}{T_0} cos\left(\frac{2\pi}{L}x\right) sin\left(\frac{2\pi}{T_0}t\right) \\ \tilde{K} + \tilde{k}\, sin\left(\frac{2\pi}{L}x\right) \\ \tilde{A}_0 + \tilde{a}_0\, sin\left(\frac{2\pi}{L}x\right) \\ \tilde{P}_e + \tilde{p}_e\, sin\left(\frac{2\pi}{L}x\right) \end{bmatrix}. \tag{4.35}$$

Replacing (4.35) into (4.7) we obtain

$$\partial_t \mathbf{Q} + \mathbf{A}(\mathbf{Q}) \partial_x \mathbf{Q} = \hat{\mathbf{S}}(x, t). \tag{4.36}$$

Source term $\hat{\mathbf{S}}(x, t)$ includes terms resulting from the fact that (4.35) is not a solution of the original system (4.7). $\hat{\mathbf{S}}(x, t)$ is computed exactly using algebraic manipulators and is not reproduced here for the sake of brevity. For the convergence rate study the following parameters are used: $L = 1.0\, m$, $T_0 = 1.0\, s$, $\tilde{A} = 4.0 \times 10^{-4}\, m^2$, $\tilde{a} = 4.0 \times 10^{-5}\, m^2$, $\tilde{q} = 0.0\, m^3\, s^{-1}$, $\tilde{K} = 50.0\, KPa$, $\tilde{k} = 500.0\, Pa$, $\tilde{P}_e = 0.0\, Pa$, $\tilde{p}_e = 50.0\, Pa$, $m = 1/2$ and $n = 0$. Since we use an explicit numerical scheme, the so called Courant-Friedrichs-Lewy (CFL) condition must be satisfied. In practice, we define our time step by ensuring that the CFL number is smaller than a given threshold. The CFL number is computed as

$$CFL = \lambda_{max}^n \frac{\Delta t}{\Delta x}, \tag{4.37}$$

where λ_{max}^n is the maximum magnitude of eigenvalues (4.12) in the entire spatial domain at time $t = t^n$. For this test we use a $CFL = 0.9$.

Table 4.1 displays the empirical convergence rates for the proposed numerical scheme up to fifth-order of accuracy in space and time. Errors were measured in the norms L_1, L_2 and L_∞. The expected convergence rates are reached for all norms. Note that highly accurate computations mean computational efficiency. For a fixed mesh a low order scheme will generally be faster than its higher order extension. On the other hand, if one fixes a given error to be acceptable, high order schemes will satisfy this requirement with considerably less computational effort. Figure 4.7 shows error versus CPU time for the second and fifth-order implementations of the ADER schemes presented in this section. The CPU time is that resulting from a sequence of successively refined meshes. It is seen that, for example, given an acceptable error of $E = 10^{-9}$, the fifth-order ADER method will be at least one order of magnitude more efficient than the second-order ADER method.

Scheme	N	L^1	L^2	L^∞	$\mathcal{O}(L^1)$	$\mathcal{O}(L^2)$	$\mathcal{O}(L^\infty)$	$t_{CPU}\,[s]$
ADER-O2	4	1.07e-05	1.23e-05	2.53e-05	-	-	-	0.14
	8	2.47e-06	2.93e-06	7.75e-06	2.1	2.1	1.7	0.42
	16	5.69e-07	6.98e-07	2.02e-06	2.1	2.1	1.9	1.53
	32	1.34e-07	1.69e-07	5.12e-07	2.1	2.0	2.0	3.27
ADER-O3	4	4.24e-06	4.79e-06	8.46e-06	-	-	-	0.39
	8	5.62e-07	6.89e-07	1.46e-06	2.9	2.8	2.5	0.86
	16	7.16e-08	8.95e-08	1.97e-07	3.0	2.9	2.9	1.90
	32	8.99e-09	1.13e-08	2.51e-08	3.0	3.0	3.0	4.13
ADER-O4	4	6.66e-06	1.64e-06	1.65e-05	-	-	-	0.68
	8	4.028e-07	4.88e-07	1.21e-06	4.0	4.0	3.8	1.36
	16	1.92e-08	2.29e-08	6.43e-08	4.4	4.4	4.2	2.24
	32	9.73e-10	1.19e-09	3.69e-09	4.3	4.3	4.1	5.89
ADER-O5	4	1.80e-06	2.02e-06	3.39e-06	-	-	-	7.20
	8	6.88e-08	8.39e-08	1.71e-07	4.7	4.6	4.3	1.38
	16	2.27e-09	2.81e-09	6.01e-09	4.9	4.9	4.8	3.64
	32	8.13e-11	9.72e-11	2.11e-10	4.8	4.9	4.8	9.08

Table 4.1: Convergence results for the ADER scheme. N is the number of cells. Errors are computed for variable A. CPU times are reported for all tests.
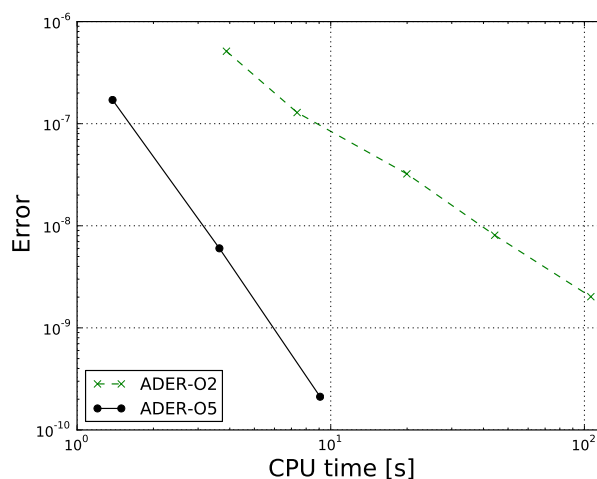
Figure 4.7: Error versus CPU time for second and fifth-order implementations of the ADER scheme.

Test with exact solution including an elastic jump

We solve a Riemann problem that intends to resemble the effect of an (idealized) Valsava manoeuvre on an internal jugular vein with incompetent valve and discontinuous mechanical properties. Note that while this test does not correspond to a physiological situation, it is still valid for testing the robustness of the numerical scheme for parameter ranges that are those of human veins.

The vessel length is $L = 0.2\,m$. Initial conditions are discontinuous at $x = 0.06\,m$. States to the left of the discontinuity are $A_L = 0.5\,A_0^L$, $U_L = 0.0\,m\,s^{-1}$, $K^L = K_{ref}$, $A_0^L = 1.0\,A_{ref}$, $p_e^L = 0.0\,mmHg$, while to the right of the discontinuity we set $A_R = 1.\,A_0^R$, $U_R = 0.0\,m\,s^{-1}$, $K^R = 10\,K_{ref}$, $A_0^R = 1.0\,A_{ref}$, $p_e^R = 20.0\,mmHg$. Reference values for vessel stiffness and cross-sectional area are $K_{ref} = 300.0\,Pa$ and $A_{ref} = 1.0 \times 10^{-4}\,m^2$. Initial conditions correspond to a vessel with discontinuous mechanical properties. Moreover, the portion of the vessel to the right of the discontinuity is compressed. Transmural pressure is sub-atmospheric to the left of the discontinuity and $20\,mmHg$ in the rest of the vessel. The exact solution of this problem was computed using an implementation of the exact Riemann solver presented in [161].

The problem was solved numerically using first and third order versions of the numerical schemes considered in this work, using 100 computational cells and a $CFL = 0.9$. Results are shown in figure 4.8. For $t > 0\,s$ an elastic jump starts travelling to the left of the initial discontinuity, while a rarefaction wave is directed in the opposite direction. Finally, a stationary contact discontinuity is observed in correspondence of discontinuous variations of mechanical properties. Both, the first and high order numerical solutions correctly capture the propagation velocity of non-linear waves (elastic jump and rarefaction) and the states to both sides of the stationary contact discontinuity. The better description of the elastic jump by the third order scheme, as compared to the one given by the first order scheme, is clearly observable.
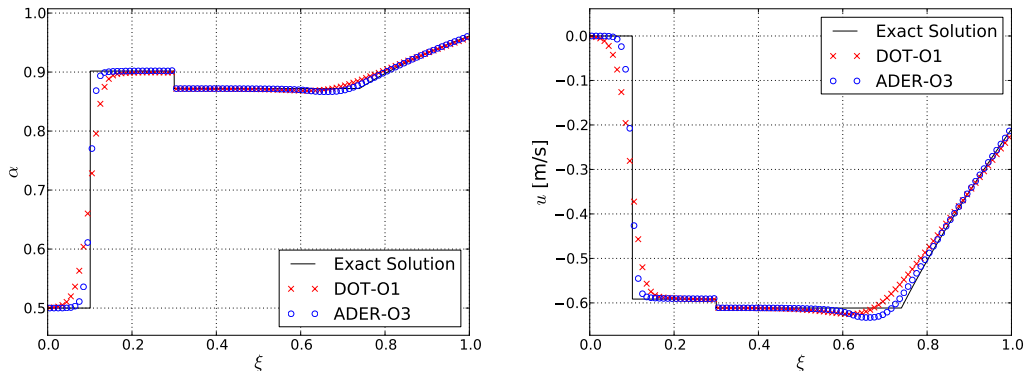
Figure 4.8: Exact solution and numerical results for the Riemann problem described in section 4.1.3 regarding the effect of an (idealized) Valsava maneuver on an internal jugular vein with incompetent valve and discontinuous mechanical properties. Results for first and third order versions of the numerical schemes used in this work. Results shown for non-dimensional cross-sectional area ($\alpha = A/A_{ref}$) (left) and velocity (right) versus non-dimensional length ($\xi = x/L$).

Junctions

The coupling of several one-dimensional vessels at branching points (for arteries) and merging points (for veins) is treated using the methodology proposed in [143], which we formulate here for the case of N_P vessels converging at node P. The computational cell involved in the coupling of the $k - th$ vessel, with $k = 1, ..., N_P$, will provide the state $Q_k^n = [A_k^n, q_k^n]^T$ at time t^n.

In order to couple the N_P vessels, we have to compute the unknowns cross-sectional area A_k^* and velocity u_k^* for each vessel converging at node P, which means that we have $2N_P$ unknowns. Quantities A_k^*, u_k^* will be used to compute fluxes at the terminal interface of the k-th vessel.

Let vessel k be discretised by N_k cells so that its local numbering is $i = 1, ..., N_k$. We define

the auxiliary function

$$g_k(I_k) = \begin{cases} 1\,, & \text{if } I_k = N_k\,, \\ -1\,, & \text{if } I_k = 1\,, \end{cases} \tag{4.38}$$

where I_k is the index of the computational cell of vessel k that converges to node P.

The first N_P equations are given by imposing conservation of mass

$$\sum_{k=1}^{N_P} g_k A_k^* u_k^* = 0 \tag{4.39}$$

and total pressure

$$p(A_1^*) + \frac{1}{2}\rho(u_1^*)^2 - p(A_k^*) - \frac{1}{2}\rho(u_k^*)^2 = 0, \quad k = 2, ..., N_P\,. \tag{4.40}$$

The remaining N_P relations are obtained by enforcing that characteristics leave the one-dimensional domain undisturbed

$$u_k^n + g_k \int_{A_{0,k}}^{A_k^n} \frac{c(\tau)}{\tau}d\tau - u_k^* - g_k \int_{A_{0,k}}^{A_k^*} \frac{c(\tau)}{\tau}d\tau = 0 \quad k = 1, ..., N_P\,. \tag{4.41}$$

Equations (4.39) to (4.41) constitute a non-linear system with $2\,N_P$ unknowns and is solved using Newton method.

The main requirements for this procedure to work are that the flow regime is sub-critical and that no elastic jumps reach node P. In fact, numerical investigations not reported in this work have shown that this algorithm fails to converge in the case of fast postural changes. Besides the lack of blood flow regulatory mechanisms, this algorithm remains the mayor limitation of the present model in order to be able to perform simulations including postural changes.

Arterioles, capillaries and venules and 1D-0D matching

For most terminal vessels, arteries are linked to veins via lumped parameter models that include arterioles, capillaries and venules, as shown in figure 4.4. We call this type of artery-vein connection a *simple connection*, since, as we will see later, some peripheral beds are formed by slightly more complex networks. The resistance of distal arteries, R_{da} is set to be equal to the characteristic impedance of the terminal artery in order to avoid non-physiological wave reflections, as suggested in [5]. The variables to be computed for each circuit are

- boundary conditions for the 1D-0D interfaces (artery-distal arteries and venule-veins): P_{art}^*, Q_{art}^*, P_{vein}^* and Q_{vein}^*,

- state variables for each lumped compartment: P_{al}, Q_{al}, P_{cp}, Q_{cp}, P_{vn} and Q_{vn}.

In order to correctly couple terminal arteries to arterioles we follow the methodology proposed in [5]. First, we impose that forward travelling waves leave the arterial domain undisturbed

$$\Gamma_5(P_{art}, Q_{art}) - \Gamma_5(P_{art}^*, Q_{art}^*) = 0\,, \tag{4.42}$$

where Γ_5 are Riemann invariants associated to forward travelling characteristics and P_{art}, Q_{art} are pressure and flow rate values for the last computational cell of the one-dimensional domain of the terminal artery. Moreover, we note that, for the pressure drop across R_{da}, the following relation must hold

$$Q_{art}^* = \frac{P_{art}^* - P_{al}}{R_{da}}\,. \tag{4.43}$$

For veins we proceed in a similar manner. Here we impose that backward traveling waves leave the domain undisturbed

$$\Gamma_1(P_{vein}, Q_{vein}) - \Gamma_1(P_{vein}^*, Q_{vein}^*) = 0\,. \tag{4.44}$$

For state variables in lumped compartments we discretise equations (4.23) using a backward Euler scheme and setting $P_{out} = P_{vein}^*$. It can be easily verified that $Q_{vein}^* = Q_{vn}$ is necessary in order to preserve mass.

Equations (4.42), (4.43), (4.44), together with a backward Euler discretization of equations (4.23) for arterioles, capillaries and venules, yield a differential-algebraic system with 9 unknowns which is solved at each time step using a Newton method.

Boundary conditions

Boundary conditions other than branching and merging points are treated using the same approach applied to junctions. That is, we impose that the characteristic that leaves the one-dimensional domain is not disturbed by boundary conditions, while we impose a given flow rate q_{bc}^* or a pressure $p(A_{bc}^*)$. In the case of fixed flow rate q_{bc}^* we compute A_{bc}^* by imposing that

$$\frac{q_{1D}^n}{A_{1D}^n} + g_{1D} \int_{A_{0,1D}}^{A_{1D}^n} \frac{c(\tau)}{\tau} d\tau - \frac{q_{bc}^*}{A_{bc}^*} - g_{1D} \int_{A_{0,1D}}^{A_{bc}^*} \frac{c(\tau)}{\tau} d\tau = 0 \,, \tag{4.45}$$

where q_{1D}^n and A_{1D}^n are flow rate and pressure at the terminal computational cell of the vessel and g_{1D} is given by (4.38). On the other hand, if we need to prescribe a pressure $p(A_{bc}^*)$, we solve (4.45) for q_{bc}^*. This type of boundary conditions is applied to the proximal end of the ascending aorta, to distal ends of terminal veins and to the proximal end of the cavas at their interface with the right atrium.

In the next section we will present all parameters necessary for the description of the arterial and venous networks, as well as for the various lumped parameter models used in this work.

4.1.4 Physiological data

One-dimensional vessels are characterized by a network topology, vessel geometry and mechanical properties. Moreover, lumped parameter models presented in section 4.1.2 make use of several parameters. In this section we present all parameters necessary for the implementation of our closed-loop model.

Geometry and parameters

Arteries. The arterial network, shown in figure 4.1, is composed by 85 arteries and was entirely taken from [101] and references therein. Table 4.3 reports geometrical parameters and wave speed c_0 assigned to each artery. Reported radii correspond to a baseline internal pressure $P_0 = 85. \, mmHg$ and therefore to $A = A_0$, as proposed in [102]. Mechanical parameters are obtained from c_0, by solving (4.11) for K, with tube law (4.16) and $A = A_0$. Table 4.2 reports the reference of location codes appearing in the next-to-last column of table 4.3.

Code	Location
1	Dural sinuses
2	Extra-cranial
3	Neck
4	Thorax
5	Abdomen
6	Upper limbs
7	Lower limbs
8	Pelvis
9	Intra-cranial

Table 4.2: Location codes indicated in tables 4.3 and 4.8.

Heart and pulmonary circulation. Parameters for heart and pulmonary circulation were taken from [102] and [154] and are reported in tables 4.4 and 4.5, respectively.

Terminal segments. Most arteries are connected to veins via a simple artery-vein connection. However, for several compartments there is a distribution of flow from one systemic artery to

multiple veins or single arteries feeding more veins. These compartments are denoted as *lumped models* A to G. Figures 4.9 to 4.11 show the corresponding circuits, whereas tables 4.6 and 4.7 report the value of parameters for each compartment.

Veins.

The venous network is shown in figure 4.2. Geometrical and mechanical parameters are reported in table 4.8. The last column of this table reports the source from which geometrical information for each venous segment was extracted. Reported radii correspond to a baseline internal pressure $P_0 = 5. \, mmHg$ and therefore to $A = A_0$. c_0 is the wave speed (4.21), from which K_v can be estimated. Note that relation (4.21) is used for all veins expect for dural sinuses, for which a $c_0 = c_{0,max}$ was used.

Since a major motivation of this work regards the study of neurovascular diseases recently linked to the venous vasculature of the head and neck, as explained in section 4.1.1, this area is described with more emphasis compared to other regions of the venous network. Most of the major veins of this region were obtained via a segmentation procedure on a patient-specific basis. Medical imaging data used in this work has been provided by the Magnetic Resonance Research Facility at the Wayne State University, Detroit, USA. In particular, we used 2D Time-of-Flight (TOF) and 3D contrast-enhanced MR-Venography (CE-MRV) sequences of the head and neck of healthy controls. Figure 4.12 (top) shows a Maximum Intensity Projection (MPI) of a TOF image for a healthy control. The geometry of major vessels was extracted using the open-source segmentation tool Vascular Modelling Toolkit (VMTK) [12]. Once the 3D domain is available, VMTK allows to compute centerlines and vessel cross-sectional area (CSA) for user-defined vessels. Figure 4.12 (bottom) shows segmentation results, as well as the centerline for a left internal jugular vein (IJV). The geometry of major head and neck veins presented in this work is from a single healthy control. The characterization of the model with patient-specific head and neck veins can be easily carried out within a few hours.

Venous valves are described by the same model used for cardiac valves, with parameters: $R = 0.003 \, mmHg \, s \, ml^{-1}$, $L = 0.0025 \, mmHg \, s^2 \, ml^{-1}$ and $B = 0.000025 \, mmHg \, s^2 \, ml^{-2}$. These parameters are similar to the ones used for cardiac valves but allow for a faster opening/closure of the venous valve. Table 4.9 shows the location of valves in the venous network.

No.	Vessel name	L [cm]	r_0 [cm]	r_1 [cm]	c_0 [m/s]	Loc.	Ref.
1	Ascending aorta	2.00	1.525	1.420	5.110	4	[102]
2	Aortic arch I	3.00	1.420	1.342	5.110	4	[102]
3	Brachiocephalic a.	3.50	0.650	0.620	5.910	4	[102]
4	R. subclavian a. I	3.50	0.425	0.407	5.290	6	[102]
5	R. carotid a.	17.70	0.400	0.370	5.920	3	[102]
6	R. vertebral a.	13.50	0.150	0.136	11.900	3	[102]
7	R. subclavian a. II	39.80	0.407	0.230	5.380	6	[102]
8	R. radius	22.00	0.175	0.140	10.120	6	[102]
9	R. ulnar a. I	6.70	0.215	0.215	8.780	6	[102]
10	Aortic arch II	4.00	1.342	1.246	5.110	4	[102]
11	L. carotid a.	20.80	0.400	0.370	5.920	3	[102]
12	Thoracic aorta I	5.50	1.246	1.124	5.110	4	[102]
13	Thoracic aorta II	10.50	1.124	0.924	5.110	4	[102]
14	Intercostal a.	7.30	0.300	0.300	7.130	4	[102]
15	L. subclavian a. I	3.50	0.425	0.407	5.290	6	[102]
16	L. vertebral a.	13.50	0.150	0.136	11.900	3	[102]
17	L. subclavian a. II	39.80	0.407	0.230	5.380	6	[102]
18	L. ulnar a. I	6.70	0.215	0.215	8.780	6	[102]
19	L. radius	22.00	0.175	0.140	10.120	6	[102]
20	Celiac a. I	2.00	0.350	0.300	5.860	5	[102]
21	Celiac a. II	2.00	0.300	0.250	6.540	5	[102]
22	Hepatic a.	6.50	0.275	0.250	6.860	5	[102]
23	Splenic a.	5.80	0.175	0.150	7.220	5	[102]
24	Gastric a.	5.50	0.200	0.200	6.400	5	[102]
25	Abdominal aorta I	5.30	0.924	0.838	5.110	5	[102]
26	Sup. mesenteric a.	5.00	0.400	0.350	5.770	5	[102]
27	Abdominal aorta II	1.50	0.838	0.814	5.110	5	[102]
28	R. renal a.	3.00	0.275	0.275	6.050	5	[102]
29	Abdominal aorta III	1.50	0.814	0.792	5.110	5	[102]
30	L. renal a.	3.00	0.275	0.275	6.050	5	[102]
31	Abdominal aorta IV	12.50	0.792	0.627	5.110	5	[102]
32	Inf. mesenteric a.	3.80	0.200	0.175	6.250	5	[102]
33	Abdominal aorta V	8.00	0.627	0.550	5.110	5	[102]
34	R. com. iliac a.	5.80	0.400	0.370	5.500	8	[102]
35	R. ext. iliac a.	14.50	0.370	0.314	7.050	8	[102]
36	R. int. iliac a.	4.50	0.200	0.200	10.100	8	[102]
37	R. deep femoral a.	11.30	0.200	0.200	7.880	7	[102]
38	R. femoral a.	44.30	0.314	0.275	8.100	7	[102]
39	R. ext. carotid a. I	4.10	0.200	0.150	8.900	2	[102]
40	L. int. carotid a. I	17.60	0.250	0.200	7.900	3	[102]
41	R. post. tibial a.	34.40	0.175	0.175	11.980	7	[102]
42	R. ant. tibial a.	32.20	0.250	0.250	9.780	7	[102]
43	R. interosseous a.	7.00	0.100	0.100	15.570	6	[102]
44	R. ulnar a. II	17.00	0.203	0.180	12.530	6	[102]
45	L. ulnar a. II	17.00	0.203	0.180	12.530	6	[102]
46	L. interosseous a.	7.00	0.100	0.100	15.570	6	[102]
47	R. int. carotid a. I	17.60	0.250	0.200	7.900	3	[102]
48	L. ext. carotid a. I	4.10	0.200	0.150	8.900	3	[102]
49	L. com. iliac a.	5.80	0.400	0.370	5.500	8	[102]
50	L. ext. iliac a.	14.50	0.370	0.314	7.050	8	[102]
51	L. int. iliac a.	4.50	0.200	0.200	10.100	8	[102]
52	L. deep femoral a.	11.30	0.200	0.200	7.880	7	[102]
53	L. femoral a.	44.30	0.314	0.275	8.100	7	[102]
54	L. post. tibial a.	34.40	0.175	0.175	11.980	7	[102]
55	L. ant. tibial a.	32.20	0.250	0.250	9.780	7	[102]
56	Basilar a.	2.90	0.162	0.162	9.330	1	[101]
57	R. post. cerebral. a. I	0.50	0.107	0.107	12.930	1	[101]
58	R. post. cerebral. a. II	8.60	0.105	0.105	13.130	1	[101]
59	R. post. communicating a.	1.50	0.073	0.073	17.240	1	[101]
60	R. int. carotid a. II	0.50	0.200	0.200	8.260	1	[101]
61	R. mid. cerebral a.	11.90	0.143	0.143	10.230	1	[101]
62	R. ant. cerebral a. I	1.20	0.117	0.117	12.030	1	[101]
63	R. ant. cererbal a. II	10.30	0.120	0.120	11.770	1	[101]
64	Ant. communicating a.	0.30	0.100	0.100	17.080	1	[101]
65	L. ant. cerebral a. II	10.30	0.120	0.120	11.770	1	[101]
66	L. ant. cerebral a. I	1.20	0.117	0.117	12.030	1	[101]
67	L. mid. cerebral a.	11.90	0.143	0.143	10.230	1	[101]
68	L. int. carotid a. II	0.50	0.200	0.200	8.260	1	[101]
69	L. post. communicating a.	1.50	0.073	0.073	17.240	1	[101]
70	L. post. cerebral a. II	8.60	0.105	0.105	13.130	1	[101]
71	L. post. cerebral a. I	0.50	0.107	0.107	12.930	1	[101]
72	L. ext. carotid a. II	6.10	0.200	0.200	8.530	3	[101]
73	R. ext. carotid a. II	6.10	0.200	0.200	8.530	3	[101]
74	L. sup. thyroid a.	10.10	0.100	0.100	16.570	3	[101]
75	R. sup. thyroid a.	10.10	0.100	0.100	16.570	3	[101]
76	L. superf. temporal a.	6.10	0.160	0.160	9.620	2	[101]
77	R. superf. temporal a.	6.10	0.160	0.160	9.620	2	[101]
78	L. maxillary a.	9.10	0.110	0.110	15.090	2	[101]
79	R. maxillary a.	9.10	0.110	0.110	15.090	2	[101]
80	L. superf. temp. fron. bran.	10.00	0.110	0.110	15.090	2	[101]
81	R. superf. temp. fron. bran.	10.00	0.110	0.110	15.090	2	[101]
82	L. superf. temp. pari. bran.	10.10	0.110	0.110	15.090	2	[101]
83	R. superf. temp. pari. bran	10.10	0.110	0.110	15.090	2	[101]
169	R. facial a.	11.60	0.130	0.130	15.090	2	[101]
170	L. facial a.	11.60	0.130	0.130	15.090	2	[101]

Table 4.3: Physiological data for arteries, taken from [101] and references therein. L: length; r_0: inlet radius; r_1: outlet radius; c_0: wave speed for $A = A_0$; *Loc*: location in the body according to table 4.2; *Ref*: bibliographic source.

	RA	RV	LA	LV	TriV	PulV	MitV	AorV
E_A [$mmHg\,ml^{-1}$]	0.06	0.55	0.07	2.75	–	–	–	–
E_B [$mmHg\,ml^{-1}$]	0.05	0.05	0.09	0.08	–	–	–	–
T_{cp} [s]	0.17	0.30	0.17	0.30	–	–	–	–
T_{rp} [s]	0.17	0.15	0.17	0.15	–	–	–	–
t_c [s]	0.80	0.00	0.80	0.00	–	–	–	–
t_r [s]	0.97	0.30	0.97	0.30	–	–	–	–
S [$mmHg\,s\,ml^{-1}$]	$P_{ra} \times 0.00050$	$P_{rv} \times 0.00050$	$P_{la} \times 0.00050$	$P_{lv} \times 0.00050$	–	–	–	–
B [$mmHg\,s^2\,ml^{-2}$]	–	–	–	–	0.000016	0.000025	0.000016	0.000025
R [$mmHg\,s\,ml^{-1}$]	–	–	–	–	0.001	0.003	0.001	0.003
L [$mmHg\,s^2\,ml^{-1}$]	–	–	–	–	0.0002	0.0005	0.0002	0.0005

Table 4.4: Parameters for heart chambers and cardiac valves, modified from [101] and references therein. RA: right atrium; RV: right ventricle; LA: left atrium; LV: left ventricle; $TriV$: tricuspid valve; $PulV$: pulmonary valve; $MitV$: mitral valve; $AorV$: aortic valve.

	E_0 [$mmHg\,ml^{-1}$]	Φ [ml]	R [$mmHg\,s\,ml^{-1}$]	L [$mmHg\,s^2\,ml^{-1}$]	S [$mmHg\,s\,ml^{-1}$]
Artery	0.02	20.0	0.040	0.0005	0.01
Capillary	0.02	60.0	0.040	0.0005	0.01
Vein	0.02	200.0	0.005	0.0005	0.01

Table 4.5: Parameters for pulmonary circulation, modified from [101] and [154]. E_0: baseline elastance; Φ: volume constant; R: resistance; L: inductance; S: viscoelasticity.

A. index	V. index	R_{da}	R_{al}	L_{al}	C_{al}	R_{cp}	L_{cp}	C_{cp}	R_{vn}	L_{vn}	C_{vn}
8	187	13.5055	17.0300	0.0180	0.0140	6.5500	0.0029	0.0014	2.1000	0.0052	0.0430
43	188	39.4048	393.7000	0.0700	0.0043	151.4000	0.0117	0.0004	48.5000	0.0209	0.0129
44	189	9.9182	19.6900	0.0180	0.0140	7.5700	0.0029	0.0014	2.4200	0.0052	0.0430
45	190	9.9182	19.6900	0.0180	0.0140	7.5700	0.0029	0.0014	2.4200	0.0052	0.0430
46	191	39.4048	393.7000	0.0700	0.0043	151.4000	0.0117	0.0004	48.5000	0.0209	0.0129
19	192	13.5055	17.0300	0.0180	0.0140	6.5500	0.0029	0.0014	2.1000	0.0052	0.0430
41	251	9.9001	30.4400	0.0210	0.0500	11.7100	0.0035	0.0010	3.7500	0.0062	0.0310
42	214	3.9602	14.0300	0.0140	0.1150	5.4000	0.0023	0.0023	1.7300	0.0042	0.0680
37	179	4.9857	13.3700	0.0140	0.1150	5.1400	0.0023	0.0023	1.6500	0.0042	0.0680
55	215	3.9602	14.0300	0.0140	0.1150	5.4000	0.0023	0.0023	1.7300	0.0042	0.0680
54	256	9.9001	30.4400	0.0210	0.0500	11.7100	0.0035	0.0010	3.7500	0.0062	0.0310
52	180	4.9857	13.3700	0.0140	0.1150	5.1400	0.0023	0.0023	1.6500	0.0042	0.0680
36	184	6.3903	23.4800	0.0180	0.0182	9.0300	0.0030	0.0014	2.8900	0.0054	0.1080
51	183	6.3903	23.4800	0.0180	0.0182	9.0300	0.0030	0.0014	2.8900	0.0054	0.1080
32	211	4.8972	30.7400	0.0200	0.0178	11.8500	0.0033	0.0011	3.7800	0.0060	0.0330
28	208	2.0247	4.3100	0.0080	0.0680	1.6600	0.0014	0.0067	0.5300	0.0024	0.2000
30	207	2.0247	4.3100	0.0080	0.0680	1.6600	0.0014	0.0067	0.5300	0.0024	0.2000
169	234	22.5976	119.6200	0.0170	0.0150	46.0070	0.0029	0.0015	14.7220	0.0051	0.0450
170	235	22.5976	119.6200	0.0170	0.0150	46.0070	0.0029	0.0015	14.7220	0.0051	0.0450
14	250	2.0050	5.6100	0.0090	0.1390	2.1600	0.0015	0.0139	0.6900	0.0027	0.4170

Table 4.6: Parameters for simple artery-vein connections, modified from [101] and references therein. The first two columns show the indexes of the linked artery and the linked vein, according to tables 4.3 and 4.8. The third column shows the resistance of distal arteries R_{da} [$mmHg\,s\,ml^{-1}$], while the remaining columns report resistance R [$mmHg\,s\,ml^{-1}$], inductance L [$mmHg\,s^2\,ml^{-1}$] and capacitance C [$ml\,mmHg^{-1}$] for arterioles, capillaries and venules respectively.
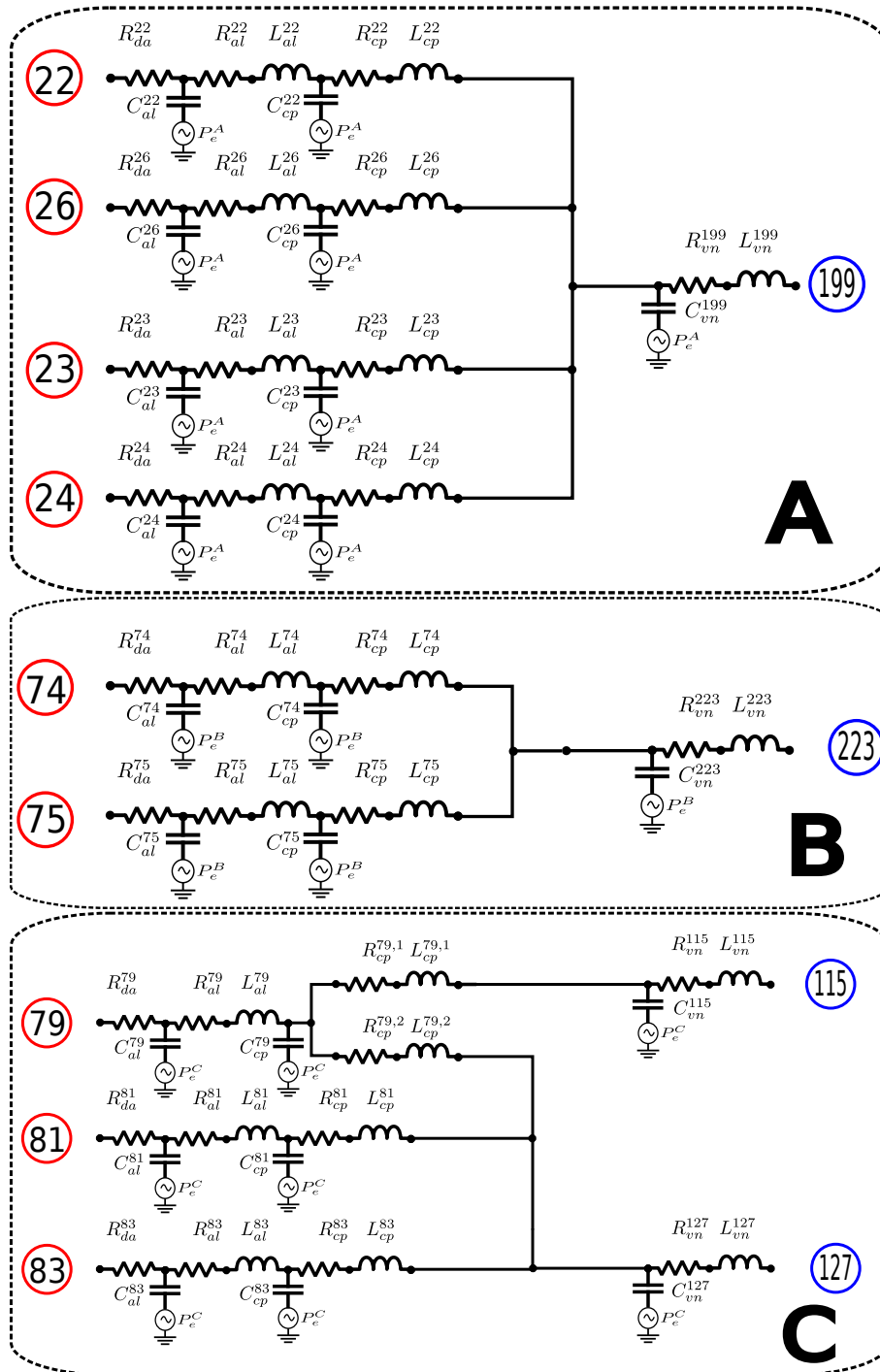
Figure 4.9: Lumped models A to C. The figure shows the indexes of feeding arteries, to the left, and collecting veins, to the right. Parameters for resistances, inductors and capacitors are found in table 4.7.
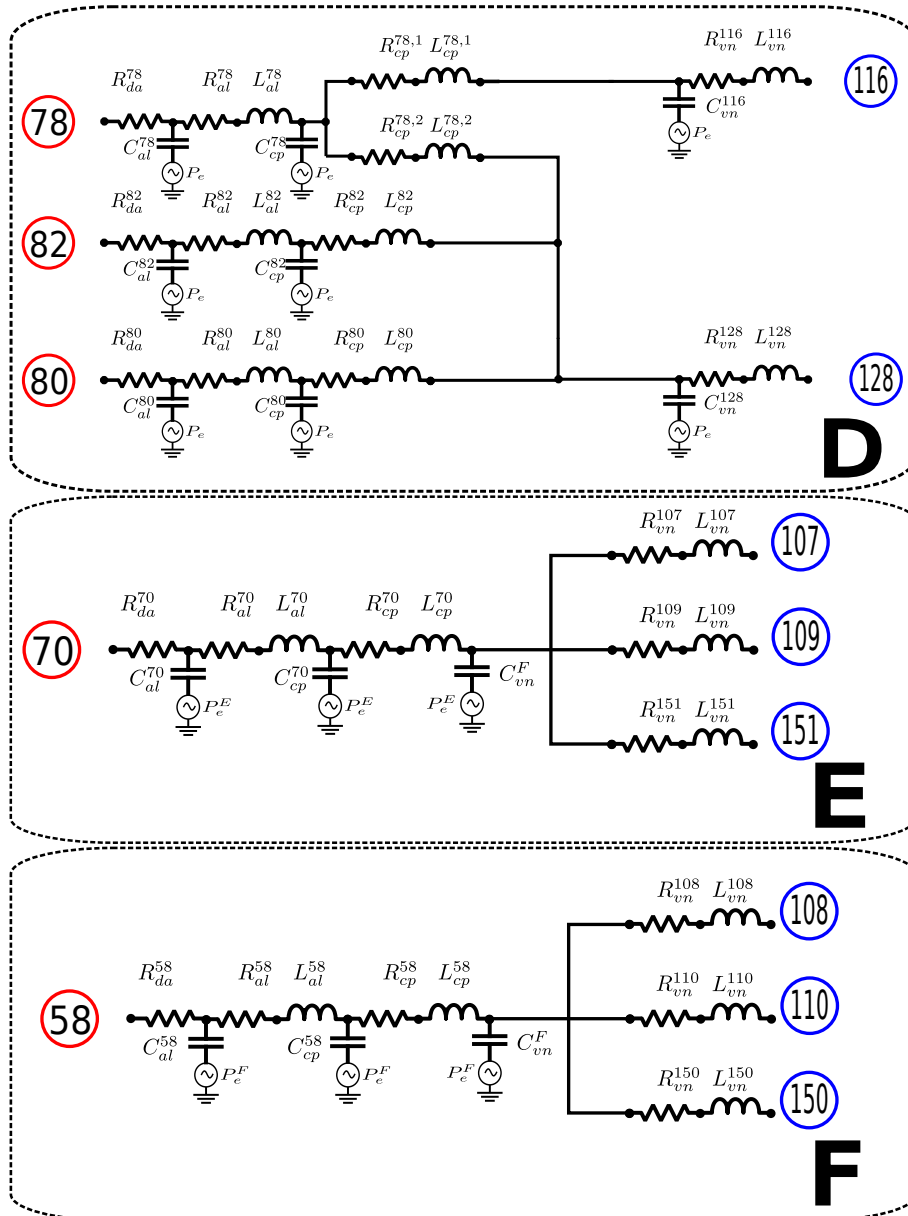
Figure 4.10: Lumped models D to F. The figure shows the indexes of feeding arteries, to the left, and collecting veins, to the right. Parameters for resistances, inductors and capacitors are found in table 4.7.
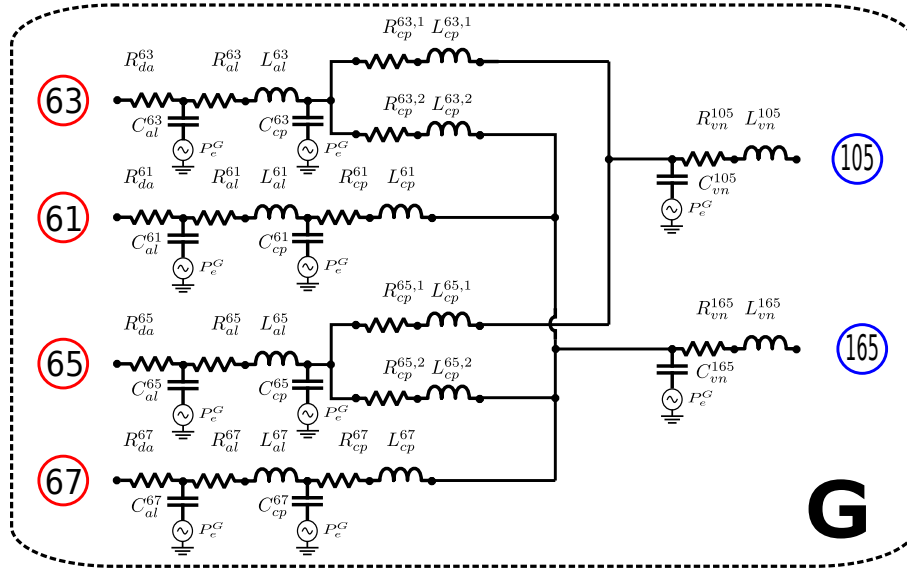
Figure 4.11: Lumped model G. The figure shows the indexes of feeding arteries, to the left, and collecting veins, to the right. Parameters for resistances, inductors and capacitors are found in table 4.7.

Parent/daughter vessel	R_{da}	R_{al}	L_{al}	C_{al}	R_{cp}	L_{cp}	C_{cp}	R_{vn}	L_{vn}	C_{vn}
Lumped model A										
22	2.7594	16.2400	0.0150	0.0210	6.2400	0.0024	0.0021	–	–	–
26	1.1634	3.8500	0.0070	0.0810	1.4800	0.0012	0.0081	–	–	–
23	7.8931	21.3300	0.0180	0.0140	8.2000	0.0030	0.0014	–	–	–
24	4.0493	8.9100	0.0120	0.0330	3.4300	0.0019	0.0032	–	–	–
199	–	–	–	–	–	–	–	0.2550	0.0013	0.5270
Lumped model B										
74	41.9356	119.6200	0.0878	0.0037	46.0070	0.0140	0.0004	–	–	–
75	41.9356	119.6200	0.0878	0.0037	46.0070	0.0140	0.0004	–	–	–
223	–	–	–	–	–	–	–	7.3610	0.0129	0.0225
Lumped model C										
79	31.5620	101.8600	0.0748	0.0037	78.3560	0.0244	0.0004	–	–	–
	–	–	–	–	78.3560	0.0244	–	–	–	–
81	31.5620	101.8600	0.0748	0.0037	39.1780	0.0122	0.0004	–	–	–
83	31.5620	102.5100	0.0753	0.0037	39.4200	0.0123	0.0004	–	–	–
115	–	–	–	–	–	–	–	25.0740	0.0440	0.0056
127	–	–	–	–	–	–	–	5.0260	0.0088	0.0281
Lumped model D										
78	31.5620	101.8600	0.0748	0.0037	78.3560	0.0244	0.0004	–	–	–
	–	–	–	–	78.3560	0.0244	–	–	–	–
82	31.5620	101.8600	0.0748	0.0037	39.1780	0.0122	0.0004	–	–	–
80	31.5620	102.5100	0.0753	0.0037	39.4200	0.0123	0.0004	–	–	–
116	–	–	–	–	–	–	–	25.0740	0.0440	0.0056
128	–	–	–	–	–	–	–	5.0260	0.0088	0.0281
Lumped model E										
70	30.1402	18.7300	0.0138	0.0070	7.2000	0.0022	0.0007	–	–	–
common param.	–	–	–	–	–	–	–	–	–	0.0018
107	–	–	–	–	–	–	–	18.4400	0.0324	–
109	–	–	–	–	–	–	–	18.4400	0.0324	–
151	–	–	–	–	–	–	–	3.0700	0.0054	–
Lumped model F										
58	30.1402	18.7300	0.0138	0.0070	7.2000	0.0022	0.0007	–	–	–
common param.	–	–	–	–	–	–	–	–	–	0.0018
108	–	–	–	–	–	–	–	18.4400	0.0324	–
110	–	–	–	–	–	–	–	18.4400	0.0324	–
150	–	–	–	–	–	–	–	3.0700	0.0054	–
Lumped model G										
63	20.6859	24.4500	0.0179	0.0070	18.8100	0.0059	0.0007	–	–	–
	–	–	–	–	18.8100	0.0059	–	–	–	–
65	20.6859	24.4500	0.0179	0.0070	18.8100	0.0059	0.0007	–	–	–
61	12.6609	10.5700	0.0078	0.0140	18.8100	0.0059	0.0014	–	–	–
	–	–	–	–	4.0700	0.0013	–	–	–	–
67	12.6609	10.5700	0.0078	0.0140	4.0700	0.0013	0.0014	–	–	–
105	–	–	–	–	–	–	–	3.7800	0.0066	0.0210
165	–	–	–	–	–	–	–	0.6900	0.0016	0.0210

Table 4.7: Parameters for complex artery-vein connections, shown in figures 4.9 to 4.11, derived from [102]. Parameter units are the same as the ones used in table 4.6.
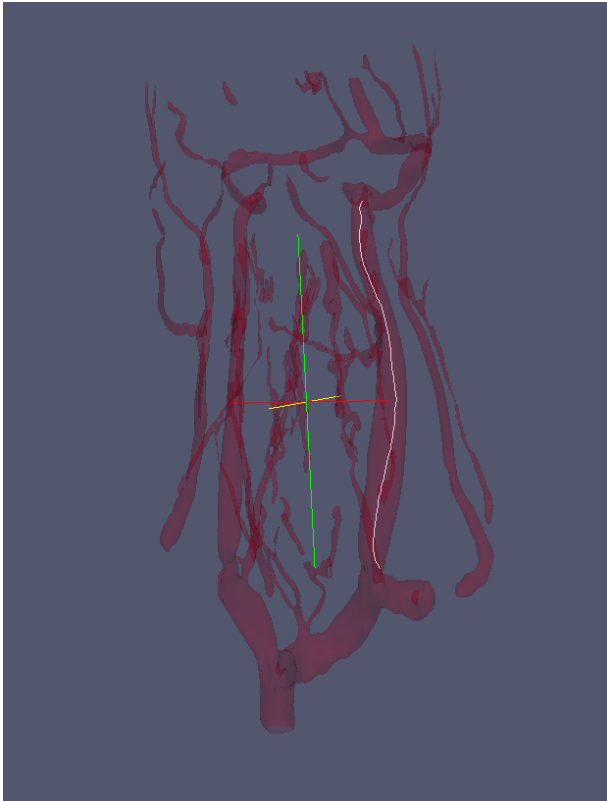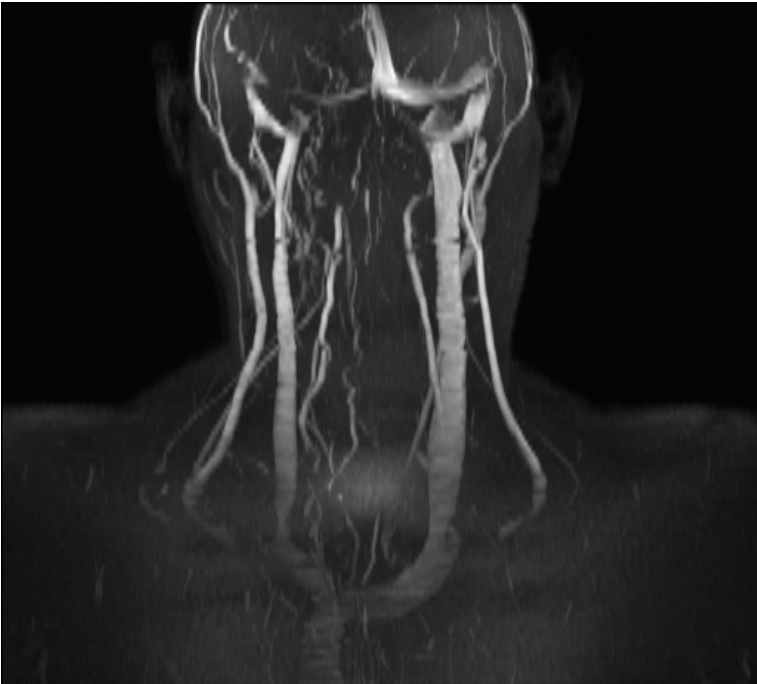
Figure 4.12: MIP-TOF for a healthy patient (top) and patient-specific segmented geometry and centerline extraction for head and neck veins (bottom).

Table 4.8: Geometrical and mechanical parameters for the venous system. L: length; r_0: inlet radius; r_1: outlet radius; c_0: wave speed for $A = A_0$; *Loc* location in the body according to table 4.2; *Ref* : bibliographic source or MRI imaging segmented geometry.

No.	Vessel name	L [cm]	r_0 [cm]	r_1 [cm]	c_0 [m/s]	Loc.	Ref.
84	Sup. vena cava I	1.50	0.800	0.800	1.000	4	MRI
85	Sup. vena cava II	2.00	0.800	0.800	1.000	4	MRI
86	R. brachiocephalic v.	4.00	0.564	0.564	1.360	4	MRI
87	L. brachiocephalic v.	7.50	0.535	0.535	1.410	4	MRI
88	L. subclavian v. I	3.00	0.564	0.564	1.360	6	[74], [141]
89	R. subclavian v. I	3.00	0.564	0.564	1.360	6	[74], [141]
90	R. ext. jugular v.	20.00	0.252	0.252	2.022	3	MRI
91	L. ext. jugular v.	20.00	0.252	0.357	1.883	3	MRI
92	R. int. jugular v. I	2.50	0.399	0.399	1.669	3	MRI
93	L. int. jugular v. I	2.50	0.564	0.618	1.315	3	MRI
94	L. vertebral v. II	11.00	0.138	0.160	2.381	3	MRI
95	R. vertebral v. II	11.00	0.138	0.160	2.381	3	MRI
96	R. deep cervical v.	13.00	0.160	0.160	2.333	3	MRI
97	L. deep cervical v.	13.00	0.160	0.160	2.333	3	MRI
98	Vertebral venous plexus	71.00	0.368	0.368	1.735	3	[153]
99	R. sigmoid sinus II	3.50	0.252	0.252	3.000	1	MRI
100	L. sigmoid sinus II	3.50	0.357	0.378	3.000	1	MRI
101	R. trans. sinus I	3.50	0.218	0.178	3.000	1	MRI
102	L. trans. sinus I	3.50	0.437	0.309	3.000	1	MRI
103	Sup. sagittal sinus I	10.00	0.319	0.367	3.000	1	MRI
104	Straight sinus	4.00	0.250	0.250	3.000	1	MRI
105	Inf. sagittal sinus	11.00	0.160	0.160	3.000	1	MRI
106	Vein of Galen	1.60	0.309	0.400	1.765	9	MRI
107	L. int. cerebral v.	5.00	0.126	0.126	2.494	9	MRI
108	R. int. cerebral v.	5.00	0.126	0.126	2.494	9	MRI
109	L. basal v. of Rosenthal I	1.00	0.126	0.126	2.494	9	MRI
110	R. basal v. of Rosenthal I	1.00	0.126	0.126	2.494	9	MRI
111	R. sup. petrosal sinus	5.70	0.149	0.149	3.000	1	MRI
112	L. sup. petrosal sinus	5.70	0.149	0.149	3.000	1	MRI
113	R. inf. petrosal sinus	3.20	0.080	0.160	3.000	1	MRI
114	L. inf. petrosal sinus	3.20	0.080	0.160	3.000	1	MRI
115	R. post. auricular v.	5.00	0.080	0.080	3.000	2	MRI
116	L. post. auricular v.	5.00	0.080	0.080	3.000	2	MRI
117	R. post. retromandibular v.	3.52	0.250	0.250	2.028	2	[174]
118	L. post. retromandibular v.	3.52	0.250	0.250	2.028	2	[174]
119	R. ant. retromandibular v.	3.15	0.235	0.235	2.072	2	[174]
120	L. ant. retromandibular v.	3.15	0.235	0.235	2.072	2	[174]
121	R. retromandibular v.	4.50	0.260	0.260	2.000	2	[174]
122	L. retromandibular v.	4.50	0.260	0.260	2.000	2	[174]
123	R. facial v. II	6.00	0.132	0.178	2.355	2	MRI
124	L. facial v. II	6.00	0.132	0.178	2.355	2	MRI
125	R. com. facial v.	0.90	0.180	0.180	2.255	2	MRI
126	L. com. facial v.	0.90	0.180	0.180	2.255	2	MRI
127	R. superf. temp. v.	5.00	0.190	0.190	2.218	2	[174]
128	L. superf. temp. v.	5.00	0.190	0.190	2.218	2	[174]
129	R. maxillary v.	1.00	0.175	0.175	2.274	2	[174], MRI
130	L. maxillary v.	1.00	0.175	0.175	2.274	2	[174], MRI
131	R. deep facial v.	0.90	0.250	0.250	2.028	2	–
132	L. deep facial v.	0.90	0.250	0.250	2.028	2	–
133	R. emissary v.	3.00	0.100	0.100	2.667	2	[155]
134	L. emissary v.	3.00	0.100	0.100	2.667	2	[155]
135	R. pterygoid plexus	0.90	0.150	0.150	2.376	2	[147]
136	L. pterygoid plexus	0.90	0.150	0.150	2.376	2	[147]
137	R. marginal sinus	4.00	0.100	0.100	3.000	1	[43]
138	L. marginal sinus	4.00	0.100	0.100	3.000	1	[43]
139	Occipittal sinus	3.50	0.235	0.235	3.000	1	[19]
141	R. mastoid emissary v.	7.20	0.175	0.175	2.274	2	[175, 105]
142	L. mastoid emissary v.	7.20	0.175	0.175	2.274	2	[175, 105]
143	R. post. condylar v.	3.00	0.315	0.315	1.857	2	MRI, [43]
144	L. post. condylar v.	3.00	0.315	0.315	1.857	2	MRI, [43]
145	R. subocc. sinus	1.00	0.450	0.450	1.566	2	[43]
146	R. lat. ant. condylar v.	3.00	0.315	0.315	1.857	2	[43]
147	L. lat. ant. condylar v.	3.00	0.315	0.315	1.857	2	[43]
150	R. Labbe v.	5.00	0.126	0.126	2.494	9	MRI
151	L. Labbe v.	5.00	0.126	0.126	2.494	9	MRI
154	L. cavernous sinus	1.50	0.100	0.100	3.000	1	MRI
155	R. cavernous sinus	1.50	0.100	0.100	3.000	1	MRI
156	Occipittal v.	5.00	0.126	0.126	2.494	2	MRI
160	Azygos v. I	2.00	0.425	0.425	1.616	4	MRI, [95]
163	R. vertebral v. I	5.00	0.160	0.160	2.333	3	MRI
164	L. vertebral v. I	5.00	0.160	0.160	2.333	3	MRI
165	Sup. sagittal sinus III	13.00	0.200	0.319	3.000	1	MRI
166	L. subocc. sinus	1.00	0.450	0.450	1.566	2	[43]
167	R. anastomotic v.	2.00	0.100	0.100	2.667	3	[43], [13]
168	L. anastomotic v.	2.00	0.100	0.100	2.667	3	[43], [13]
171	R. great saphenous v. I	7.50	0.222	0.230	2.100	7	[179], [6]
172	L. great saphenous v. I	7.50	0.222	0.230	2.100	7	[179], [6]
173	L. post. tibial v. I	17.30	0.150	0.150	2.376	7	[94], [6]
174	L. ant. tibial v. I	16.00	0.150	0.150	2.376	7	[94], [6]
175	R. popliteal v.	19.00	0.340	0.340	1.798	7	[82], [6]
176	L. popliteal v.	19.00	0.340	0.340	1.798	7	[82], [6]
177	L. femoral v.	25.40	0.350	0.350	1.775	7	[82], [6]
178	R. femoral v.	25.40	0.350	0.350	1.775	7	[82], [6]
179	R. deep femoral v.	12.60	0.350	0.350	1.775	7	[6]
180	L. deep femoral v.	12.60	0.350	0.350	1.775	7	[6]
181	R. ext. iliac v.	14.40	0.500	0.500	1.472	8	[82], [6]
182	L. ext. iliac v.	14.40	0.500	0.500	1.472	8	[82], [6]
183	L. int. iliac v.	5.00	0.150	0.150	2.376	8	[82], [6]
184	R. int. iliac v.	5.00	0.150	0.150	2.376	8	[82], [6]
185	R. com. iliac v. II	2.00	0.575	0.575	1.342	8	[126], [6]
186	L. com. iliac v. II	2.00	0.575	0.575	1.342	8	[126], [6]
187	R. radial v.	40.60	0.200	0.200	2.184	6	[6]
188	L. interosseous v.	7.00	0.100	0.100	2.667	6	[6]
189	R. ulnar v. II	30.60	0.200	0.200	2.184	6	[6]
190	L. ulnar v. II	30.60	0.200	0.200	2.184	6	[6]
191	L. interosseous v.	7.00	0.100	0.100	2.667	6	[6]
192	L. radial v.	40.60	0.200	0.200	2.184	6	[6]
193	L. subclavian v. III	27.00	0.520	0.520	1.437	6	[74], [141]
194	R. subclavian v. III	27.00	0.520	0.520	1.437	6	[74], [141]
195	L. subclavian v. II	3.00	0.520	0.520	1.437	6	[74], [141]
196	R. subclavian v. II	3.00	0.520	0.520	1.437	6	[74], [141]
197	L. ulnar v. I	10.00	0.200	0.200	2.184	6	[6]
198	Inf. vena cava I	2.00	0.762	0.762	1.053	5	[57], [6]
199	Hepatic v.	6.80	0.485	0.485	1.500	5	[59], [6]

Table 4.8 – continued from previous page

No.	Vessel name	L [cm]	r_0 [cm]	r_1 [cm]	c_0 [m/s]	Loc.	Ref.
200	Inf. vena cava II	1.50	0.762	0.762	1.053	5	[57], [6]
201	inf. vena cava III	1.50	0.762	0.762	1.053	5	[57], [6]
202	Inf. vena cava IV	12.50	0.762	0.762	1.053	5	[57], [6]
203	Inf. vena cava V	8.00	0.762	0.762	1.053	5	[57], [6]
204	R. com. iliac v. I	3.80	0.575	0.575	1.342	8	[126], [6]
205	L. com. iliac v. I	3.80	0.575	0.575	1.342	8	[126], [6]
206	R. ulnar v. I	10.00	0.200	0.200	2.184	6	[6]
207	L. renal v.	3.20	0.250	0.250	2.028	5	[6]
208	R. renal v.	3.20	0.250	0.250	2.028	5	[6]
209	Ascending lumbar v.	23.00	0.200	0.200	2.184	5	[147]
210	hemiazygos v.	23.00	0.280	0.280	1.946	5	[147]
211	Inf. mesenteric v.	6.00	0.450	0.450	1.566	5	[6]
212	R. post. tibial v. I	17.30	0.150	0.150	2.376	7	[94], [6]
213	R. ant. tibial v. I	16.00	0.150	0.150	2.376	7	[94], [6]
214	R. ant. tibial v. II	2.00	0.600	0.600	1.300	7	[94], [6]
215	L. ant. tibial v. II	2.00	0.600	0.600	1.300	7	[94], [6]
216	R. lumbar v.	3.80	0.100	0.100	2.667	5	[147]
217	L. lumbar v.	3.80	0.100	0.100	2.667	5	[147]
218	R. sup. thyroid v.	4.00	0.150	0.150	2.376	3	MRI, [173]
219	L. sup. thyroid v.	4.00	0.150	0.150	2.376	3	MRI, [173]
220	R. mid. thyroid v.	3.00	0.100	0.100	2.667	3	MRI, [173]
221	L. mid. thyroid v.	3.00	0.100	0.100	2.667	3	MRI, [173]
222	Inf. thyroid v.	7.00	0.126	0.126	2.494	3	MRI
223	Thyroid connection	2.00	0.160	0.160	2.333	3	–
224	R. int. jugular v. II	3.00	0.357	0.357	1.759	3	MRI
225	L. int. jugular v. II	3.00	0.564	0.564	1.360	3	MRI
226	R. int. jugular v. III	2.70	0.252	0.357	1.883	3	MRI
227	L. int. jugular v. III	2.70	0.564	0.564	1.360	3	MRI
228	R. int. jugular v. IV	6.80	0.252	0.252	2.022	3	MRI
229	L. int. jugular v. IV	6.80	0.399	0.564	1.506	3	MRI
230	R. sigmoid sinus I	1.50	0.252	0.252	3.000	1	MRI
231	L. sigmoid sinus I	1.50	0.378	0.399	3.000	1	MRI
232	R. trans. sinus II	3.50	0.178	0.252	3.000	1	MRI
233	L. trans. sinus II	3.50	0.309	0.357	3.000	1	MRI
234	R. facial v. I	2.00	0.113	0.132	2.514	2	MRI
235	L. facial v. I	2.00	0.113	0.132	2.514	2	MRI
236	Sup. sagittal sinus II	2.00	0.319	0.319	3.000	1	MRI
240	Intra-cavernous sinus	2.00	0.126	0.126	3.000	1	[147], [43]
242	R. int. jugular v. V	1.00	0.399	0.399	1.669	3	MRI
243	L. int. jugular v. V	1.00	0.618	0.618	1.271	3	MRI
244	Azygos v. II	28.00	0.425	0.425	1.616	4	MRI, [95]
245	Inf. vena cava VI	13.30	0.762	0.762	1.053	5	[126], [6]
246	L. basal v. of Rosenthal II	7.00	0.126	0.126	2.494	9	MRI
247	R. basal v. of Rosenthal II	7.00	0.126	0.126	2.494	9	MRI
250	Intercostal v.	2.00	0.400	0.400	1.667	4	[147]
251	R. post. tibial v. II	17.30	0.150	0.150	2.376	7	[94], [6]
252	R. ant. tibial v. II	16.00	0.150	0.150	2.376	7	[94], [6]
253	R. great saphenous v. II	37.50	0.145	0.188	2.308	7	[179], [6]
254	L. great saphenous v. II	37.50	0.145	0.188	2.308	7	[179], [6]
255	L. ant. tibial v. II	16.00	0.150	0.150	2.376	7	[94], [6]
256	L. post. tibial v. I	17.30	0.150	0.150	2.376	7	[94], [6]
257	R. great saphenous v. III	30.00	0.188	0.222	2.168	7	[179], [6]
258	L. great saphenous v. III	30.00	0.188	0.222	2.168	7	[179], [6]
259	Confluence of sinuses	1.00	0.010	0.010	3.000	1	MRI

No.	Left vessel index	Right vessel index
1	193	195
2	194	196
3	244	160
4	257	171
5	258	172
6	253	257
7	254	258
8	175	178
9	176	177
10	251	212
11	256	173
12	252	213
13	255	174
14	92	242
15	93	243

Table 4.9: Location of valves in the venous network shown in figure 4.2. Valves allow flow from left to right vessel.

Flow measurements

In addition to morphological data, Phase-Contrast (PC) MRI flow quantification data was gathered by the MR Research Facility at the Wayne State University, Detroit (USA) and made

available for the validation of our model. Flow was acquired in the neck at three levels and for dural sinuses, including the Superior Sagittal Sinus, the Straight Sinus and both Transverse Sinuses. Figure 4.13 shows the three acquisition planes for neck veins and the acquisition plane for dural sinuses. Flow measurements were performed in the same MRI session when TOF and CE-MRV sequences were acquired, so that morphological and flow quantification data are patient-specific. PC-MRI sequences were processed with an in-house tool of the MR Research Facility in order to extract time resolved flow rates over the cardiac cycle [70]. A maximum encoding velocity (VENC) of $50\,cm\,s^{-1}$ was used. For a detailed description of the acquisition procedure refer to [70].

After having presented physiological data necessary for the construction of our closed-loop model, we proceed in the next section with a thorough validation of our computational results, comparing them versus literature data and to PC-MRI flow quantification data.
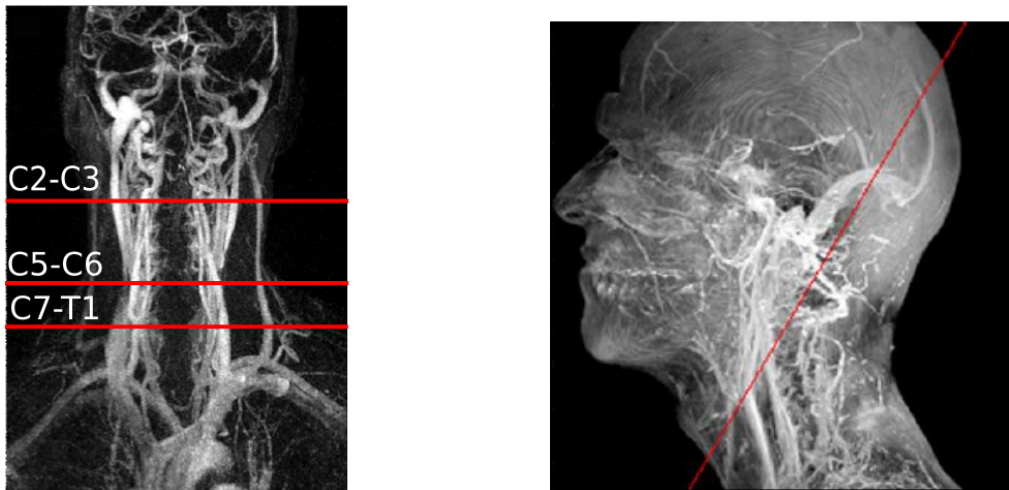
Figure 4.13: Planes at which PC-MRI flow measures were acquired for neck veins at C2-C3, C5-C6 and C7-T1 levels (left) and for dural sinuses (right). The three acquisition planes along the neck allow to evaluate how flow rate increases as tributary veins merge the internal jugular veins, whereas the acquisition plane for dural sinuses allows the evaluation of flow for the Superior Sagittal Sinus, the Straight Sinus and both Transverse Sinuses.

4.1.5   Computational results

In this section we present computational results in order to perform a thorough validation of our closed-loop model. The one-dimensional domain was divided into cells with a length of $\Delta x = 1\,cm$, imposing however a minimum of 3 computational cells in each vessel. Setting the CFL number of $CFL = 0.9$, the average time step was equal to $1.5 \times 10^{-4}\,s$. We note that the time step is computed at each computational step. Other relevant parameters are blood viscosity $\mu = 0.0045\,Pa\,s$ and density $\rho = 1050\,kg\,m^{-3}$. Initial velocity was set to $u = 0\,m\,s^{-1}$ everywhere and initial pressures were chosen as reported in table 4.10. We note that the specification of initial conditions is crucial, especially in the case of a closed-loop model, since they will define the periodic condition that the model will reach. The model reached a periodic state after approximately 15 cardiac cycles. For friction loses we assume a Poiseuille velocity profile so that $f = 8\pi\mu\,u/\rho$. All computations were performed using a third order accurate version of our numerical scheme.

Heart

Figure 4.14 shows computed pressures and volumes for each cardiac chamber. Pressure variation over the cardiac cycle well represents physiological conditions, for both atria and ventricles. The same observation is valid for volume curves. Stroke volume of the left ventricle is around $80\,ml$, in accordance with physiological values [99].

Compartment	$P_{ini} \, [mmHg]$
Arteries	70.0
Veins	5
Heart chambers & pulmonary compartments	10.0
Arterioles	45.0
Capillaries	25.0
Venules	10.0

Table 4.10: Inital pressure values for all compartments.
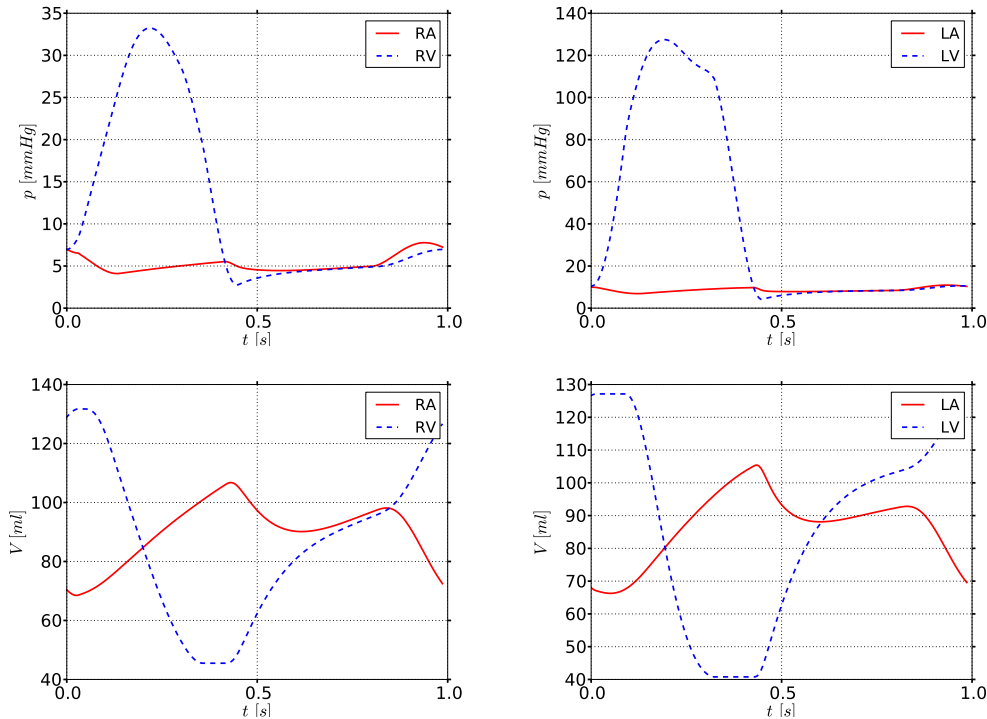
Figure 4.14: Computed pressures (top) and volumes (bottom) for the four cardiac chambers. RA: Right Atrium; RV: Right Ventricle; LA: Left Atrium; LV: Left Ventricle.

Arteries

Figures 4.15 and 4.16 show a comparison between computational results and data reported in the literature for average flow rates in major systemic arteries and cerebral arteries, respectively. The agreement is satisfactory in both cases, with computational results always located within physiological ranges.

Figures 4.17 and 4.18 show computed pressure and flow rate along the aorta and major leg arteries. Pressure waveforms in systemic arteries well reproduce physiological patterns, with steepening of the wave and increase in systolic peak pressure as the wave travels away from the heart. Pressure ranges in the arterial system fall within normal values. Pulse pressure in the ascending aorta is equal to $40 \, mmHg$, while it reaches a value of $66 \, mmHg$ in the femoral artery.

Computed pressure and flow rate in head and neck arteries are shown in figure 4.19. While correct flow distribution was already assessed in figure 4.16, flow waveforms correspond to measurements reported in [78] and [133].

Capillary beds

Figure 4.20 shows computed pressure in arterioles, capillaries and venules at selected locations in lumped compartments E to G. Pressure values in all compartments vary around
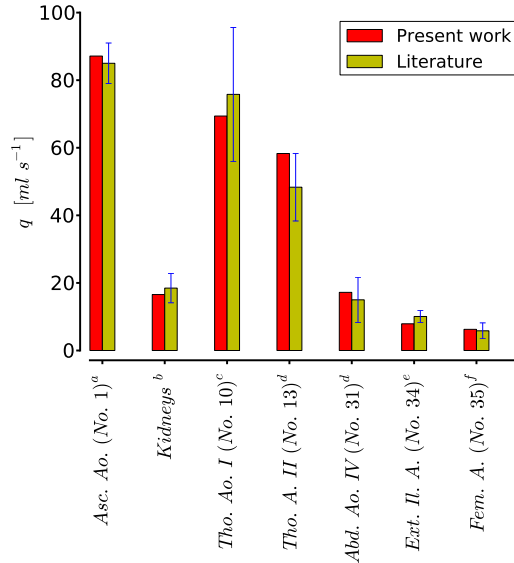
Figure 4.15: Blood flow distribution along the aorta and major leg arteries: computational results *vs* literature data (average and standard deviation). Asc. Ao.: Ascending Aorta; Kidneys: sum of both Renal Arteries; Tho. Ao.: Thoracic Aorta; Abd. Ao.: Abdominal Aorta; Ext. Il. A.: External Iliac Artery; Fem. A.: Femoral Artery. Vessel numbers refer to table 4.3 and figure 4.1. References: [a]Murgo *et al.* [120]; [b]Wolf *et al.* [176]; [c]Zitnik *et al.* [186]; [d]Cheng *et al.* [51]; [e]Itzchak *et al.* [86]; [f]Lewis *et al.* [100].

physiologically reasonable values: $40 - 60\,mmHg$ for arterioles, $20 - 30\,mmHg$ for capillaries and $13 - 17\,mmHg$ for venules.

Veins

Figure 4.21 shows a comparison of computed mean flow rates in selected systemic veins vs data reported in the literature. The agreement is satisfactory, showing a correct distribution of venous return between superior vena cava (SVC) and inferior vena cava (IVC).

Regarding average flow rates in head and neck veins, in figure 4.22 we compare our computational results with patient-specific PC-MRI flow quantification data. Flow distribution between Superior Sagittal Sinus (SSS) and Straight Sinus (StS) and consequently between both Transverse Sinuses (TS) matches measured data. Flow distribution between left and right Internal Jugular Veins (IJVs) correctly represents measurements, with an increase of flow as we move from C2-C3 level to C5-C6 level. The increased flow rate is related to the contribution of collaterals, such as the common facial vein and thyroid veins.

Pressure and flow rate waveforms in systemic veins are shown in figure 4.23. Blood flow in systemic veins is highly pulsatile, with a biphasic behaviour. By biphasic we mean that, contrary to what happens in arteries, there are two marked peaks in both, pressure and flow. This pulsatility is due to the direct connection of caval veins to the right atrium and the consequent retrograde pressure pulses traveling opposite to blood flow direction [99, 131]. The first flow peak, which is normally the highest one, is due to atria relaxation and consequently filling of this chamber, whereas the second one is related to the opening of the tricuspid valve. Depending on the degree of valvular competence, flow may be retrograde after the second peak. Computed flow waveforms resemble the expected biphasic behaviour and reflect the great influence of the right atrium in systemic venous flow patterns.

In the case of dural sinuses (major intracranial veins) and neck veins, time-resolved PC-MRI flow rate data is available. Computed pressure and flow rate, as well as PC-MRI flow measurements are shown in figures 4.24 to 4.26. We note that flow rate measurements correspond to the same patient for which major head and neck veins were characterized. Computed flow rate waveforms well reproduce measured ones, with a biphasic behaviour and the highest peak in
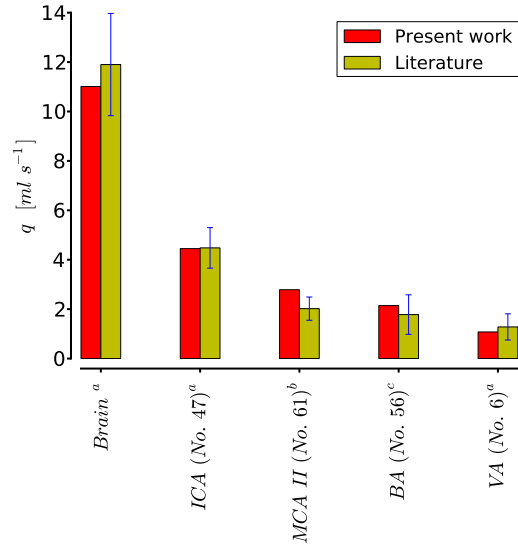
Figure 4.16: Blood flow in head and neck arteries: computational results *vs* literature data (average and standard deviation). Brain: sum of average flow rate in both internal carotid and vertebral arteries; ICA: Internal Carotid Artery; MCA: Middle Cerebral Artery; BA: Basilar Artery; VA: Vertebral Artery. Vessel numbers refer to table 4.3 and figure 4.1. References: [a]Stoquart-ElSankari *et al.* [152]; [b]Stock *et al.* [151]; [c]Boorder *et al.* [33].

correspondence of ventricular systole. There are however expected discrepancies between our computational results and PC-MRI flow data. In particular, there is a mismatch in average flow rate at C5-C6 and C7-T1 levels for the left internal jugular vein (figures 4.25(l) and 4.26(f)). This missing mass influences also the matching between time resolved measurements and computational results at those locations. The mass mismatch is due to the fact that cerebral blood flow is not imposed in the model, but is a result of computations. Since we are characterizing only major head and neck veins, while using a *standard* network of arteries, veins and capillary bed, this kind of results is expected.

There are certainly other factors that will influence venous waveforms which were not taken into account in the present model. In the next section we identify these factors and discuss their potential influence.

4.1.6 Discussion

Closed-loop models make it possible to study a wide range of physiological and pathological conditions [102, 30], avoiding the imposition of boundary conditions. On the other hand, their construction requires the characterization of a complex multi-scale set of models and their coupling. Therefore, such models have to be thoroughly validated, comparing computational results to physiological realistic situations and, ideally, to measurements. In section 4.1.5 we have presented computational results for major compartments described by the proposed model, comparing them to physiological data reported in the literature and to MRI derived flow quantification data. We have seen that heart dynamics are well described, with a correct interaction among heart chambers and between the left ventricle and the ascending aorta. Waveform patterns in the arterial system are in accordance with general physiological data and blood flow distribution among organs is reasonable.

The same conclusions made for the arterial system can be drawn for the venous circulation. The one-dimensional description of the venous district of our model is in fact a novel aspect of the present work. The emphasis given to the venous system in this work can not be found in previous works that presented models with a one-dimensional description of this cardiovascular district [141, 6], even in the context of closed-loop models [170]. Always with regard to the venous system, a distinctive aspect of the present work is represented by the detailed description of head and neck veins, which takes into account collateral pathways for cerebral venous
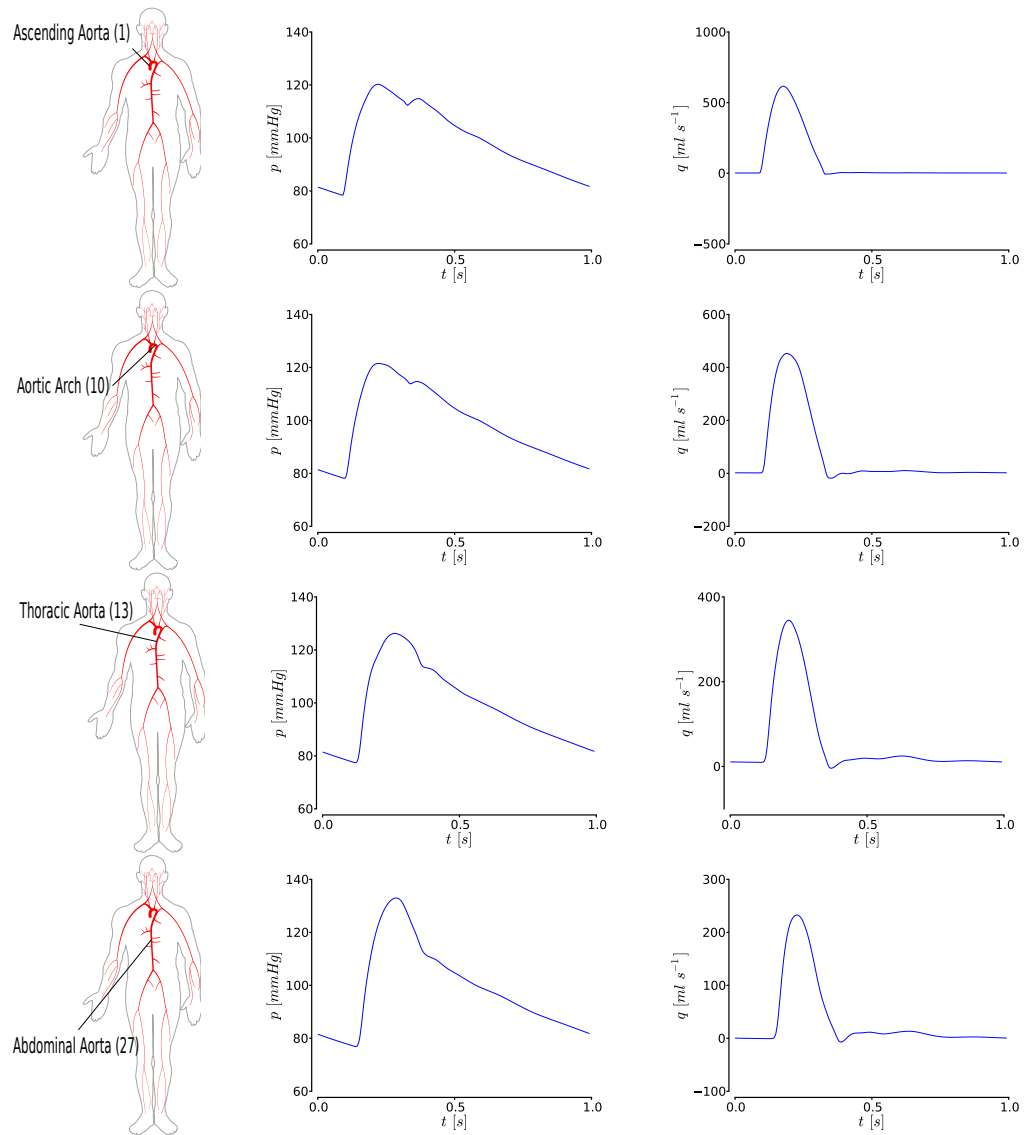
Figure 4.17: Computed pressure and flow rate along the aorta.
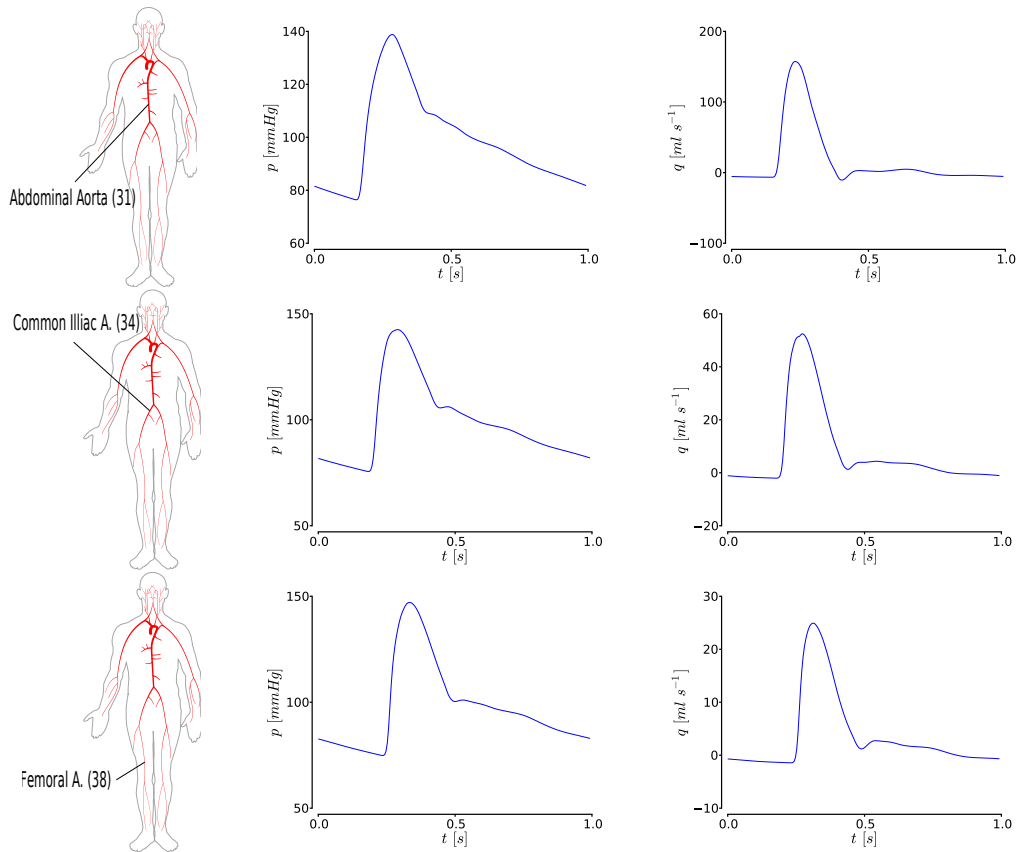
Figure 4.18: Computed pressure and flow rate in the aorta and major leg arteries.

drainage. This choice is motivated by the future applications envisaged in the context of this work with regard to the performance of a computational study of haemodynamical aspects of CCSVI [183].

Our experience, derived from modelling several patients for which MRI-derived geometry and PC-MRI time-resolved flow rate measurements were available, suggests us that a patient-specific characterization of major head and neck veins via medical imaging-derived geometries is necessary to satisfactorily reproduce measurements. In order to illustrate this fact we report a limited number of computational results for a second healthy control. The model is kept as described in section 4.1.4, except for some major head and neck veins, which are modified according to patient-specific MRI-derived geometrical information. Modified vessels are reported in table 4.11. In figure 4.27 we compare measured and computed average flow rates at two levels of internal jugular veins (unfortunately no measurement for dural sinuses are available for this patient). We can see that measured average flow at these locations is different from the one previously reported (see figure 4.22). We can also observe that modifying the venous network in this region is sufficient for obtaining a satisfactory agreement between measured and computed flow distribution. In figure 4.28 we show time-resolved flow measurements and computed flow rates in two veins. As for the healthy control presented in section 4.1.5, also in this case the amplitude of the first peak in the flow rate waveform is satisfactorily reproduced.
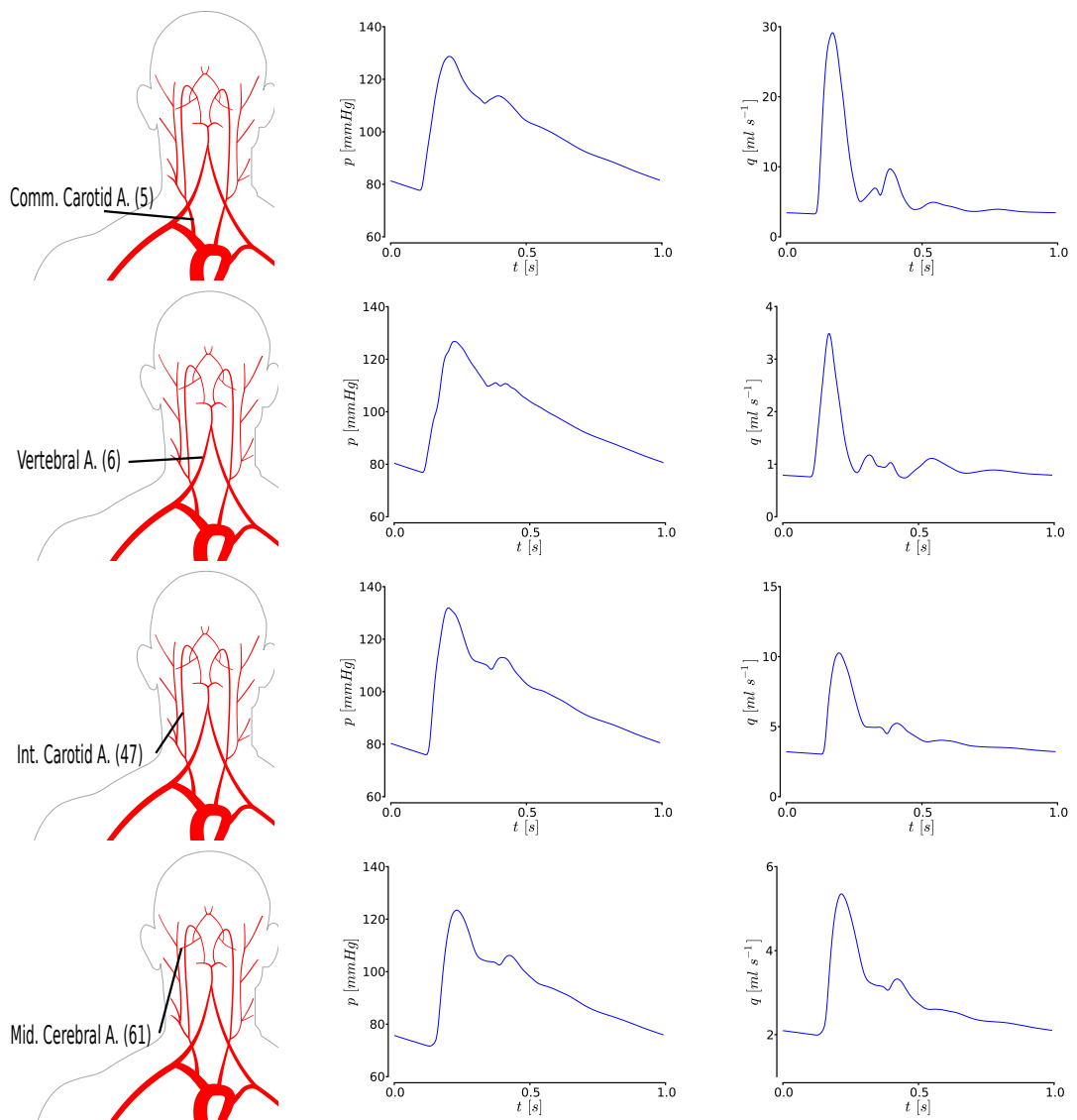
Figure 4.19: Computed pressure and flow rate in head and neck arteries.
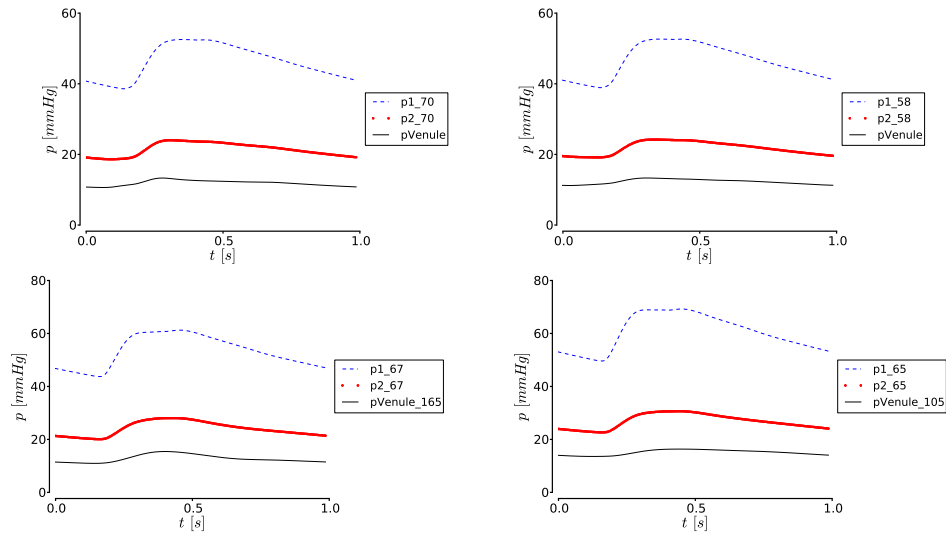
Figure 4.20: Computed pressure values for arterioles, capillaries and venules for selected elements of lumped compartments E (top left), F (top right) and G (bottom row). $p1$ stands for arterioles, $p2$ for capillaries and $pVenule$ for venules. Numbers correspond to the vessels that are connected to lumped compartment elements.
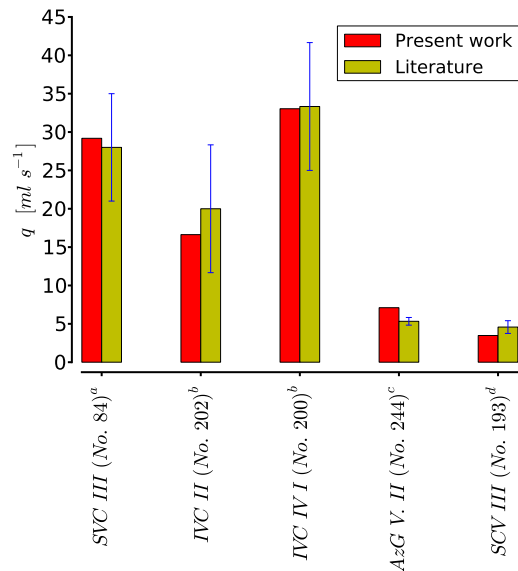
Figure 4.21: Blood flow in selected systemic veins: computational results vs literature data (average and standard deviation). SVC: Superior Vena Cava; IVC: Inferior Vena Cava; AzG V.: Azygos Vein; SCV: Subclavian Vein. Vessel numbers refer to figure 4.2 and table 4.8. References: [a] Be'eri $et\ al.$ [24]; [b] Cheng $et\ al.$ [51]; [c] Nabeshima $et\ al.$ [123]; [d] Fortune & Feustel [74].
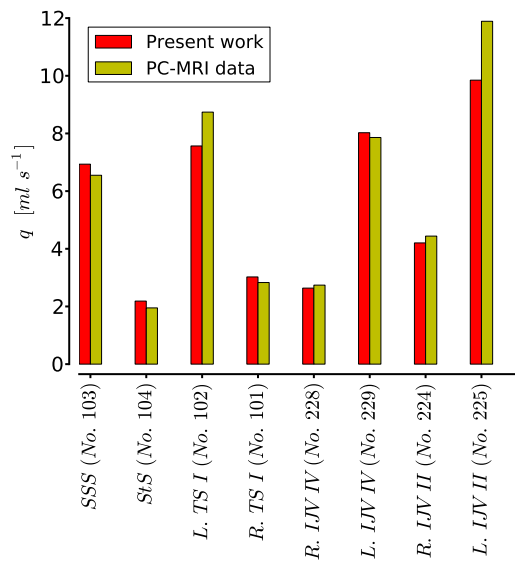
Figure 4.22: Blood flow in head and neck veins: computational results *vs* MRI flow quantification data. SSS: Superior sagittal Sinus; StS: Straight Sinus; TS: Transverse Sinus; IJV: Internal Jugular Vein. Vessel numbers refer to figure 4.2 and table 4.8.
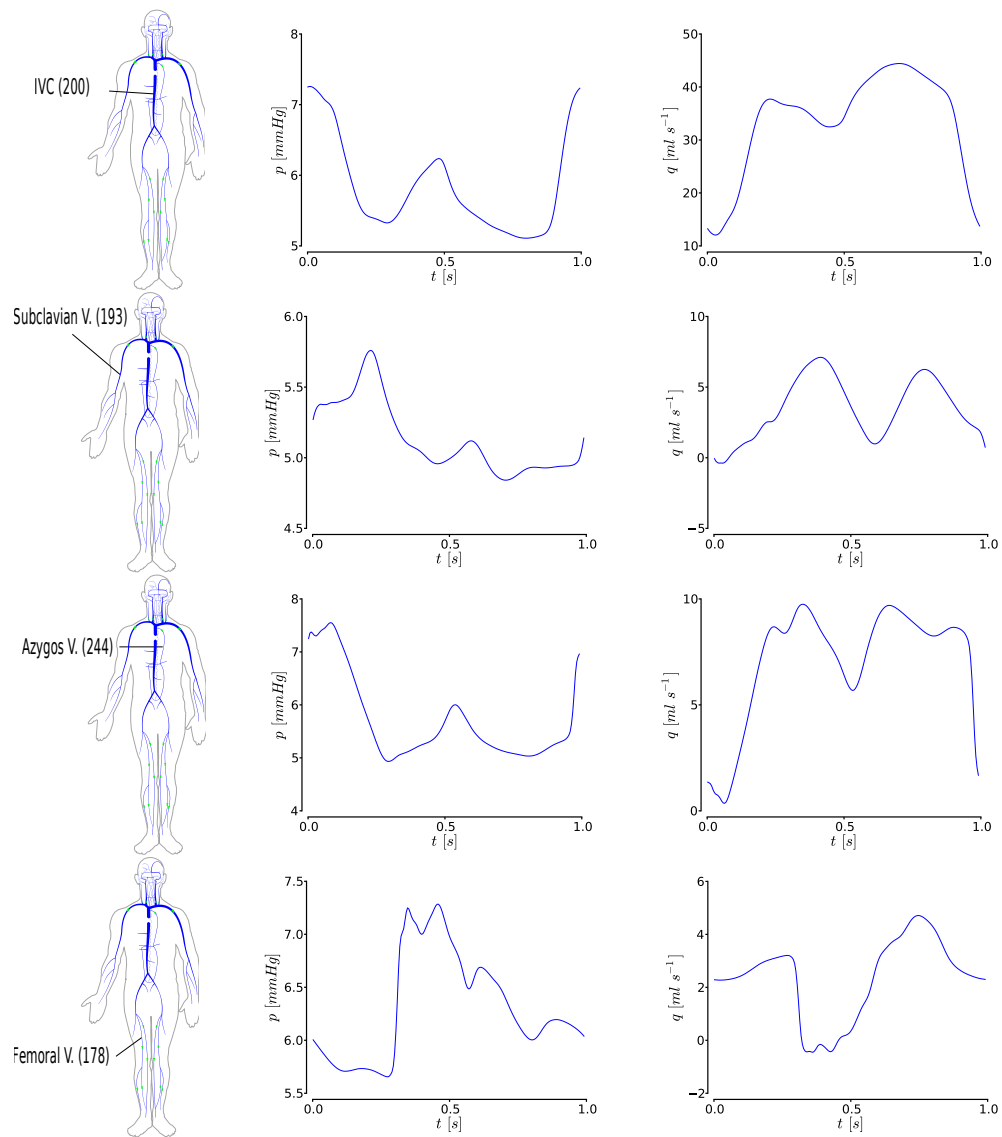
Figure 4.23: Computed pressure and flow rate in selected systemic veins.
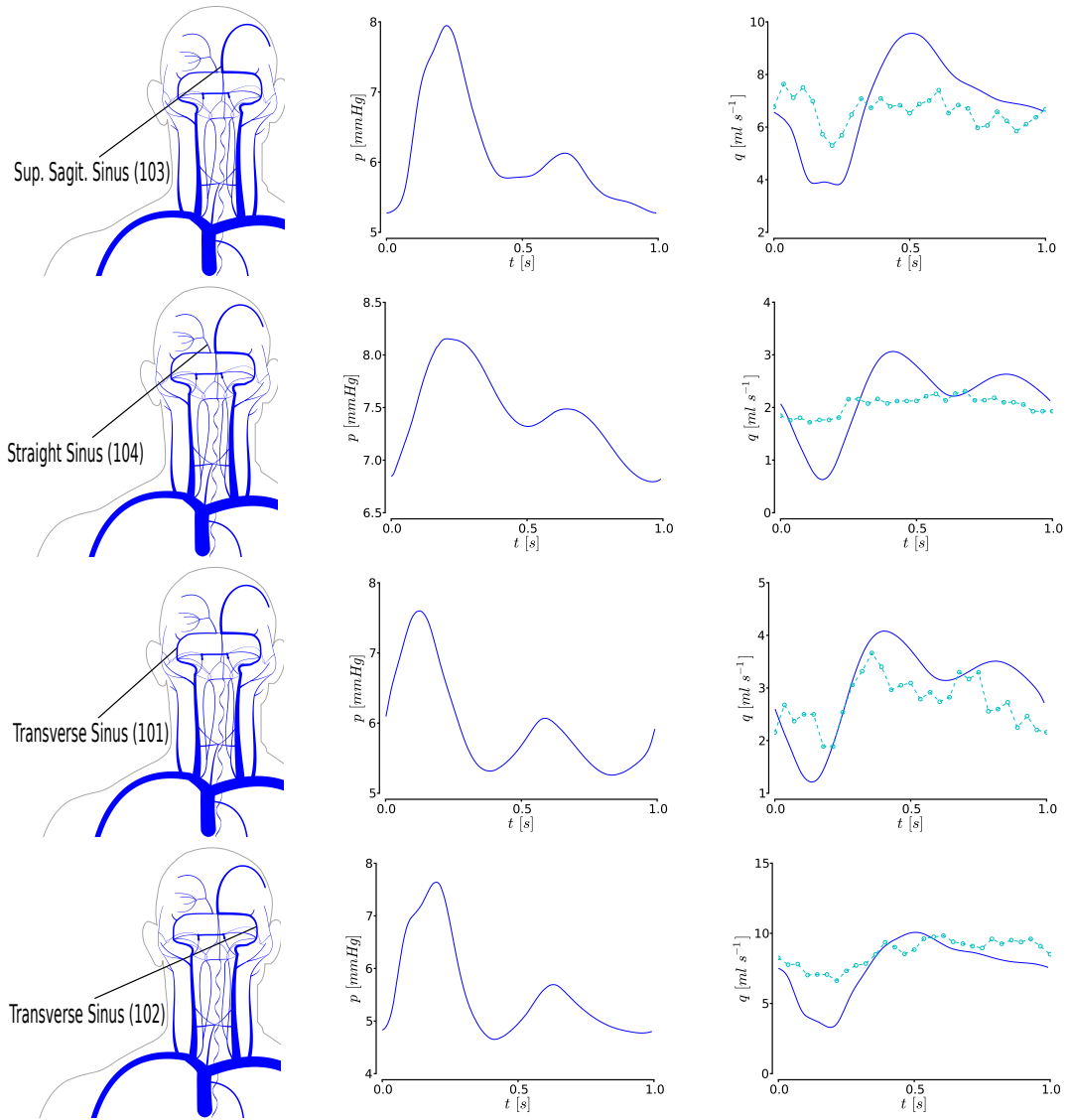
Figure 4.24: Computed pressure and flow rate in dural sinuses. PC-MRI flow quantification data is shown with symbols and dashed lines.
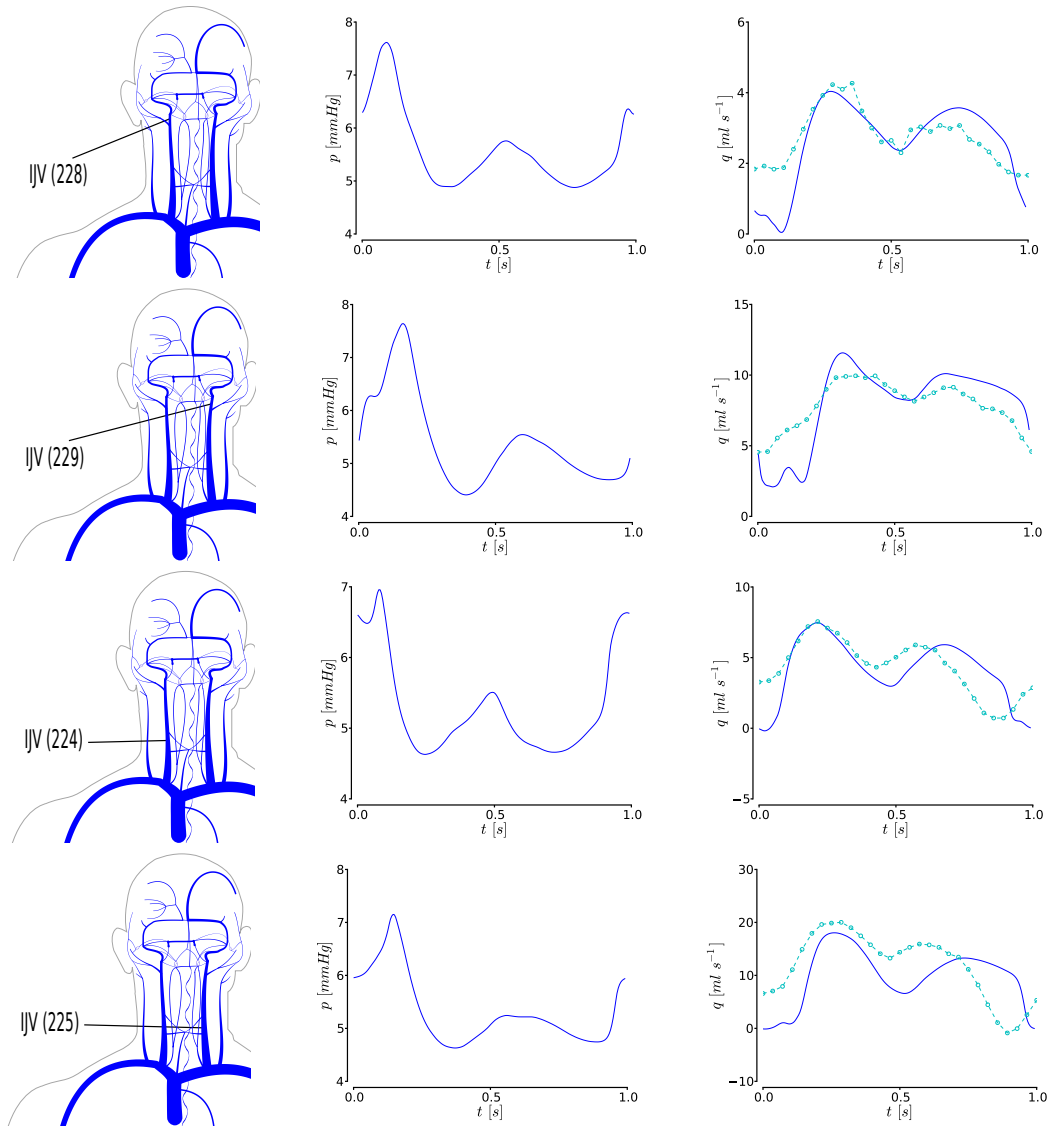
Figure 4.25: Computed pressure and flow rate in internal jugular veins. PC-MRI flow quantification data is shown with symbols and dashed lines.
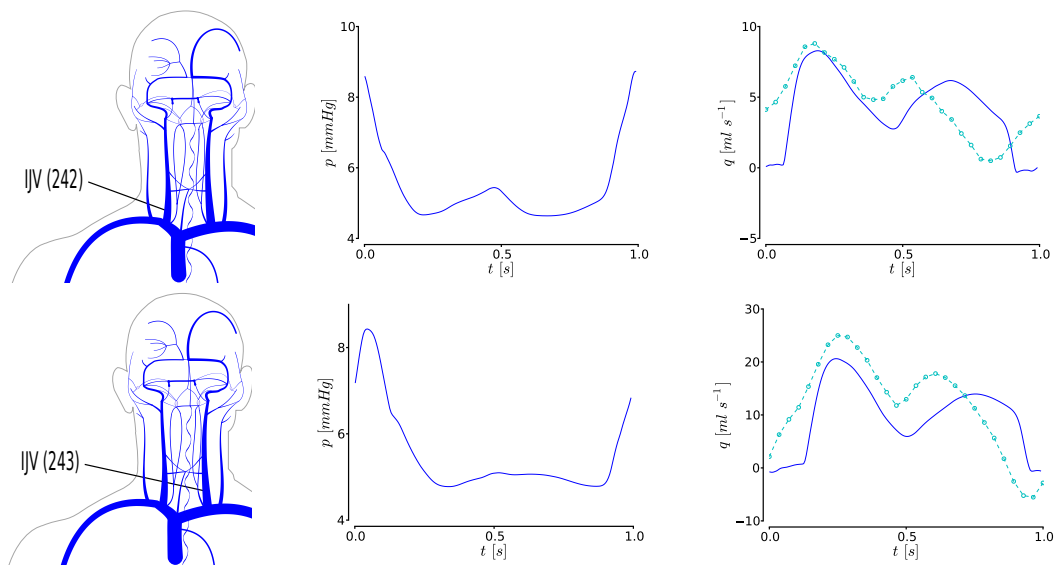
Figure 4.26: Computed pressure and flow rate in internal jugular veins (cont. from figure 4.25). PC-MRI flow quantification data is shown with symbols and dashed lines.

Table 4.11: Geometrical and mechanical parameters for modified head and neck veins of alternative venous network. L: length; r_0: inlet radius; r_1: outlet radius; c_0: wave speed for $A = A_0$; Loc location in the body according to table 4.2; Ref: MRI imaging derived segmented geometry.

No.	Vessel name	L [cm]	r_0 [cm]	r_1 [cm]	c_0 [m/s]	Loc.	Ref.
92	R. int. jugular v. I	2.50	0.472	0.505	1.494	3	MRI
99	R. sigmoid sinus II	3.50	0.309	0.252	3.000	1	MRI
101	R. trans. sinus I	3.50	0.219	0.219	3.000	1	MRI
102	L. trans. sinus I	3.50	0.334	0.178	3.000	1	MRI
224	R. int. jugular v. II	3.00	0.437	0.472	1.558	3	MRI
226	R. int. jugular v. III	2.70	0.357	0.437	1.673	3	MRI
227	L. int. jugular v. III	2.70	0.399	0.564	1.506	3	MRI
228	R. int. jugular v. IV	6.80	0.309	0.357	1.814	3	MRI
229	L. int. jugular v. IV	6.80	0.399	0.399	1.669	3	MRI
230	R. sigmoid sinus I	1.50	0.252	0.309	3.000	1	MRI
232	R. trans. sinus II	3.50	0.219	0.309	3.000	1	MRI
233	L. trans. sinus II	3.50	0.178	0.399	3.000	1	MRI
242	R. int. jugular v. V	1.00	0.505	0.505	1.463	3	MRI
259	Confluence of sinuses	1.00	0.219	0.219	3.000	1	MRI
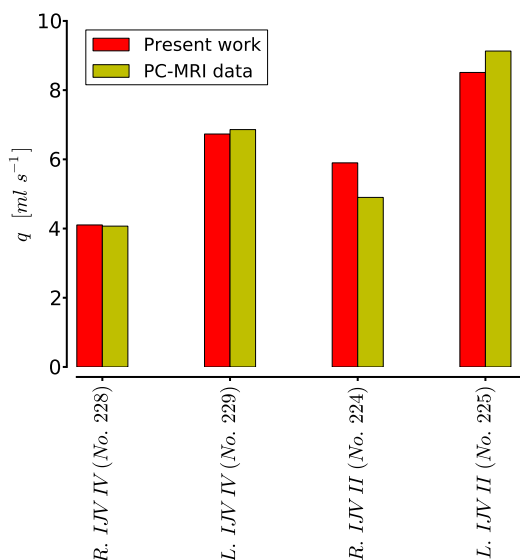
Figure 4.27: Blood flow in neck veins for a venous network modified according to in table 4.11: computational results *vs* MRI flow quantification data. IJV: Internal Jugular Vein. Vessel numbers refer to figure 4.2 and table 4.11.

Computational results for the venous district show that the non-pulsatile character of venous blood flow is a myth. In fact, we can see how right atrium retrograde pressure waves greatly influence venous flow, creating a biphasic flow pattern. This behaviour is well-known to the medical community and must be reproduced by any model of the venous system [131, 99].

The pulsatility of venous blood flow will be further influenced by factors. The most significant ones are respiration, gravity and venous tone regulation. The satisfactory agreement between computational results and MRI-derived data for a subject at rest in supine position suggests that none of these factors plays a crucial role in the determination of venous flow patterns in body regions where measurements were available. In order to determine the effect of respiration on venous flow pulsatility we have performed a simulation in which intra-thoracic and intra-abdominal pressures vary, as proposed by [154], according to

$$P_k = \begin{cases} P_{k,a} + P_{k,b} \left(1 - \exp(-\frac{\hat{t}}{\tau})) \right) & \text{if} \quad \hat{t} \le t_{insp}, \\ P_{k,a} + P_{k,b} \exp(-\frac{(\hat{t} - t_{insp})}{\tau})) & \text{if} \quad \hat{t} > t_{insp}, \end{cases} \quad \text{with} \quad k = th, abd, \quad (4.46)$$

where $\hat{t} = mod(t, t_{resp})$, t_{resp} is the duration of a respiratory cycle, t_{insp} is the duration of the inspiration phase, τ is a decay constant, $P_{k,a}$ and $P_{k,b}$ are the baseline pressure and variation
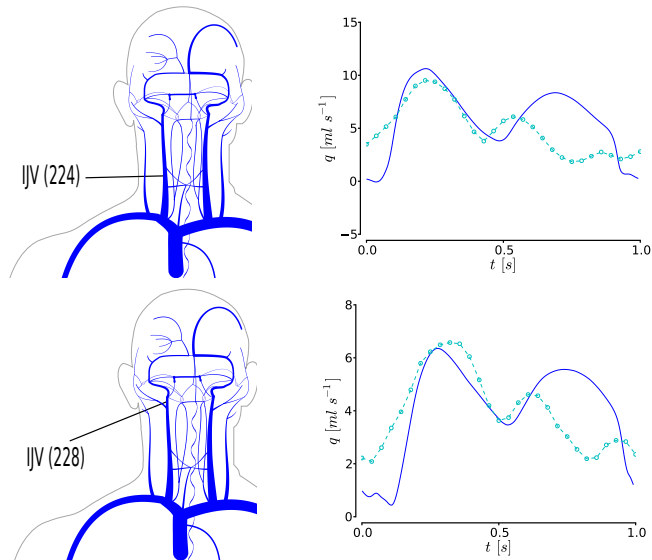
Figure 4.28: Computed pressure and flow rate in internal jugular veins for a venous network modified according to in table 4.11 . PC-MRI flow quantification data is shown with symbols and dashed lines.

amplitude, respectively. According to [154], the duration of the respiratory cycle is $t_{resp} = 5\,s$, with an inspiration phase of $t_{insp} = 2\,s$ and a decay constant $\tau = 0.3\,s$. Moreover, baseline intra-thoracic pressure is $P_{th,a} = -3.7\,mmHg$ and its variation amplitude is $P_{th,b} = -1.8\,mmHg$. For the intra-abdominal cavity we use the same time coefficients as for the intra-thoracic cavity, while baseline pressure is $P_{ab,a} = 1\,mmHg$ and variation amplitude is $P_{ab,b} = 1.8\,mmHg$, according to [146]. In figure 4.29 we show computational results for two veins, one located in the neck and the other one in the abdomen, for a period of 10 seconds. It can be clearly seen that while there is a modulation of flow and pressure due to respiration, the shape of pressure and flow waves is chiefly determined by the right heart. However, we expect that in the case of respiratory manoeuvres, such as Valsava and Müller manoeuvres, or other situations such as postural changes and exercise, respiration along with venous tone regulation and muscle compression will play a crucial role in the determination of venous hemodynamics.

The introduction of gravity during postural changes will introduce transient flow accelera-tion and vessel collapse above the right atrium due to negative transmural pressure [16, 87]. Under these circumstances the wave speed for veins in the collapse region will certainly lead to transcritical flows and therefore will make the algorithm used to treat junctions unsuitable. This fact was confirmed by preliminary numerical experiments that we do not report here. Therefore, it is necessary to introduce new methodologies for the treatment of junctions. This subject is in fact being currently investigated by the authors.

Venous tone regulation due to postural changes will act simultaneously with blood flow regulation in other compartments, such as arterioles [99]. We plan to include mathematical models of the baroreflex regulatory system, as the one proposed in [31].

A further aspect that will play a crucial role for the correct description of postural changes is the use of a realistic tube law (4.18). The authors are convinced about the fact that the pressure-area relationship used in this work has to be improved in order to correctly represent transient phases due to postural changes.

Having always the motivation of this work in mind, another element to be added to the present model is that of the interaction between brain parenchyma, cerebro-spinal flow and cerebral vasculature. Some work attempting to model this complex phenomena is readily avail-able [104] and will be used as a starting point.
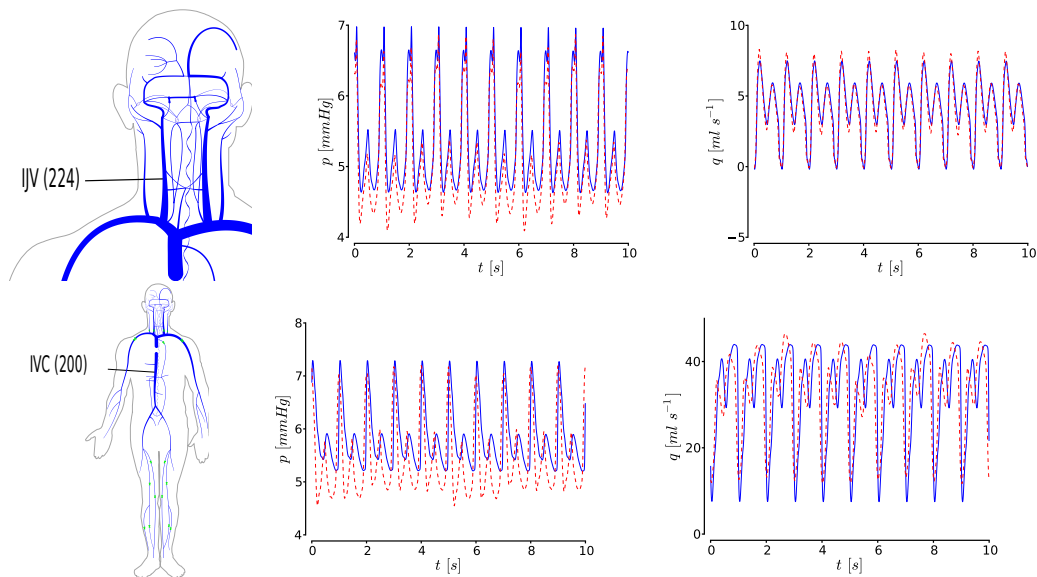
Figure 4.29: Computed pressure and flow rate for the right internal jugular vein (top row) and the inferior vena cava (bottom row). Continuous lines correspond to results obtained without including respiration and dashed lines represent results obtained including variation of intra-thoracic and intra-abdominal pressures as specified by equation (4.1.6).

4.1.7   Summary and concluding remarks

We have presented a closed-loop, multi-scale model comprising lumped-parameter models for the heart, the pulmonary circulation and the microvasculature, together with one-dimensional description of medium to large arteries and veins. A novel feature of the model is the detailed description of the venous system, particularly that part related to the head and neck. This is so because we are chiefly interested in the application of the model to the theoretical study of the connection between the venous vasculature and a class of neurodegenerative diseases. Regarding the lumped-parameter models, their numerical aspects are well researched. However, concerning the one-dimensional models, the hyperbolic character of the governing equations poses significant challenges to the numerical modeller. Particular issues are vessel collapse, choking, elastic jump formation and geometric-type source terms. In this model we have deployed state-of-the-art numerical methodologies that are able to cope with these challenges. These issues are particularly relevant to the modelling of the venous system, which is significantly more challenging than the well-researched arterial system. A systematic assessment and validation exercise has been carried out, making abundant use of published results, as well as recent measurements of flow in head and neck veins, kindly provided to us by our collaborators. For this portion of the domain we have performed a patient-specific characterisation of major vessels. We have shown that this step is necessary in order to correctly reproduce PC-MRI derived flow patterns in a patient-specific manner. We have also discussed some potential improvements to the model in order to correctly describe postural changes, which will be the subject of a forthcoming publication.

4.2 An enhanced closed-loop model for the study of cerebral venous blood flow

4.2.1 Introduction

The closed-loop model for the cardiovascular system presented in section 4.1 is extended in order to account for two fundamental mechanisms affecting cerebral venous blood flow: the interaction between intracranial pressure and cerebral vasculature and the Starling resistor behaviour of intracranial veins. Computational results are compared with MRI-derived flow measurements and the major determinants of cerebral venous flow waveforms are discussed taking into account current physiological concepts and model-driven considerations.

The role of veins in intracranial pressure dynamics, as well as their own physiology is poorly understood [152]. Recent developments on the possible link between extra-cranial venous anomalies and neurological conditions, like the description of the Chronic Cerebro-Spinal Venous Insufficiency (CCSVI) condition and its association to Multiple Sclerosis (MS) [183], have increased the interest of the medical community to improve our understanding on the physiology of cerebral venous return. This interest was further enhanced by very recent findings on altered cerebrospinal fluid flow dynamics in patients with MS [107] and by the improvement observed for this dynamics, as well as for clinical course of the disease, after MS patients were treated for CCSVI via percutaneous transluminal angioplasty [187].

Several models for the study the interaction between cerebral vessels and intracranial pressure have been constructed. A remarkable example is the model by Ursino [165], where the author presented a lumped parameter model that describes the time variation of intracranial pressure as a result of changes in blood volume and cerebrospinal fluid generation and absorption. Following this work, many other researchers have used lumped parameter models to study physiological and pathological aspects of the interaction between the cerebral vasculature and intracranial pressure, see for example [166, 7, 150]. A step forward in terms of the spatial resolution of this kind of models, which is absent in the above mentioned models, is the work by Linninger *et al.* [104], where they presented a multiple compartment model, which treated the intracranial cavity as a set of differentiated compartments such as the subarachnoid space, the brain parenchyma, the ventricles, and the different vascular compartments. All the above-cited models are of lumped parameter models, therefore, their use for the study of pulse wave propagation phenomena is not feasible. Since we are interested in assessing the interactions between extra-cranial venous anomalies and intra-cranial hemodynamics, we are interested in coupling, at least as a first degree of sophistication, a lumped parameter model for intracranial pressure with pulse wave propagation, or one-dimensional, models for the hemodynamics.

In this section we extend the closed-loop model for the cardiovascular system presented in [117], in order to account for two factors that are relevant to cerebral blood flow. The first aspect is the interaction of the cerebral vasculature with the pulsating intracranial pressure. To take into account this aspect we incorporate the model for intracranial pressure presented in [165], which describes the variation of intracranial pressure in time as a result of the variation of cerebral blood volume. The second aspect is of particular importance for the venous side of cerebral circulation and regards the Starling resistor. There is experimental evidence that shows how pressure in cerebral veins is always higher than intracranial pressure, for a wide range of intracranial pressure values, independently of the pressure in downstream vessels such as the dural sinuses [90, 106]. The underlying mechanism is still object of debate, with some researchers speaking in favor of a purely hydraulic mechanism [10] and others hypothesizing a more complex control mechanism [55]. Moreover, there is evidence of distinct morphological and mechanical properties of the terminal portion of cerebral veins, in correspondence of the point where they drain into the dural sinuses [172, 54, 55, 49]. In order to model the effect observed by experimentalists, we have added several cerebral veins to the venous network presented in [117] and implemented a simple model for a Starling resistor element, proposed by Mynard [121], at the terminal point of each cerebral vein.

In order to validate our computational results, we compare them with MRI-derived flow measurements and obtain a satisfactory agreement. Moreover, we study the influence of intracranial pressure and the Starling resistor elements on our computational results by switching on and off each component of the model and assessing the impact of such changes.

The rest of the chapter is structured as follows: in section 4.2.2 we describe the components of the model that have been changed or added with respect to the previously presented model. In section 4.2.3 we present computational results and compare them to MRI-derived flow measurements. A discussion on the results is performed in section 4.2.4, with special attention to the role played by the different ingredients of the model in shaping cerebral venous waveforms. We conclude with section 4.2.5, where the presented work is summarized and final conclusions are draw.

4.2.2   Methods

The model presented in this section is an extension of a closed-loop model for the cardiovascular system presented in [117]. In this work, its description is limited to those items that have been changed or added to the previous version of the model. The reader is referred to [117] and references therein for aspects that are not covered by the present work.

Mathematical model of the cardiovascular system

Our model is composed by one-dimensional networks of major arteries and veins, while lumped parameter models are used for the heart, the pulmonary circulation and capillary beds linking arteries and veins (see figure 4.30). A distinct aspect of this model is that geometrical information for major head and neck veins were obtained from the segmentation of MRI data. This patient-specific characterization allowed us to compare computational results *vs.* patient-specific MRI-derived flow quantification data, as reported in [117].

One-dimensional blood flow in elastic vessels is described by the following first-order, non-linear hyperbolic system

$$\begin{cases} \partial_t A + \partial_x q = 0\,, \\ \partial_t q + \partial_x \left(\hat{\alpha} \dfrac{q^2}{A} \right) + \dfrac{A}{\rho} \partial_x p = -f\,, \end{cases} \tag{4.47}$$

where x is the axial coordinate along the longitudinal axis of the vessel; t is time; $A(x,t)$ is the cross-sectional area of the vessel; $q(x,t)$ is the flow rate; $p(x,t)$ is the average internal pressure over a cross-section; $f(x,t)$ is the friction force per unit length of the tube; ρ is the fluid density and $\hat{\alpha}$ is a coefficient that depends on the assumed velocity profile. Throughout this work we will take $\hat{\alpha} = 1$, which corresponds to a blunt velocity profile.

To close the system we adopt a tube law, whereby the internal pressure $p(x,t)$ is related to the cross-sectional area $A(x,t)$ and other parameters, namely

$$p(x,t) = p_e(x,t) + K(x) \left[\left(\dfrac{A(x,t)}{A_0(x)} \right)^m - \left(\dfrac{A(x,t)}{A_0(x)} \right)^n \right] + P_0\,. \tag{4.48}$$

Here $p_e(x,t)$ is the external pressure, $K(x)$, m, n and $A_0(x)$ are parameters that take into account mechanical and geometrical properties of the vessel. For a discussion on the choice of these parameters for both, arteries and veins, the reader is referred to [117] and references therein.

Figure 4.31 shows the venous network used in this work. A set of cortical cerebral veins draining into the superior and inferior sagittal sinuses were added to the venous network presented in [117]. Moreover, a Starling resistor element was added to the end of each cerebral vein (see section 4.2.2). Table 4.12 shows geometrical and mechanical properties of vessels added or changed with respect to the venous network used in [117]. As a consequence of the venous network extension, the lumped parameter compartment linking middle and anterior cerebral arteries to the inferior and superior sagittal sinuses has been modified. The new configuration of this lumped compartment is shown in figure 4.32 and coefficients for lumped elements are reported in table 4.13.

In the following sections new aspects of the closed-loop model presented in [117] are motivated and described.

Figure 4.30: Schematic representation of the closed-loop model presented in [117]. Major arteries and veins are described with a one-dimensional model, whereas heart, pulmonary circulation, arterioles, capillaries and venules are represented as lumped parameter models

Figure 4.31: Head and neck veins. Numbers refer to those used in Table 4.12, where geometrical and mechanical parameters for each vessel are reported.

Figure 4.32: Lumped-parameter compartment **G** resulting from incorporating cortical veins. Numbers on the left refer to feeding arteries, see [117]. Numbers on the right refer to veins draining into sagittal sinuses and are those in Table 4.12.

Table 4.12: Geometrical and mechanical parameters for veins added or changed to the venous network presented in [117]. L: length; r_0: inlet radius; r_1: outlet radius; c_0: wave speed for $A = A_0$; $Type$: vessel type (1: dural sinus, 2: cerebral vein); Ref: bibliographic source or MRI imaging segmented geometry.

No.	Vessel name	L [cm]	r_0 [cm]	r_1 [cm]	c_0 [m/s]	Type	Ref.
103	Sup. sagittal sinus	2.50	0.350	0.367	5.000	1	MRI
106	Vein of Galen	0.60	0.366	0.400	1.703	9	MRI
149	Sup. sagittal sinus	4.33	0.229	0.258	5.000	1	MRI
150	R. Labbe v.	5.00	0.150	0.150	2.376	9	MRI
151	L. Labbe v.	5.00	0.150	0.150	2.376	9	MRI
152	Sup. sagittal sinus	4.33	0.258	0.287	5.000	1	MRI
153	Sup. sagittal sinus	2.50	0.334	0.350	5.000	1	MRI
157	Sup. sagittal sinus	5.00	0.300	0.334	5.000	1	MRI
158	Cerebral vein	5.00	0.150	0.150	2.376	9	[172]
159	Cerebral vein	5.00	0.150	0.150	2.376	9	[172]
161	Cerebral vein	5.00	0.150	0.150	2.376	9	[172]
162	Cerebral vein	5.00	0.150	0.150	2.376	9	[172]
165	Sup. sagittal sinus	4.33	0.200	0.229	5.000	1	MRI
236	Sup. sagittal sinus	2.00	0.287	0.300	5.000	1	MRI
237	Cerebral vein	5.00	0.150	0.150	2.376	9	[172]
238	Cerebral vein	5.00	0.150	0.150	2.376	9	[172]
239	Cerebral vein	5.00	0.150	0.150	2.376	9	[172]
241	Inf. sagittal sinus	3.67	0.160	0.160	5.000	1	MRI
245	Cerebral vein	3.00	0.150	0.150	2.376	9	[172]
248	Inf. sagittal sinus	3.67	0.160	0.160	5.000	1	MRI
249	Cerebral vein	3.00	0.150	0.150	2.376	9	[172]
260	Cerebral vein	3.00	0.150	0.150	2.376	9	[172]
261	Terminal cerebral vein	1.00	0.150	0.150	5.000	1	[172]
262	Terminal cerebral vein	1.00	0.150	0.150	5.000	1	[172]
263	Terminal cerebral vein	1.00	0.150	0.150	5.000	1	[172]
264	Terminal cerebral vein	1.00	0.150	0.150	5.000	1	[172]
265	Terminal cerebral vein	1.00	0.150	0.150	5.000	1	[172]
266	Terminal cerebral vein	1.00	0.150	0.150	5.000	1	[172]
267	Terminal cerebral vein	1.00	0.150	0.150	5.000	1	[172]
268	Terminal cerebral vein	1.00	0.150	0.150	5.000	1	[172]
269	Terminal cerebral vein	1.00	0.150	0.150	5.000	1	[172]
270	Terminal cerebral vein	1.00	0.150	0.150	5.000	1	[172]
271	Terminal cerebral vein	1.00	0.309	0.366	1.804	9	MRI
272	Terminal cerebral vein	1.00	0.150	0.150	5.000	1	MRI
273	Terminal cerebral vein	1.00	0.150	0.150	5.000	1	MRI

Intracranial pressure

The cranial cavity can be considered as a space of fixed volume which contains the brain parenchyma, the cerebrospinal fluid (CSF) and the cerebral vasculature. This cavity is then connected to the spinal cavity, which exhibits an elastic behaviour, allowing for volume changes. Variations in intracranial blood volume produce fluctuations of intracranial pressure and, consequently, an exchange of CSF between the intracranial and spinal subarachnoid spaces. In this work intracranial pressure is modeled as proposed in [166]. In this simple model the evolution of intracranial pressure in time is given by

$$C_{ic} \frac{dp_{ic}}{dt} = \frac{dV_{cv}}{dt} + \frac{p_c - p_{ic}}{R_f} - \frac{p_{ic} - p_{SSS}}{R_0} \,, \tag{4.49}$$

where p_{ic}, p_c and p_{SSS} are the intracranial pressure, capillary pressure and the superior sagittal sinus pressure, respectively. V_{cv} is the volume of the cerebral vasculature, given by the sum of the volume occupied by arteries, arterioles, capillaries, venules and veins located inside the cranium. C_{ic} is the intracranial compliance, computed as

$$C_{ic} = \frac{1}{k_e \, p_{ic}} \,, \tag{4.50}$$

where k_e is the elastance coefficient of the craniospinal system. In this work we use $k_e = 0.15 \, ml^{-1}$ [165]. R_f and R_0 are CSF filtration and re-absorption resistances. CSF filtration from the subarachnoid space towards the dural sinuses has been shown to vary linearly with the pressure difference $p_{ic} - p_{sss}$ [68]. A CSF outflow resistance of $R_0 = 15 \, mmHg \, min \, ml^{-1}$, in accordance with [68], is considered throughout this work. Moreover, R_f is set to $R_f = 48.33 \, mmHg \, min \, ml^{-1}$, in order to obtain an average CSF filtration flow rate of $q_{csf,f} = 400 \, \mu l \, min^{-1}$. Note that since physiological cerebral blood flow is approximately $q_{CBF} = 720 \, ml \, min^{-1}$, the time scales of intracranial pressure variations due to an imbalance of CSF filtration and absorption will by several orders of magnitude longer than a cardiac cycle.

Parent/daughter vessel	R_{da}	R_{al}	L_{al}	C_{al}	R_{cp}	L_{cp}	C_{cp}	R_{vn}	L_{vn}	C_{vn}
Lumped model G										
63	20.6859	24.4500	0.0179	0.0070	18.8100	0.0059	0.0007	–	–	–
	–	–	–	–	18.8100	0.0059	–	–	–	–
65	20.6859	24.4500	0.0179	0.0070	18.8100	0.0059	0.0007	–	–	–
61	12.6609	10.5700	0.0078	0.0140	18.8100	0.0059	0.0014	–	–	–
	–	–	–	–	4.0700	0.0013	–	–	–	–
ISS	–	–	–	–	–	–	–	–	–	0.0210
249	–	–	–	–	–	–	–	11.3400	0.0199	–
245	–	–	–	–	–	–	–	11.3400	0.0199	–
260	–	–	–	–	–	–	–	11.3400	0.0199	–
SSS	–	–	–	–	–	–	–	–	–	0.1050
158	–	–	–	–	–	–	–	4.8300	0.0109	–
159	–	–	–	–	–	–	–	4.8300	0.0109	–
161	–	–	–	–	–	–	–	4.8300	0.0109	–
162	–	–	–	–	–	–	–	4.8300	0.0109	–
237	–	–	–	–	–	–	–	4.8300	0.0109	–
238	–	–	–	–	–	–	–	4.8300	0.0109	–
239	–	–	–	–	–	–	–	4.8300	0.0109	–

Table 4.13: Parameters for artery-vein connection shown in figure 4.32, derived from [102]. R_{da} is the resistance for distal arteries, in $mmHg\,s\,ml^{-1}$, R is the resistance in $mmHg\,s\,ml^{-1}$, L the inductance in $mmHg\,s^2\,ml^{-1}$ and C the capacitance in $ml\,mmHg^{-1}$, for arterioles, capillaries and venules respectively. Venule capacitance is divided into the superior sagittal sinus (SSS) and the inferior sagittal sinus (ISS). Vessel numbers refer to figure 4.31 for veins and to the network presented in [117] for arteries.

Equation (4.49) is integrated with a forward Euler scheme and requires the computation of the time variation of the cerebral vasculature $\frac{dV_{cv}}{dt}$. This term is approximated by tracking V_{cv} in time in order to be able to compute

$$\frac{dV_{cv}^n}{dt} = \frac{V_{cv}^n - V_{cv}^{n-1}}{dt},$$

where superscript n refers to the current time step of the simulation.

The initial volume of each compartment is computed as follows:

- the volume of intracranial vascular compartments as: $V_a = 30\,ml$, $V_{al} = 16\,ml$, $V_{cap} = 20\,ml$, $V_{ven} = 70\,ml$ and $V_v = 13\,ml$, for arteries, arterioles, capillaries, venules and veins, respectively [104].

- The initialization pressures for arteries $P_a^0 = 70\,mmHg$ and for veins $P_v^0 = 5\,mmHg$ define the volumes of intracranial arteries and veins, $V_a = 3.52\,ml$ and $V_v = 20.36\,ml$.

- Then, we set $V_{al} = 16\,ml + (30\,ml - V_a)$, $V_{cap} = 20\,ml$ and $V_{ven} = 70\,ml + (13\,ml - V_v)$.

- These volumes correspond to $V_{cv}^0 = 162\,ml$, with a distribution of cerebral blood volume (CBV) between arteries-arterioles and capillaries-venules-veins over total volume of 30 % and 70 %, respectively.

- The volume of each compartment is update at each time step by the mass conservation principle.

The computed intracranial pressure will act on intracranial one-dimensional vessels, as well as on lumped parameter model, as a prescribed external pressure.

Starling resistor

The pressure difference that governs cerebral blood flow (CBF) in physiological conditions is the Cerebral Perfusion Pressure (CPP), defined as the difference between arterial and intracranial pressure [90, 106, 136]. This characteristic behaviour of CBF, where the downstream pressure is the intracranial pressure and not the central venous pressure was the reason for the medical community to consider CBF as a flow phenomenon governed by a *Starling resistor*.

The Starling resistor [93] is an experimental device in which a collapsible tube is connected to two rigid tubes at its extremities and located in a chamber of fixed volume with variable ambient pressure [53]. One can change inlet, outlet and chamber pressure (often called external pressure) and observe the resulting flow patterns. The collapsible nature of the tube produces peculiar effects, being flow limitation the one of interest for this work. In practice, there is a range of

pressure values for which the flow rate through the tube becomes practically independent of the downstream pressure and the dominant pressure difference is given by the upstream and the external pressures. This happens when the external pressure is much higher than the outlet pressure. For a thorough analysis of the mathematical background of flow limitation the reader is referred to [140], for example.

There is undeniable experimental evidence suggesting that for physiological conditions the brain as a whole behaves as a Starling resistor [89, 106, 136]. Intracranial veins are flexible thin-walled tubes surrounded by the brain parenchyma or CSF, depending on their location, that drain into the various dural sinuses (superior sagittal, inferior sagittal, straight and transverse sinuses). Dural sinuses are located in the dura matter and are therefore considerably more rigid than cerebral veins. Moreover, there is evidence of drastic variations of the morphology and mechanical properties of cerebral veins in correspondence of the point where they drain into the dural sinuses [172, 54, 55, 178, 49]. These considerations led to the hypothesis that the terminal portion of cerebral veins acts as a Starling resistor. These observations are supported by pressure measurements in animals [90, 106] that indicate that the relation

$$p_a \geq p_{cv} \geq p_{ic} \geq p_{ds} \,, \tag{4.51}$$

holds for wide ranges of p_{ic}. Here p_a, p_{cv} and p_{ds} are arterial, cerebral venous and dural sinuses pressures, respectively.

As a first attempt to model this phenomenon, we introduce a Starling resistor (SR) in the terminal portion of cerebral veins of our venous network. Following [121], that made use of this concept to model the zero-flow pressure in capillary beds. The resistance to flow in the SR element is

$$R_{SR} = \begin{cases} R_{SR}^0 \,, & \text{if } p_{up} \geq p_{ic} \,, \\ \infty \,, & \text{if } p_{up} < p_{ic} \,, \end{cases} \tag{4.52}$$

while flow across the SR element is

$$q_{SR} = \begin{cases} \dfrac{p_{up} - p_{ic}}{R_{SR}} \,, & \text{if } p_{down} \leq p_{ic} \,, \\[4mm] \dfrac{p_{up} - p_{down}}{R_{SR}} \,, & \text{if } p_{down} > p_{ic} \,. \end{cases} \tag{4.53}$$

$p_{up,down}$ are pressures upstream and downstream of the SR element with respect to flow towards the heart. SR elements are placed in proximity of the extremity of cerebral veins that connect to dural sinuses. Note that if the external pressure is higher than the venous pressure, the SR element collapses completely and does not allow for flow. Moreover, if downstream pressure is lower than the external pressure, flow across the SR element is limited to that given by the pressure difference between the cerebral vein and the external pressure. Table 4.14 shows the pairs of vessels between which a SR element has been placed. Flow rate in individual cerebral veins is always below $1\,ml\,s^{-1}$, therefore we choose to set $R_{SR}^0 = 1\,mmHg\,g\,ml^{-1}\,s$ in order to create a moderate pressure drop across the SR element.

Venous valves

Venous valves are located between two one-dimensional vessels and govern flow across this interface. Here we adopt the model proposed in [122], where variation in time of flow rate across the valve, q_v, is approximated as

$$\frac{dq_v}{dt} = \frac{1}{L} \left(p_{up} - p_{down} - Bq_v|q_v| \right) \,, \tag{4.54}$$

where $p_{up,down}$ are upstream/downstream pressures with respect to valve flow direction. L is a blood inertance term and B is a resistive term due to flow separation. L and B are computed as

$$L = \frac{\rho l_{eff}}{A_{eff}} \,, \quad B = \frac{\rho}{2A_{eff}^2} \,. \tag{4.55}$$

No.	Left vessel index	Right vessel index
1	158	261
2	159	262
3	161	263
4	162	264
5	237	265
6	238	266
7	239	267
8	249	268
9	245	269
10	260	270
11	271	106
12	150	272
13	151	273

Table 4.14: Location of Starling resistor elements in the venous network shown in figure 4.31.

A_{eff} is the effective area of the valve, while l_{eff} is taken to be the diameter of A_{eff}. The effective area varies according to the valve state $\zeta \in (0, 1)$ in the following manner

$$A_{eff} = (A_{eff,max} - A_{eff,min})) \, \zeta(t) + A_{eff,min} \,. \tag{4.56}$$

In order to allow modelling healthy and pathological situations, $A_{eff,min}$ and $A_{eff,max}$ are defined as

$$A_{eff,min} = M_{rg} A_{ann} \,, \quad A_{eff,max} = M_{st} A_{ann} \,. \tag{4.57}$$

A_{ann} is called annulus area and is normally taken as the average of the reference area of the two vessels connected to the valve. As specified in[122], setting $M_{rg} = 0$ and $M_{st} = 1$ corresponds to a healthy valve, while $M_{rg} > 0$ corresponds to an incompetent valve while $M_{st} < 1$ represents a stenotic valve. The valve state ζ is governed by

$$\frac{d\zeta}{dt} = \begin{cases} (1 - \zeta) K_{vo} \left(\Delta p - \Delta p_{vo} \right) \,, & \text{if } \Delta p > \Delta p_{vo} \,, \\ \zeta K_{vc} \left(\Delta p - \Delta p_{vc} \right) \,, & \text{if } \Delta p < \Delta p_{vc} \,, \end{cases} \tag{4.58}$$

where $\Delta p_{vo,vc}$ are opening/closure threshold pressures, here taken to be $\Delta p_{vo} = \Delta p_{vc} = 0 \, mmHg$ and $K_{vo,vc}$ are opening/closure rates taken to be $K_{vo} = K_{vc} = 1.0 \, Pa^{-1} \, s^{-1}$.

4.2.3 Results

In this section, after describing the basic setting of the simulations regarding the spatial discretization and initial conditions, we present the computational results obtained, concentrating our attention on head and neck veins.

Model setting

One-dimensional vessels were divided in non-overlapping segments with a characteristic length of $\Delta x = 1 cm$, imposing however that a single vessel should contain at least 3 computational cells. The one-dimensional blood flow equations (4.47) were solved using a third-order version of the ADER scheme presented in [116], with an average time step $\Delta t = 1.58 \times 10^{-4} \, s$. The friction looses term f was taken as $f = 8 \, \pi \, \mu u / \rho$ with $\mu = 0.0045 \, Pa \, s$ and $\rho = 1060 \, kg/m^3$. At time $t = 0$, $u = 0 \, m/s$ was imposed in the entire network and pressure in each model compartment was set as specified in table 4.15. A periodic solution was obtained after 15-16 cardiac cycles. Results shown in the following sections regard the time interval $18 \, s \leq t \leq 19 \, s$.

Computational results *vs* MRI-derived measurements

Figure 4.33 shows a comparison of computed and MRI-derived average flow rates for a set of selected cerebral vessels. The agreement between model outputs and measured quantities is satisfactory.

Compartment	P_{ini} [mmHg]
Arteries	70.0
Veins	5
Heart chambers & pulmonary compartments	10.0
Arterioles	45.0
Capillaries	25.0
Venules	10.0
Intracranial pressure	9.0

Table 4.15: Inital pressure values for all compartments of the closed-loop model.

A comparison between MRI-derived and computed flow rate waves is shown in figures 4.34 and 4.35, together with computed pressure waves. Again, as for time-averaged quantities, the agreement is satisfactory. We observe the highly pulsatile nature of flow waveforms in neck veins and the progressive reduction of the pulsatility as one moves away from the right atrium.

Starling resistor and intracranial pressure effects in cerebral venous hemodynamics

Figure 4.36 shows the computed pressure in the superior sagittal sinus and in a cerebral vein, together with the intracranial pressure for four model settings. In figure 4.36a we observe the effect of including both, the intracranial pressure and the SR elements. Pressure in cerebral veins is always higher than intracranial pressure, while pressure in the superior sagittal sinus is governed by downstream conditions. If the SR elements are not considered, as shown in figure 4.36b, cerebral veins and the superior sagittal sinus are directly connected. Another consequence of considering SR elements is the higher intracranial pressure values obtained compared to the ones computed when SR elements are not present. These higher values derive from the fact that at the begining of the simulation cerebral veins will inflate until internal pressure exceeds intracranial pressure and only then SR elements will allow circulation of blood across them. Results excluding the time variation of intracranial pressure over time are analogous to the previously discussed ones, see figures 4.36c and 4.36d.

Another interesting effect of SR elements in cerebral venous hemodynamics is the reduction of pulsatility of velocity in cerebral vessels, as shown in figure 4.37. The reduced pulsatility of intracranial pressure as compared to the pulsatility of pressure in the dural sinuses greatly reduces the pulsatility of flow in cerebral veins and, as a consequence, in dural sinuses. This pulsatility reduction improves the agreement between computational results and MRI-derived flow rate waveforms, as shown in figure 4.38.

4.2.4 Discussion

In this section we discuss the results previously presented putting special emphasis in factor contributing to cerebral venous flow waveforms.

Flow distribution

The flow distribution between superior sagittal and straight sinus in this model is mainly determined by the configuration of the microcirculation network and affluent cerebral veins. These networks were constructed taking into account the rather constant ration of flow distribution between superior and straight sinuses, evidenced in [152]. The same inter-subject homogeneity observed for flow distributions ratios between straight and superior sagittal sinuses is not found between left and right transverse sinuses and, consequently, between left and right internal jugular veins [152]. The agreement of flow distribution in these vessels between computational results and MRI-derived data, as shown in figure 4.33, is a result of the patient-specific characterization performed for major head and neck veins, as shown in [117].
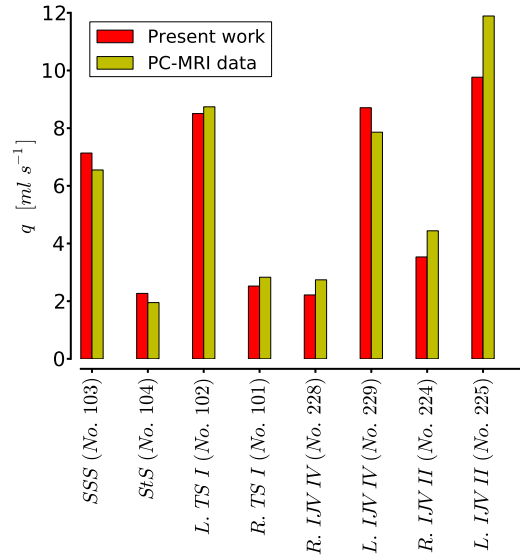
Figure 4.33: Blood flow in head and neck veins: computational results *vs* MRI flow quantification data. SSS: Superior sagittal Sinus; StS: Straight Sinus; TS: Transverse Sinus; IJV: Internal Jugular Vein. Vessel numbers refer to figure 4.31 and table 4.12.

Intracranial pressure

The shape of the intracranial pressure wave is defined by the interaction of variations in CBV and CSF exchange between the cranial and spinal subarachnoid spaces. Based on 65 short-term pressure recordings on patients with a variety of intracranial disorders, Avezaat *et al.* [17] showed that mean pulsatile change in CBV is 1.6 ml (0.36 - 4.38 ml). In our model this value is around 1 ml. Moreover, cerebral arterial plus arteriolar blood volume is 30% of total CBV, while venous plus capillary fraction is around 70%, in accordance with measurements reported in [85]. These distribution pattern was assigned as initial condition and is maintain throughout the cardiac cycle, as shown in figure 4.39. The role played by each vascular compartment in shaping intracranial pressure can be better understood by considering figure 4.40, which shows the time variation of blood volume minus the average blood volume occupied by each compartment. The leading compartment in terms of volume changes is the arteriolar compartment. We recall that this compartment represents the resistance, inertance and compliance of distal arteries and arterioles. On the other hand, veins seem to play a rather passive role, being compressed by high intracranial pressure and expanding during the diastolic phase.

Cerebral venous flow waveforms

The shape of flow rate waveforms in dural sinuses is less pulsatile than venous flow in neck veins [152]. This experimental observation is also found in our MRI measurements and confirmed by our computational results.

Some authors claim that the pulsatility of cerebral venous flow is due to the compression of venous vasculature by intracranial pressure and used this concept to reproduce the jugular venous flow waveforms [92]. The results presented in this work suggest that this phenomenon is influencing cerebral venous flow only marginally and could by no means be the explanation of venous flow waveforms at the level of internal jugular veins. In fact, volume changes in venules and veins over the cardiac cycle are rather modest, as shown in figure 4.40.

The model component that is mainly influencing the shape of cerebral venous flow rate waveforms is the presence of Starling resistor elements at the point where cerebral veins drain into the dural sinuses. These elements guarantee a pressure difference between cerebral veins and dural sinuses that is favorable to flow over the entire cardiac cycle. Removing the SR elements from the network results in highly pulsatile flow in all transverse sinuses, as shown in
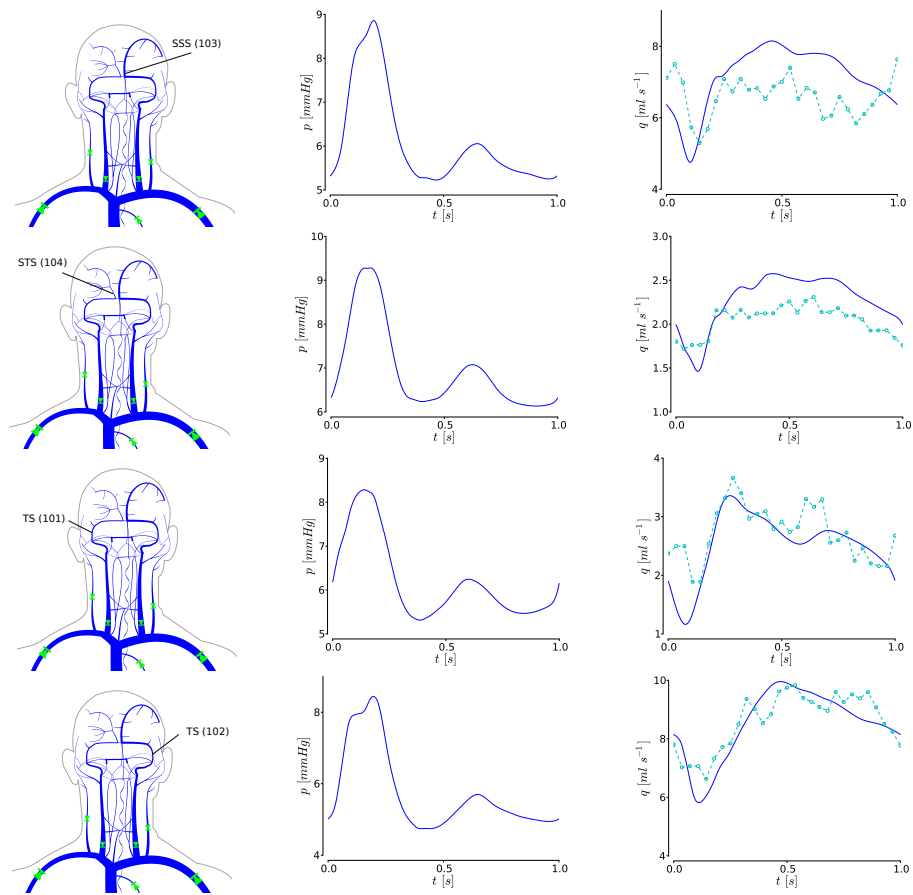
Figure 4.34: Computed pressure and flow rate in dural sinuses. PC-MRI flow quantification data is shown with symbols and dashed lines.
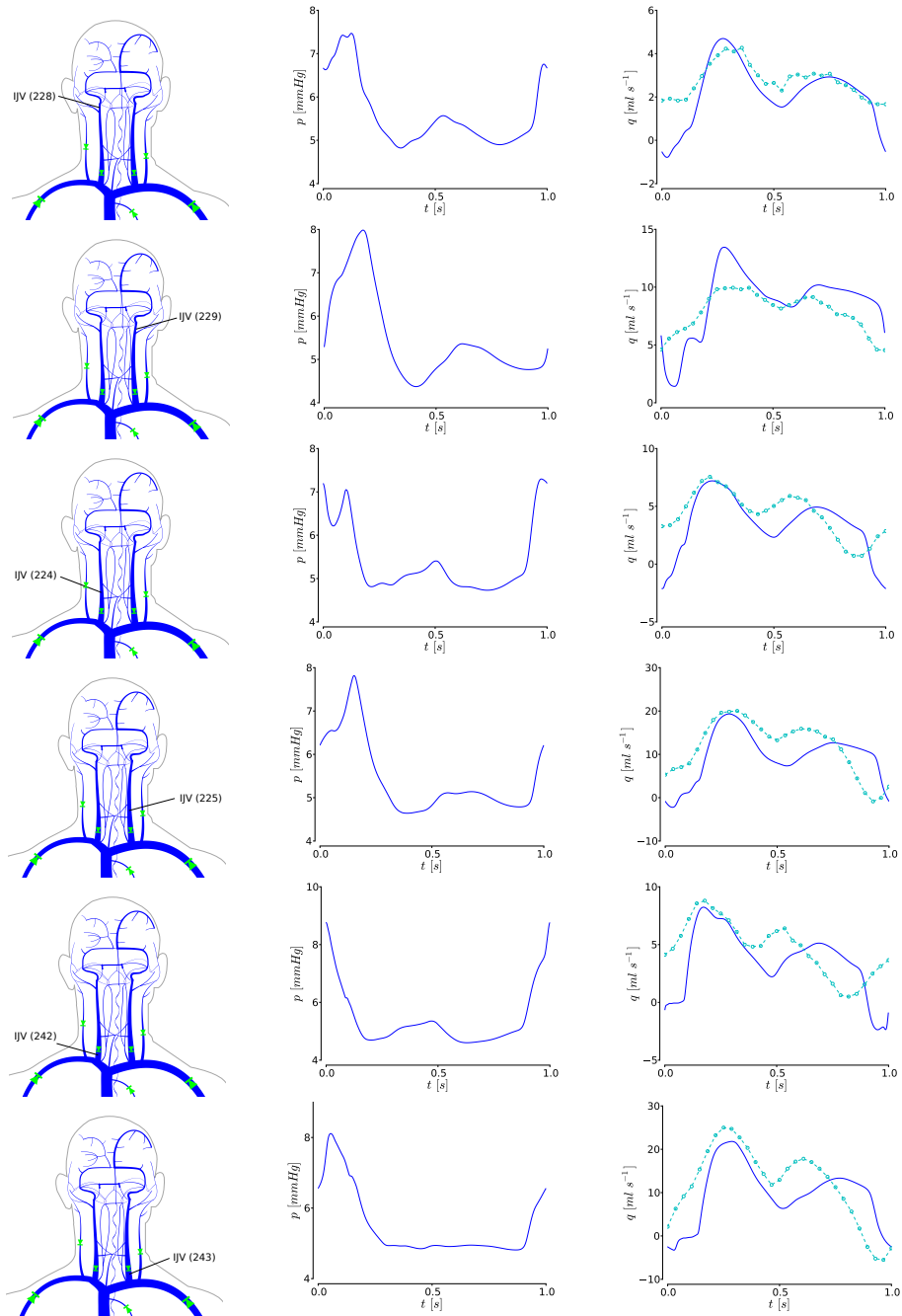
Figure 4.35: Computed pressure and flow rate in internal jugular veins. PC-MRI flow quantification data is shown with symbols and dashed lines.
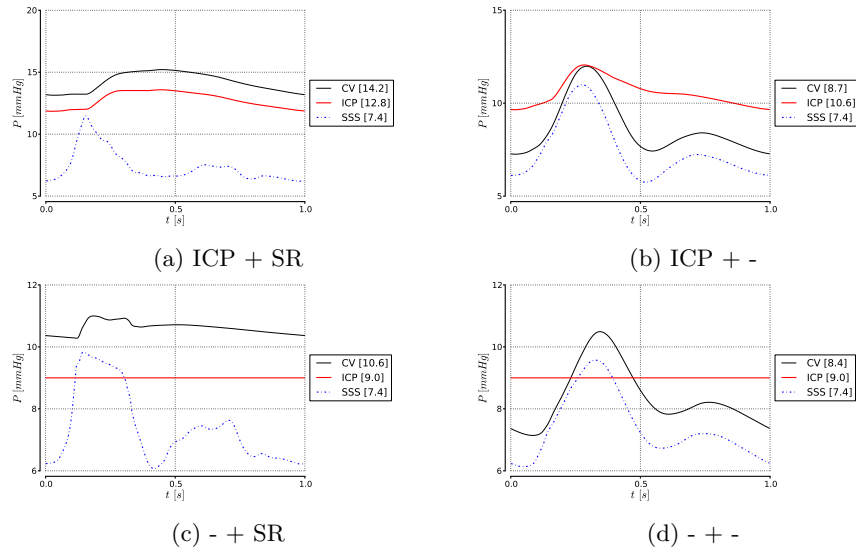
Figure 4.36: Effect of a Starling resistor element and intracranial pressure on computed pressure. CV: cerebral vein (No. 158); ICP: intracranial pressure; SSS: superior sagittal sinus (No. 165).

figure 4.37.

Limitations

A major limitation of this work is the simple representation of intracranial pressure. In fact, our intracranial pressure model admits no spatial variability and pressure changes are affecting all vascular components instantaneously and in the same way. A future model should include an enriched version of the present intracranial pressure model, in order to account for spatial differences in intracranial pressure.

Another aspect that must be improved is the extension of both, the cerebral and venous one-dimensional networks. More extensive networks would allow for a gradual filling of successive generations of vessels and this could contribute to a better description of the intracranial pressure shape.

4.2.5 Concluding remarks

We have extended a closed-loop model for the cardiovascular system with emphasis in the cerebral venous system in order to account for the effect of intracranial pressure and Starling resistor elements on cerebral venous hemodynamics. Computational results were compared to MRI-derived flow measurements. Finally, the major determinants of cerebral venous flow waveforms were studied and discussed. The current model represents a computational tool for the study of pathologies related to extra-cranial venous anomalies and their interaction with intracranial hemodynamics.
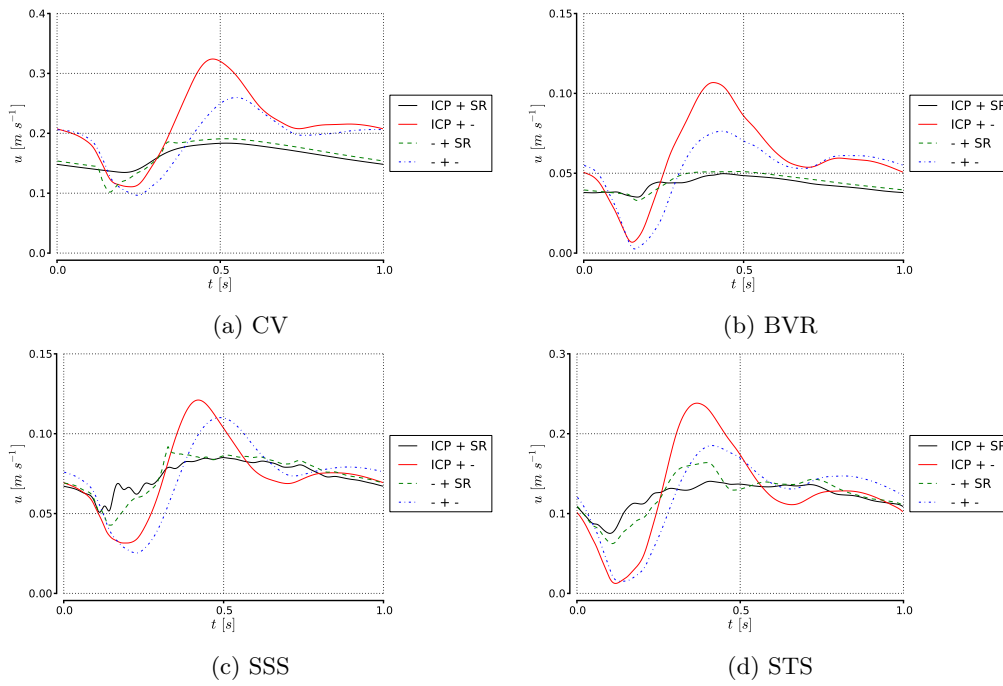
Figure 4.37: Effect of a Starling resistor element and intracranial pressure on computed velocity in cerebral venous vessels. CV: cerebral vein (No. 158); BVR: basal vein of Rosenthal (No. 247); SSS: superior sagittal sinus (No. 165); STS: straight sinus (No. 104).
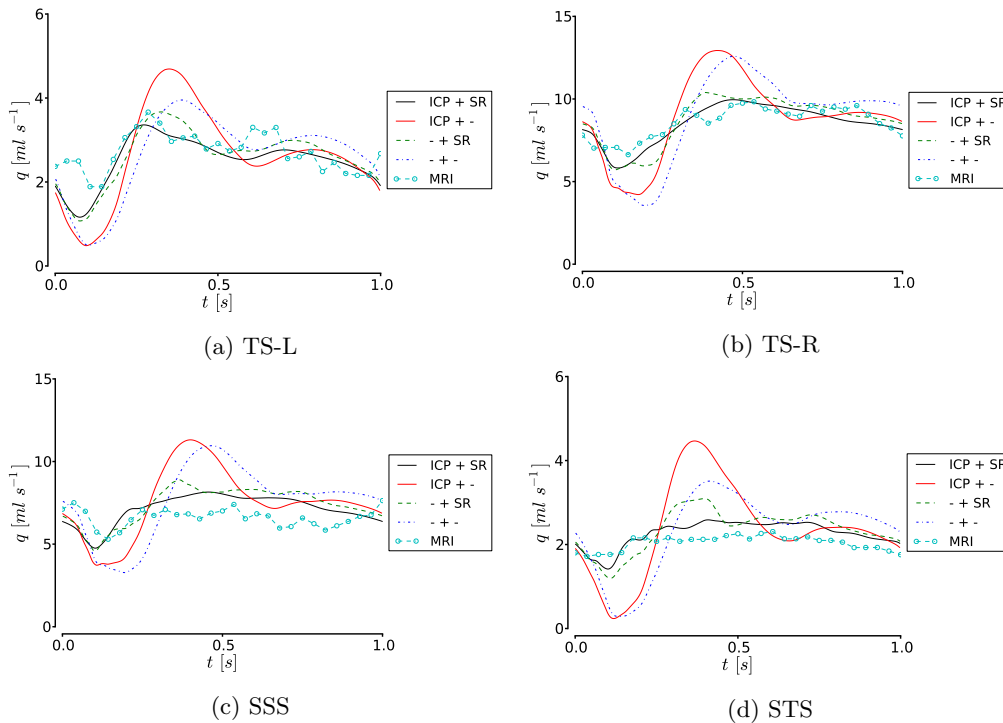
Figure 4.38: Effect of a Starling resistor element and intracranial pressure on computed velocity in dural sinuses. TS-R: right transverse sinus (No. 101); TS-L: left transverse sinus (No. 102); SSS: superior sagittal sinus (No. 103); STS: straight sinus (No. 104).
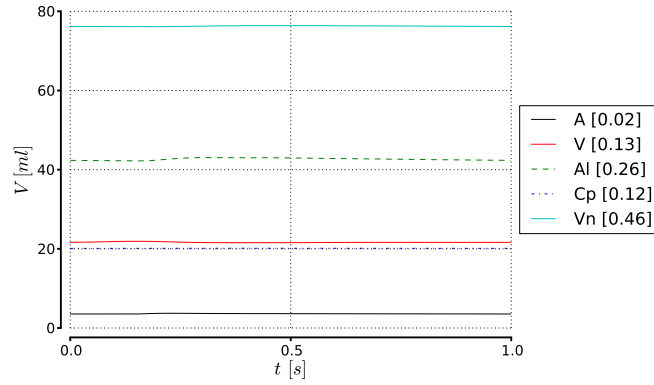
Figure 4.39: Cerebral blood volumes over a cardiac cycle for arteries (A), veins (V), arterioles and distal arteries (Al), capillaries (Cp) and venules (Vn). Values between square brackets represent the average fraction occupied by the respective compartment with respect to total cerebral blood volume.
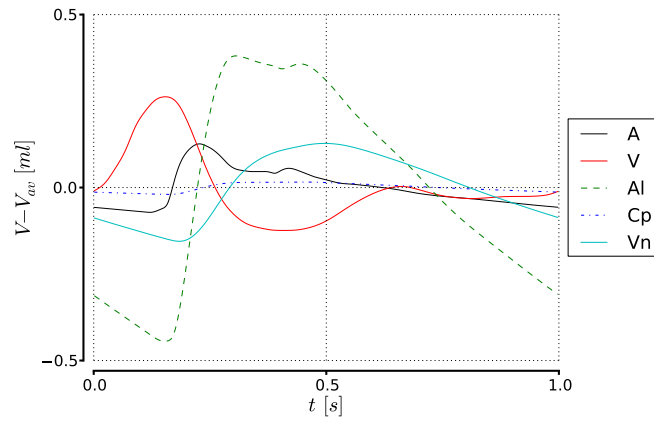
Figure 4.40: Volume variation in time minus average volume over the cardiac cycle for different intracranial vascular compartments.

4.3   Sensitivity analysis

The model presented in this chapter makes use of a large number of parameters, as clearly seen in the previous sections. It is therefore important to explore the sensitivity of the model outputs to variations in parameters. A thorough analysis would require the estimation of the uncertainty of the model outputs based on the non deterministic nature of parameters. Uncertainty quantification in the context of one-dimensional models for blood flow in arterial networks was carried out by Xiu & Sherwin [177] and, recently, by Chen *et al.* [50]. The implementation of the tools described in these works requires a considerable effort and the computational cost is high, making it unfeasible to perform such kind of studies in the context of this thesis.

Here, we limit our study to simply assessing the sensitivity of the model output to controlled variations of parameters, in a similar fashion to the work of Alastruey [1] and of Mynard [121]. Let us call χ one of our reference model outputs and θ one of our reference scalar parameters. Note that χ could be the aortic pressure, the inferior vena cava flow rate, etc. A variation of a parameter from θ to θ_1 will result in a new model output χ_1. If only one parameter is changed, then the difference between χ and χ_1 is a result of the sensitivity of the model output to that parameter. Once that χ and χ_1 are available, we can compute two types of sensitivity: the mean sensitivity and the wave sensitivity.

We define mean sensitivity S_{mean} as

$$S_{mean} = \frac{\bar{\chi}_1 - \bar{\chi}}{\bar{\chi}}, \tag{4.59}$$

where $\bar{\chi}$ is the mean value of the model output χ over a cardiac cycle.

In order to compute the wave sensitivity S_{wave}, we first define

$$\chi' = \frac{\chi - \bar{\chi}}{max(\chi) - min(\chi)}, \quad \chi'_1 = \frac{\chi_1 - \bar{\chi}_1}{max(\chi_1) - min(\chi_1)}, \tag{4.60}$$

where maximum and minimum values of χ and χ_1 are intended over the cardiac cycle. S_{wave} is then defined as

$$S_{wave} = \frac{1}{N} \sqrt{\sum_{k=1}^{k=N} \left(\chi_{1,k} - \chi_k \right)^2}, \tag{4.61}$$

where N is the number of sampling points inside the cardiac cycle.

We have decided to concentrate our sensitivity analysis on the venous portion of the cardiovascular system. This choice is motivated by the fact that other researchers have already carried out similar studies for the arterial system and for the heart [121, 1]. Therefore, we have identified 25 parameters, listed in table 4.16, that could influence blood flow in the venous system, in particular in the head and neck regions. The reference value for these parameters was then increased and decreased by 25%. Furthermore, we considered pressure and flow rate in 6 vessels, as well as the intracranial pressure p_{ic}, as model outputs to be monitored. The chosen vessels are: the ascending aorta (nr. 1); the superior vena cava (nr. 84); the straight sinus (nr. 104); one cortical vein (nr. 158); the superior sagittal sinus, distal portion (nr. 165); the left internal jugular vein (nr. 225).

Tables 4.16 and 4.17 show the mean and wave sensitivities for the investigated parameters and model output signals. The meaning of S_{mean} is clear, since it represents the percentage change in the observed model output. On the other hand, the meaning of S_{wave} is more obscure, as it represents a norm of the difference between the shapes of two waves. In order to clarify its interpretation, in figure 4.41 we show pressure and flow rate for the reference solution, together with solutions showing increasing values of S_{wave}. It is evident that values in the range $|S_{wave}| < 0.001$ regard waveforms with very little variations, while for $|S_{wave}| > 0.004$ waveform changes start to be more pronounced.

The amount of information contained in tables 4.16 and 4.17 is large. Here we summarize the main aspects emerging from their analysis:

- The model output signals are moderately sensitive to inspected parameters in terms of S_{mean}. In fact, most S_{mean} values are below 10%.

- Initial heart chamber pressures, followed by initial arterial and venous pressures are the most influential parameters in terms of S_{mean}. This is an expected behavior. In fact, since ours is a closed-loop model, changing initial pressure values is equivalent to changing the total blood volume of the system.

- Ascending aorta: pressure and flow rate in this vessel are more sensitive to parameters regarding the right ventricle in comparison to those regarding the right atrium, being the baseline elastance E_b the parameter for which both, mean arterial pressure and total blood flow show the highest sensitivity.

- Superior vena cava: this vein is representative of the situation of main systemic veins. Due to its proximity to the heart and its direct connection to the right atrium, the model output at this location is highly sensitive to heart parameters. S_{mean} and S_{wave} values registered for other parameters are low if compared to those observed for other venous segments.

- Internal jugular vein: observing sensitivity in this vessel is representative of the situation encountered in neck veins. We observe that S_{wave} values are almost always below 0.005, showing that waveforms in these veins are not extremely sensitive to the parameters here considered. Nevertheless, an obvious dependence is observed.

- Dural sinuses: observations for these vessels are similar to those related to internal jugular veins. Also in this case S_{wave} values are below 0.005 for almost every parameter.

- Cortical vein: this vessels show a similar S_{mean} sensitivity to the one observed for other venous segments. On the other hand, these vessels show a lower S_{wave} sensitivity if compared to other veins. This might be explained by the fact that flow and pressure in these vessels are strongly linked to the intracranial pressure.

- Intracranial pressure: it is interesting to observe that intracranial pressure is more sensitive to changes in some heart parameters and vein tube law parameters than to changes in the capacitance of intracranial lumped compartments. As expected, the dependence of intracranial pressure on parameters like k_e is rather high. Also its high dependence on the initial value used for the intracranial pressure is evident. All these considerations regard the S_{mean} sensitivity. Intracranial pressure S_{wave} sensitivity to the parameters taken for this study is very low.

- Viscosity: blood viscosity has shown to be more relevant for veins than for arteries, in terms of S_{mean} sensitivity. In turn, it appears to have almost no effect on waveforms, as shown by its low S_{wave} values for all observed model outputs.
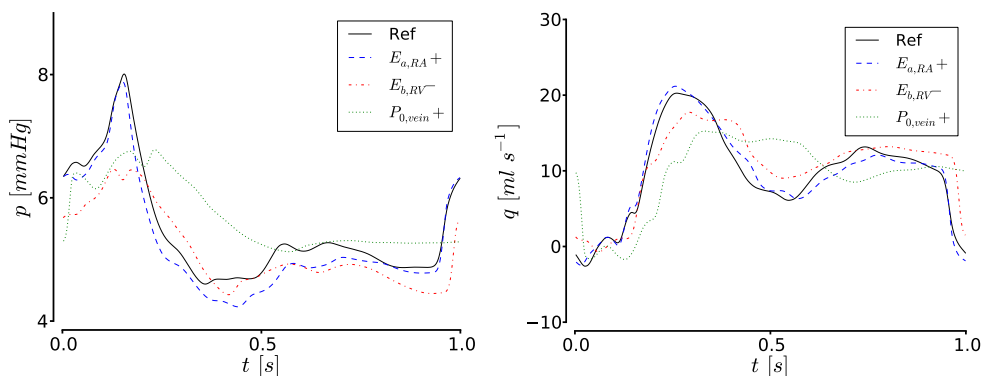
Figure 4.41: Pressure and flow rate for the left internal jugular vein (nr. 225) for the reference model output and for three cases with different S_{wave} values. $S_{wave} = 0.002$ for case $E_{a,RA}+$, $S_{wave} = 0.006$ for case $E_{b,RV}-$ and $S_{wave} = 0.010$ for case $P_{0,vein}+$.

Parameter	P_1	Q_1	P_{84}	Q_{84}	P_{104}	Q_{104}	P_{158}	Q_{158}	P_{165}	Q_{165}	P_{225}	Q_{225}	p_{ic}
$E_{a,RA}+$	-0.002	-0.001	**-0.031**	0.008	**-0.029**	-0.001	-0.003	-0.001	**-0.028**	-0.001	**-0.040**	0.006	-0.003
$E_{a,RA}-$	0.003	0.001	**0.040**	-0.002	**0.038**	0.003	0.004	0.003	**0.038**	0.003	**0.053**	**0.013**	0.005
$E_{a,RV}+$	**0.021**	**0.024**	**-0.058**	**0.027**	**-0.027**	**0.023**	**0.010**	**0.023**	**-0.021**	**0.023**	**-0.037**	**0.015**	0.009
$E_{a,RV}-$	**-0.031**	**-0.038**	**0.089**	**-0.042**	**0.043**	**-0.034**	**-0.015**	**-0.036**	**0.035**	**-0.036**	**0.060**	**-0.013**	-0.013
$E_{b,RA}+$	-0.002	-0.005	**0.036**	-0.009	**0.037**	-0.003	0.002	-0.003	**0.036**	-0.003	**0.053**	0.003	0.002
$E_{b,RA}-$	0.001	0.003	**-0.048**	0.018	**-0.046**	0.002	-0.002	0.002	**-0.045**	0.002	**-0.067**	**0.021**	-0.003
$E_{b,RV}+$	**-0.057**	**-0.067**	0.102	**-0.072**	**0.039**	**-0.063**	**-0.030**	**-0.064**	**0.027**	**-0.064**	**0.060**	**-0.032**	-0.027
$E_{b,RV}-$	**0.087**	**0.096**	-0.104	0.105	**-0.028**	**0.094**	**0.048**	**0.096**	**-0.018**	**0.096**	**-0.060**	**0.097**	0.043
$\alpha_{RA}+$	-0.001	-0.001	0.005	-0.003	0.006	-0.001	-0.000	-0.001	0.005	-0.001	0.008	-0.001	-0.000
$\alpha_{RA}-$	0.001	0.002	-0.006	0.004	-0.006	0.001	0.000	0.001	-0.006	0.001	-0.009	0.002	0.000
$\alpha_{RV}+$	-0.006	-0.008	**0.023**	-0.011	**0.010**	-0.006	-0.003	-0.006	0.008	-0.006	**0.014**	-0.002	-0.002
$\alpha_{RV}-$	0.005	0.005	**-0.021**	0.005	**-0.010**	0.006	0.002	0.006	-0.008	0.006	**-0.013**	0.001	0.002
$K_{vo}+$	0.000	0.000	0.000	0.000	-0.000	0.000	-0.000	0.000	-0.000	0.000	-0.000	0.001	-0.000
$K_{vo}-$	-0.000	-0.000	-0.000	-0.000	0.000	-0.000	0.000	-0.000	0.000	-0.000	0.000	-0.001	0.000
$K_{vc}+$	0.000	0.000	0.000	0.002	-0.004	0.000	-0.000	0.000	-0.004	0.000	-0.005	0.000	-0.000
$K_{vc}-$	0.000	-0.000	-0.001	-0.001	0.007	-0.000	0.001	-0.000	0.006	-0.000	0.009	0.006	0.001
$c_{0,sinuses}+$	0.000	-0.000	-0.000	-0.000	-0.009	-0.001	0.008	-0.001	**-0.012**	-0.001	-0.001	0.002	0.009
$c_{0,sinuses}-$	-0.000	0.000	0.000	0.000	**0.020**	0.002	**-0.014**	0.002	**0.027**	0.002	0.001	-0.002	**-0.015**
$c_{0,min}+$	0.002	0.001	0.003	-0.001	0.001	0.003	-0.007	0.005	0.000	0.004	-0.000	0.008	-0.008
$c_{0,min}-$	0.001	0.001	**-0.019**	0.005	-0.008	0.000	0.009	-0.001	-0.004	-0.001	-0.003	**-0.014**	0.008
$c_{0,max}+$	0.006	0.007	**-0.013**	0.009	-0.005	**0.014**	**-0.060**	**0.019**	-0.006	**0.018**	**-0.011**	**0.031**	**-0.065**
$c_{0,max}-$	0.002	0.001	**-0.022**	0.000	**-0.017**	0.004	**0.048**	**-0.011**	**-0.012**	-0.008	**-0.014**	**-0.032**	**0.036**
$P_{0,vein}+$	**-0.020**	**-0.025**	**-0.046**	0.007	**0.023**	**-0.016**	-0.007	**-0.025**	**0.029**	**-0.024**	**0.042**	**-0.037**	-0.013
$P_{0,vein}-$	0.009	**0.012**	**-0.010**	0.004	**-0.017**	0.008	-0.007	**0.014**	**-0.014**	0.013	**-0.015**	**0.018**	-0.005
k_e+	0.005	0.004	**-0.018**	0.002	-0.009	-0.004	**0.063**	-0.004	-0.007	-0.004	**-0.012**	-0.007	**0.070**
k_e-	0.004	0.005	**-0.017**	0.008	-0.008	**0.015**	**-0.061**	**0.015**	-0.006	**0.015**	-0.010	0.008	**-0.070**
R_{SR}^0+	0.005	0.004	**-0.018**	0.003	-0.009	0.005	**0.027**	0.001	-0.008	0.001	**-0.011**	-0.003	**0.011**
R_{SR}^0-	0.004	0.005	**-0.017**	0.006	-0.008	0.005	**-0.023**	0.009	-0.006	0.010	**-0.011**	0.004	-0.008
$\mu+$	0.010	-0.000	**-0.024**	-0.013	**0.040**	-0.014	0.006	**-0.022**	**0.048**	**-0.021**	-0.010	**-0.017**	0.001
$\mu-$	-0.000	**0.011**	**-0.011**	**0.028**	**-0.059**	**0.026**	-0.001	**0.034**	**-0.064**	**0.034**	**-0.011**	**0.019**	0.003
$C_{Vn,head}+$	0.005	0.006	**-0.018**	0.006	-0.008	0.002	**0.022**	0.002	-0.007	0.002	**-0.011**	-0.001	**0.025**
$C_{Vn,head}-$	0.005	0.006	**-0.018**	0.008	-0.008	0.009	**-0.018**	0.009	-0.007	0.009	**-0.011**	0.006	**-0.021**
$C_{Cp,head}+$	0.005	0.004	**-0.017**	0.005	-0.008	0.005	0.002	0.005	-0.007	0.005	**-0.011**	0.001	0.002
$C_{Cp,head}-$	0.005	0.004	**-0.017**	0.005	-0.008	0.005	0.002	0.005	-0.007	0.005	**-0.011**	0.001	0.001
$C_{Al,head}+$	0.005	0.004	**-0.017**	0.004	-0.008	0.004	0.007	0.004	-0.007	0.004	**-0.010**	-0.001	0.008
$C_{Al,head}-$	0.005	0.005	**-0.017**	0.005	-0.009	0.006	-0.003	0.006	-0.008	0.006	**-0.012**	0.002	-0.004
$P_{ini,A}+$	**0.023**	**0.024**	0.005	**0.025**	0.012	**0.026**	0.007	**0.026**	0.013	**0.026**	0.008	**0.025**	0.005
$P_{ini,A}-$	**-0.012**	**-0.013**	**-0.039**	**-0.012**	**-0.027**	**-0.014**	-0.002	**-0.014**	**-0.025**	**-0.014**	**-0.029**	**-0.020**	-0.001
$P_{ini,V}+$	**0.024**	**0.025**	0.009	**0.026**	0.014	**0.034**	**-0.029**	**0.034**	0.015	**0.034**	0.012	**0.030**	-0.036
$P_{ini,V}-$	**-0.036**	**-0.039**	**-0.071**	**-0.038**	**-0.055**	**-0.045**	0.014	**-0.046**	**-0.052**	**-0.046**	**-0.056**	**-0.053**	0.020
$P_{ini,Heart}+$	0.170	0.173	0.205	0.172	0.186	0.182	0.114	0.184	0.188	0.184	0.191	0.189	0.106
$P_{ini,Heart}-$	-0.169	-0.174	-0.230	-0.162	-0.187	-0.182	-0.106	-0.184	-0.180	-0.184	-0.179	-0.195	-0.098
$P_{ini,Al}+$	**0.014**	**0.015**	-0.004	**0.017**	0.004	**0.026**	**-0.056**	**0.026**	0.005	**0.026**	0.001	**0.021**	**-0.065**
$P_{ini,Al}-$	-0.004	-0.005	**-0.031**	-0.006	**-0.020**	**-0.016**	**0.064**	**-0.016**	**-0.018**	**-0.016**	**-0.023**	**-0.018**	**0.073**
$P_{ini,Cp}+$	0.010	**0.010**	**-0.010**	0.010	-0.002	**0.012**	0.002	**0.012**	-0.001	**0.012**	-0.005	0.008	0.001
$P_{ini,Cp}-$	-0.001	-0.001	**-0.024**	-0.001	**-0.014**	-0.001	0.002	-0.001	**-0.013**	-0.001	**-0.017**	-0.006	0.003
$P_{ini,Vn}+$	0.008	0.009	**-0.012**	0.010	-0.004	**0.015**	**-0.029**	**0.015**	-0.002	**0.015**	-0.006	0.009	**-0.034**
$P_{ini,Vn}-$	0.000	0.000	**-0.025**	0.000	**-0.015**	-0.007	**0.044**	-0.007	**-0.013**	-0.007	**-0.017**	-0.009	**0.050**
$P_{ini,ICP}+$	0.008	0.001	**-0.020**	-0.011	**-0.013**	-0.042	0.306	-0.042	-0.011	-0.042	**-0.017**	-0.037	0.345
$P_{ini,ICP}-$	0.002	0.008	**-0.015**	0.019	-0.005	0.043	-0.268	0.035	-0.004	0.034	-0.006	0.038	-0.318

Table 4.16: Mean sensitivity S_{mean} for pressure and flow rate in the ascending aorta and several veins. Numbers refer to tables 4.3 and 4.8.

Parameter	P_1	Q_1	P_{84}	Q_{84}	P_{104}	Q_{104}	P_{158}	Q_{158}	P_{165}	Q_{165}	P_{225}	Q_{225}	p_{ic}
$E_{a,RA}+$	0.000	0.000	0.001	0.002	0.002	0.001	0.000	0.000	0.002	0.001	0.002	0.002	0.000
$E_{a,RA}-$	0.000	0.000	0.002	**0.003**	0.002	0.002	0.000	0.000	0.003	0.002	0.003	0.002	0.000
$E_{a,RV}+$	0.000	0.000	0.001	0.002	0.003	0.002	0.001	0.000	**0.003**	0.003	0.003	0.003	0.001
$E_{a,RV}-$	0.000	0.000	0.001	0.002	**0.003**	**0.003**	0.001	0.002	**0.004**	**0.003**	**0.003**	**0.004**	0.001
$E_{b,RA}+$	0.000	0.000	0.002	**0.003**	0.003	0.002	0.001	0.000	**0.004**	0.002	**0.003**	0.003	0.001
$E_{b,RA}-$	0.000	0.000	0.002	0.002	0.003	0.002	0.001	0.000	0.003	0.002	0.002	0.003	0.001
$E_{b,RV}+$	0.000	0.000	0.001	0.002	**0.004**	**0.004**	0.001	0.002	**0.005**	**0.004**	**0.004**	**0.004**	0.001
$E_{b,RV}-$	0.000	0.000	0.001	**0.004**	**0.005**	**0.004**	0.001	0.000	**0.006**	**0.004**	**0.006**	**0.005**	0.001
$\alpha_{RA}+$	0.000	0.000	0.001	0.001	0.001	0.000	0.000	0.000	0.001	0.000	0.001	0.001	0.000
$\alpha_{RA}-$	0.000	0.000	0.001	0.001	0.001	0.001	0.000	0.000	0.001	0.001	0.001	0.001	0.000
$\alpha_{RV}+$	0.000	0.000	0.000	0.001	0.001	0.001	0.000	0.000	0.001	0.001	0.001	0.001	0.000
$\alpha_{RV}-$	0.000	0.000	0.000	0.001	0.001	0.001	0.000	0.000	0.001	0.001	0.001	0.001	0.000
$K_{vo}+$	0.000	0.000	0.000	0.000	0.000	0.000	0.000	0.000	0.000	0.000	0.000	0.000	0.000
$K_{vo}-$	0.000	0.000	0.000	0.000	0.000	0.000	0.000	0.000	0.000	0.000	0.000	0.000	0.000
$K_{vc}+$	0.000	0.000	0.000	0.001	0.001	0.001	0.000	0.000	0.001	0.001	0.001	0.001	0.000
$K_{vc}-$	0.000	0.000	0.000	0.001	0.001	0.001	0.000	0.000	0.001	0.001	0.001	0.001	0.000
$c_{0,sinuses}+$	0.000	0.000	0.000	0.000	0.002	0.003	0.001	0.000	**0.004**	**0.003**	0.000	0.001	0.001
$c_{0,sinuses}-$	0.000	0.000	0.000	0.000	0.003	0.003	0.003	0.000	**0.005**	**0.005**	0.001	0.001	**0.003**
$c_{0,min}+$	0.000	0.000	0.000	0.001	0.003	0.003	0.001	0.000	**0.004**	**0.003**	0.003	**0.003**	0.001
$c_{0,min}-$	0.000	0.000	0.002	0.002	**0.004**	**0.003**	0.001	0.000	**0.005**	**0.004**	**0.004**	**0.004**	0.001
$c_{0,max}+$	0.000	0.000	0.000	0.001	0.002	0.003	0.001	0.003	**0.003**	0.002	0.002	0.003	0.001
$c_{0,max}-$	0.000	0.000	0.000	0.002	**0.004**	**0.004**	0.001	0.002	**0.004**	**0.004**	**0.004**	**0.004**	0.001
$P_{0,vein}+$	0.000	0.000	0.003	**0.004**	**0.011**	**0.008**	0.002	0.000	**0.010**	**0.004**	**0.010**	**0.011**	0.002
$P_{0,vein}-$	0.000	0.000	0.001	0.002	**0.006**	**0.005**	0.002	0.000	**0.007**	**0.005**	**0.005**	**0.006**	0.002
k_e+	0.000	0.000	0.000	0.001	0.001	0.001	0.001	0.000	0.001	0.001	0.001	0.001	0.000
k_e-	0.000	0.000	0.000	0.001	0.001	0.001	0.001	0.001	0.001	0.001	0.001	0.001	0.000
$R^0_{SR}+$	0.000	0.000	0.000	0.001	0.001	0.001	0.000	0.000	0.001	0.001	0.001	0.001	0.000
$R^0_{SR}-$	0.000	0.000	0.000	0.001	0.001	0.001	0.001	0.000	0.001	0.001	0.001	0.001	0.000
$\mu+$	0.000	0.000	0.000	0.001	0.001	0.001	0.000	0.001	0.001	0.001	0.001	0.001	0.000
$\mu-$	0.000	0.000	0.000	0.001	0.001	0.001	0.001	0.001	0.001	0.001	0.001	0.001	0.001
$C_{Vn,head}+$	0.000	0.000	0.000	0.000	0.001	0.001	0.001	0.001	0.001	0.001	0.001	0.001	0.001
$C_{Vn,head}-$	0.000	0.000	0.000	0.001	0.001	0.001	0.001	0.002	0.001	0.001	0.001	0.001	0.001
$C_{Cp,head}+$	0.000	0.000	0.000	0.001	0.001	0.001	0.000	0.000	0.001	0.001	0.001	0.001	0.000
$C_{Cp,head}-$	0.000	0.000	0.000	0.001	0.001	0.001	0.000	0.000	0.001	0.001	0.001	0.001	0.000
$C_{Al,head}+$	0.000	0.000	0.000	0.001	0.001	0.001	0.001	0.001	0.001	0.001	0.001	0.001	0.001
$C_{Al,head}-$	0.000	0.000	0.000	0.001	0.001	0.001	0.002	0.002	0.002	0.002	0.001	0.001	0.002
$P_{ini,A}+$	0.000	0.000	0.000	0.000	0.000	0.000	0.000	0.000	0.000	0.000	0.000	0.000	0.000
$P_{ini,A}-$	0.000	0.000	0.000	0.001	0.001	0.001	0.000	0.000	0.002	0.002	0.002	0.002	0.000
$P_{ini,V}+$	0.000	0.000	0.000	0.000	0.000	0.001	0.000	0.001	0.000	0.001	0.000	0.000	0.000
$P_{ini,V}-$	0.000	0.000	0.001	0.002	0.003	0.002	0.001	0.000	**0.003**	0.003	0.003	**0.003**	0.001
$P_{ini,Heart}+$	0.001	0.001	0.001	0.002	**0.006**	**0.005**	0.002	0.002	**0.007**	**0.005**	**0.005**	**0.006**	0.003
$P_{ini,Heart}-$	0.001	0.000	0.002	**0.004**	**0.009**	**0.007**	0.002	0.000	**0.009**	**0.005**	**0.009**	**0.009**	0.002
$P_{ini,Al}+$	0.000	0.000	0.000	0.000	0.000	0.001	0.000	0.002	0.001	0.001	0.000	0.000	0.000
$P_{ini,Al}-$	0.000	0.000	0.000	0.001	0.001	0.001	0.000	0.000	0.001	0.001	0.001	0.001	0.000
$P_{ini,Cp}+$	0.000	0.000	0.000	0.000	0.000	0.000	0.000	0.000	0.001	0.001	0.001	0.001	0.000
$P_{ini,Cp}-$	0.000	0.000	0.000	0.001	0.001	0.001	0.000	0.000	0.001	0.001	0.001	0.001	0.000
$P_{ini,Vn}+$	0.000	0.000	0.000	0.000	0.001	0.001	0.000	0.000	0.001	0.001	0.001	0.001	0.000
$P_{ini,Vn}-$	0.000	0.000	0.000	0.001	0.001	0.001	0.000	0.000	0.001	0.001	0.001	0.001	0.000
$P_{ini,ICP}+$	0.000	0.000	0.000	0.000	0.001	0.002	0.001	0.000	0.001	0.001	0.001	0.001	0.000
$P_{ini,ICP}-$	0.000	0.000	0.000	0.001	**0.005**	**0.006**	**0.008**	**0.004**	**0.006**	**0.005**	0.001	0.002	0.002

Table 4.17: Wave sensitivity S_{wave} for pressure and flow rate in the ascending aorta and several veins. Numbers refer to tables 4.3 and 4.8.

Chapter 5

Study of hemodynamical aspects of CCSVI

5.1 Introduction

The recent description of the Chronic Cerebro-Spinal Venous Insufficiency (CCSVI) condition by Zamboni *et al.* [183, 181] and, especially, its association to a neurodegenerative disease like Multiple Sclerosis, has pointed the attention of the international medical community to the role played by the venous system in the etiology of a wide range of neurological diseases [25]. For example, Bateman has linked the cerebral venous system to the development of Idiopathic Intracranial Hypertension [22], Normal Pressure Hydrocephalus [21] and senile dementia [23]. Another interesting case is the work by Andeweg, that has found that cerebral venous obstruction can cause hydrocephalus under certain conditions [8, 9]. All these examples have motivated the usage of mathematical tools to improve our understanding on physiological and pathological aspects of the venous system. Besides works carried out using lumped parameter models, like the work by Stevens *et al.* [150], where they studied the effect of cerebral venous thrombosis on intracranial pressure, this is, to the best of our knowledge, the first study where one-dimensional models are used to study a venous pathology regarding the cerebro-spinal venous system.

The diagnosis of the CCSVI condition is based in five criteria. The difficulty in assessing these criteria is most probably at the base of the highly heterogeneous results obtained by researchers around the world on the association between this disease and Multiple Sclerosis. The five CCSVI diagnosis criteria are [183]:

1. reflux in internal jugular veins and/or vertebral veins in supine and upright posture;

2. reflux in deep cerebral veins (basal vein of Rosenthal, internal cerebral veins, vein of Galen, etc.);

3. high-resolution B-mode evidence of internal jugular vein stenoses;

4. flow not Doppler-detectable in the internal jugular veins and/or vertebral veins;

5. reverted postural control of main cerebral venous outflow pathways.

If two criteria are fulfilled by a patient, a selective catheter venography is performed to confirm the non-invasive assessment. In case of the detection of impaired flow, a percutaneous transluminal angioplasty is performed in order to re-establish normal flow. As previously said, the aspect that made this venous pathology of such a high interest in the medical community and also in the mass-media is that it was associated to Multiple Sclerosis, a neurological disease. In their first open-label study on 65 Multiple Sclerosis patients, Zamboni *et al.* [183] found that 90% of the examined patients were positive for CCSVI, whereas non of the 235 controls was diagnosed for CCSVI.

After the seminal work by Zamboni and coworkers the research on the role played by the cerebral venous system has literally exploded. Several studies have confirmed Zamboni's hypothesis on the association of CCSVI to Multiple Sclerosis whereas many others have found

no association between both pathologies. Currently, an animated debate is taking place in the medical community with many researchers speaking in favor of Zamboni's results and many being completely against this association. In any case, a meta-analysis study, that took into account all available studies on CCSVI and Multiple Sclerosis, has shown that there is a strong association between both diseases [96].

The effort of researchers in the field of medical sciences is directed to confirm/refuse the association between both diseases. However, the extent of the impact of extracranial venous anomalies on cerebral venous hemodynamics remains largely unknown and poorly explored. In this context, the use of mathematical models based on first principles could be of fundamental importance for improving our understanding on the physiology of cerebral venous return and the consequences of altered cerebral venous flow patterns on the central nervous system.

In this work we perform a first theoretical study of the CCSVI condition. We concentrate on purely hydraulic effects, neglecting the role that regulatory systems like the baroreflex or cerebral blood flow autoregulation possibly play. We follow two different strategies. First, we consider a healthy venous network and perturb its geometry by artificially introducing stenoses at certain locations in order to compare the hemodynamical states associated to the different venous configurations. Then, we use the geometry of a real Multiple Sclerosis patient to characterize the venous network of our model and perform a comparison of results obtained with the network of the healthy control and that of the Multiple Sclerosis patient.

The rest of this chapter is structured as follows. After briefly reviewing our mathematical model of the cardiovascular system in section 5.2, we report our computational results in section 5.3. After a discussion on the results obtained, reported in section 5.4, we conclude with section 5.5, where final remarks are made.

5.2 Mathematical model of the cardiovascular system

Our model is composed by one-dimensional networks of major arteries and veins, while lumped parameter models are used for the heart, the pulmonary circulation and capillary beds linking arteries and veins (see figure 5.1). A distinct aspect of this model is that geometrical information for major head and neck veins were obtained from the segmentation of MRI data. This patient-specific characterization allowed us to compare computational results *vs.* patient-specific MRI-derived flow quantification data, as reported in [117]. The model also takes into account the pulsation of intracranial pressure and the presence of Starling resistor elements at the point where cerebral veins drain into dural sinuses. Full details on the construction of this model are provided in [117] and [115].

One-dimensional blood flow in elastic vessels is described by the following first-order, non-linear hyperbolic system

$$\begin{cases} \partial_t A + \partial_x q = 0 \,, \\ \partial_t q + \partial_x \left(\hat{\alpha} \dfrac{q^2}{A} \right) + \dfrac{A}{\rho} \partial_x p = -f \,, \end{cases} \tag{5.1}$$

where x is the axial coordinate along the longitudinal axis of the vessel; t is time; $A(x,t)$ is the cross-sectional area of the vessel; $q(x,t)$ is the flow rate; $p(x,t)$ is the average internal pressure over a cross-section; $f(x,t)$ is the friction force per unit length of the tube; ρ is the fluid density and $\hat{\alpha}$ is a coefficient that depends on the assumed velocity profile. Throughout this work we will take $\hat{\alpha} = 1$, which corresponds to a blunt velocity profile.

To close the system we adopt a tube law, whereby the internal pressure $p(x,t)$ is related to the cross-sectional area $A(x,t)$ and other parameters, namely

$$p(x,t) = p_e(x,t) + K(x) \left[\left(\dfrac{A(x,t)}{A_0(x)} \right)^m - \left(\dfrac{A(x,t)}{A_0(x)} \right)^n \right] + P_0 \,. \tag{5.2}$$

Here $p_e(x,t)$ is the external pressure, prescribed, $K(x)$, m, n and $A_0(x)$ are parameters that take into account mechanical and geometrical properties of the vessel. For a discussion on the choice of these parameters for both, arteries and veins, the reader is referred to [117] and references therein.

The only element of the model that was not previously presented regards the treatment of stenotic vessels. In the next section we explain how these vessels are treated.
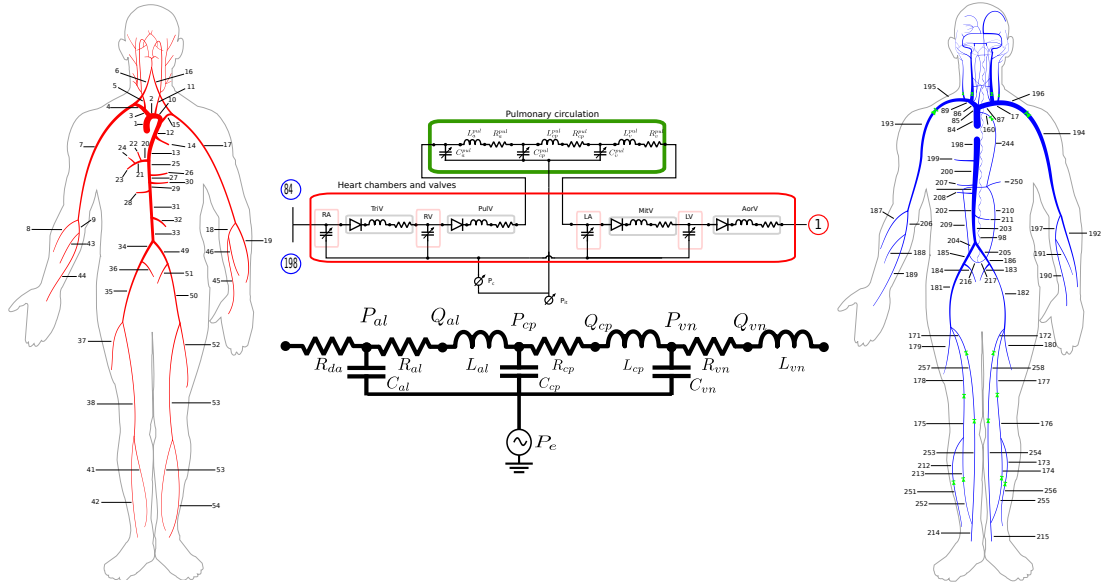
Figure 5.1: Schematic representation of the closed-loop model presented in [117]. Major arteries and veins are described with a one-dimensional model, whereas heart, pulmonary circulation, arterioles, capillaries and venules are treated as lumped parameter models

5.2.1 Stenoses

In the case of a stenosis, an additional source term is included in the second equation of system (5.1). We use the expression proposed in [139] in which the additional term accounting for energy loss at the stenosis is

$$f_{STENO} = N \frac{Q}{A} \tag{5.3}$$

with

$$N = \frac{Q \, K_{STENO}}{2 \, L}, \tag{5.4}$$

where L is the length of the stenotic portion of the vessel and K_{STENO} is given by

$$K_{STENO} = 2 \left\{ \frac{K_v}{Re_0} + \frac{K_t}{2} \left(\frac{S_0}{S_1} - 1 \right)^2 \right\} \left(\frac{S_1}{S_0} \right)^2 . \tag{5.5}$$

Re_0 is the Reynolds number in the unobstructed section (upstream of the stenosis), S_0 is the unobstructed cross-sectional area, S_1 is the stenosed cross-sectional area, K_v represents viscous losses and K_t is related to turbulent effects. As proposed in [139], K_v is

$$K_v = 32 \frac{L_a}{D_0} \left(\frac{S_0}{S_1} \right)^2 , \tag{5.6}$$

with

$$L_a = 0.83L + 1.64D_1 . \tag{5.7}$$

K_t takes fixed value of $K_t = 1.52$. f_{STENO} is applied to all computational cells within the stenotic portion of the vessel. For details on this methodology for incorporating the effect of stenoses in one-dimensional blood flow models see [139] or the more recent work in [148].
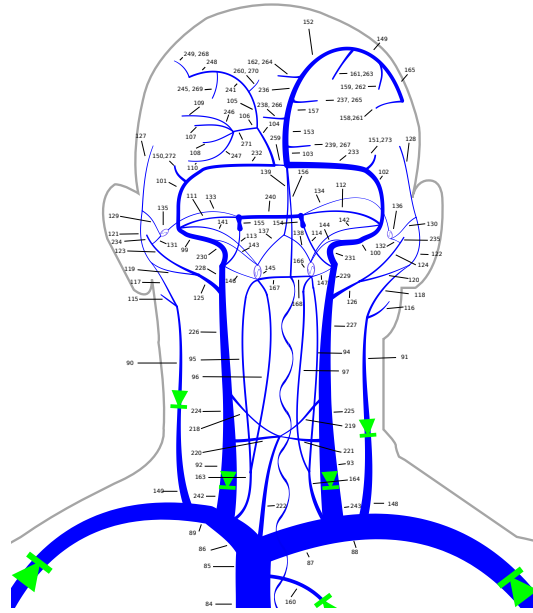
Figure 5.2: Head and neck veins. Numbers refer to those used in table VIII of [117], where geometrical and mechanical parameters for each vessel are reported.

5.3   Results

We have followed two different strategies in order to assess the impact of extracranial stenoses on cerebral hemodynamics. In the first case we consider our standard venous network, which corresponds to a healthy subject with a high level of collateralization, and artificially construct stenoses in the internal jugular veins. In the second case we consider a real Multiple Sclerosis patient that presents an altered extracranial venous network. Following the approach described in [117], we characterize our venous network with the patient's geometry and run our model on the modified network in order to assess the differences between the hemodynamical states of the healthy subject and the Multiple Sclerosis patient.

5.3.1   Effect of stenoses on a reference venous network

Zamboni *et al.* [183] identified four CCSVI patterns. We want to study the hemodynamical impact of two of such configurations by modifying our standard venous network and observing the impact of the altered geometry on cerebral venous hemodynamics. We introduce a stenosis by reducing the reference cross-sectional area of the vessel A_0 to a stenotic reference area $A_0^s = 0.1\,A_0$ and by adding an additional dissipative source term to the momentum equation, as explained in section 5.2.1. Stenoses are placed at locations shown in figure 5.3. Case A regards a CCSVI pattern where one internal jugular vein and the azygous vein are stenotic, whereas in case B both internal jugular veins and the azygous vein are stenotic. The stenosis length is always of $L = 2\,cm$ and stenotic vessels are discretized using a characteristic mesh length of $\Delta x = 0.1\,cm$. All other model setting specifications are identical to the ones reported in section 4.2.

In figure 5.4 we show the computed pressure and flow rate for the healthy control and both CCSVI cases at post- and pre-stenotic locations. Pressure drops between these two locations are almost negligible in the case of the healthy subject, whereas in the case of a stenotic vessels mean pressures experience a drop of around $\Delta P_{steno} \approx 1.5\,mmHg$, in agreement with measured pressure drops in stenotic internal jugular veins [183]. Another direct consequence of the presence of a stenosis is the drastic reduction of blood flow in the corresponding vessel. For example, in case A, the pressure incremenet caused by the stenosis results in a reduction of average flow rate from $9.83\,ml\,s^{-1}$ to $3.12\,ml\,s^{-1}$, which corresponds to a reduction of 70%. A further interesting consequence of unilateral stenoses is that when flow through the left internal
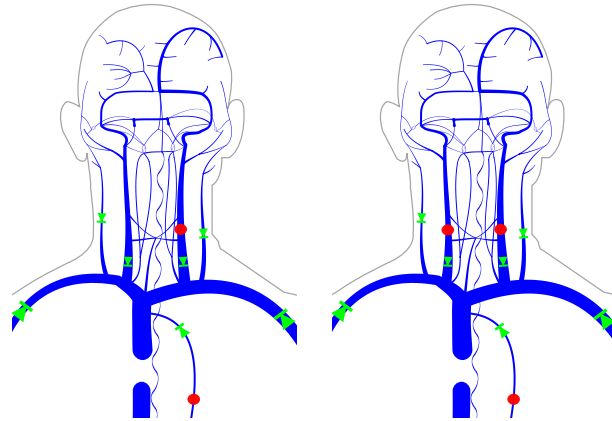
Figure 5.3: CCSVI cases A, and B. Red points indicate the vessels at which stenoses were placed.

jugular vein is impaired, part of the blood is diverted into the right internal jugular vein, as shown by flow increments verified in this vessel for case A.

Figure 5.5 shows computed pressure and flow rate for both external jugular veins. It can be seen how unilateral and bilateral internal jugular vein stenoses cause severe flow increments in these vessels. These increments are due to the pressure increment in stenotic internal jugular veins and a consequent redirection of flow from these vessels towards the external jugular veins via flow inversion in the common facial vein, not shown here.

Having seen the impact of stenoses in extracranial hemodynamics, we move now to the intracranial region. Figure 5.6 shows pressure and flow rate in the superior sagittal sinus and in the straight sinus. As expected, pressure increments verified at extracranial locations are transmitted upstream and can be encountered in the dural sinuses.

The next point to be clarified is if the observed pressure increments affect pressure in cerebral veins. These veins are upstream of the Starling resistor and therefore pressure at this location is already higher than the intracranial pressure and, consequently, than that of the dural sinuses. In our model there is an indirect effect of stenoses on cerebral veins. The mechanism that induces pressure increments in cerebral veins works as follows. After the simulation is started, the solution reaches a periodic state for most vessels in around 20 cardiac cycles. Pressure increments can be observed in extracranial vessels and dural sinuses. On the other hand, due to the Starling resistor, pressure in cerebral veins increases only slightly. At this point there is an imbalance between CSF generation and absorption, since CSF absorption depends linearly on the pressure difference between the intracranial pressure and the superior sagittal sinus pressure. CSF starts to accumulate and intracranial pressure slowly increases until a new dynamic equilibrium is reached. The dynamics of CSF generation and absorption is slow and therefore the new periodic state is reached only after more than 1500 cardiac cycles. The periodic intracranial pressure waveforms for the healthy control and both CCSVI cases are shown in figure 5.7. These new values of intracranial pressure will cause a pressure increment in cerebral veins with respect to the values obtained for the healthy control, as shown in figure 5.8.
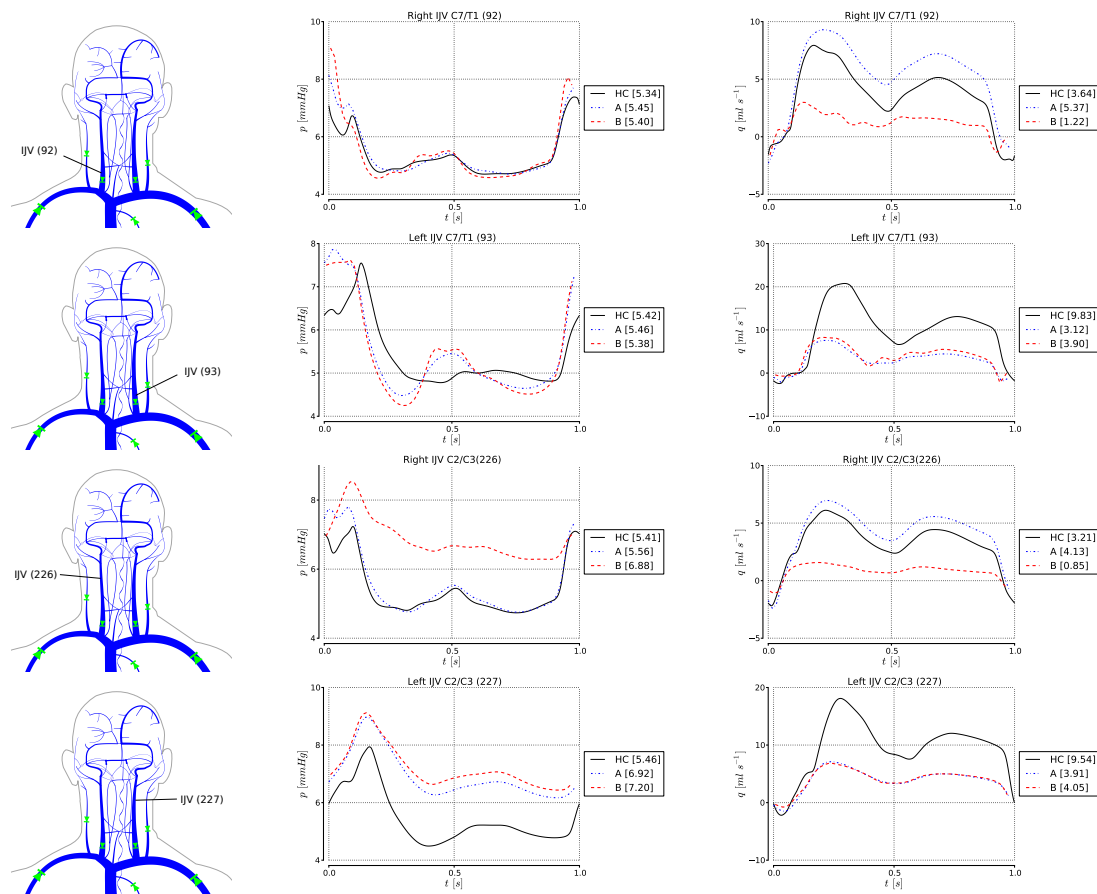
Figure 5.4: Computed pressure and flow rate in internal jugular veins for the three model configurations, the standard venous network and CCSVI cases A and B.
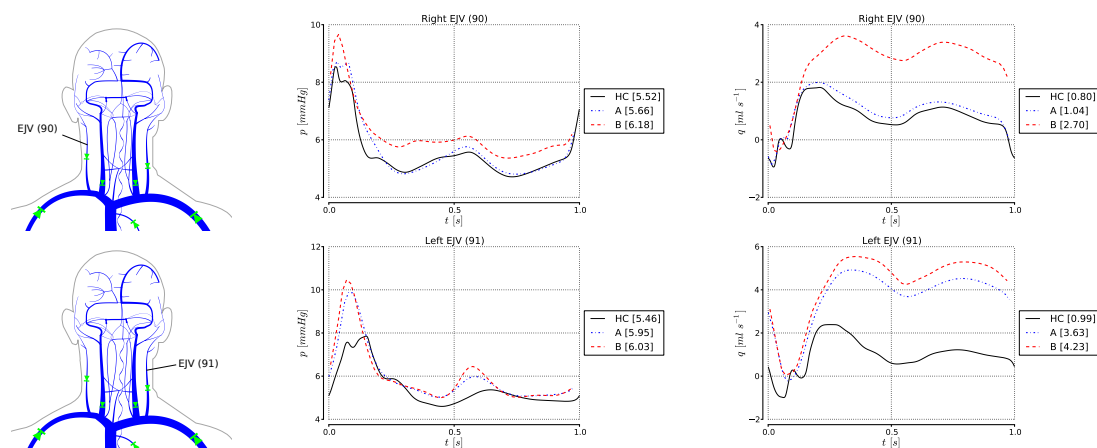
Figure 5.5: Computed pressure and flow rate in external jugular veins for the three model configurations, the standard venous network and CCSVI cases A and B.
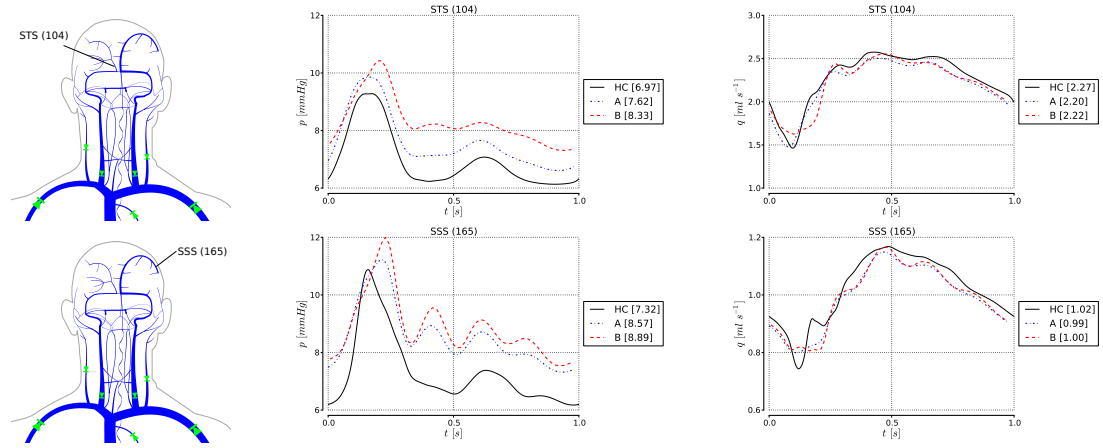
Figure 5.6: Computed pressure and flow rate in dural sinuses for the three model configurations, the standard venous network and CCSVI cases A and B.
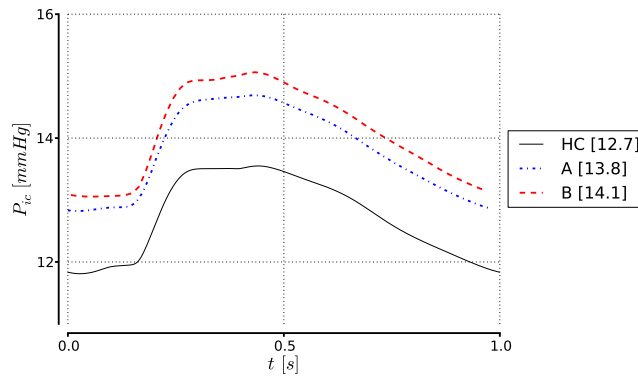
Figure 5.7: Intracranial pressure for a healthy control and two CCSVI cases.
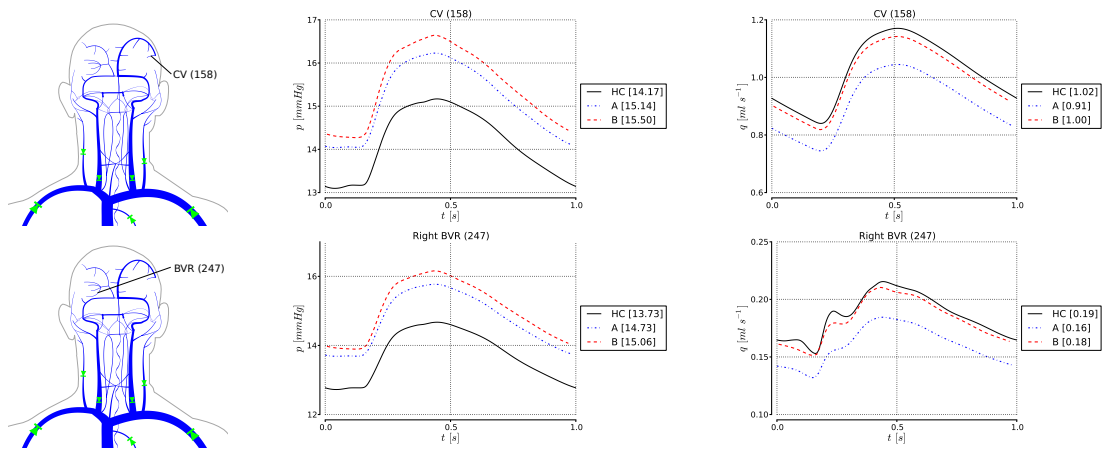
Figure 5.8: Computed pressure and flow rate in a cortical veins and in the basal vein of Rosenthal for the three model configurations, the standard venous network and CCSVI cases A and B.

5.3.2   Comparison of a healthy subject *vs* a MS/CCSVI patient

In this section we consider a Multiple Sclerosis patient with a severely disturbed extracranial venous network. Figure 5.9 shows a set of Maximum-Intensity-Projection (MIP) images deriving from a Time-Of-Flight (TOF) Magnetic Resonance Venography (MRV) for the subject under consideration. The picture to the left shows an anterior view, whereas the central and right pictures are sagittal views showing the right and the left internal jugular veins, respectively. As clearly seen in the anterior view, the left internal jugular vein has its flow severely impaired with loss of signal (red arrows). Flow signals are high in collaterals, such as the vertebral vein (light blue arrow) and the left external jugular vein. In the central picture a moderate narrowing of the right internal jugular vein can be observed (confirmed by segmentation). Finally, the right picture shows how the left internal jugular vein drains into the anterior jugular vein via the common facial vein (light blue arrow).

In order to model this patient, major head and neck vein geometries were segmented following the procedure described in [117] and the following changes to the standard model presented in [115] were made:

- The venous network topology was modified. The resulting network is shown in figure 5.10. The most evident difference with respect to the standard network shown in figure 5.2 is that in this case the superior sagittal sinus drains into the right transverse sinus and the straight sinus drains into the left transverse sinus. Moreover, the anterior jugular vein, connecting the common facial vein to the junction of brachiocephalic veins, was added to the network (shown in red).

- The geometry of major head and neck veins was changed according to MRI-derived patient-specific geometries. The geometrical and mechanical properties of the venous network are reported in table 5.1.

- Stenoses were introduced in vessels 224 ($A_0^s = 0.5\,A_0$) and 225 ($A_0^s = 0.1\,A_0$). These vessels correspond to the right and left internal jugular veins, respectively. As for the cases reported in section 5.3.1, the length of stenoses is $L = 2\,cm$ and the stenotic vessels are discretized using a $\Delta x = 0.1\,cm$.
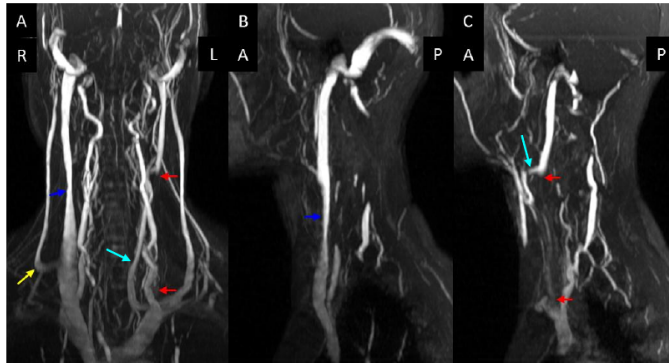
Figure 5.9: Maximum-Intensity-Projection of Time-Of-Flight Magnetic Resonance Venoraphy for a Multiple Sclerosis patient with severe stenosis in the left internal jugular vein, draining into the anterior jugular vein via the common facial vein (light blue arrow). Image was kindly provided by Prof. E. M. Haacke.

Figure 5.10: Head and neck veins for a MS patient. Numbers refer to those used in table 5.1, where geometrical and mechanical parameters for each vessel are reported.

Table 5.1: Geometrical and mechanical parameters for veins added or changed to the venous network presented in [117] in order to model the Multiple Sclerosis patient presented in section 5.3.2. L: length; r_0: inlet radius; r_1: outlet radius; c_0: wave speed for $A = A_0$; $Type$ vessel type (1: dural sinus, 2: cerebral vein); Ref: bibliographic source or MRI imaging segmented geometry.

No.	Vessel name	L [cm]	r_0 [cm]	r_1 [cm]	c_0 [m/s]	Type	Ref.
84	Sup. vena cava	1.50	0.800	0.800	1.000	4	MRI
85	Sup. vena cava	2.00	0.800	0.800	1.000	4	MRI
86	R. brachiocephalic v.	4.00	0.564	0.564	1.360	4	MRI
87	L. brachiocephalic v.	7.50	0.535	0.535	1.410	4	MRI
90	R. ext. jugular v.	10.00	0.252	0.252	2.022	3	MRI
91	L. ext. jugular v.	10.00	0.252	0.304	1.951	3	MRI
92	R. int. jugular v.	2.50	0.357	0.557	1.553	3	MRI
93	L. int. jugular v.	2.50	0.250	0.250	2.028	3	MRI
94	L. vertebral v.	11.00	0.300	0.300	1.894	3	MRI
95	R. vertebral v.	11.00	0.138	0.160	2.381	3	MRI
96	R. deep cervical v.	13.00	0.160	0.160	2.333	3	MRI
97	L. deep cervical v.	13.00	0.300	0.300	1.894	3	MRI
98	Vertebral venous plexus	71.00	0.368	0.368	1.735	3	[153]
99	R. sigmoid sinus	3.00	0.437	0.399	5.000	1	MRI
100	L. sigmoid sinus	3.00	0.310	0.310	5.000	1	MRI
101	R. trans. sinus	3.00	0.437	0.437	5.000	1	MRI
102	L. trans. sinus	3.50	0.281	0.310	5.000	1	MRI
103	Sup. sagittal sinus	2.50	0.350	0.367	5.000	1	MRI
104	Straight sinus	4.00	0.250	0.250	5.000	1	MRI
105	Inf. sagittal sinus	3.67	0.160	0.160	5.000	1	MRI
106	Vein of Galen	0.60	0.366	0.400	1.703	9	MRI
107	L. int. cerebral v.	5.00	0.126	0.126	2.494	9	MRI
108	R. int. cerebral v.	5.00	0.126	0.126	2.494	9	MRI
109	L. basal v. of Rosenthal	1.00	0.126	0.126	2.494	9	MRI
110	R. basal v. of Rosenthal	1.00	0.126	0.126	2.494	9	MRI
111	R. sup. petrosal sinus	5.70	0.149	0.149	5.000	1	MRI
112	L. sup. petrosal sinus	5.70	0.149	0.149	5.000	1	MRI
113	R. inf. petrosal sinus	3.20	0.080	0.160	5.000	1	MRI
114	L. inf. petrosal sinus	3.20	0.080	0.160	5.000	1	MRI
115	R. post. auricular v.	5.00	0.080	0.080	3.000	2	MRI
116	L. post. auricular v.	5.00	0.080	0.080	3.000	2	MRI
117	R. post. retromandibular v.	3.52	0.250	0.250	2.028	2	[174]
118	L. post. retromandibular v.	3.52	0.250	0.250	2.028	2	[174]
119	R. ant. retromandibular v.	3.15	0.235	0.235	2.072	2	[174]
120	L. ant. retromandibular v.	3.15	0.235	0.235	2.072	2	[174]
121	R. retromandibular v.	4.50	0.260	0.260	2.000	2	[174]
122	L. retromandibular v.	4.50	0.260	0.260	2.000	2	[174]
123	R. facial v.	6.00	0.132	0.178	2.355	2	MRI
124	L. facial v.	6.00	0.132	0.178	2.355	2	MRI
125	R. com. facial v.	0.90	0.180	0.180	2.255	2	MRI
126	L. com. facial v.	0.90	0.360	0.360	1.753	2	MRI
127	R. superf. temp. v.	5.00	0.190	0.190	2.218	2	[174]
128	L. superf. temp. v.	5.00	0.190	0.190	2.218	2	[174]
129	R. maxillary v.	1.00	0.175	0.175	2.274	2	[174], MRI

Table 5.1 – continued from previous page

No.	Vessel name	L [cm]	r_0 [cm]	r_1 [cm]	c_0 [m/s]	Type	Ref.
130	L. maxillary v.	1.00	0.175	0.175	2.274	2	[174], MRI
131	R. deep facial v.	0.90	0.250	0.250	2.028	2	–
132	L. deep facial v.	0.90	0.250	0.250	2.028	2	–
133	R. emissary v.	3.00	0.100	0.100	2.667	2	[155]
134	L. emissary v.	3.00	0.100	0.100	2.667	2	[155]
135	R. pterygoid plexus	0.90	0.150	0.150	2.376	2	[147]
136	L. pterygoid plexus	0.90	0.150	0.150	2.376	2	[147]
137	R. marginal sinus	4.00	0.100	0.100	5.000	1	[43]
138	L. marginal sinus	4.00	0.100	0.100	5.000	1	[43]
139	Occipittal sinus	3.50	0.235	0.235	5.000	1	[19]
140	R. ext. jugular v.	10.00	0.252	0.252	2.022	3	MRI
141	R. mastoid emissary v.	7.20	0.175	0.175	2.274	2	[175, 105]
142	L. mastoid emissary v.	7.20	0.350	0.350	1.775	2	[175, 105]
143	R. post. condylar v.	3.00	0.315	0.315	1.857	2	MRI, [43]
144	L. post. condylar v.	3.00	0.600	0.600	1.300	2	MRI, [43]
145	R. subocc. sinus	1.00	0.450	0.450	1.566	2	[43]
146	R. lat. ant. condylar v.	3.00	0.315	0.315	1.857	2	[43]
147	L. lat. ant. condylar v.	3.00	0.600	0.600	1.300	2	MRI
148	L. ext. jugular v.	10.00	0.304	0.357	1.820	3	MRI
149	Sup. sagittal sinus	4.33	0.229	0.258	5.000	1	MRI
150	R. Labbe v.	5.00	0.150	0.150	2.376	9	MRI
151	L. Labbe v.	5.00	0.150	0.150	2.376	9	MRI
152	Sup. sagittal sinus	4.33	0.258	0.287	5.000	1	MRI
153	Sup. sagittal sinus	2.50	0.334	0.350	5.000	1	MRI
154	L. cavernous sinus	1.50	0.100	0.100	5.000	1	MRI
155	R. cavernous sinus	1.50	0.100	0.100	5.000	1	MRI
156	Occipittal v.	5.00	0.126	0.126	2.494	2	MRI
157	Sup. sagittal sinus	5.00	0.300	0.334	5.000	1	MRI
158	Cerebral vein	5.00	0.150	0.150	2.376	9	[172]
159	Cerebral vein	5.00	0.150	0.150	2.376	9	[172]
160	Azygos v.	2.00	0.425	0.425	1.616	4	MRI, [95]
161	Cerebral vein	5.00	0.150	0.150	2.376	9	[172]
162	Cerebral vein	5.00	0.150	0.150	2.376	9	[172]
163	R. vertebral v.	5.00	0.160	0.160	2.333	3	MRI
164	L. vertebral v.	5.00	0.160	0.160	2.333	3	MRI
165	Sup. sagittal sinus	4.33	0.200	0.229	5.000	1	MRI
166	L. subocc. sinus	1.00	0.450	0.450	1.566	2	[43]
167	R. anastomotic v.	2.00	0.100	0.100	2.667	3	[43], [13]
168	L. anastomotic v.	2.00	0.100	0.100	2.667	3	[43], [13]
218	R. sup. thyroid v.	4.00	0.150	0.150	2.376	3	MRI, [173]
219	L. sup. thyroid v.	4.00	0.150	0.150	2.376	3	MRI, [173]
220	R. mid. thyroid v.	3.00	0.100	0.100	2.667	3	MRI, [173]
221	L. mid. thyroid v.	3.00	0.100	0.100	2.667	3	MRI, [173]
222	Inf. thyroid v.	7.00	0.126	0.126	2.494	3	MRI
223	Thyroid connection	2.00	0.160	0.160	2.333	3	–
224	R. int. jugular v.	3.00	0.357	0.357	1.759	3	MRI
225	L. int. jugular v.	3.00	0.250	0.250	2.028	3	MRI
226	R. int. jugular v.	2.70	0.357	0.357	1.759	3	MRI
227	L. int. jugular v.	2.70	0.250	0.250	2.028	3	MRI
228	R. int. jugular v.	6.80	0.357	0.357	1.759	3	MRI
229	L. int. jugular v.	6.80	0.250	0.250	2.028	3	MRI
230	R. sigmoid sinus	1.00	0.399	0.357	5.000	1	MRI
231	L. sigmoid sinus	1.00	0.310	0.250	5.000	1	MRI
232	R. trans. sinus	3.00	0.437	0.437	5.000	1	MRI
233	L. trans. sinus	3.50	0.437	0.281	5.000	1	MRI
234	R. facial v.	2.00	0.113	0.132	2.514	2	MRI
235	L. facial v.	2.00	0.113	0.132	2.514	2	MRI
236	Sup. sagittal sinus	2.00	0.287	0.300	5.000	1	MRI
237	Cerebral vein	5.00	0.150	0.150	2.376	9	[172]
238	Cerebral vein	5.00	0.150	0.150	2.376	9	[172]
239	Cerebral vein	5.00	0.150	0.150	2.376	9	[172]
240	Intra-cavernous sinus	2.00	0.126	0.126	5.000	1	[147], [43]
241	Inf. sagittal sinus	3.67	0.160	0.160	5.000	1	MRI
242	R. int. jugular v.	1.00	0.557	0.557	1.372	3	MRI
243	L. int. jugular v.	1.00	0.250	0.250	2.028	3	MRI
244	Azygos v.	28.00	0.425	0.425	1.616	4	MRI, [95]
245	Cerebral vein	3.00	0.150	0.150	2.376	9	[172]
246	L. basal v. of Rosenthal	7.00	0.126	0.126	2.494	9	MRI
247	R. basal v. of Rosenthal	7.00	0.126	0.126	2.494	9	MRI
248	Inf. sagittal sinus	3.67	0.160	0.160	5.000	1	MRI
249	Cerebral vein	3.00	0.150	0.150	2.376	9	[172]
250	Intercostal v.	2.00	0.400	0.400	1.667	4	[147]
259	Confluence of sinuses	1.00	0.437	0.437	5.000	1	MRI
260	Cerebral vein	3.00	0.150	0.150	2.376	9	[172]
261	Terminal cerebral vein	1.00	0.150	0.150	5.000	1	[172]
262	Terminal cerebral vein	1.00	0.150	0.150	5.000	1	[172]
263	Terminal cerebral vein	1.00	0.150	0.150	5.000	1	[172]
264	Terminal cerebral vein	1.00	0.150	0.150	5.000	1	[172]
265	Terminal cerebral vein	1.00	0.150	0.150	5.000	1	[172]
266	Terminal cerebral vein	1.00	0.150	0.150	5.000	1	[172]
267	Terminal cerebral vein	1.00	0.150	0.150	5.000	1	[172]
268	Terminal cerebral vein	1.00	0.150	0.150	5.000	1	[172]
269	Terminal cerebral vein	1.00	0.150	0.150	5.000	1	[172]
270	Terminal cerebral vein	1.00	0.150	0.150	5.000	1	[172]
271	Terminal cerebral vein	1.00	0.309	0.366	1.804	9	MRI
272	Terminal cerebral vein	1.00	0.150	0.150	5.000	1	MRI
273	Terminal cerebral vein	1.00	0.150	0.150	5.000	1	MRI
274	Anterior jugular vein	8.00	0.178	0.282	2.087	3	MRI

Figure 5.11 shows computed average flow rates and MRI-derived measurements for several head and neck veins. The agreement between computations and measurements is satisfactory. Flow from the superior and straight sinus, together with that draining from the veins of Labbe, is distributed correctly into the left and right transverse sinus. Flow is then correctly reproduced in neck veins, with a strong flow reduction in the left internal jugular vein and a consequent flow diversion into the anterior jugular vein.

In figures 5.12 and 5.11 we show computational results for pressure and flow rate, together with time-resolved MRI flow quantification data for dural sinuses and internal jugular veins, respectively. The agreement between computed and measured flow waveforms is not as good

as the one reported in [115] for healthy subjects. In fact measured flow shows a less pulsatile pattern, especially in dural sinuses and in internal jugular veins at C2/C3 level. This reduced pulsatility could be due to a higher venous pressure at the level of dural sinuses that would then reduce the influence of right atrial pulsations in this region. Another cause for these discrepancies could be drastic differences in material properties for the veins of the Multiple Sclerosis patient.

A comparison between the hemodynamical state of the healthy subject and of the Multiple Sclerosis patient is shown in figures 5.14 to 5.18. Flow in external jugular veins is higher in the Multiple Sclerosis patient than in the healthy control (figure 5.14). This is due to the fact that both internal jugular veins are stenotic. Moreover, the Multiple Sclerosis patient has a right-dominant internal jugular vein and therefore flow through this vessel is higher than in the case of the healthy subject, which has a left-dominant internal jugular vein. Pressure values upstream from stenoses are around $0.8\,mmHg$ higher than the ones observed downstream. This pressure increments are also observed in the superior sagittal sinus (figure 5.16) and result in an increase in intracranial pressure (figure 5.17) and, consequently, in pressure of cerebral veins, such as cortical veins and deep cerebral veins (figure 5.18). The mechanism by which this pressure increments take place is the same as the one introduced in section 5.3.1.
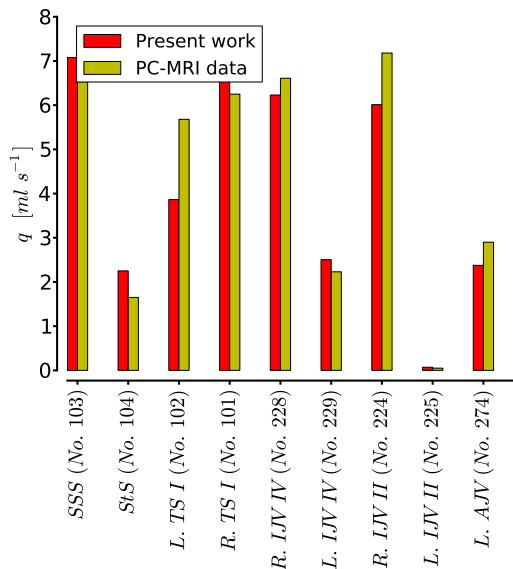

Figure 5.11: Blood flow in head and neck veins for the Multiple Sclerosis patient presented in section 5.3.2: computational results *vs* MRI flow quantification data. SSS: Superior sagittal Sinus; StS: Straight Sinus; TS: Transverse Sinus; IJV: Internal Jugular Vein. Vessel numbers refer to figure 5.10 and table 5.1.

5.4 Discussion

Bhadelia *et al.* [28] investigated the effect of jugular vein compression on flow waveforms. In particular, they observed that flow showed a reduced pulsatility after jugular vein compression, as seen in our numerical results for stenotic vessels (see figure 5.4). Another consequence of the presence of stenoses is the pressure increment verified upstream of the cross-sectional area restriction. The computed pressure drops are within the ranges reported in [183].

Although not fully understood, the role of extracranial anomalies in cerebral venous hemo-dynamics is undeniable from the point of view of the experimental evidence [96]. Furthermore, their influence has recently been extended to the CSF system. Magnano *et al.* [107] have shown that Multiple Sclerosis patients had altered CSF dynamics. In a successive work, the same team of authors showed that treating the subset of these patients that were also positive for CCSVI via a percutaneous transluminal angioplasty restored normal CSF dynamics and improved the

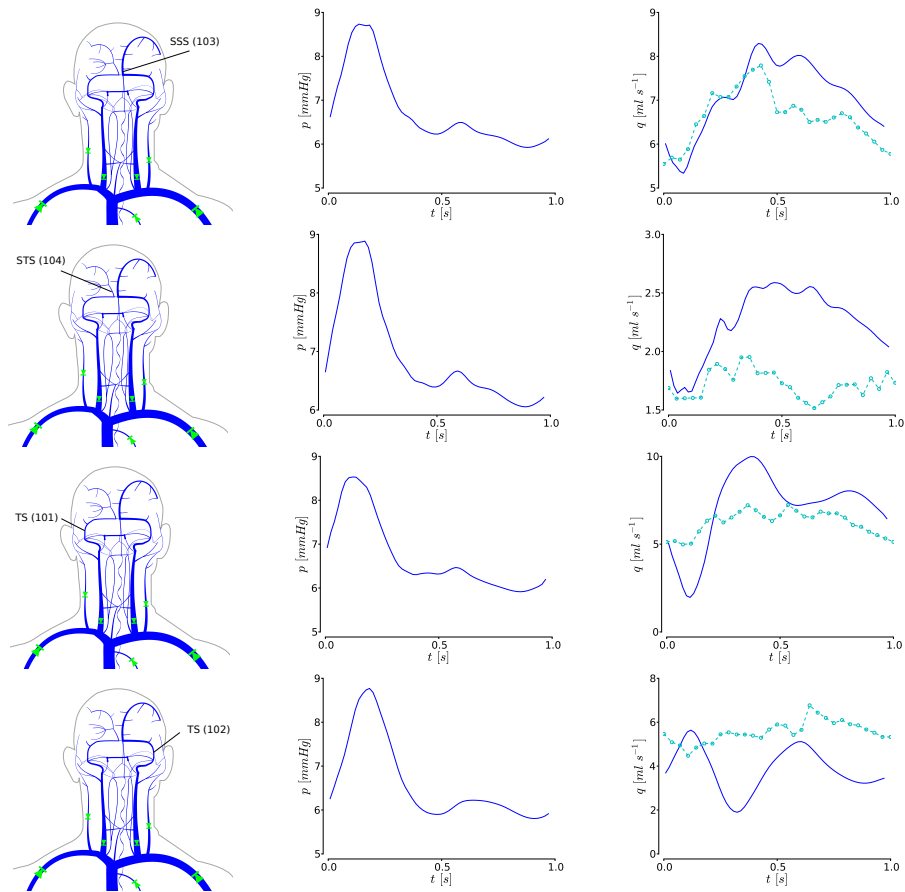Figure 5.12: Computed pressure and flow rate in dural sinuses for the Multiple Sclerosis patient presented in section 5.3.2. PC-MRI flow quantification data is shown with symbols and dashed lines.
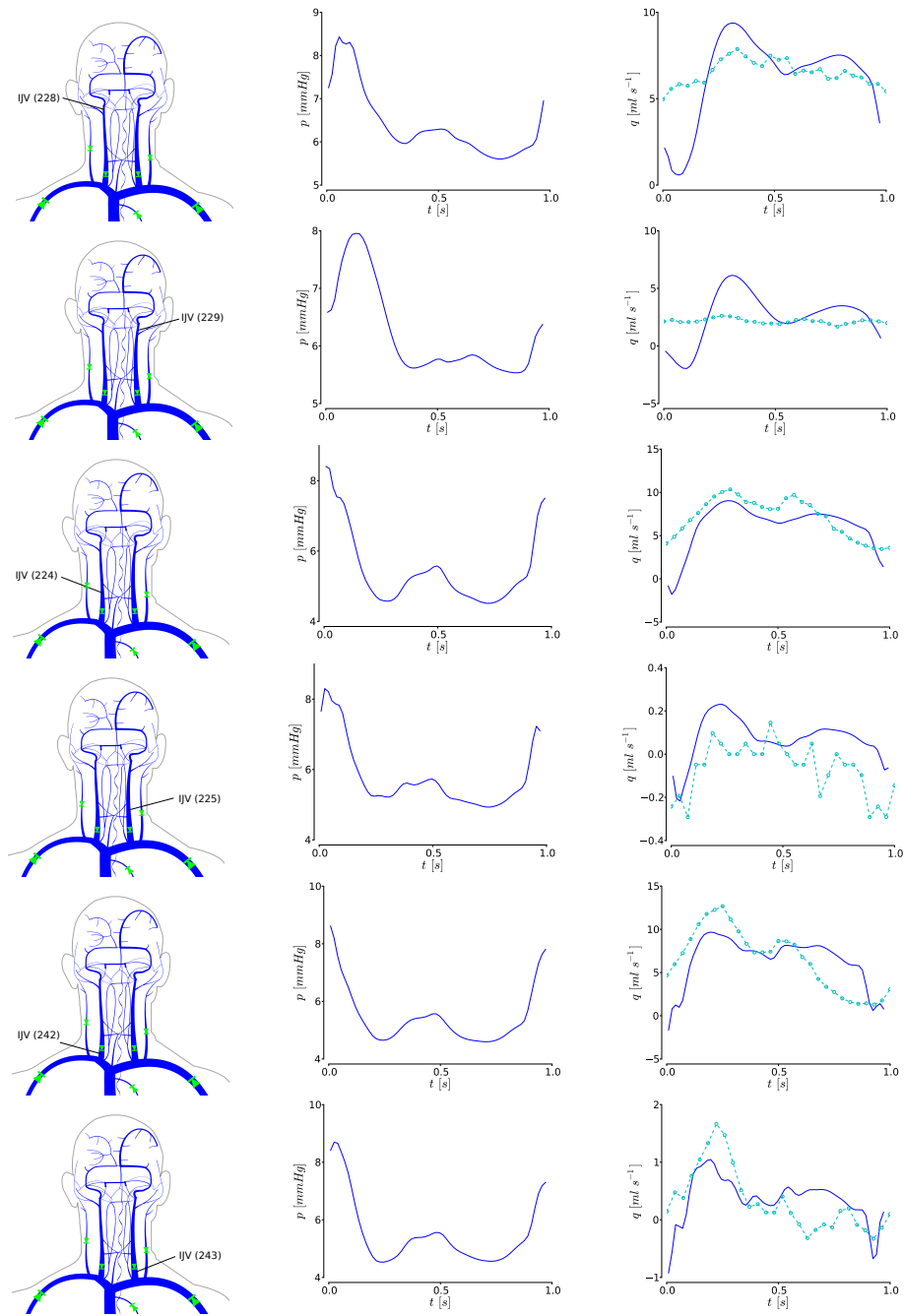
Figure 5.13: Computed pressure and flow rate in internal jugular veins for the Multiple Sclerosis patient presented in section 5.3.2. PC-MRI flow quantification data is shown with symbols and dashed lines.
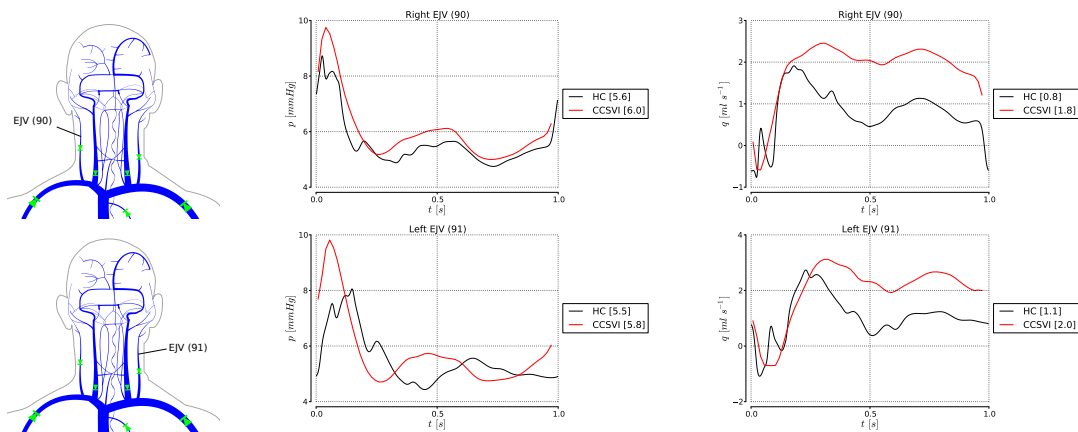
Figure 5.14: Computed pressure and flow rate in external jugular veins for a healthy control and for the Multiple Sclerosis patient presented in section 5.3.2.
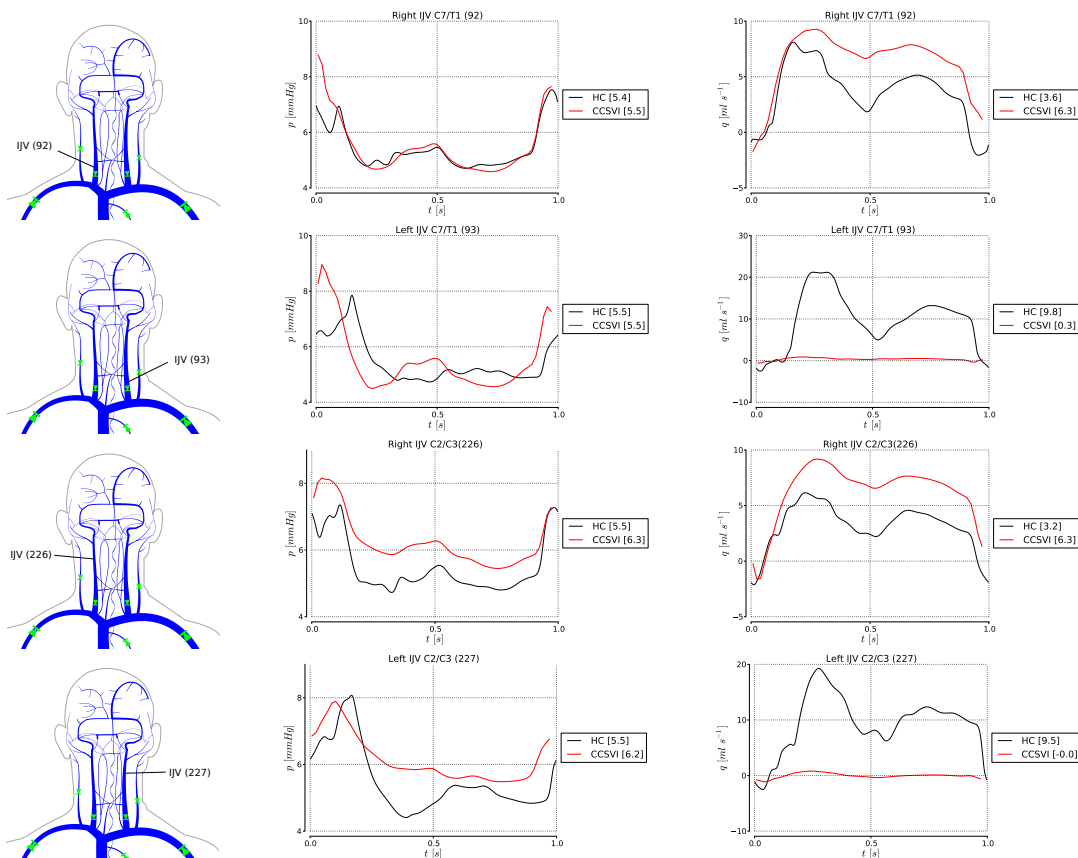
Figure 5.15: Computed pressure and flow rate in internal jugular veins for a healthy control and for the Multiple Sclerosis patient presented in section 5.3.2.
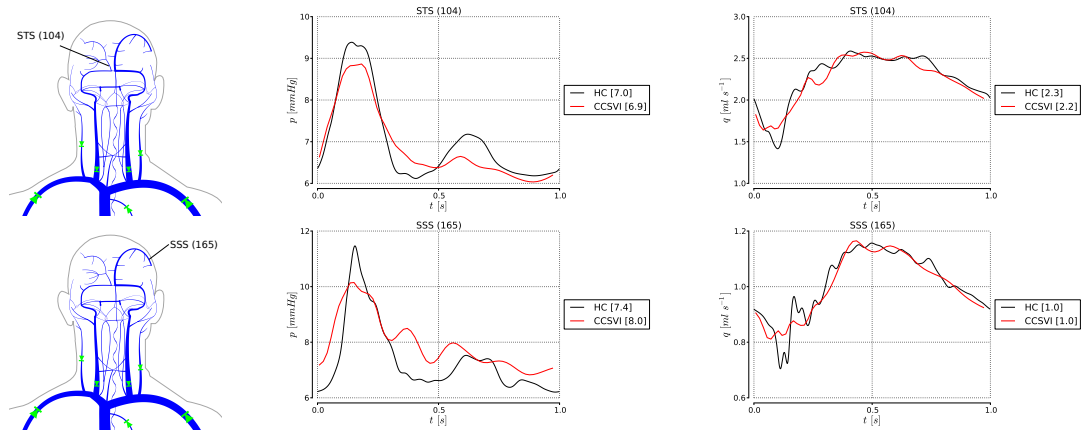
Figure 5.16: Computed pressure and flow rate in dural sinuses for a healthy control and for the Multiple Sclerosis patient presented in section 5.3.2.

Figure 5.17: Intracranial pressure for a healthy control and for the Multiple Sclerosis patient presented in section 5.3.2.

Figure 5.18: Computed pressure and flow rate in a cortical veins and in the basal vein of Rosenthal for a healthy control and for the Multiple Sclerosis patient presented in section 5.3.2.

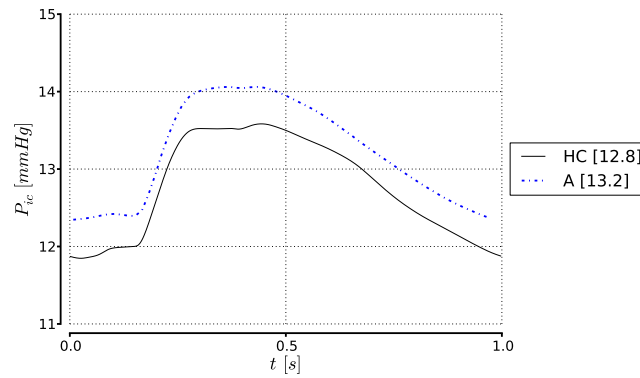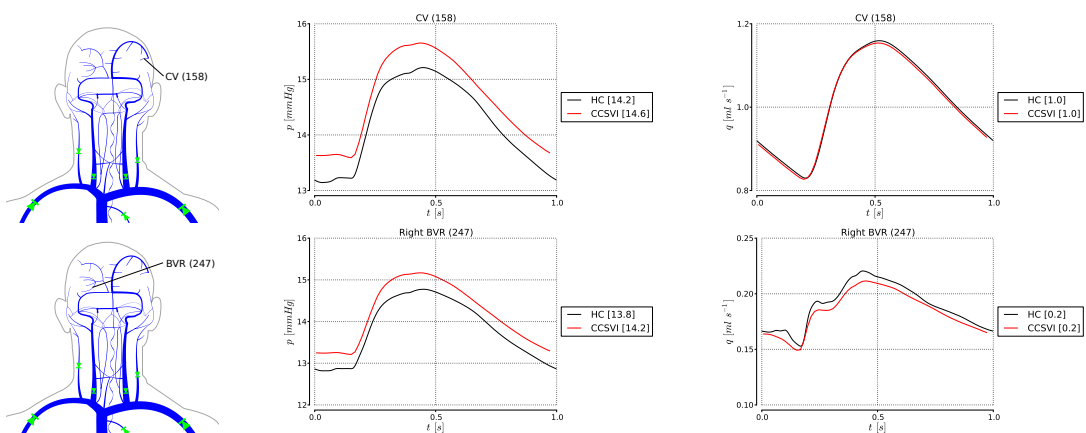clinical course of the neurodegenerative disease [187].

Our computations clearly show that extracranial anomalies have a direct impact on intracranial hemodynamics. Pressure increments in extracranial vessels are observed also at the intracranial level. In turn, these changes influence the balance between CSF generation and absorption and lead to an increment in intracranial pressure and, consequently, in the pressure of cerebral veins.

The determination of the clinical significance of altered intracranial venous hemodynamics observed for CCSVI patients lies beyond the scope of this work. We think that the results presented in this work confirm medical observations on the influence of extracranial anomalies on intracranial cerebral venous hemodynamics. However, we note that our analysis of the CCSVI condition is far from being definitive. From the five diagnosis criteria for CCSVI, four are functional and require postural changes and respiratory maneuvers to be assessed [183]. Modelling postural changes poses several challenges. The most immediate one is related to the collapsible nature of veins and the consequent development of transcritical flows, at least during transient phases induced by postural changes. Although we are using robust numerical schemes for one-dimensional vessels, the algorithm used to treat junctions and bifurcations represents a weak point in out methodology that does not allow for modelling these regimes. A second difficulty regards the role played by regulatory mechanisms such as cerebral auto-regulation or the baroreflex control mechanism during postural changes. Such control processes have been applied to models including one-dimensional networks of arteries [3, 31] and never to model postural changes. To the best of our knowledge, applications regarding postural changes have always made use of lumped parameter models [127, 169]. A third difficulty regards the poor description of the mechanical properties of veins that is being currently used. This need is motivated by the fact that a more accurate description of mechanical properties of veins will result in a better description of venous volume changes in the head and neck due to postural changes and respiratory maneuvers, enhancing the predictive capacities of our mathematical model.

5.5 Concluding remarks

We have presented the first theoretical study on the hemodynamical impact of extracranial venous anomalies in cerebral venous hemodynamics. To perform our study we followed two different strategies. In the first case we considered a standard venous network, corresponding to a healthy subject, and artificially perturbed its geometry in order to include stenoses at certain locations. The second strategy regarded the modelling of a Multiple Sclerosis patient that presented severely altered extracranial veins. In both cases we could confirmed that extracranial perturbations affect intracranial venous hemodynamics. The flow patterns and pressure increments computed by our model are in agreement with experimental evidence. However, the clinical significance of perturbations caused by extracranial anomalies is still matter of debate. We conclude by stressing the fact that this study represents only a partial assessment of the impact of CCSVI on cerebral venous circulation. In this study we studied the impact of CCSVI for a subject in supine posture. However, CCSVI diagnosis criteria require to be assessed in supine and upright postures.

The CCSVI condition was a motivating example for the development of more detailed mathematical models of the venous system [117, 115]. However, we think that further improvements are necessary in terms of mathematical models and numerical tools in order to be able to perform a complete assessment of the implications of extracranial venous anomalies in cerebral venous hemodynamics. In the next chapter we summarize the achievements of this thesis and individuate possible fields of improvement.

Chapter 6

Conclusions

In this chapter we discuss the results achieved during this PhD project and possible future work, motivated by the obtained achievements and the encountered limitations.

6.1 Achievements

As done throughout this thesis, we can divide the obtained achievements in three main fields: the design of numerical schemes, the development of models with emphasis on the venous system and the theoretical study of the CCSVI condition. We now make some considerations on each one of these fields.

6.1.1 Design of numerical schemes

The treatment of geometric-type source terms in one-dimensional blood flow models by means of well-balanced schemes has not been explicitly addressed by the community dealing with cardiovascular mathematics before the beginning of this thesis. We have therefore introduced the use of well-balanced finite volume schemes in this context. The numerical schemes proposed in this thesis are high-order accurate in space and time and highly robust. Moreover, these numerical schemes conserve mass at a discrete level, a natural property of finite volume schemes. This feature becomes essential in the context of cardiovascular hemodynamics if long simulations are to be performed, especially if using closed-loop models where the total mass of the system determines the sought periodic solution.

We have designed well-balanced numerical schemes by means of finite volume-type path-conservative numerical schemes. The development of this type of numerical schemes is a highly active and productive research field of applied mathematics. Specific characteristics of the mathematical model adopted in this thesis forced us to fully deploy the theory that supports their development. Moreover, the ideas used for the design of both numerical schemes presented in chapter 3, show that the numerical treatment of non-conservative hyperbolic systems requires to take into account specific aspects of the underlying partial differential equations. A last consideration on this aspect is that the approach used in section 3.2 is applicable to other non-conservative systems of practical relevance, being the shallow water equations one of the most important examples.

6.1.2 Modelling venous hemodynamics

Since the early 80's, several mathematical models based on the one-dimensional blood flow equations have been proposed by the scientific community. This type of models was widely applied to understand a vast range of physiological and pathological phenomena. Nevertheless, models including a one-dimensional description of major veins were extremely rare. In fact, besides the work of [121], there was no closed-loop model including a detailed description of the venous system. Causes for this imbalanced between the development of mathematical models for the arterial and venous systems in favor of the first one can be found in the lack of motivating medical applications and in the difficulties inherent to the modelling of this low-pressure system.

During this PhD project we have developed a closed-loop model of the cardiovascular system with emphasis in head and neck veins. We have collected anatomical data, as well as flow measurements, in order to construct our model and validate its outputs. The information used to construct this model does not derive only from medical images, but it is also based on an extensive literature search which provided anatomical information of those regions for which medical images were not available. We believe that the publication of the model and its presentation in several international conferences and workshops has increased the interest of the scientific community dealing with cardiovascular mathematics in the modelling of the venous system.

6.1.3 Theoretical study of the CCSVI condition

The association of the CCSVI condition to Multiple Sclerosis has generated a significant amount of interest from the medical community, patients and the mass media. However, the considerable lack of knowledge of physiological aspects of the venous system and the pressure exerted by patients looking for a cure to Multiple Sclerosis have made the debate on the validity of Zamboni's hypothesis on the role played by CCSVI in the etiology of Multiple Sclerosis rather intense.

One of the goals of this thesis was that of contributing to a better understanding of the purely physical aspects of the CCSVI condition. As shown in chapter 4, a mathematical model with a sufficiently detailed description of the venous system had to be constructed. Using this tool, we have performed the first study in which mathematical modelling is used to study the CCSVI condition. We were able to compute the effect of extracranial venous anomalies on cerebral venous hemodynamics and compare the hemodynamic states of a patient and of a reference healthy control. We clearly showed that extracranial venous anomalies affect intracranial hemodynamics by increasing cerebral venous pressure and affecting intracranial pressure. Nevertheless, the theoretical study of the CCSVI condition presented in chapter 5 is far from complete. In fact, the diagnosis of CCSVI is based on criteria that require measurements to be performed in supine and upright positions, as well as performing moderate respiratory manoeuvres. The mathematical modelling of such operations poses methodological difficulties and requires more sophisticate models to be used.

In the next section we describe the most significant aspects of the presented mathematical model that should be improved or implemented in order to enhance the predictive character of this tool.

6.2 Future work

We think that the work presented in this thesis constitutes a starting point in the field of mathematical modelling of the venous system. We have explored aspects that are often disregarded when modelling the arterial system, such as the choice of the correct formulation of the mathematical model and the collapsible nature of veins. Moreover, we have constructed a mathematical model with a level of detail for the venous system that, to the best of our knowledge, has never been reached before.

The progress made in this field of applied mathematics during this PhD research project is surely due, at least partially, to the great debate generated by the description of the CCSVI condition and its association to Multiple Sclerosis. However, it is still the complexity of this disease that shows us that mathematical models of the venous system are in its infancy. As evidenced in the previous paragraphs, our capacity for exploring the hemodynamical aspects of the CCSVI condition, as well as other pathologies involving the venous system, are limited by the mathematical models and numerical tools that are currently available. Therefore, there are several aspects to be improved or introduced in the computational framework developed during this PhD research project.

Methodological limitations of the currently available tools derive from the fact that flow in veins, during postural changes, can change its regime. The treatment of elastic jumps is well tolerated by the numerical methodology for one-dimensional vessels, but this is not the case for the algorithm used for treating junctions and bifurcations. Having a more robust method

for treating this delicate component of the model would constitute a significant advance in this field of research.

The second aspect limiting a complete study of the CCSVI condition and many other pathological situations, is the modelling of postural changes. These manoeuvres represent significant changes in the state of the cardiovascular system and neglecting the role of regulatory mechanisms such as the baroreflex and cerebral autoregulation is not allowed. The literature offers examples where these processes were modelled, most of the times in the context of lumped parameter models. Incorporating these tools in the existing model represents a mandatory task for more detailed studies of the CCSVI condition.

A third point to be improved is the extension of cerebral vascular networks. The arterial and venous networks used in this thesis show a rather advanced level of detail if compared to available one-dimensional models. However, we know that in reality the complexity of these networks is much higher, with collateral circuits in both compartments. A better description of these networks will enhance the capacity of the model to better describe a wide range of diseases, being always the CCSVI condition one of them.

A last challenge is represented by the need of embedding one-dimensional models for blood flow in more complex models for the cerebrospinal fluid and brain parenchyma dynamics. The use of models that allow for a spatial differentiation between ventricles, brain parenchyma and the spinal sub-arachnoid space will allow for a more refined analysis of the impact of venous anomalies in this important compartment.

Bibliography

[1] J. Alastruey. *Numerical modelling of pulse wave propagation in the cardiovascular system: development, validation and clinical applications.* PhD thesis, Department of Aeronautics and Bioengineering, Imperial College, London, 2006.

[2] J. Alastruey, A. W. Khir, K. S. Matthys, P. Segers, and S. J. Sherwin. Pulse wave propagation in a model human arterial network: Assessment of 1-D visco-elastic simulations against *in vitro* measurements. *Journal of Biomechanics*, 44:2250–2258, 2011.

[3] J. Alastruey, S. M. Moore, K. H. Parker, T. David, J. Peiró, and S. J. Sherwin. Reduced modelling of blood flow in the cerebral circulation: Coupling 1-D, 0-D and cerebral autoregulation models. *International Journal for Numerical Methods in Fluids*, 56(8):1061–1067, 2008.

[4] J. Alastruey, K. H. Parker, J. Peiró, S. M. Byrd, and S. J. Sherwin. Modelling the circle of Willis to assess the effects of anatomical variations and occlusions on cerebral flows. *Journal of Biomechanics*, 40:1794–1805, 2007.

[5] J. Alastruey, K. H. Parker, J. Peiró, and S. J. Sherwin. Lumped Parameter Outflow Models for 1-D Blood Flow Simulations: Effect on Pulse Waves and Parameter Estimation. *Communications in Computational Physics*, 4:317–336, 2008.

[6] M. T. Alirezaye-Davatgar. *Numerical Simulation of Blood Flow in the Systemic Vasculature Incorporating Gravitational Force with Application to Cerebral Circulation.* PhD thesis, Graduate School of Biomedical Engineering - University of New South Wales, 2006.

[7] K. Ambarki, O. Baledent, G. Kongolo, R. Bouzerar, S. Fall, and M. Meyer. A New Lumped-Parameter Model of Cerebrospinal Hydrodynamics During the Cardiac Cycle in Healthy Volunteers. *IEEE Transactions on Biomedical Engineering*, 54:483–491, 2007.

[8] J. Andeweg. Intracranial venous pressures, hydrocephalus and effects of cerebrospinal fluid shunts. *Child's Nervous System*, 5(5):318–323, 1989.

[9] J. Andeweg. The anatomy of collateral venous flow from the brain and its value in aetiological interpretation of intracranial pathology. *Neuroradiology*, 38(7):621–628, 1996.

[10] C. Anile, P. De Bonis, A. Di Chirico, A. Ficola, A. Mangiola, and G. Petrella. Cerebral blood flow autoregulation during intracranial hypertension: a simple, purely hydraulic mechanism. *Childs Nervous System*, 25:325–335, 2009.

[11] M. Anliker, M. K. Wells, and E. Ogden. The transmission characteristics of large and small pressure waves in the abdominal vena cava. *IEEE Transactions on Bio-Medical Engineering*, 16:262–273, 1969.

[12] L. Antiga, M. Piccinelli, L. Boti, B. Ene-Iordache, A. Remuzzi, and D. A. Steinmann. An imaged-based modeling framework for patient-specific computational hemodynamics. *Medical and Biological Engineering and Computing*, 46:1097–1112, 2008.

[13] K. I. Arnautovic, O. Al-Metfy, T. Glenn, A. F. Krisht, and M. M. Husain. The suboccipital cavernous sinus. *Journal of Neurosurgery*, 86:252–262, 1997.

[14] E. O. Attinger. Wall Properties of Veins. *IEEE Transactions on Bio-Medical Engineering*, 16:253–261, 1969.

[15] E. Audusse, F. Bouchut, M. Bristeau, R. Klein, and B. Perthame. A fast and stable well-balanced scheme with hydrostatic reconstruction for shallow water flows. *SIAM Journal on Scientific Computing*, 25:2050–2065, 2004.

[16] P. Avasthey. Venous pressure changes during orthostasis. *Cardiovascular Research*, 6:657–663, 1972.

[17] C. J. Avezaat and J.M. Eijndhoven. The role of the pulsatile pressure variations in intracranial pressure monitoring. *Neurosurgical Review*, 9(1-2):113–120, 1986.

[18] A. P. Avolio. Multi-branched model of the human arterial system. *Medical and Biological Engineering and Computing*, 18:709–718, 1980.

[19] N. Balak, G. Ersoy, U. Uslu, N. Tanriöver, L. Tapul, G. Cetin, N. Isik, and I. Elmaci. Microsurgical and histomorphometric study of the occipital sinus: Quantitative measurements using a novel approach of stereology. *Clinical Anatomy*, 23:386–393, 2010.

[20] S. Bassez, P. Flaud, and M. Chauveau. Modeling of the Deformation of Flexible Tubes Using a Single Law: Application to Veins of the Lower Limb in Man. *Journal of Biomechanical Engineering*, 123:58–65, 2001.

[21] G. A. Bateman. Vascular compliance in normal pressure hydrocephalus. *American Journal of Neuroradiology*, 21(9):1574–1585, 2000.

[22] G. A. Bateman. Vascular hydraulics associated with idiopathic and secondary intracranial hypertension. *American Journal of Neuroradiology*, 23:1180–1186, 2002.

[23] G. A. Bateman, C. R. Levi, P. Schofield, Y. Wang, and E. C. Lovett. The venous manifestations of pulse wave encephalopathy: windkessel dysfunction in normal aging and senile dementia. *Neuroradiology*, 50(6):491–497, 2008.

[24] E. Beeri, S. E. Maier, M. J. Landzberg, T. Chung, and T. Geva. In Vivo Evaluation of Fontan Pathway Flow Dynamics by Multidimensional Phase-Velocity Magnetic Resonance Imaging. *Circulation*, 98(25):2873–2882, 1998.

[25] C. Beggs. Venous hemodynamics in neurological disorders: an analytical review with hydrodynamic analysis. *BMC Medicine*, 11(1):142, 2013.

[26] A. Bermudez and M. E. Vazquez. Upwind methods for hyperbolic conservation laws with source terms. *Computers & Fluids*, 23(8):1049–1071, 1994.

[27] R. Bernetti, V. A. Titarev, and E. F. Toro. Exact solution of the Riemann problem for shallow water equations with discontinuous bottom geometry. *Journal of Computational Physics*, 227:3212–3243, 2008.

[28] R. A. Bhadelia, A. R. Bogdan, and S. M. Wolpert. Cerebrospinal fluid flow waveforms: effect of altered cranial venous outflow. *Neuroradiology*, 40(5):283–292, 1998.

[29] P. J. Blanco and R. A. Feijóo. Role of the variational formulation in the dimensionally-heterogeneous modeling of the human cardiovascular system. In D. Ambrosi, A. Quarteroni, and G. Rozza, editors, *Modelling Physiological Flows*. Springer-Verlag, 2011.

[30] P. J. Blanco, M. R. Pivello, S. A. Urquiza, and R. A. Feijóo. On the potentialities of 3D-1D coupled models in hemodynamics simulations. *Journal of Biomechanics*, 42:919–930, 2009.

[31] P. J. Blanco, P. R. Trenhago, L. G. Fernandes, and R. A. Feijóo. On the integration of the baroreflex control mechanism in a heterogeneous model of the cardiovascular system. *International Journal for Numerical Methods in Biomedical Engineering*, 28(4):412–433, 2012.

[32] P. J. Blanco, S. A. Urquiza, and R. A. Feijóo. Assessing the influence of heart rate in local hemodynamics through coupled 3D-1D-0D models. *International Journal for Numerical Methods in Biomedical Engineering*, 26:890–903, 2010.

[33] M. J. Boorder, J. Hendrikse, and J. ven der Grond. Phase-Contrast Magnetic Resonance Imaging Measurements of Cerebral Autoregulation With a Breath-Hold Challenge: A Feasibility Study. *Stroke*, 35:1350–1354, 2004.

[34] N. Botta, R. Klein, S. Langenberg, and S. Lützenkirchen. Well balanced finite volume methods for nearly hydrostatic flows. *Journal of Computational Physics*, 196:539–565, 2004.

[35] B. S. Brook, S. A. E. G. Falle, and T. J. Pedley. Numerical solutions for unsteady gravity-driven flows in collapsible tubes: evolution and roll-wave instability of a steady state. *Journal of Fluid Mechanics*, 396:223–256, 1999.

[36] B. S. Brook and T. J. Pedley. A model for time-dependent flow in (giraffe jugular) veins: uniforme tube properties. *Journal of Biomechanics*, 35:95–107, 2002.

[37] R. W. Brower, R. R. Reddy, and A. Noordergraaf. Difficulties in the further development of venous hemodynamics. *IEEE Transactions on Bio-Medical Engineering*, 16:335–338, 1969.

[38] A. Caiazzo, G. Montecinos, L. O. Müller, E. M. Haacke, and E. F. Toro. Computational haemodynamics in stenotic internal jugular veins. *Journal of Mathematical Biology*. Submitted for publication to the Journal of Mathematical Biology in May 2013.

[39] A. Canestrelli, A. Siviglia, M. Dumbser, and E. F. Toro. Well-balanced high-order centred schemes for non-conservative hyperbolic systems. Applications to shallow water equations with fixed and mobile bed. *Advances in Water Resources*, 32:834–844, 2009.

[40] S. Canic. Blood flow through compliant vessels after endovascular repair: wall deformations induced by the discontinuous wall properties. *Computing and Visualization in Science*, 4:147–155, 2002.

[41] S. Canic and E. H. Kim. Mathematical analysis of the quasilinear effects in a hyperbolic model blood flow through compliant axi-symmetric vessels. *Mathematical Methods in the Applied Sciences*, 26:1161–1186, 2003.

[42] C. G. Caro, T. J. Pedley, R. C. Schroter, and W. A. Seed. *The Mechanics of the Circulation*. Cambridge University Press, second edition, 2012.

[43] R. D. Caruso, A. E. Rosenbaum, J. K. Chang, and S. E. Joy. Craniocervical junction venous anatomy on enhanced mr images: The suboccipital cavernous sinus. *American Journal of Neuroradiology*, 20:1127–1131, 1999.

[44] C. E. Castro, E. F. Toro, and M. Käser. ADER scheme on unstructured meshes for shallow water: simulation of tsunami waves. *Geophysical Journal International*, 189:1505–1520, 2012.

[45] M. J. Castro, J. M. Gallardo, J. A. López-García, and C. Parés. Well-balanced high order extensions of Godunov's method for semilinear balance laws. *SIAM Journal on Numerical Analysis*, 46:1012–1039p, 2008.

[46] M. J. Castro, P. G. LeFloch, M. L. Munoz-Ruiz, and C. Parés. Why many theories of shock waves are necessary: Convergence error in formally path-consistent schemes. *Journal of Computational Physics*, 227:8107–8129, 2008.

[47] M. J. Castro, A. Milanés, and C. Parés. Well-balanced numerical schemes based on a Generalized Hydrostatic Reconstruction technique. *Mathematical Models and Methods in Applied Science*, 17:2055–2113, 2007.

[48] Vincenzo Casulli, Michael Dumbser, and Eleuterio F. Toro. Semi-implicit numerical modeling of axially symmetric flows in compliant arterial systems. *International Journal for Numerical Methods in Biomedical Engineering*, 28(2):257–272, 2012.

[49] J. Chen, X. Wang, L. Luan, B. Chao, B. Pang, H. Song, and Q. Pang. Biological characteristics of the cerebral venous system and its hemodynamic response to intracranial hypertension. *Chinese Medical Journal*, 125:1303–1309, 2012.

[50] P. Chen, A. Quarteroni, and G. Rozza. Simulation-based uncertainty quantification of human arterial network hemodynamics. *International Journal for Numerical Methods in Biomedical Engineering*, 29(6):698–721, 2013.

[51] C. P. Cheng, R. J. Herfkens, and C. A. Taylor. Inferior vena caval hemodynamics quantified in vivo at rest and during cycling exercise using magnetic resonance imaging. *American Journal of Physiology: Heart and Circulatory Physiology*, 284:H1161–H1167, 2002.

[52] S. Cirovic, C. Walsh, and W. D. Fraser. A Model of Cerebral Blood Flow During Sustained Acceleration. Technical Report DCIEM-98-P-88, Defence and Civil Inst of Environmental Medicine, Downsview ONT (CAN), 1999.

[53] W. A. Conrad. Pressure-flow relationships in collapsible tubes. *IEEE Transactions on Biomedical Engineering*, 16(4):284–295, 1969.

[54] A. Dagain, J.R. Vignes, R. Dulou, G. Dutertre, J.M. Delmas, J. Guerin, and D. Liguoro. Junction between the great cerebral vein and the straight sinus: An anatomical, immunohistochemical, and ultrastructural study on 25 human brain cadaveric dissections. *Clinical Anatomy*, 21(5):389–397, 2008.

[55] A. Dagain, R. Vignes, R. Dulou, J. Delmas, T. Riem, J. Guerin, and D. Liguoro. Study of the junction between the cortical bridging veins and basal cranial venous sinus. *Neurochirurgie*, 55:19–24, 2009.

[56] G. Dal Maso, P. G. LeFloch, and F. Murat. Definition and weak stability of nonconservative products. *Journal de Mathématiques Pures et Appliquées*, 74:483–548, 1995.

[57] K. Das, S. A. Begum, S. Dey, M. A. Quddus, and A. S. Mohiuddin. Sonographic measurement of inferior vena cava diameter - a noninvasive tool to detect acute blood loss. *Ibrahim Medical College Journal*, 5, 2011.

[58] O. Delestre and P. Y. Lagree. A well-balanced finite volume scheme for blood flow simulation. *International Journal for Numerical Methods in Fluids*, 72:177–205, 2012.

[59] T. S. Desser, D. Y. Sze, and R. B. Jeffrey. Imaging and Intervention in the Hepatic Veins. *American Journal of Roentgenology*, 180:1583–1591, 2003.

[60] F. Doepp, F. Paul, J. M. Valduezza, K. Schmierer, and S. J. Schreiber. No Cerebrocervical Venous Congestion in Patients with Multiple Sclerosis. *Annals of Neurology*, 68:173–183, 2010.

[61] G. Drzawiecki, S. Field, I. Moubarak, and J. Li. Vessel growth and collapsible pressure area relationship. *American Journal of Physiology - Heart and Circulatory Physiology*, 273:H2030–H2043, 1997.

[62] M. Dumbser, D. S. Balsara, E. F. Toro, and C. Munz. A unified framework for the construction of one-step finite volume and discontinuous Galerkin schemes on unstructured meshes. *Journal of Computational Physics*, 227:8209–8253, 2008.

[63] M. Dumbser, M. Castro, C. Parés, and E. F. Toro. ADER schemes on unstructured meshes for nonconservative hyperbolic systems: Applications to geophysical flows. *Computers & Fliuds*, 38:1731–1748, 2009.

[64] M. Dumbser, C. Enaux, and E. F. Toro. Finite volume schemes of very high order of accuracy for stiff hyperbolic balance laws. *Journal of Computational Physics*, 227:3971–4001, 2008.

[65] M. Dumbser, A. Hidalgo, M. Castro, C. Parés, and E. F. Toro. FORCE schemes on unstructured meshes II: Non-conservative hyperbolic systems. *Computational Methods in Applied Mechanics and Engineering*, 199:625–647, 2010.

[66] M. Dumbser and E. F. Toro. On Universal Osher-Type Schemes for General Nonlinear Hyperbolic Conservation Laws. *Communications in Computational Physics*, 10:635–671, 2011.

[67] M. Dumbser and E. F. Toro. A Simple Extension of the Osher Riemann Solver to Non-conservative Hyperbolic Systems. *Journal of Scientific Computing*, 48:70–88, 2011.

[68] J. Ekstedt. CSF hydrodynamic studies in man. 2. Normal hydrodynamic variables related to CSF pressure and flow. *Journal of Neurology, Neurosurgery & Psychiatry*, 41(4):345–353, 1978.

[69] D. Elad, R. D. Kamm, and A. H. Shapiro. Choking Phenomena in a Lung-Like Model. *Journal of Biomechanical Engineering*, 109:1–9, 1987.

[70] W. Feng, D. Utriainen, G. Trifan, S. Elias, S. Sethi, J. Hewett, and E. M. Haacke. Characteristics of flow through the internal jugular veins at cervical C2/C3 and C5/C6 levels for multiple sclerosis patients using MR phase contrast imaging. *Neurological Research*, 34:802–809, 2012.

[71] J. E. Flaherty, J. B. Keller, and S. I. Rubinow. Post buckling behavior of elastic tubes and rings with opposite sides in contact. *SIAM Journal on Applied Mathematics*, 23:446–455, 1972.

[72] L. Formaggia, D. Lamponi, and A. Quarteroni. One-dimensional models for blood flow in arteries. *Journal of Engineering Mathematics*, 47:251–276, 2003.

[73] L. Formaggia, A. Quarteroni, and A. Veneziani. *Cardiovascular Mathematics: Modeling and simulation of the circulatory system.* Springer-Verlag Italia, Milano, 2009.

[74] J. B. Fortune and P. Feustel. Effect of patient position on size and location of the subclavian vein for percutaneous puncture. *Archives of Surgery*, 138:996–1000, 2003.

[75] J. Fullana and S. Zaleski. A branched one-dimensional model of vessel networks. *Journal of Fluid Mechanics*, 621:183–204, 2009.

[76] J. Gisolf, J. J. van Lieshout, K. van Heusden, F. Pott, W. J. Stok, and J. M. Karemaker. Human cerebral venous outflow pathway depends on posture and central venous pressure. *Journal of Physiology*, 560:317–327, 2004.

[77] L. Grinberg, T. Anor, E. Cheever, J. R. Madsen, and G. E. Karniadakis. Simulation of the human intracranial arterial tree. *Philosophical Transactions of the Royal Society - A*, 367:2371–2386, 2009.

[78] M. N. Gwilliam, N. Hoggard, D. Capener, P. Singh, A. Marzo, P. K. Verma, and I. D. Wilkinson. MR derived volumetric flow rate waveforms at locations within the common carotid, internal carotid, and basilar arteries. *Journal of Cerebral Blood Flow & Metabolism*, 29:1975–1982, 2009.

[79] E. M. Haacke, W. Feng, D. Utriainen, G. Trifan, Z. Wu, Z. Latif, Y. Katkuri, J. Hewett, and D. Hubbard. Patients with Multiple Sclerosis with Structural Venous Abnormalities on MR Imaging Exhibit and Abnormal Flow Distribution of the Internal Jugular Veins. *Journal of Vascular and Interventional Radiology*, 23:60–68, 2012.

[80] E. M. Haacke, M. Liu, and H. Xu. Investigating venous abnormaities and white matter hypersensitivities in Idiopathic Parkinsons Disease using magnetic resonance imaging. 2013. Submitted for publication.

[81] A. Harten, B. Engquist, S. Osher, and S. R. Chakravarthy. Uniformly High Order Accurate Essentially Non-oscillatory Schemes, III. *Journal of Computational Physics*, 71:231–303, 1987.

[82] B. S. Hertzber, M. A. Kliewer, D. M. DeLong, K. J. Lalouche, E. K. Paulson, M. G. Frederick, and B. A. Carroll. Sonographic Assessment of Lower Limb Vein Diameters: Implications for the Diagnosis and Characterization of Deep Venous Thrombosis. *American Journal of Radiology*, 168:1253–1257, 1997.

[83] A. Hidalgo and M. Dumbser. ADER Schemes for Nonlinear Systems of Stiff Advection-Diffusion-Reaction Equations. *Journal of Scientific Computing*, 48:173–189, 2011.

[84] H. Ho, K. Mithraratne, and P. Hunter. Numerical simulation of blood flow in an anatomically-accurate cerebral venous tree. *IEEE Transactions on Medical Imaging*, 2012.

[85] H. Ito, I. Kanno, H. Iida, J. Hatazawa, E. Shimosegawa, H. Tamura, and T. Okudera. Arterial fraction of cerebral blood volume in humans measured by positron emission tomography. *Annals of Nuclear Medicine*, 15:111–116, 2001.

[86] Y. Itzchak, M. Modan, R. Adar, and V. Deutsch. External iliac artery blood flow in patients with arteriosclerosis obliterans. *American Journal of Roentgenology*, 125:437–441, 1975.

[87] T. Iwabuche, E. Sobata, K. Ebina, H. Tsubakisaka, and M. Takiguchi. Dural sinus pressure: various aspects in human brain surgery in children and adults. *American Journal of Physiology - Heart and Circulatory Physiology*, pages H389–H396, 1986.

[88] G. Jiang and C. Shu. Efficient Implementation of Weighted ENO Schemes. *Journal of Computational Physics*, 126:202–228, 1996.

[89] I. H. Johnston, J. O. Rowan, A. M. Harper, and W. B. Jennett. Raised intracranial pressure and cerebral blood flow. III. Venous outflow tract pressures and vascular resistances in experimental intracranial hypertension. *Journal of Neurology, Neurosurgery & Psychiatry*, 37:392–402, 1974.

[90] I. H. Johnston, J. O. Rowan, A. M. Harper, and W. B. Jennett. Raised intracranial pressure and cerebral blood flow. IV. Intracranial pressure gradients and regional cerebral blood flow. *Journal of Neurology, Neurosurgery & Psychiatry*, 37:392–402, 1974.

[91] R. D. Kamm and A. H. Shapiro. Unsteady flow in a collapsible tube subjected to external pressure or body forces. *Journal of Fluid Mechanics*, 95:1–78, 1979.

[92] J. Kim, N. A. Thacker, P. A. Bromiley, and A. Jackson. Prediction of the Jugular Venous Waveform Using a Model of CSF Dynamics. *American Journal of Neuroradiology*, 28:983–989, 2007.

[93] F. P. Knowlton and E. H. Starling. The influence of variations in temperature and blood pressure on the performance of the isolated mammalian heart. *Journal of Physiology*, 44:206–219, 1912.

[94] R. Kölegard, I. B. Mekjavic, and O. Eiken. Increased distensibility in dependent veins following prolonged bedrest. *European Journal of Applied Physiology*, 106:547–554, 2009.

[95] T. Kutoglu, M. Turut, N. Kocabiyik, H. Ozan, and M. Yildrim. Anatomical analysis of azygos vein system in human cadavers. *Romanian Journal of Morphology & Embryology*, 53:1051–1056, 2012.

[96] A. Laupacis, E. Lillie, A. Dueck, S. Straus, L. Perrier, J. M. Burton, R. Aviv, K. T. MMath, T. Feasby, and J. Spears. Association between chronic cerebrospinal venous insufficiency and multiple sclerosis: a meta-analysis. *Canadian Medical Association Journal*, 183:E1203–E1212, 2011.

[97] R. J. LeVeque. Balancing source terms and flux gradients in high-resolution Godunov methods: the quasi-steady wave-propagation algorithm. *Journal of Computational Physics*, 146:346–365, 1998.

[98] R. J. LeVeque. *Finite-Volume Methods for Hyperbolic Problems*. Cambridge University Press, 2004.

[99] J. R. Levick. *An introduction to cardiovascular physiology*. Hodder Arnold, 2010.

[100] P. Lewis, Psaila J. V., Davies W. T., K. McCarty, and J.P. Woodcock. Measurement of volume flow in the human common femoral artery using a duplex ultrasound system. *Ultrasound in Medicine and Biology*, 10:777–784, 1986.

[101] F. Y. Liang, K. Fukasaku, H. Liu, and S. Takagi. A computational model study of the influence of the anatomy of the circle of willis on cerebral hyperperfusion following carotid artery surgery. *BioMedical Engineering OnLine*, 10(1):84, 2011.

[102] F. Y. Liang, S. Takagi, R. Himeno, and H. Liu. Biomechanical characterization of ventricular-arterial coupling during aging: A multi-scale model study. *Journal of Biomechanics*, 42:692–704, 2009.

[103] F. Y. Liang, S. Takagi, R. Himeno, and H. Liu. Multi-scale modeling of the human cardiovascular system with applications to aortic valvular and arterial stenoses. *Medical and Biological Engineering and Computing*, 47:743–755, 2009.

[104] A. A. Linninger, M. Xenos, B. Sweetman, S. Ponkshe, X. Guo, and R. Penn. A mathematical model of blood, cerebrospinal fluid and brain dynamics. *Journal of Mathematical Biology*, 59:729–759, 2009.

[105] R. G. Louis, M. Loukas, C. T. Wartmann, R. S. Tubbs, N. Apaydin, A. A. Gupta, G. Spentzouris, and J. R. Ysique. Clinical anatomy of the mastoid and occipital emissary veins in a large series. *Surgical Radiologic Anatomy*, 31:139–144, 2009.

[106] J. M. Luce, J. S. Huseby, W. Kirk, and J. Butler. A Starling resistor regulates cerebral venous outflow in dogs. *Journal of Applied Physiology*, 53:1496–1503, 1982.

[107] C. Magnano, C. Schirda, B. Weinstock-Guttman, D. S. Wack, E. Lindzen, D. Hojnacki, N. Bergsland, C. Kennedy, P. Belov, M. G. Dwyer, G. U. Poloni, C. Beggs, and R. Zivadinov. Cine Cerebrospinal Fluid Imaging in Multiple Sclerosis. *Journal of Magnetic Resonance Imaging*, 36:825–834, 2012.

[108] E. Marchandise and P. Flaud. Accurate modelling of unsteady flows in collapsible tubes. *Computer Methods in Biomechanics and Biomedical Engineering*, 13:279–290, 2010.

[109] K. S. Matthys, J. Alastruey, J. Peiró, A. W. Khir, P. Segers, P. R. Verdonck, K. H. Parker, and S. J. Sherwin. Pulse wave propagation in a model human arterial network: Assessment of 1-D numerical simulations against *in vitro* measurements. *Journal of Biomechanics*, 40:3476–3486, 2007.

[110] G. Montecinos, L. Müller, and E. F. Toro. Hyperbolic reformulation of a 1D viscoelastic blood flow model and ADER finite volume schemes. *Journal of Computational Physics*, 2014. In Press.

[111] G. I. Montecinos, C. E. Castro, M. Dumbser, and E. F. Toro. Comparison of solvers for the generalized Riemann problem for hyperbolic systems with source terms. *Journal of Computational Physics*, 231:6472–6494, 2012.

[112] A. H. Moreno, A. I. Katz, and L. D. Gold. An integrated approach to the study of the venous system with steps toward a detailed model of the dynamics of venous return to the right heart. *IEEE Transactions on Bio-Medical Engineering*, 16:308–324, 1969.

[113] L. O. Müller, G. I. Montecinos, and E. F. Toro. Some issues in modelling venous haemo-dynamics. In P. García-Navarro M. E. Vázquez-Cendón, A. Hidalgo and L. Cea, editors, *Numerical Methods for Hyperbolic Equations: Theory and Applications. An international conference to honour Professor E. F. Toro*, pages 347–354. Taylor & Francis Group, Boca Raton London New York Leiden, 2013.

[114] L. O. Müller, C. Parés, and E. F. Toro. Well-balanced high-order numerical schemes for one-dimensional blood flow in vessels with varying mechanical properties. *Journal of Computational Physics*, 242:53 – 85, 2013.

[115] L. O. Müller and E. F. Toro. An enhanced closed-loop model for the study of cerebral venous blood flow. Submitted for publication to the Journal of Biomechanics in March 2014.

[116] L. O. Müller and E. F. Toro. Well-balanced high-order solver for blood flow in net-works of vessels with variable properties. *International Journal for Numerical Methods in Biomedical Engineering*, 29:1388–1411, 2013.

[117] L. O. Müller and E. F. Toro. A global multiscale mathematical model for the human circulation with emphasis on the venous system. *International Journal for Numerical Methods in Biomedical Engineering*, pages n/a–n/a, 2014. In Press.

[118] L. O. Müller, E. F. Toro, and E. M. Haacke. A theoretical study of the CCSVI condition. Submitted for publiction to the Journal of the Royal Society Interface in March 2014.

[119] M. L. Munoz-Ruiz and C. Parés. On the Convergence and Well-Balanced Property of Path-Conservative Numerical Schemes for Systems of Balance Laws. *Journal of Scientific Computing*, 48:274–295, 2011.

[120] J. P. Murgo, N. Westerhof, J. P. Giolma, and S. A. Altobelli. Aortic input impedance in normal man: relationship to pressure wave forms. *Circulation*, 62(1):105–16, 1980.

[121] J. P. Mynard. *Computer modelling and wave intensity analysis of perinatal cardiovascular function and dysfunction*. PhD thesis, Department of Paedriatics, The University of Melbourne, 2011.

[122] J. P. Mynard, M. R. Davidson, D. J. Penny, and J. J. Smolich. A simple, versatile valve model for use in lumped parameter and one-dimensional cardiovascular models. *International Journal for Numerical Methods in Biomedical Engineering*, 28(6-7):626–641, 2012.

[123] M. Nabeshima, F. Moriyasu, K. Nishikawa, N. Hamato, M. Fujimoto, and T. Nada. Azygos venous blood flow: measurement with direct bolus imaging. *Radiology*, 195:467–470, 1995.

[124] J. H. Nippa, R. H. Alexander, and R. Folse. Pulse wave velocity in human veins. *Journal of Applied Physiology*, 30:558–563, 1971.

[125] A. Noordergraaf and E. Kresch. Introduction. *IEEE Transactions on Bio-Medical Engineering*, 16:235, 1969.

[126] L. Oguzkurt, F. Tercan, M. A. Pourbagher, O. Kizilkilic, R. Turkoz, and F. Boyvat. Computed tomography findings in 10 cases of iliac vein compression (May-Thurner) syndrome. *Europen Journal of Radiology*, 55:421–245, 2005.

[127] M. S. Olufsen, J. Ottesen, H. Tran, L. M. Ellwein, L. A. Lipsitz, and V. Novak. Blood pressure and blood flow variation during postural change from sitting to standing: model development and validation. *Journal of Applied Physiology*, 99:1523–1537, 2005.

[128] S. Osher and F. Solomon. Upwind difference schemes for hyperbolic systems of conservation laws. *Mathematcs of Computation*, 38:339–374, 1982.

[129] C. Parés. Numerical methods for nonconservative hyperbolic systems: a theoretical framework. *SIAM Journal on Numerical Analysis*, 44:300–321, 2006.

[130] C. Parés and M. Castro. On the well-balance property of Roe's method for nonconservativehyperbolic systems. Applications to shallow-water systems. *ESAIM: Mathematical Modelling and Numerical Analysis*, 38:821–852, 2004.

[131] M. C. Patel, L. H. Berman, H. A. Moss, and S. J. McPherson. Subclavian and Internal Jugular Veins at Doppler US: Abnormal Cardiac Pulsatility and Respiratory Phasicity as a Predictor of Complete Central Occlusion. *Radiology*, 211(2):579–583, 1999.

[132] T. J. Pedley, B. S. Brook, and R. S. Seymour. Blood pressure and flow rate in the giraffe jugular vein. *Philosophical Transactions: Biological Sciences*, 351:855–866, 1996.

[133] P. Reymond, F. Merenda, F. Perren, D. Rüfenacht, and N. Stergiopulos. Validation of a one-dimensional model of the systemic arterial tree. *American Journal of Physiology - Heart and Circulatory Physiology*, 297:H208–H222, 2009.

[134] M. A. Rhodes. *CCSVI as the cause of multiple sclerosis: the science behind the controversial theory.* McFarland & Company, Inc., 2011.

[135] P. L. Roe. Upwind differencing schemes for hyperbolic conservation laws with source terms. In C. Carasso, P. Raviart, and D. Serre, editors, *Proc. First International Conference on Hyperbolic Problems*, pages 41–51. Springer, 1986.

[136] S. Rossitti. Pathophysiology of increased cerebrospinal fluid pressure associated to brain arteriovenous malformations: The hydraulic hypothesis. *Surgical Neurology International*, 4(1):42, 2013.

[137] B. W. Schaaf and P. H. Abbrecht. Digital computer simulation of human systemic arterial pulse wave transmission: a nonlinear model. *Journal of Biomechanics*, 5:345–364, 1972.

[138] B. Schaller. Physiology of cerebral venous blood flow: from experimental data in animals to normal function in humans. *Brain Research Reviews*, 46:243–260, 2004.

[139] B. D. Seeley and D. F. Young. Effect of geometry on pressure losses across models of arterial stenoses. *Journal of Biomechanics*, 4:430–448, 1976.

[140] A. H. Shapiro. Steady flow in collapsible tubes. *Journal of Biomechanical Engineering*, 99:126–147, 1977.

[141] C. Sheng, S. N. Sarwal, K. C. Watts, and A. E. Marble. Computational simulation of blood flow in human systemic circulation incorporating an external force field. *Medical and Biological Engineering and Computing*, 33, 1995.

[142] S. J. Sherwin, L. Formaggia, J. Peiró, and V. Franke. Computational modelling of 1D blood flow with variable mechanical properties and its application to the simulation of wave propagation in the human arterial system. *International Journal for Numerical Methods in Fluids*, 43:673–700, 2003.

[143] S. J. Sherwin, V. Franke, J. Peiró, and K. H. Parker. One-dimensional modelling of a vascular network in space-time variables. *Journal of Engineering Mathematics*, 47:217–250, 2003.

[144] A. V. Singh and P. Zamboni. Anomalous venous blood flow and iron deposition in multiple sclerosis. *Journal of Cerebral Blood Flow & Metabolism*, 29:1867–1878, 2009.

[145] A. Siviglia and M. Toffolon. Steady analysis of transcritical flows in collapsible tubes with discontinuous mechanical properties: implications for arteries and veins. *Journal of Fluid Mechanics*, 736:195–215, 2013.

[146] M. F. Snyder and V. C. Rideout. Computer simulation studies of the venous circulation. *IEEE Transactions on Bio-Medical Engineering*, 16:325–334, 1969.

[147] S. Standring. *Gray's anatomy: the anatomical basis of clinical practice.* Gray's Anatomy: The Anatomical Basis of Clinical Practice. Churchill Livingstone/Elsevier, 2008. www.expertconsultbook.com EEM6FRM.

[148] B. N. Steele, J. Wan, J. P. Ku, T. J. Hughes, and C. A. Taylor. In Vivo Validation of a One-Dimensional Finite-Element Method for Predicting Blood Flow in Cardiovascular Bypass Grafts. *IEEE Transactions on Biomedical Engineering*, 50:649–655, 2003.

[149] N. Stergiopulos, D. F. Young, and T. R. Rogge. Computer simulation of arterial flow with applications to arterial and aortic stenoses. *Journal of Biomechanics*, 25(12):1477 – 1488, 1992.

[150] S. A. Stevens, M. Previte, W. D. Lakin, N. J. Thakore, P. L. Penar, and B. Hamschin. Idiopathic intracranial hypertension and transverse sinus stenosis: a modelling study. *Mathematical Medicine and Biology*, 24:85–109, 2007.

[151] K. W. Stock, S. G. Wetzel, P. A. Lyrer, and E. W. Rad. Quantification of blood flow in the middle cerebral artery with phase-contrast MR imaging. *European Radiology*, 10(11):1795–1800, 2000.

[152] S. Stoquart-ElSankari, P. Lehmann, A. Villette, M. Czosnyka, M. Meyer, H. Deramond, and O. Baledent. A phase-contrast MRI study of physiologic cerebral venous flow. *Journal of Cerebral Blood Flow & Metabolism*, 29:1208–1215, 2009.

[153] M. D. Stringer, M. Restieaux, A. L. Fisher, and B. Crosado. The vertebral venous plexuses: The internal veins are muscular and external veins have valves. *Clinical Anatomy*, 25:609–618, 2012.

[154] Y. Sun, M. Beshara, R. J. Lucariello, and S. A. Chiaramida. A comprehensive model for right-left heart interaction under the influence of pericardium and baroreflex. *American Journal of Physiology*, 272:H1499–515, 1997.

[155] S. Tanoue, H. Kiyosue, M. Okahara, Y. Sagara, Y. Hori, J. Kashiwagi, and H. Mori. Para-Cavernous Sinus Venous Structures: Anatomic Variations and Pathologic Conditions Evaluated on Fat-Suppressed 3D Fast Gradient-Echo MR Images. *American Journal of Neuroradiology*, 27:1083–1089, 2006.

[156] E. F. Toro. On Glimm-related schemes for conservation laws. Technical Report MMU-9602, Department of Mathematics and Physics, Manchester Metropolitan University, 1996.

[157] E. F. Toro. *Shock-Capturing Methods for Free-Surface Shallow Flows.* Wiley and Sons Ltd., Chichester, New York, first edition, 2001.

[158] E. F. Toro and S. J. Billett. Centred TVD schemes for hyperbolic conservation laws. *IMA Journal of Numerical Analysis*, 20:47–79, 2000.

[159] E. F. Toro, R. Millington, and L. Nejad. Towards very high order Godunov schemes. In E. F. Toro, editor, *Godunov Methods. Theory and Applications*, volume 1, pages 897–902. Kluwer/Plenum Academic Publishers, New York, Boston and London, 2001. Conference in Honour of S K Godunov.

[160] E. F. Toro and A. Siviglia. Simplified blood flow model with discontinuous vessel properties: Analysis and exact solutions. In D. Ambrosi, A. Quarteroni, and G. Rozza, editors, *Modeling of Physiological Flows*, volume 5 of *MS&A Modeling, Simulation and Applications*, pages 19–39. Springer Milan, 2012.

[161] E. F. Toro and A. Siviglia. Flow in collapsible tubes with discontinuous mechanical properties: mathematical model and exact solutions. *Communications in Computational Physics*, 13(2):361–385, 2013.

[162] E. F. Toro and V. A. Titarev. Solution of the generalized Riemann problem for advection-reaction equations. *Proceedings of the Royal Society A*, 458:271–281, 2002.

[163] E.F. Toro. *Riemann Solvers and Numerical Methods for Fluid Dynamics: A Practical Introduction*. Springer-Verlag, Berlin Heidelberg, third edition, 2009. ISBN 978-3-540-25202-3.

[164] S. A. Urquiza, P. J. Blanco, M. J. Vénere, and R. A. Feijóo. Multidimensional modelling for the carotid artery blood flow. *Computational Methods in Applied Mechanics and Engineering*, 2005.

[165] M. Ursino. A mathematical study of human intracranial hydrodynamics part 1. The cerebrospinal fluid pulse pressure. *Annals of Biomedical Engineering*, 16(4):379–401, 1988.

[166] M. Ursino and C. A. Lodi. A simple mathematical model of the interaction between intracranial pressure and cerebral hemodynamics. *Journal of Applied Physiology*, 82:1256–1269, 1997.

[167] D. Utriainen, W. Feng, S. Elias, Z. Latif, D. Hubbard, and E. M. Haacke. Using magnetic resonance imaging as a means to study chronic cerebral spinal venous insufficiency in multiple sclerosis patients. *Techniques in Vascular and Interventional Radiology*, 15:101–112, 2012.

[168] F. N. van der Vosse and N. Stergiopulos. Pulse wave propagation in the arterial tree. *Annual Review in Fluid Mechanics*, 43:467–499, 2011.

[169] K. van Heusden, J. Gisolf, W. J. Stok, S. Dijkstra, and J. M. Karemaker. Mathematical modeling of gravitational effects on the circulation: importance of the time course of venous pooling and blood volume changes in the lungs. *American Journal of Physiology - Heart and Circulatory Physiology*, 291:H2152–H2165, 2006.

[170] Y. V. Vassilevski, S. S. Simakov, and S. A. Kapranov. A multi-model approach to intravenous filter optimization. *International Journal for Numerical Methods in Biomedical Engineering*, 26(7):915–925, 2010.

[171] M. E. Vázquez-Cedón. Improved treatment of source termns in upwind schemes for the shallow water equations in channels with irregular geometry. *Journal of Computational Physics*, 148:497–526, 1999.

[172] J. Vignes, A. Dagain, J. Guerin, and D. Liguoro. A hypothesis of cerebral venous system regulation based on a study of the junction between the cortical bridging veins and the superior sagittal sinus. *Journal of Neurosurgery*, 107:1205–1210, 2007.

[173] N. Wafae, K. Hirose, C. Franco, G. C. Wafae, C. R: Ruiz, L. Daher, and O. C. Person. The anatomy of the human thyroid veins and its surgical application. *Folia Morphologica*, 67:221–225, 2008.

[174] L. Wei-hua, W. Shao-ping, and L. Xin. Anatomical observation of the retromandibular vein by mandibular angle ostectomy. *Journal of Clinical Rehabilitative Tissue Engineering Research*, 14:9113–9117, 2010.

[175] J. D. Werner, G. P. Siskin, K. Mandato, M. Englander, and A. Herr. Review of venous anatomy for venographic interpretation in chronic cerebrospinal venous insufficiency. *Journal of Vascular and Interventional Radiology*, 22:1681–1690, 2011.

[176] R. L. Wolf, B. F. King, V. E. Torres, D. M. Wilson, and R. L. Ehman. Measurement of normal renal artery blood flow: cine phase-contrast MR imaging vs clearance of p-aminohippurate. *American Journal of Roentgenology*, 161:995–1002, 1993.

[177] D. Xiu and S. J. Sherwin. Parametric uncertainty analysis of pulse wave propagation in a model of a human arterial network. *Journal of Computational Physics*, 226:1385–1407, 2007.

[178] Y. Yu, J. Chen, Z. Si, G. Zhao, S. Xu, G. Wang, F. Ding, L. Luan, L. Wu, and Q. Pang. The Hemodynamic Response of the Cerebral Bridging Veins to Changes in ICP. *Neurocritical Care*, 12(1):117–123, 2010.

[179] H. Zachrisson, M. Lindenberger, D. Hallman, M. Ekman, D. Neider, and T. Länne. Diameter and compliance of the greater saphenous vein - effect of age and nitroglicerine. *Clinical Physiology and Functional Imaging*, 31:300–306, 2011.

[180] M. Zagzoule and J. P. Marc-Vergnes. A global mathematical model of the cerebral circulation in man. *Journal of Biomechanics*, 19:1015–1022, 1986.

[181] P. Zamboni and R. Galeotti. The chronic cerebrospinal venous insufficiency syndrome. *Phlebology*, 25:269–279, 2010.

[182] P. Zamboni, R. Galeotti, E. Menegatti, A. M. Malagoni, S. Gianesini, I. Bartolomei, F. Mascoli, and F. Salvi. A prospective open-label study of endovascular treatment of chronic cerebrospinal venous insufficiency. *Journal of Vascular Surgery*, 50:1348–1358, 2009.

[183] P. Zamboni, R. Galeotti, E. Menegatti, A. M. Malagoni, G. Tacconi, S. Dall'Ara, I. Bartolomei, and F. Salvi. Chronic cerebrospinal venous insufficiency in patients with multiple sclerosis. *Journal of Neurology, Neurosurgery and Psychiatry*, 80:392–399, 2009.

[184] P. Zamboni, E. Menegatti, B. Weinstock-Guttman, M. G. Dwyer, C. Schirda, A. M. Malagoni, D. Hojnacki, C. Kennedy, N. Bergsland, C. Magnano, I. Bartolomei, F. Salvi, and R. Zivadinov. Hypoperfusion of brain parenchyma is associated with the severity of chronic cerebrospinal venous insufficiency in patients with multiple sclerosis. *BMC Medicine*, 9, 2011.

[185] P. Zamboni, E. Menegatti, B. Weinstock-Guttman, C. Schirda, J. L. Cox, A. M. Malagoni, D. Hojnacki, C. Kennedy, E. Carl, M. G. Dwyer, N. Bergsland, R. Galeotti, S. Hussein, I. Bartolomei, F. Salvi, M. Ramanathan, and R. Zivadinov. CSF dynamics and brain volume in multiple sclerosis are associated with extracranial venous flow anomalies: a pilot study. *International Angiology*, 29:140–148, 2010.

[186] R. S. Zitnik, F. S. Rodich, H. W. Marshall, and E. H. Wood. Continuously recorded changes of thoracic aortic blood flow in man in response to leg exercise in supine position. *Circulation Research*, 17(2):97–105, 1965.

[187] R. Zivadinov, C. Magnano, R. Galeotti, C. Schirda, E. Menegatti, B. Weinstock-Guttman, K. Marr, I. Bartolomei, J. Hagemeier, A. Malagoni, D. Hojnacki, K. Kennedy, E. Carl, C. Beggs, F. Salvi, and P. Zamboni. Changes of cine cerebrospinal fluid dynamics in patients with multiple sclerosis treated with percutaneous transluminal angioplasty: A case-control study. *Journal of Vascular and Interventional Radiology*, 24(6):829–838, 2013.

[188] R. Zivadinov, G. U. Poloni, C. Schirda, C. Magnano, E. Carl, N. Bergsland, D. Hojnacki, C. Kennedy, C. Beggs, M. G. Dwyer, and B. Weinstock-Guttman. Decreased brain venous vasculature visibility on susceptibility-weighted imaging venography in patients with multiple sclerosis is related to chronic crebrospinal venous insufficiency. *BMC Neurology*, 11, 2011.